

**Particle Dispersion, Agglomeration and Deposition in Fully-Coupled
Turbulent Channel Flow using Large Eddy Simulation and Discrete
Element Method**

By

Mohammad Afkhami

Submitted in accordance with the requirements for the degree of
Doctor of Philosophy



The University of Leeds
School of Chemical and Process Engineering

December, 2014

The candidate confirms that the work submitted is his own, except where work which has formed part of jointly authored publications has been included. The contribution of the candidate and the other authors to this work has been explicitly indicated below. The candidate confirms that appropriate credit has been given within the thesis where reference has been made to the work of others.

In this thesis work from a jointly authored publication (Afkhami et al. 2015) has been used in section 5.1. The work contained within this publication is directly attributable to the candidate where the co-authors have provided overall guidance and expertise.

Afkhami, M., Hassanpour, A., Fairweather, M., and Njobuenwu, D. O. 2015. Fully coupled LES-DEM of particle interaction and agglomeration in a turbulent channel flow. *Computers & Chemical Engineering*, 78, 24-38.

This copy has been supplied on the understanding that it is copyright material and that no quotation from the thesis may be published without proper acknowledgement.

The right of Mohammad Afkhami to be identified as Author of this work has been asserted by him in accordance with the Copyright, Designs and Patents Act 1988.

© 2015 The University of Leeds and Mohammad Afkhami

Acknowledgements

My most sincere gratitude must be expressed first and foremost to my supervisors, Dr. Ali Hassanpour and Professor Michael Fairweather who have both provided me with invaluable guidance, advice and encouragement throughout the duration of my research. Special thanks must also go to Dr. Derrick Njobuenwu who has offered support and guidance on all aspects of my research.

I must extend my gratitude to my peers and colleagues in the Institute of Particle Science and Engineering and in particular to the nuclear research group, including Professor Bruce Hanson, Professor Simon Biggs, Professor Mojtaba Ghadiri, Dr. Tariq Mahmud, Dr. Joseph Antony, Dr. James Young, Dr. Timothy Hunter, Dr. David Harbottle, Dr. Jonathan Adams, Dr. Jun Yao, Dr. Robert Woolley, Dr. Hugh Rice, Dr. Marco Colombo, Dr. Massih Pasha, Dr. Matthew Garlick, Dr. Akinola Falola and all of the student members. The nuclear research group meetings, and frontiers and student seminars have provided a great opportunity to learn about different research areas, discuss ideas and gain different perspectives on my research work. I am also thankful to the people whose technical assistance made this work possible, the IT and ARC1 team of the University and the support team from DEM Solutions Ltd.

Without the financial support of the Engineering and Physical Science Research Council (EPSRC) this research would not have been able to take place and as such I am very grateful to have been awarded the opportunity to undertake this research.

Finally thanks must go to my family; my parents, Hossein and Fatemeh, and my brother and sister, Ehsan and Layla who have always been hugely supportive in everything I have done and without their unwavering support I would not be where I am today.

Abstract

The incentive for this research is to gain insight into fundamental aspects of turbulent fluid-particle flows. The project investigates the influence of inter-particle collisions on the particle and fluid phase variables in the context of particle agglomeration, dispersion and deposition for turbulent bounded flows laden with low particle numbers. The mathematical modelling technique used is large eddy simulation (LES), with flow solutions provided by this method coupled to a discrete element method (DEM) to predict particle motion and interaction. The results have been compared with single-phase bounded flows in order to investigate the effect of the particles on turbulence statistics. The four-way coupled simulations are also contrasted with one-way coupled (flow affects the particles only) results in which the inelastic collisions between particles are neglected.

The influence of different particle surface energies, particle size, particle density, particle concentration and flow Reynolds numbers on particle agglomeration is investigated. The turbulent structure of the flow is found to dominate the motion of the particles, although the agglomeration rate is found to be strongly influenced by all of the variables noted above, with most of the particle-particle interactions taking place at locations close to the channel walls, aided by the higher turbulence levels and concentration of particles in these regions.

The research proposed makes an original contribution to the literature in applying advanced predictive techniques which have not been coupled and applied to the problem of cohesive particle-interaction effects in turbulent flows before. It yields a fundamental understanding of how particles interact, and how these interactions result in the formation of agglomerates which affect the dispersion and deposition of particles within the flow. The overall results are relevant, and underpinning, to processes employed in a wide range of applications in the industrial and health sectors.

Table of Content

1	Introduction	1
1.1	Context and Rationale	1
1.2	Industrial Relevance	1
1.3	Objectives and thesis structure	5
2	Literature Review	7
2.1	Introduction	7
2.2	Introduction to two-phase flow	7
2.3	Experimental Approaches to Two-Phase Flow	11
2.3.1	Laser Doppler Anemometry (LDA)	11
2.3.2	Phase Doppler Anemometry (PDA)	12
2.3.3	Ultrasonic Doppler Velocity Profiling (UDVP)	12
2.3.4	Particle Image Velocimetry (PIV)	13
2.3.5	Holographic Particle Image Velocimetry (HPIV)	13
2.4	Numerical Approaches to the Fluid Phase	14
2.4.1	Direct Numerical Simulation	14
2.4.2	Large Eddy Simulation	15
2.4.3	Reynolds Averaged Navier Stokes	18
2.4.4	Comparison of DNS, LES and RANS	19
2.5	Numerical Approaches to the Particle Phase	20
2.5.1	Numerical Approaches to Particle Motion	20
2.5.2	Fluid-Particle Coupling Schemes	26
2.5.3	Numerical Approaches to Inter-Particle and Wall-Particle Collisions	28
2.6	Review of Numerical and Experimental Studies in Turbulent Bounded Flow	34
2.6.1	Single-Phase Experiments	34
2.6.2	Two-Phase Experiments	35
2.6.3	Single-Phase Numerical Studies	38

2.6.4	Two-Phase Numerical Studies	38
2.7	Conclusion of the Literature Review	48
3.	Numerical Methodology of the LES-DEM Approach	49
3.1	Introduction	49
3.2	Fluid-Phase Modelling	49
3.3	Large Eddy Simulation	50
3.3.1	Filtering Operation	50
3.3.2	Governing Equations	50
3.3.3	Sub-Grid Scale Modelling	51
3.3.4	Boundary Conditions	53
3.3.5	Solution Procedure	56
3.4	Discrete Element Method	59
3.4.1	Governing equations	59
3.4.2	Interaction: fluid forces on particle	63
3.4.3	Interaction: particle forces on fluid	63
3.4.4	Interaction: particle forces on particle	65
4	Fluid-Particle Coupling and Comparison	73
4.1	Flow Configuration and Initial Conditions	74
4.2	Single-Phase Flow	76
4.2.1	Shear Reynolds number 150	78
4.2.2	Shear Reynolds number 300	82
4.2.3	Shear Reynolds number 590	85
4.2.4	Conclusion on single phase	87
4.3	Two-Phase Flow	87
4.3.1	Effects of particles and agglomeration on fluid velocity statistics	89
4.3.2	Effects of particle-particle contacts on particle velocity statistics	97
4.4	Conclusion to fluid-particle coupling and comparison	114

5	Sensitivity Studies on Particle Dispersion and Agglomeration	116
5.1	Effects of surface energy on particle agglomeration	117
5.2	Effects of Reynolds number on particle agglomeration	129
5.3	Effects of particle density on agglomeration	139
5.4	Effects of particle size on agglomeration	161
5.5	Effects of particle concentration on agglomeration	167
5.6	Conclusions to sensitivity studies on particle dispersion and agglomeration	171
6	Particle Dispersion, Deposition and Agglomeration	173
6.1	Effects of gravity on particle dispersion, deposition and agglomeration	173
6.2	Effects of surface energy on dispersion, deposition and agglomeration	176
6.3	Conclusions to Particle Dispersion, Deposition and Agglomeration	194
7	Conclusion and Further Work	196
7.1	Conclusion	196
7.2	Recommendations for Further Work	200
	Bibliography	202
	Appendix A: Sensitivity Study on Fluid Phase	218
A. 1	Mesh Size	218
A. 2	Time Step	221
A. 3	Subgrid Scale Models	223
A. 4	Spatial Discretisation	225
A. 5	Gradient and Derivatives	227
A. 6	Pressure-Velocity Coupling Method	229
A. 7	Ending note to sensitivity study on fluid phase	231

List of tables

Table 1.1	Measured and calculated values of the work of adhesion for different systems	4
Table 1.2	Elastic modulus and Poisson's ratio for materials	4
Table 2.1	Selected studies on liquid–solid/gas–solid channel flows	35
Table 2.2	Selected studies on liquid–solid/gas–solid channel flows	37
Table 4.1	Particle physical properties	88
Table 4.2	Particle parameters used in the simulations	88
Table 4.3	Comparison of effect of main forces (drag and .lift) on particles (streamwise)	113
Table 4.4	Comparison of effect of main forces (drag and .lift) on particles (wall-normal)	114
Table 5.1	Particle physical properties	116
Table 5.2	Fluid and particle parameters used in the simulations	117
Table 5.3	Sticking velocity of different surface energy particles	126
Table 5.4	Sticking velocity of different density particles (0.05 j m^{-2})	150
Table 5.5	Comparison of effect of main forces (drag and .lift) on particles ($t = 0.2 - 0.22\text{s}$)	156
Table 5.6	Comparison of effect of mean contact attributes on particles ($t = 0.2 - 0.22\text{s}$)	159
Table 5.7	Sticking velocity of different sized particles	165
Table 6.1	Comparison of effect of the mean of main forces (Gravity, Lift, and Drag) on particles ($t = 7,948$)	176
Table 6.2	Sticking velocity of different surface energy particles	187
Table 6.3	Comparison of effect of main forces (Gravity, Lift, and Drag) on particles ($t = 7,948$)	190

Nomenclatures

Roman Letters

A	Area
a	Particle contact radius
a_c	Particle contact radius at JKR pull-off force
B	Number of particle-particle contacts
C	SGS model parameter
C_D	Stokes coefficient, dimensionless
C_{fs}	Static friction coefficient
C_{fs}	Rolling friction coefficient
d_p	Particle diameter
e	Coefficient of restitution
E^*	Equivalent Young's modulus
E_i	Impact kinetic energy
$-E_n$	Normal energy loss
E_r	Rebound kinetic energy
E_T	Total energy
$-E_T$	Total energy loss
$-E_t$	Tangential energy loss
f_c	Pull-off force
f_{ce}	Elastic JKR pull-off force
f_i	Source term
F_c	Contact force
$F_{coupling}$	Coupling force
F_g	Gravitational force
F_L	Lift force
$F_{L,Mei}$	Mei Lift Force
$F_{L,Saff}$	Saffman Lift Force
F_{max}^*	JKR equivalent maximum contact force
F_n	Normal contact force
F_{nc}	Non-contact force
F_r	Rolling Friction
F_t	Tangential contact force

F_{van}	Van der Waals force
g	Gravitational acceleration
G	Shear modulus
G	Filter function
G^*	Equivalent shear modulus
h	half height of rectangular channel
I	Moment of inertia
K	Von Karman constant
k_n	Normal contact stiffness
k_p	Particle kinetic energy
k_s	Subtest kinetic energy
k_t	Tangential contact stiffness
l	Length scale
L_s	Mixing length for the subgrid scales
L_x, L_y, L_z	channel length in x, y, z directions
m_p	Particle mass
M	Torque
m^*	Equivalent mass
N	Total number of sample points of the particle
n_b	Number of particle-particle contacts
n_p^{max}	Local particle concentration
n_p^{max}	Maximum particle number density
n_c	Number of sample points
n_{col}	Number of collisions
n_p	Particle number density
n_i	normal vector directed from a particle centroid to its contact
R	Particle radius
R^*	Equivalent radius
Re	Reynolds number
Re_p	Particle Reynolds number
Re_s	Particle Reynolds number of shear flow
S	Rate of strain
SE	Surface Energy
St	Particle Stokes number

t	Time
t_h	Hertz time of contact
t_{crit}	Critical time-step for a mass-spring system
Δt	Integration time-step
T_R	Rayleigh time-step
$T.K.E$	Turbulent Kinetic Energy
U_x	Time-averaged fluid velocity in streamwise direction
$U'_{x,rms}, U'_{y,rms}, U'_{z,rms}$	Fluid velocity fluctuation components in x, y, z directions
$U'_x U'_z$	Time-averaged xz -component of the Reynolds stress tensor
u_b	Bulk fluid velocity
u_p	Wall parallel velocity
u_x, u_y, u_z	Fluid velocity components in x, y, z directions
u_τ	Shear velocity
V	Volume
V_p	Particle Volume
V_x	Time-averaged particle velocity in streamwise direction
$V'_{x,rms}, V'_{y,rms}, V'_{z,rms}$	Particle fluctuation components in x, y, z directions
$V'_x V'_z$	Time-averaged xz -component of the particle Reynolds stress tensor
v_{crit}	Particle critical velocity
v_i	Particle impact velocity
v_n	Particle velocity normal
v_r	Particle rebound velocity
v_s	Particle sticking velocity
v_t	Tangential particle velocity
v_x, v_y, v_z	Particle velocity components in x, y, z directions
v_{12}	Relative impact velocity between two particles
$v_{n,12}$	Relative impact velocity normal between two particles
$v_{t,12}$	Relative impact velocity tangential between two particles
W_e	Elastic work
x, y, z	Cartesian coordinate system
$\Delta x, \Delta y, \Delta z$	Grid resolution in x, y, z directions

Greek Alphabets

α_f	Contact breakage overlap of JKR model
α_n	Normal contact overlap
α_t	Tangential contact overlap
B	Viscous damping coefficient
δ_{ij}	Cartesian components of unit tensor (Kronecker delta)
ϕ_f	Fluid Volume fraction (total)
ϕ_p	Solid Volume fraction (total)
$\phi_{p,m}$	Solid Mass fraction (total)
Δ	Filter width
E	Voidage
ε_s	Solid volume fraction per Cell
ΔF_s	Increment of tangential force
H	Shear rate
ρ_f	Fluid Density
ρ_p	Particle Density
Λ	Mean number density
τ_F	Fluid time step
τ_P	Particle time step
τ_{ij}	Mean viscous stress tensor
τ_w	Mean wall shear stress
M	Dynamic viscosity
ν	Kinematic viscosity
ν_s	SGS viscosity
Y	Poisson's ratio
v_r	Normal relative velocity of two particles in contact
ω_f	Vorticity of flow
ω_p	Particle angular velocity
γ_n	Normal damping coefficient
γ_t	Tangential damping coefficient

List of Acronyms

CFD	Computational Fluid Dynamics
DNS	Direct Numerical Simulation
HPIV	Holographic Particle Image Velocimetry
HWA	Hot-wire Anemometry
LDA	Laser Doppler Anemometry
LDV	Laser Doppler Velocimetry
LES	Large Eddy Simulation
LPT	Lagrangian Particle Tracking
PDA	Phase Doppler Anemometry
PDF	Probability Density Function
PIV	Particle Image Velocimetry
RANS	Reynolds Averaged Navier Stokes
SGS	Sub-Grid Scale

Superscripts

(+)	Dimensionless form of variable
-----	--------------------------------

1 Introduction

1.1 Context and Rationale

In our day to day lives we are constantly exposed to fluid flows containing solid particles. Particle-fluid two- or multi-phase flows are part of us; we breathe them in, drink them, and they flow in our blood. These mixtures can be found in nature, such as the lava expelled by volcanoes to fundamental technologies such as cement, ceramics, and plastics. Within any industry, the majority of the most demanding flows through channels, ducts, or pipes are those in which turbulence plays an imperative role, or indeed, in which turbulence is the phenomenon of interest. From a practical point of view, fluids encountered usually contain solid particles and are found in many engineering systems including aerospace, biological, chemical, civil, mechanical, and nuclear applications. Therefore, understanding the fundamental aspects of turbulent fluid-particle flows is of relevance to processes employed in a wide range of applications, such as oil and gas flow assurance in pipes, powder dispersion from dry powder inhalers and particle re-suspension in nuclear waste ponds. Despite their importance, little is known about the influence of inter-particle collisions on the particle and fluid phase characteristics in the context of particle dispersion, agglomeration and deposition in such turbulent, bounded flows laden with large particle numbers.

1.2 Industrial Relevance

A major flow assurance problem encountered in oil and gas production is ‘scale’ which is formed by inorganic, sparingly soluble salts from aqueous brines. The build-up of scale on pipe walls occurs under supersaturated conditions, for instance in the mixing of incompatible types of water; formation water from the bottom hole and the injected seawater. The deposited scale adheres to the surfaces of the producing well tubing and on parts of water handling equipment, where it accumulates over time and decreases flow rates in reservoirs, pumps, valves and topside facilities. The performance of equipment that involve heat transfer processes (e.g. boilers and heat exchangers) are further lowered due to a decrease in heat exchange rates. These phenomena are also encountered in the downstream (e.g. distillation plants), where the build-up of mineral

deposits damages equipment parts. In order to amend or replace these parts, operations have to be put on halt and are usually associated with high costs.

A number of pharmaceutical companies are developing different pulmonary insulin delivery systems Ghosh and Collier (2007). The delivery system has a significant influence on the clinical efficacy. All delivery systems are used to provide regular insulin through the respiratory tract, either in powder form or in solution. The Exubera system developed by Nektar Therapeutics is a dry powder inhaler and has been used by Pfizer. It is the most widely studied pulmonary insulin delivery system available (Rosenstock, 2002, Quattrin et al., 2004, Hollander et al., 2004). The powder is present in amorphous form and hence is more stable during storage (Shaikh et al., 2005). Although, a pulse of compressed air is required to de-agglomerate the dry powder into an aerosol, this mechanism is very complex and much research is required to fully understand this process (Rave et al., 2005). Another difficulty associated with pulmonary drug delivery is in determining the deposition site of the administered dose (Laube et al., 1998). Factors that influence the deposition of a drug within the respiratory tract are the physical and chemical properties of the fluid medium and the nature of the aerosol particles. To achieve an effective drug delivery for dry powder inhalers, dispersion and deposition behaviour of particles in turbulent air should be studied in depth with a view to quantifying the conditions favouring de-agglomeration of powders and delivery by deposition into the lungs airways.

In the nuclear industry a large amount of existing nuclear waste such as heaps of used nuclear reactor parts and decaying fuel rods, line the bottom of the polluted, radioactive waters of the cooling ponds. Here, parts of these contaminated metals have dissolved and accumulated into a sludge that emits heavy and potentially lethal doses of radiation. For this sludge to be treated and disposed of it first has to be removed from the bottom of the ponds via pumping. To effectively transport nuclear waste sludge, a better understanding of the behaviour of particles within the flow in terms of their dispersing and agglomerating characteristics, tendency to form solid beds, and also their re-suspension characteristics is required. Many other factors have to also be taken into account, making it a very complex task, these include; particle size/shape, distribution, surface chemistry, temperature, composition, sheer yield stress, and compressive yield stress. Moreover, the vast number of insoluble particles in the carrier phase is a factor

which brings about many complications in the transportation of slurry flows. These small particles have a tendency to come together and create agglomerates, which then stick together to form gels. This process is controlled by the temperature, salt concentration, and PH value of the slurry (Hyatt et al., 2009). One of the major problems encountered in the transportation of slurries is that the waste (a large number of insoluble particles) can plug up the pipes and/or ducts. This is caused by a number of factors; changes between flow regimes, deposition at a pipe bend, crystal growth on the surfaces of pipes, settling of solid particles due to a low flow rate or high solid volume fraction, and chemical instability resulting in the particles coming together to form agglomerates and potentially gels (Hyatt et al., 2009). Other problems include pipe/duct corrosion, ineffective pumping of waste materials, and pipe/duct erosion due to materials in flow. The ability to accurately predict the rheological behaviour of nuclear sludge would potentially lead to fewer costs, less waste, faster and safer nuclear waste removal, less doubts in radiological impact assessments, more efficient clean up, reduced labour, boost in community confidence, and smaller land for waste disposal.

The examples given above represent a wide range of different processes where particle transport in turbulent flow is existent. In such processes many types of particles can be found, that vary in size, shape, density and material. It is common for particulate fouling experiments to use standard sub-micron or micron scale particles (yeast (Hughes et al., 2006); latex beads (Kuznar and Elimelech, 2007, Hildich and Zhang, 1995), fat globules (Echizen and Unno, 2001)) so as to investigate the depositing behaviour of colloid suspensions as a function of diverse operating conditions (system chemistry (Kuznar and Elimelech, 2007), hydraulic state). The particles used in this thesis are theoretical particles that are in the micron range and spherical in shape. From an experimental perspective, they can be likened to and compared with glass beads or latex particles (Johnson et al., 2007, Johnson et al., Chang et al., 2003, Chang et al., 2008, Kuznar and Elimelech, 2007, Ma et al., 2009, Duursma et al., 2009). Table 1-1 summarises some of the data reported in literature for adhesion force measurements of particles (2 – 20 μm) that can be encountered in two-phase flows and the contact mechanics model used by the authors to calculate the work of adhesion (WA). The measurements have been made with atomic force microscopy (AFM), performed either in liquid or gaseous systems. Table 1-2 shows the Elastic modulus and Poisson's ratio for the materials presented in Table 1-1.

Investigating the behaviour of multiphase flow using experimental techniques alone would be uneconomical. Mathematical models are a key tool in the processing of multiphase flow, especially since there is currently little characterisation of multiphase flow available. Moreover, this field encompasses a broad range of flows within pipes, vessels and other equipment. Computational Fluid Dynamics (CFD) is a method with the ability to create a better understanding and optimisation of such systems. Although for the mathematical models to be successful, it is necessary to have reliable experimental data to compare against. Conversely mathematical models can shine light on areas where more experimental data is required and therefore potentially guide experimental studies, facilitating cost effective process design and continued operation. In this work, the mathematical modelling technique used is based on the large eddy simulation (LES) methodology embodied in the commercial CFD code FLUENT, with flow solutions provided by this method coupled to a second commercial code, EDEM, based on the discrete element method (DEM) used in the prediction of particle motion and interaction.

Table 1-1 Measured and calculated values of the work of adhesion for different systems

Ref.	System		Probe		Lit. Results		
	Surface Chemistry	Medium	R [nm] or [μm]	K [N/m]	W _A [mJ/m ²] Predicted	Determined	Model used
(Leite et al., 2003)	Si - mica	Water	23	0.13	110	83	DMT
	Si - mica	Air			215	173	
(Biggs and Spinks, 1998)	PS - mica	Dry N ₂	5	27 ± 1	102.4	148.5/122.5	JKR/MP
(Nalaskowski et al., 2003)	PE - SiO ₂	Water	5-9	27 - 30	21	4.4	JKR C = 1.5
	PE - SiO ₂ (heat)				35	21	
	PE - CH ₃				66	64	

Table 1-2 Elastic modulus and Poisson's ratio for materials

Material	Young's modulus [GPa]	Poisson's ratio	Source
PS	2.8 - 3.5	0.38	(Fried, 1995)
PTFE	0.41	0.46	(Fried, 1995)
Mica	34.5	0.205	(Matsuoka and Kato, 1995)
Si	107	0.27	(Barsoum, 1997)
SiO ₂	94	0.17	(Barsoum, 1997)

1.3 Objectives and thesis structure

There is insufficient uniformity and comprehensiveness in available literature for turbulent particle dispersion and agglomeration in wall-bounded flows. This is a consequence of several reasons (related to the intrinsic complexity of turbulent transfer phenomena and particle collision/contact mechanisms) and is augmented by the uncertainty in methodologies, mainly owing to the large number of physical and computational parameters involved and to the indistinct influence of several of them. The work presented in this thesis is a small step towards better understanding the rheological behaviour of complex multiphase flows encountered in industry and therefore can be said to underpin their behaviour. The objectives of this report are given below;

1. Produce reliable and consistent predictions for particle dispersion within turbulent channel flow; compare single phase LES results against DNS data.
2. Analyse the physics underlying the particle-fluid interactions and particle-particle interactions.
3. Examine the connection between momentum (excluding gravity) dominated aspects and the action of fluid turbulence and particle agglomeration in the flow.
4. Investigate the effects of particle surface energy, concentration, size and density on particle dispersion and agglomeration characteristics.
5. Investigate the effects of particle surface energy on dispersion, deposition and agglomeration in gravity dominated systems.
6. Show evidence for the potential of LES-DEM modelling techniques to give insight into processes that are of relevance to the processing of multiphase flow, and capable of predicting their transport behaviour.

This thesis is structured according to the following format. Chapter 2 compares different computational and experimental techniques used in measuring single and multiphase flow in consort with associated literature. In Chapter 3, the concept of LES and DEM is outlined with a focus on the numerical methods, coupling procedure and contact models. Chapter 4 provides comparison of the single phase and the effects of particles and agglomerates on the fluid phase characteristics. Chapter 5 explores the sensitivity of the agglomeration process to fluid Reynolds number, particle surface energy,

concentration, size and density. Chapter 6 investigates particle dispersion, deposition and agglomeration for different surface energy particles in a gravity system. Chapter 7 provides a summary of the findings of the thesis, concluding remarks and potential areas of future work.

2 Literature Review

2.1 Introduction

This chapter begins by introducing some of the parameters relevant when classifying two-phase flow. Followed by an overview of relevant experimental and modelling and simulation techniques frequently used for observing, characterising and predicting two-phase flows. As previously mentioned, experimental methods are also of importance to this report, as they are used to gain insight into complex two-phase flows and provide experimental data required for the validation of the computational models. Finally, an overview of published work on relevant experimental and numerical works is given. The chapter concludes with an outline of how the current work adds to the areas of research discussed.

2.2 Introduction to two-phase flow

Particle-laden flows comprise of a gas or liquid (continuous) phase and small, immiscible, and typically dilute particles (dispersed or particle phase). In most literature relevant to this work, for reasons of simplicity, both phases are considered to have constant properties.

Particle-laden flows can be classified into three general categories with respect to their inter-particle collisions: dilute (collision-free) flows, medium concentration (collision-dominated) flows, and dense (contact-dominated) flows (Tsuji, 2000). These inter-particle collisions can be related to the particle volume fraction. The volume fraction, ϕ_p for a poly-dispersed particle size is given as $\phi_p = \sum_N V_p / V$ which simplifies to $\phi_p = NV_p / V$ for a mono-dispersed particle size, with N as the number of particles, V_p the volume of a particle, and V the total volume occupied by the particles and the fluid. The transport efficiency and solid deposition property can be controlled by varying the volume fraction of the solid phase (i.e. ϕ_p), since fluid and particle densities are typically constant for most solid-liquid flows, making ϕ_p the variable of concern.

In order to efficiently transport particles in wall-bounded turbulent flow it is essential to be able to predict the rate at which particles are transported, deposited and re-

suspended. The flow is considered to be homogenous when its velocity exceeds the critical velocity. The critical velocity is the velocity required to maintain a sufficient level of turbulence for particles to remain suspended within the flow field. From a practical point of view however, no flow is homogeneous, for that reason Crowe et al. (1998) classified homogeneous two-phase flow as one that has less than 20% decrease in particle concentration throughout the pipe cross section. A large difference in the density of the liquid and the solid phase leads to a large critical velocity, i.e. for low density fluids, a large critical velocity is required to keep particles in suspension. Figure 2.1 is a schematic that shows the critical velocity together with the particle impact velocity as a function of the particle size.

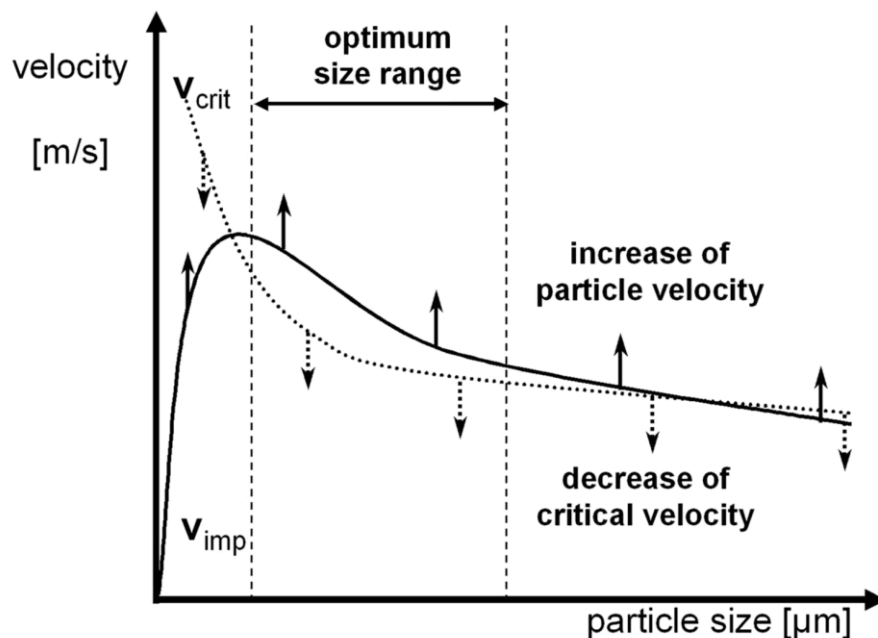


Figure 2.1 Process optimisation by varying critical velocity (v_{crit}), impact velocity (v_i) and size distribution (Schmidt et al., 2009).

The interaction between particles and turbulent flow is complex, due to all of the parameters involved, for example, particle volume fraction ϕ_p , particle Reynolds number Re_p , particle Stokes number St , gravity g , inter-particle spacing, wall roughness and velocity gradient of the flow. The physical parameters that are the most influential on flow and particle behaviour are the flow Reynolds number Re and particle Stokes number St which quantifies the response of the dispersed phase to the perturbations created by the turbulence field. The Reynolds number is useful in examining any type of flow when there is large velocity gradient present (i.e., shear). It designates the relative

significance of the viscous effect in relation to the inertia effect; it is proportional to inertial force divided by viscous force. Reynolds number can be defined for several different conditions where the fluid is in motion relative to a surface. In the case of fluids of variable viscosity (i.e., non-Newtonian fluids) or variable density (e.g. compressible gases) unique rules apply; this research is not concerned with such flows. For flow in a pipe or tube, the bulk Reynolds number is commonly defined as:

$$\text{Re}_b = \frac{\rho_f \bar{u}_b h}{\mu} = \frac{\bar{u}_b h}{\nu} = \frac{Qh}{\nu A} \quad 2-1$$

Where: u_b is the bulk velocity of the fluid, μ is the dynamic viscosity of the fluid, h is a characteristic linear dimension, ν is the kinematic viscosity of fluid, ρ_f is the density of the fluid, Q is the volumetric flow rate, and A is the pipe cross-sectional area. It is worth noting that L is the internal diameter for pipe flows; the equivalent diameter is used for different shapes such as square and rectangular ducts.

The shear Reynolds number is formed by replacing the velocity term in the Particle Reynolds number by the shear velocity $u_\tau = (\tau_w / \rho_f)^{1/2}$, where τ_w is the mean shear stress at the wall. The shear Reynolds number is therefore given by:

$$\text{Re}_\tau = \frac{\bar{u}_\tau h}{\nu} \quad 2-2$$

In general, a particle Reynolds Number has the form:

$$\text{Re}_p = \frac{\bar{v} d_p}{\nu} \quad 2-3$$

Where: v is particle velocity and d_p is particle diameter.

Shirolkar, J S, *et al.* (1996) expresses the relaxation time of a particle as the rate of response of particle acceleration to the relative velocity between the particle and the carrier fluid:

$$\tau_p = \frac{24\rho_p d_p^2}{18\mu_f C_D \text{Re}_p} \quad 2-4$$

Where: ρ_p is the particle density, d_p is the particle diameter, and C_D is the drag coefficient and can be obtained from the equation below (Shirolkar, J S, et al. 1996):

$$C_D = \left(\frac{24}{\text{Re}_p} \right) \left(1 + 0.15 \text{Re}_p^{0.687} \right) \text{for } \text{Re}_p < 10^3 \quad 2-5$$

The particle Stokes number St is the ratio of the characteristic time of a particle to a characteristic time of the flow. A $St \ll 1$ designates that the particle will nearly follow the fluid phase motion, and a $St \gg 1$ designates that the particle motion will be unaltered by the fluid phase. It is defined as the non-dimensional particle relaxation time τ_p^+ ,

$$St = \tau_p^+ = \frac{\tau_p}{\tau_f} \quad 2-6$$

Where: τ_f is the turbulent integral time scale defined as $\tau_f = \nu / u_\tau^2$ and $\tau_p = \rho_p d_p^2 / 18\mu_f$ is the particle relaxation time which represents a typical timescale of the particle's reaction to changes in the carrier phase velocity; this can be assumed to be the particle's inertia with respect to the fluid which contains it.

The particles can also have significant effects on the turbulence characteristics of two-phase flows, depending on their size and concentration. In two-phase flow, the particle phase can be categorised into one of two types; mono-dispersed, where all particles are of the same size or poly-dispersed, in which the particles have a range of sizes. Particle shape is also an important parameter in two-phase flow. In reality particles are not usually completely spherical, and sphericity is a measure of how spherical an object is. Wadell (1935) defined the sphericity of a particle as the ratio of the surface area of a sphere (with the same volume as the given particle) to the surface area of the particle. Because of the difficulty associated in modeling the behaviour of non-spherical particles in turbulent flows, however, most of research to date has been conducted using

spherical particles. Although, more recently investigations are being carried out on non-spherical particles such as Loth (2008) and (Njobuenwu and Fairweather, 2014).

2.3 Experimental Approaches to Two-Phase Flow

This section gives a general overview of the different experimental techniques used for investigating turbulent two-phase flow.

2.3.1 Laser Doppler Anemometry (LDA)

Laser Doppler anemometry (LDA), sometimes referred to as laser Doppler velocimetry (LDV), is a technique more commonly used in the measurement of two-phase flows, and first used by Yeh and Cummins (1964). Small particles that are neutrally buoyant (a condition in which a physical body's average density is equal to the density of the fluid in which it is immersed) and scatter light are introduced into the flow. These particles are then illuminated using light at a set frequency.

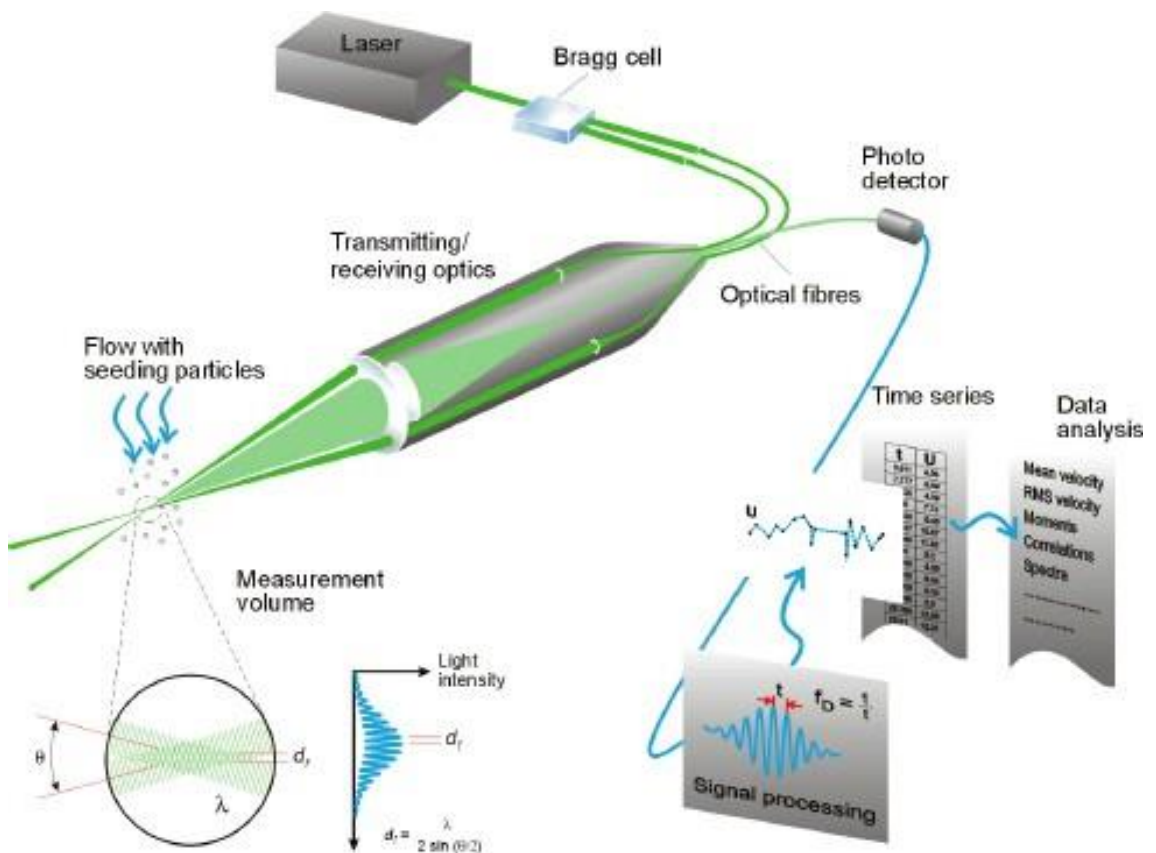


Figure 2.2 Set up for LDA (Dantec Dynamics, 2015)

The technique uses a sensor aligned to the flow such that the fringes are perpendicular to the flow direction. As particles in the flow pass through the fringes, they reflect incident light from the regions of constructive interference into a photodetector. The velocity of the liquid flow can be found from the velocity of the tracer particles, by measuring the Doppler frequency shift of the scattered light (see Figure 2.2). The drawback with this technique is that it can't always differentiate between the tracer and normal particles in the dispersed phase. Kulick et al. (1994) overcame this dilemma by using amplitude discrimination for relatively large particles in a mono-dispersed flow; however it's not as effective for particles in the dispersed phase or polydispersed. For more information on LDA the reader is directed to Durst and Kikura (1995).

2.3.2 Phase Doppler Anemometry (PDA)

PDA is an extension to LDA and a common non-intrusive technique used in measuring the velocity and size of a particle passing the measurement spot in a two-phase flow. This technique has the aptitude to measure the size of homogeneous spherical particles from the change in phase between signals of light detected by the LDA. The PDA method has been improved over the years, for example Gréhan et al. (1993) added a receiving unit, eliminating errors due to particle trajectories. Van de Wall and Soo (1997) used PDA to determine the transport properties (correlation, power spectrum, and diffusivity) of a gas-solid flow by adding a short time shift. For a more detailed description of the method, the user is directed to Bauckhage (1988).

2.3.3 Ultrasonic Doppler Velocity Profiling (UDVP)

The UDVP technique measures the instantaneous fluid velocity profile through the detection of the Doppler shift frequency of echoed ultrasounds as a function of time. The particles in the flow scatter an ultrasonic pulse transmitted by the device. The frequency of the echoed signal undergoes a Doppler shift and the received signal is then filtered to remove background noise before being compared to the originally transmitted frequency. The velocity profile along the measurement axis can be calculated from a specified angle and measurement distance. Significant works to have successfully used this measurement technique include Takeda (1986), Ouriev and Windhab (2002), and Yamanaka et al. (2002) were able to investigate highly concentrated suspensions using the UDVP approach.

2.3.4 Particle Image Velocimetry (PIV)

PIV is a more recent technique used to measure two and multi-phase flow. It is an optical technique for fluid visualisation of multiphase flows; properties such as the instantaneous velocity can be obtained using this method. In PIV, tracer particles are fed into the fluid that are typically assumed to follow the flow dynamics. The device produces two consecutive pulses of a planar laser light sheets. The images of the tracer particles incident to the light sheet are then recorded either by video or photographically. The displacement of the particle images is measured and used to calculate the properties of the flow being studied, however difficulties still remain in distinguishing between tracer particles and small particles in the dispersed phase (see Figure 2.3). For further information on PIV the reader is directed to Westerweel (1997).

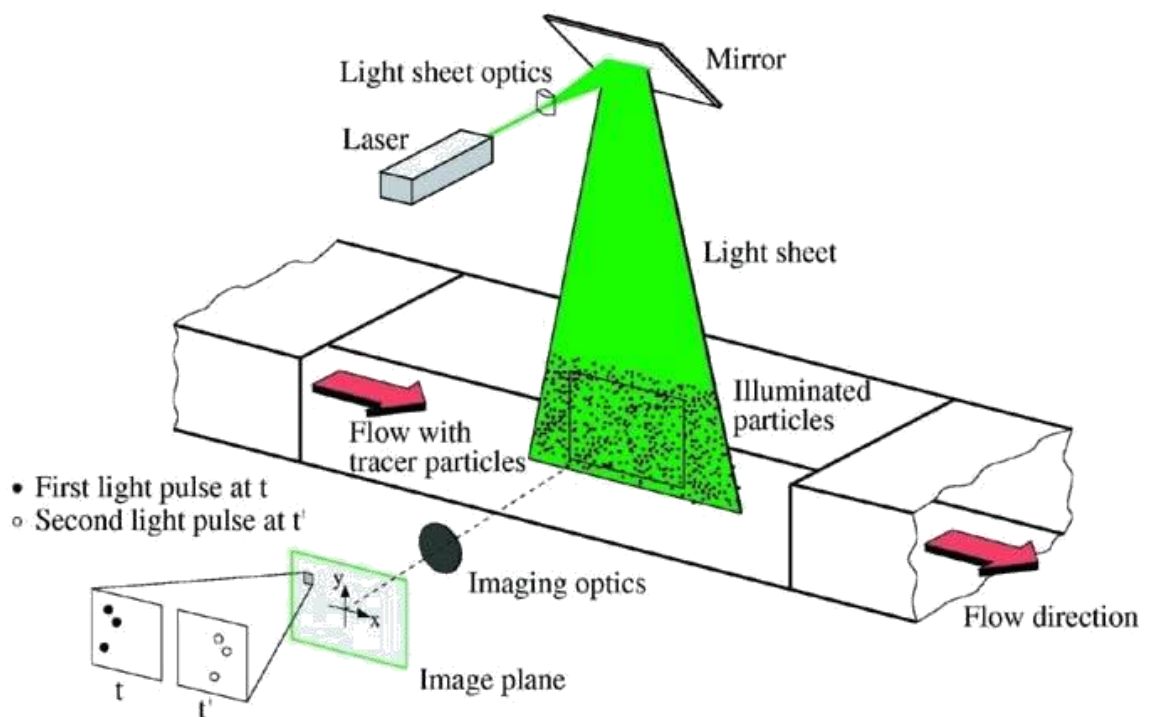


Figure 2.3 Set up for PIV (Institute of Aerodynamics and flow Technology, 2015).

2.3.5 Holographic Particle Image Velocimetry (HPIV)

HPIV is an extension to two-dimensional PIV, which is based on the recording of double exposure images of tracer particles in a flow field. The local velocities are calculated by measuring the displacement of the particles, and recording the

instantaneous three-dimensional velocity distribution over an entire volume sample. For more detailed information on HPIV the reader is directed to Zhang et al. (1997). Non-intrusive experimental techniques have provided the data required to validate the computational models used to predict single- and two-phase flows. It is important to mention, however, that these techniques are associated with some difficulties, such as problems with differentiating between tracer particles and the dispersed-phase within a flow, in addition to having limited application because of the precise nature of the instrument set-up and the optimal operational conditions required for accurate measurement.

The shortcomings of experimental techniques means that a more complete approach in predicting two-phase flow behaviour can be achieved by combining experimental and modelling studies.

2.4 Numerical Approaches to the Fluid Phase

This section gives a review of the different methods used for the modelling of turbulent flows that can be applied to two-phase flows. All the techniques use the Navier-Stokes equations of motion to calculate the velocity field within a Newtonian fluid. More information on these equations and their derivation can be found in standard fluid mechanics text books such as Bird et al. (1960).

2.4.1 Direct Numerical Simulation

In direct numerical simulation (DNS) the time dependent Navier-Stokes equations are solved numerically for a turbulent fluid flow, including the entire flow length and time scales, no turbulence model is used. This method has the ability to accurately generate instantaneous results such as turbulence parameters, their transport and budgets at any point within the flow. It can also be used to examine highly developed experimental methods such as the calibration of hot-wire or -film anemometry probes. In order for DNS to capture and solve all time and length scales in the flow, it uses suitably fine numerical solution meshes which require small time increments, placing a large workload on computational resources. Because of its time dependent computationally intense nature, DNS is computationally limited to flows with a relatively low Reynolds

number, and for simple geometries. The use of DNS as a method to simulate industrially relevant flows in the near future seems unpromising. The main use of DNS at present is as an engineering tool to improve current and less computationally expensive simulations and models of two-phase flow (e.g. RANS and LES), on top of bettering our understanding of such flows. For an in-depth review of DNS and its capabilities the reader is directed to Moin and Mahesh (1998).

2.4.2 Large Eddy Simulation

Large eddy simulation (LES) is a transient method in which the large, energy-containing turbulent eddies are computed within a flow via a time dependent simulation, whereas, the smaller eddies are taken to be homogeneous. Figure 2.4 shows the relationship between energy spectrum and length scale. The method employs a spatial filtering operation to differentiate between large and small eddies. A cut-off width and filtering function are selected with the aim of resolving all the eddies with a length greater than the cut off width, and modelling the smaller eddies (Figure 2.5). Coarser numerical grids can be used in LES compared to DNS, and it is therefore less computationally expensive making it more applicable to higher Reynolds number flows. The main justification for using LES instead of Reynolds Averaged Navier Stokes (RANS) is that by modelling “less” of the turbulence and explicitly solving for more of it, the error in the turbulence modelling assumptions will not be as consequential. Furthermore, it is hypothesized that the smaller eddies are self-similar and will thus lend themselves to simpler and more universal models. The downside of the approach is the computational expense, which although less than DNS, it is still excessive compared to RANS due to its three dimensional time dependent nature. The most common method of simulating industrial flows is still time averaged solutions (i.e., RANS) due to quicker run times. For a more detailed review of LES the reader is directed to text books such as Mason (1994), Lesieur and Metais (1996), and Meneveau and Katz (2000).

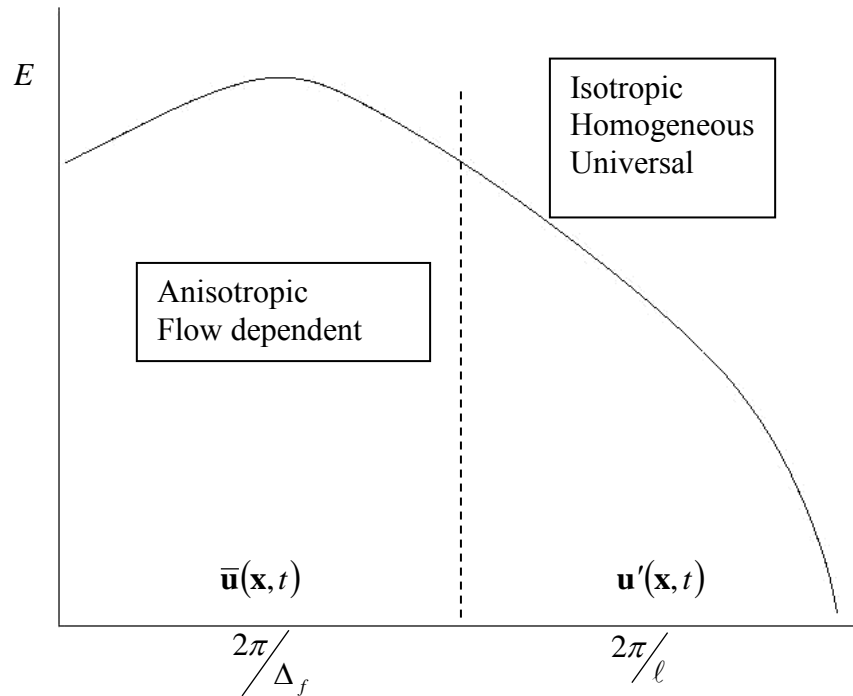



Figure 2.4 Energy spectrum against the length scale

N-S equation

$$\frac{\partial u_i}{\partial t} + \frac{\partial u_i u_j}{\partial x_j} = -\frac{1}{\rho} \frac{\partial p}{\partial x_i} + \frac{\partial}{\partial x_j} \left(\nu \frac{\partial u_i}{\partial x_j} \right)$$



Filtered N-S equation

$$\frac{\partial \bar{u}_i}{\partial t} + \frac{\partial \bar{u}_i \bar{u}_j}{\partial x_j} = -\frac{1}{\rho} \frac{\partial \bar{p}}{\partial x_i} + \frac{\partial}{\partial x_j} \left(\nu \frac{\partial \bar{u}_i}{\partial x_j} \right) - \frac{\partial \tau_{ij}}{\partial x_j}$$

Figure 2.5 Filtering the Navier-Stokes equation

The modelling of the small scale turbulence below the cut-off width, usually referred to as sub-grid scale (SGS) modelling, is an important consideration in LES. The most commonly used SGS model is the eddy viscosity model suggested by Smagorinsky (1963) and improved by Lilly (1967). This technique was applied to industrially related flows by Deardorff (1970). In the Smagorinsky model the eddy viscosity is assumed proportional to the SGS characteristic length scale and to a characteristic turbulent velocity. The drawback of the Smagorinsky model is that it can be ‘very dissipative’ in regions close to the wall. In particular, the model struggles with predicting the transition in a boundary layer for initially laminar flows on a flat plate Lesieur and Metais (1996). More information can be found on the Smagorinsky model in Pope III (2000). Several

variations of the Smagorinsky model have been introduced over the last few decades, which involve alternative ways in defining the eddy viscosity. Schumann (1975) introduced the kinetic energy model by adding another scalar transport equation to calculate the SGS kinetic energy. Kraichnan (1976) introduced a model which gave ideal solutions for mixing layers and accurately described the decay of three dimensional isotropic turbulence. His methodology detailed that when observing the way that the eddy viscosity reacts with different wave number modes, it would be more accurate for the eddy viscosity to depend on a wave number magnitude based on the spectral eddy viscosity. Germano et al. (1991) developed a dynamic SGS model, by changing the decomposition of the turbulent stresses used in the Smagorinsky model. Métais and Lesieur (1992) introduced an alternative to the Smagorinsky model, the structure function model, in which the action of the spectral eddy viscosity was recreated in physical space. More information on the performance of different SGS models can be found in Vreman et al. (1997).

This thesis is mainly concerned with particle agglomeration, which is in turn dependent on the phenomena controlling the segregation and collision of particles driven by turbulent flow. In such flows, the fluid-particle interactions lead to two phenomena, which both contribute to the collisions, specifically, the non-uniform particle distribution (particle segregation effect) and the relative motion of neighbouring particles. As mentioned above, LES only captures the large scales of fluid turbulence. The elimination of these structures from the flow field means that their interactions with particles are only partially captured. It is important therefore, to identify the minimal physics required to model particle motion. A schematic of the minimal near-wall turbulent coherent structures is shown in Figure 2.6. The incapability of LES to accurately predict near-wall accumulation is directly linked to filtering, which eliminates both energy and flow structures from the LES turbulent flow field. In general, a smaller cell size corresponds to a smaller filter length. Therefore, the grid can be refined to the level where these scales are resolved. It is important to note that, smaller particles are greater effected by small scales of turbulence which means that a coarser grid can be used for larger particles. In this work, the grid refinement and sub-grid model used is based on sensitivity tests and open literature.

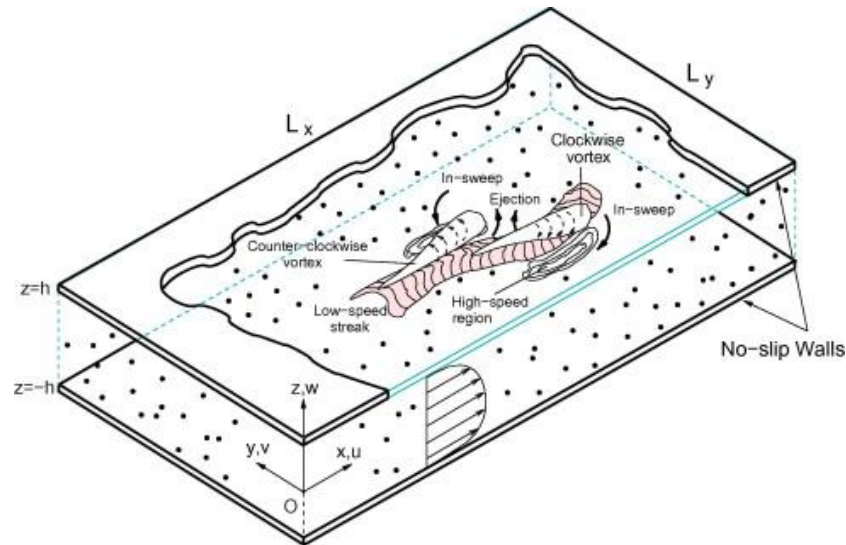


Figure 2.6 Particle-laden turbulent gas flow in a channel: sketch of the computational domain and minimal schematics of near-wall turbulent coherent structures (Soldati and Marchioli, 2009).

2.4.3 Reynolds Averaged Navier Stokes

It is possible to remove the necessity to completely resolve all turbulent motions in the flow field, by separating the instantaneous flow field into mean and fluctuating components. The time averaging operation on the momentum equations lead to a loss in details of the flow contained in instantaneous fluctuations, which create a number of unknown correlations. The fluctuating components are predicted in terms of their time-averaged root-mean square (rms) values, giving the mean profiles of the flow. These unknown terms are commonly referred to as Reynolds stress terms; therefore an additional model is required to capture the effects of turbulence. The common RANS turbulence models are classified according to the number of additional transport equations that need to be solved in conjunction with the RANS equations themselves. These turbulence models include the: mixing length, Spalart-Allmaras, $k-\varepsilon$, $k-\omega$, algebraic stress, and Reynolds stress models (RSM); $k-\varepsilon$ and RSM being the most frequently used. RANS is the most commonly used method of numerical modelling due to its robustness, computational efficiency, and practicality.

2.4.4 Comparison of DNS, LES and RANS

Of the methodologies mentioned above, RANS is the least computationally demanding and has been used to model many single and two-phase flows of practical importance due to its relative speed and robustness compared to LES and DNS. However, RANS is not a transient simulation and not suited for accurately studying particle-particle collisions in dispersed turbulent flow, even if a method is employed to recreate the instantaneous fluid velocities that are lost from the Reynolds averaging procedure. LES is capable of generating real time instantaneous fluid velocities, and the increase in computational capacity over recent years has made LES an approach that can be used to investigate high Reynolds number two-phase flow.

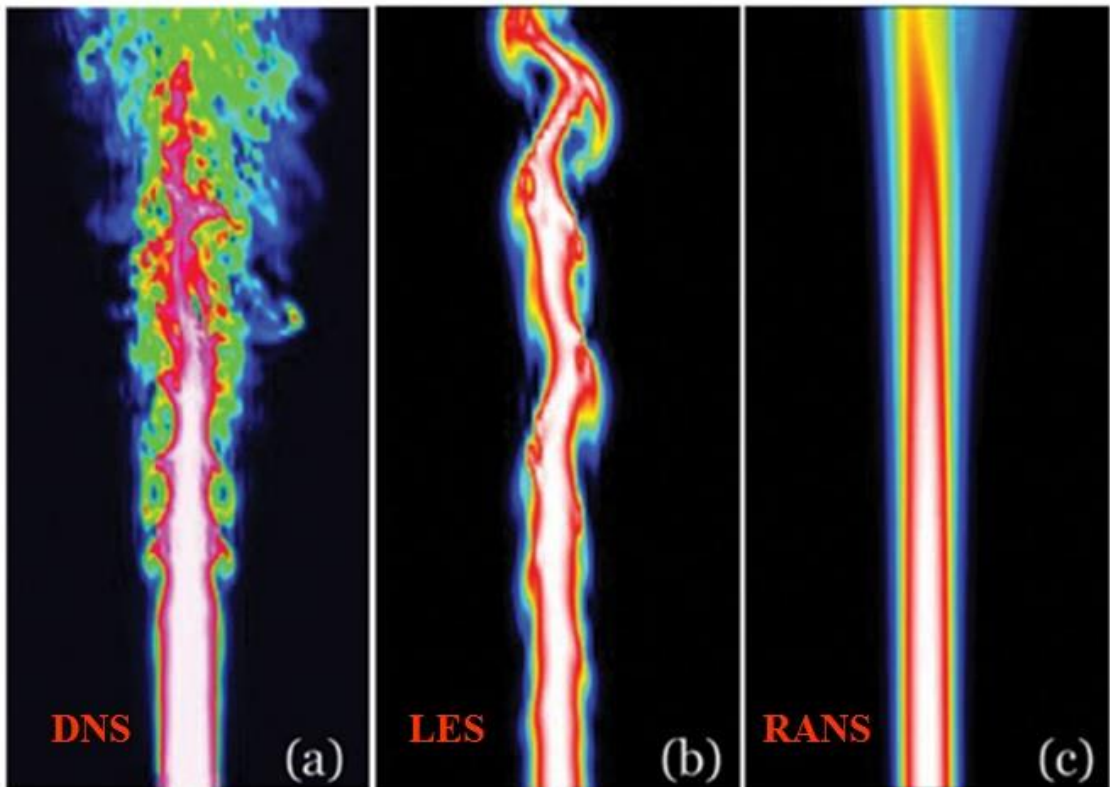


Figure 2.7 Velocity contours of DNS (a), LES (b) and RANS (c) (ENEA, 2015)

DNS provides more accurate predictions than LES; however, it is limited by its immense computational demand and therefore better suited for the validation of LES and RANS models and also academic studies (Figure 2.7). For the reasons given, LES is the most promising in delivering accurate solutions for two-phase flow with industrial applications in the context of particle dispersion, agglomeration and deposition. To

ensure the fluid turbulence is accurately represented, different SGS models and discretisation schemes have been studied here (see Appendix).

2.5 Numerical Approaches to the Particle Phase

2.5.1 Numerical Approaches to Particle Motion

The fluid phase directly influences particle motion, leading to numerous particle-fluid interaction forces. It is important that these interaction forces are appropriately taken into account. For two- and multi-phase flows, the fluid and particle mechanics can be calculated theoretically by solving the Navier–Stokes equations for continuum fluid together with boundary and initial conditions and Newton’s equations of motion for discrete particles. In practical systems, the number of particles present is typically high; therefore, the number of governing equations that have to be solved for the movement of each individual particle is also high. Moreover, the fluid field resolution must be small enough to resolve the flow of continuum fluid through the pores between particles of close proximity. Therefore, this theoretical technique has to be simplified when applied to numerical approaches in relation to the time and length scales.

The main difficulty of modelling two-phase flow is representing the mutual effects between the fluid flow and the solids motion through coupling between phases. The current techniques used to model particle flow can be divided into two categories: the continuum or Eulerian approach at a macroscopic level and the discrete or Lagrangian approach at a microscopic level. Both models treat the fluid phase as a continuum. The Lagrangian and Eulerian approach are described in terms of the corresponding meshes in Figure 2.8. It is possible to conceptualise the Lagrangian mesh as being drawn on the body. The mesh deforms with the body; and both the nodes and the material points change position as the body deforms. But, the position of the material points relative to the nodes stays fixed. Alternatively, the Eulerian mesh is a background mesh. The body flows through the mesh as it deforms; the nodes remain fixed and the materials points move through the mesh. The position of a material point relative to the nodes varies with the motion (Belytschko et al., 2013). These two approaches are further discussed below.

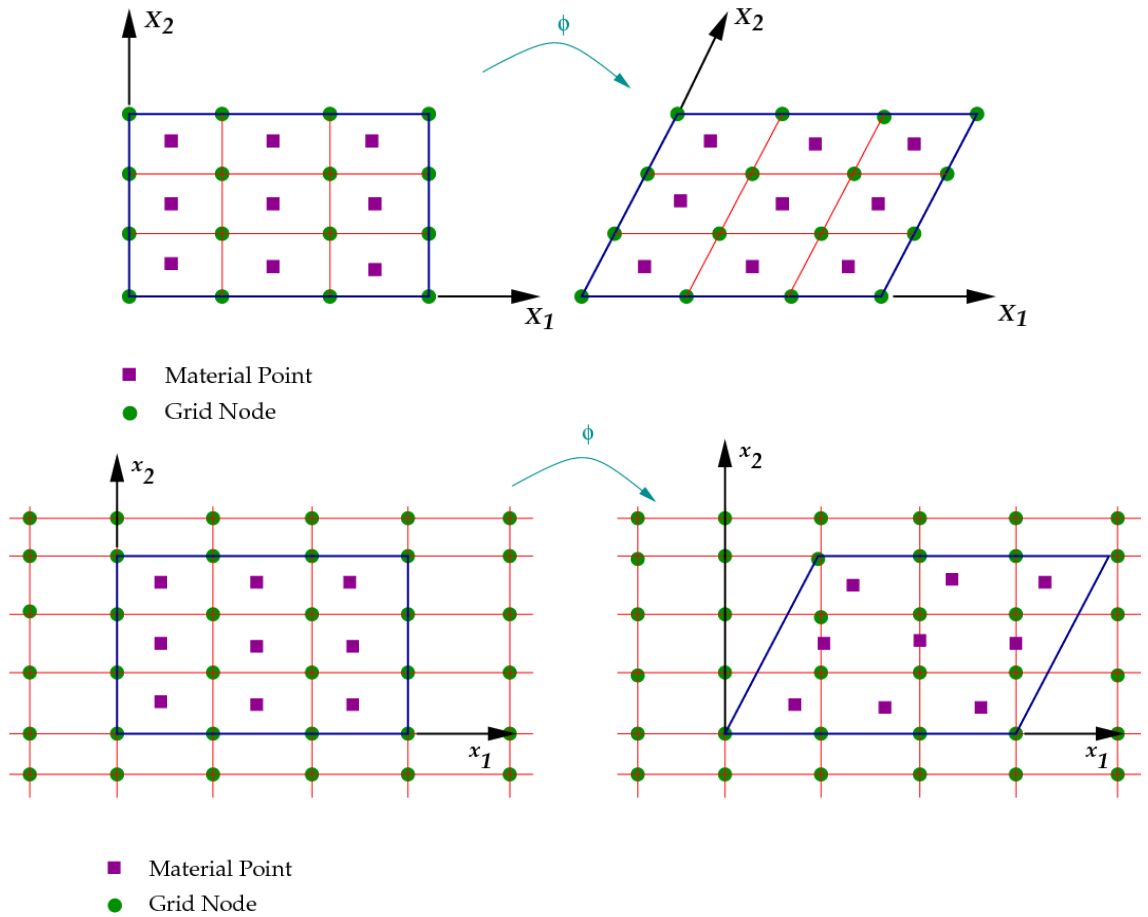


Figure 2.8 Schematic of (a) Lagrangian Mesh and (b) Eulerian Mesh (Banerjee, 2015)

2.5.1.1 Eulerian Approach (Two-Fluid Model)

In the Eulerian approach, also known as the two-fluid model (TFM), the particle properties are defined at computational nodes that coincide with the nodes of the fluid phase. The same Eulerian treatment is applied to both phases, in which the particle phase can be treated with the same discretisation and numerical solution methods as the carrier phase. This approach uses balance equations to consider the relative inter-phase mass, momentum and energy difference based on a point volume description of the particles by introducing the local volume fraction of each phase, ϕ_f and ϕ_p , closed with constitutive relations together with initial and boundary conditions. The mass conservation equations for the fluid phase and the solid phase can be written as:

$$\frac{\partial}{\partial t}(\phi_f \rho_f) + \frac{\partial}{\partial x_i}(\phi_f \rho_f u_i) = 0 \quad 2-7$$

$$\frac{\partial}{\partial t}(\phi_s \rho_s) + \frac{\partial}{\partial x_i}(\phi_s \rho_s u_i) = 0 \quad 2-8$$

Where ρ_f and ρ_s are the densities of the fluid and particle, respectively, and u is the fluid velocity. The volume fractions of each phases are constrained to be supplementary, i.e. $\phi_f + \phi_p = 1$. The momentum conservation equation for the fluid phase and the solid phase are respectively:

$$\frac{\partial}{\partial t}(\phi_f \rho_f u_j) + \frac{\partial}{\partial x_i}(\phi_f \rho_f u_j u_i) = -\phi_f \frac{\partial p}{\partial x_j} + \frac{\partial \tau_{ij}}{\partial x_j} + \phi_f \rho_f g_j + \bar{S}^{sf} \quad 2-9$$

$$\frac{\partial}{\partial t}(\phi_s \rho_s v_j) + \frac{\partial}{\partial x_i}(\phi_s \rho_s v_j v_i) = -\phi_s \frac{\partial p}{\partial x_j} + \frac{\partial \tau_{ij}^s}{\partial x_j} + \phi_s \rho_s g_j - \bar{S}^{sf} \quad 2-10$$

Where the source term \bar{S}^{sf} is defined as $\bar{S}^{sf} = K^{sf}(v_j - u_j)$ when the disperse phase is made of solid particles, and K^{sf} is the drag coefficient between the phases.

For dense flows, the drag force becomes very difficult to calculate due to the increase in particle concentration and decrease in the fluid volume fraction. This leads to a steep fluid velocity gradient and consecutively a greater shear stress acting on the particle surface. To improve the accuracy of the drag force, particle configuration, particle–fluid slip velocity, and particle and fluid properties have to be considered in more depth. There are two main methods to calculate particle–fluid drag force. The classic method relies on empirical correlations for either bed pressure drop or bed expansion experiment, examples include Ergun (1952); Wen and Yu, (1966) and Richardson (1971), respectively. The Ergun and Wen & Yu drag model is:

$$F_d = \frac{\beta V (u - v) |u - v|}{1 - \varepsilon} \quad 2-11$$

Where V is the particle volume, u and v are the fluid and particle velocity, ε is voidage/porosity and

$$\beta = \begin{cases} \frac{150(1-\varepsilon)^2 n}{\varepsilon L^2} + \frac{1.75(1-\varepsilon)\rho|u-v|}{L^2} & \varepsilon < 0.8 \\ \frac{3}{4} C_D \rho \varepsilon^{-1.65} (1-\varepsilon)|v-u| & \varepsilon \geq 0.8 \end{cases} \quad 2-12$$

Where ρ is the fluid density, C_D is the drag coefficient and L is the diameter of the particle

The effects on drag of neighbouring particles in the system can be taken into account by adding a porosity correction term as seen in the Di Felice drag model (equation 2-13). For further information on this drag model the reader is directed to a paper by Di Felice (1994).

$$F_d = 0.5 C_D \rho_f A_p (u-v)|u-v| \cdot \varepsilon^{-(\chi+1)} \quad 2-13$$

where χ is given by:

$$\chi = 3.7 - 0.65 \exp\left[-\frac{(1.5 - \log_{10} \text{Re})^2}{2}\right] \quad 2-14$$

The two-fluid approach can give acceptable predictions for flows with high particle volume fractions where, because of the relatively close proximities of the particles, the particle-phase can be considered as a continuum. For that reason, the grid cell can be many times larger than the particle size. This minimises the number of governing equations, and gives faster run times. The efficiency of TFM depends on constitutive or closure models for the particle phase and the momentum exchange between phases which cannot be determined in the framework. This is even more important when different particle types are involved that have to be considered as different phases. Since for each particle size a separate transport equation, and subsequent discretisation and linearisation is required. Many theories have been formulated for different materials and flow regimes. However, at present, there is no universal continuum theory appropriate for all flow conditions. Therefore, phenomenological assumptions must be made to determine the constitutive relations and boundary conditions, which have

restricted application (see, for example, Zhang et al., 1998). In effect, there is much work being done to achieve a general model to describe granular flow (see, for example, Jaeger et al., 1996; de Gennes, 1999). For a detailed review of the two-fluid approach for two-phase flows the reader is directed to Enwald *et al.* (1996). For further information on TFM and its implications the reader is directed to summaries given by Gidaspow (1994), Kuipers and van Swaaij (1997) and Arastoopour (2001).

2.5.1.2 Lagrangian Particle Tracking

The Lagrangian approach is capable of providing dynamic data, such as the trajectories of and transient forces acting on individual particles, which is currently almost impossible to obtain through experimental approaches. The advantage of this method is that there are no global assumptions on the particles such as uniform constituency, steady-state behaviour and/or constitutive relation. The increase in processing speed and power of computers has allowed LPT to be commonly used for the tracking of particles.

For a particle secluded in fluid, the trajectory of an individual particle and drag resistance can be calculated by applying Newton's equation of motion to the particles. The drag coefficient of the particle, C_d , depends on the properties of the fluid and the Reynolds number. The correlation used to calculate the drag force is different for each region, there are three regions: Stoke's Law region, the transition region and Newton's law region. Until now, several such forces have been incorporated in LPT, these include pressure gradient force, particle–fluid drag and other unsteady forces for instance Saffman and Magnus lift forces, Basset force and virtual mass force, (e.g., Li et al., 1999; Xiong et al., 2005; Potic et al., 2005). Saffman lift occurs when the particle is placed in a flow with local shear and when the Particle Reynolds number is smaller than unity, which generally applies to micron-size particles. Whereas, the Magnus lift is due to the particle rotation creating a velocity differential, which in turn leads to the development of a pressure differential on the particle surface. The pressure gradient force, generally, takes account of the buoyancy and the acceleration pressure gradient in fluid, which involves the virtual mass force and the Basset force. The virtual mass is a factor in the force needed to speed up the surrounding fluid; it is sometimes referred to as the apparent mass as it is equal to adding a mass to a particle. The Basset force represents the viscous effects; it describes the force brought about by the lagging boundary layer development as the relative velocity changes with time. As stated by

Hjelmfel and Mockros (1966), the Basset term and virtual mass term tend to a negligible value under certain conditions, such as small density ratio ($\rho_f/\rho_s \sim 10^{-3}$). The employment of these forces in the numerical approach to the particle phase depends on the physical properties of the fluid and particle phase.

When LPT is coupled to RANS modelling, an additional model is required to recreate the instantaneous fluid velocities that are lost from the Reynolds averaging procedure. An additional model for the calculation of turbulent fluctuation is not required in DNS and LES as the instantaneous velocities given to the LPT are obtained directly from the simulation results. More information on numerical models for two phase flows using different Lagrangian particle tracking methods can be found in Crowe *et al.*, (1996).

The more recent method to calculate particle–fluid drag force relies on numerical simulation, which involves DNS (Choi and Joseph, 2001) and Lattice–Boltzmann (LB) computation (Zhang *et al.*, 1999b). In spite of its accuracy, the numerical approach has only been used in comparatively simple systems, due to its computationally high demanding nature.

2.5.1.3 Comparison of Eulerian and Lagrangian Approach for Particle Motion

The Eulerian approach, removes the details of particle flow, as it requires an averaging of the particle properties of all particles that find themselves in a given mesh fluid cell (see Figure 2.9). The LPT approach is advantageous compared to the Eulerian approach as the governing equations for the translational and rotational motion of particles can be numerically solved by determining the forces and torques at each time step, and eventually determining the velocities, trajectories and the transient forces of every particle in a considered system. This provides detailed statistics for use in the analysis of particle behaviour. Most importantly, with LPT it is possible to incorporate deterministic particle-particle interactions that are discussed later in this chapter.

The Lagrangian approach is suitable for all flows; however, it is essential for dilute and medium concentration flows, where the particle concentration is low. A drawback with the Lagrangian treatment of the particle phase is that once the number of particles becomes large, it may require an immense amount of computational power to track a sufficiently large sample of particles required for statistical convergence. In addition, if

the particles are sufficiently light or at a high concentration where they are in relative close proximity, they behave essentially like a second fluid. In such a case, an Eulerian treatment of the dispersed phase is plausible. In this thesis, all flows considered have volume fractions below 10^{-4} , making LPT the most appropriate technique to use for the work detailed in following chapters.

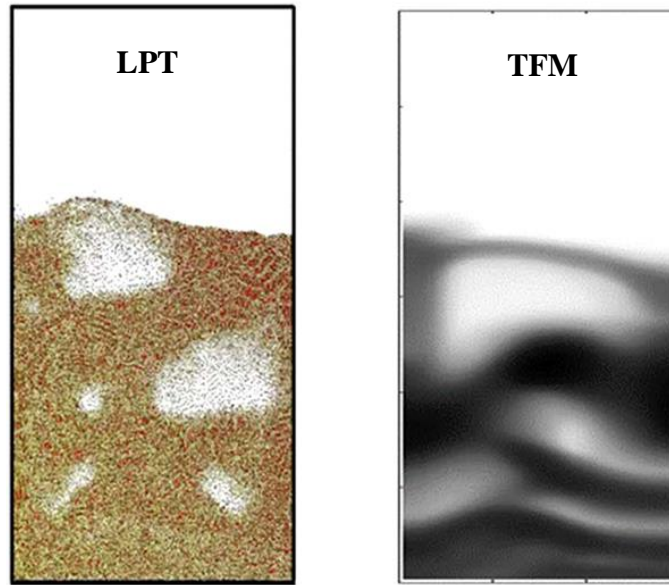


Figure 2.9 Multiscale approaches for dense fluid-particle flows: LPT and TFM based on the Kinetic Theory of Granular Flow (Deen and Kuipers, 2014).

2.5.2 Fluid-Particle Coupling Schemes

In this research, one-way coupled flow refers to flow in which the collisions between particles are neglected and the flow affects the particles only, in two-way coupled flow the particles affect the flow and flow affects the particles, and finally in four-way coupled simulations the influence of inter-particle collisions on the particle and fluid phase variables are also considered. Other important parameters include particle-wall interaction (reflecting or absorbing wall, and wall effects), particle rotation and the various forces acting on the particles (e.g. the hydrodynamic forces). To ensure the accuracy of the numerical modelling approach, these variables must be considered and accounted for where possible.

The volume fraction is often the only determinant to which coupling approach is used. One-way coupled simulations are usually used for particle volume fractions less than

10^{-6} ; with the trajectory of the particles controlled by the carrier phase and with the particles having a negligible effect on the flow. One-way coupling only requires a mono-directional coupling procedure, making it dynamic for one phase only. In recent literature, one-way coupling approaches have usually been employed when using DNS of the fluid to predict the behaviour of particles in complex turbulent flows.

Two-way coupled simulations tend to be used when investigating particle volume fractions in the range 10^{-6} to 10^{-3} , where there is a mutual interaction between the particles and the fluid; the turbulent flow influences the particle trajectory and the particle itself influences the flow momentum (Squires and Eaton, 1990). Particles impact on the carrier flow in a number of ways, including the wake generation of turbulence, streamline distortion, alteration of velocity gradients, and turbulence generation or damping owing to the drag forces on the particles (Crowe, 2000). When examining the effect of particles on a flow a number of factors are important, including the particle size and shape, the relative density between the fluid and the particle, and the motion of the particles (Humphrey et al., 1990).

Finally, four-way/full coupling is usually considered in simulations if the volume fraction is greater than 10^{-3} , with the particles having an effect on the carrier fluid and with particle motion significantly influenced by particle-particle interactions (see Figure 2.10). These flows exhibit very complex behaviour and have only recently been studied using computational modelling techniques. Such flows are observed in dense conveying, where the shear and collisional forces are usually low.

The criteria given above only apply to systems that contain particles of low Stokes number (inertia). For systems where particles of high inertia are used, particle-particle interactions are common in wall-bounded turbulent flows even at low volume fractions, due to the effects of gravity and fluid turbulence. In contrast to previous works, where only particle volume fraction is used to determine the coupling approach, here, the particle Stokes is also considered. This study uses high inertia particles, therefore, despite operating between volume fractions of about 10^{-5} – 10^{-4} , a fully coupled approach has been adopted. This research aims to show that a high particle volume fraction is not required to promote particle agglomeration in turbulent channel flows.

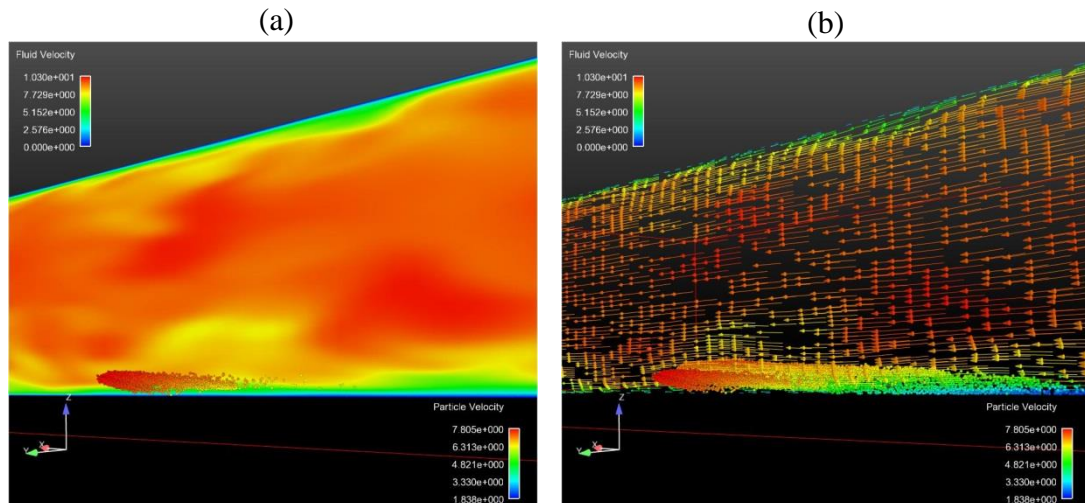


Figure 2.10 Velocity contours (a) and vectors (b) of fluid and particle phase in fully-coupled flow

2.5.3 Numerical Approaches to Inter-Particle and Wall-Particle Collisions

The three main discrete modelling techniques include the Monte Carlo method, cellular automata method, and discrete element method (DEM). This thesis focuses on the latter, for further information on the other two approaches the reader is referred to Matuttis and Chen (2014).

Discrete Element Method (DEM) was devised by Cundall and Strack (1979) as a numerical tool to model failure phenomena of granular materials in geo-mechanics. In DEM, a granular medium is modelled in a discrete manner as a set of colliding circular rigid particles with translational and rotational degrees of freedom. The resultant forces on a particle can be calculated entirely from its interaction with the contacting particles and surrounding fluid. In the case of a fine particle system, however, it is necessary to also consider non-contact forces such as van der Waals and electrostatic forces. The particle trajectories are determined by integrating Newtonian equations of motion (see Chapter 3).

Particle interactions can be modelled as either hard- or soft-sphere contact models (van der Hoef et al., 2008). In the hard-sphere approach, the trajectories of particles are determined by momentum conserving binary collisions. This model assumes that each particle can contact only with one other particle at a time. It also assumes that contact between a pair of particles is instantaneous and the inter-particle forces are expressed as

momentum exchange between each pair of contacting particles. In these simulations, the collisions are calculated sequentially according to the order of events. The hard-sphere models are significantly faster than the soft-sphere models for dispersed systems.

This thesis concentrates on the soft-body approach (Luding, 2005), where particle interactions can be multiple and enduring. The approach uses particle overlap to compute contact forces; based on the extent of the overlap and the relative impact velocity of colliding elements. The relations between the amount of overlap and the resulting contact force are frequently referred to as elastic models. An advantage of soft-body models is that they can incorporate long range interactions forces.

2.5.3.1 Contact forces between particles

For DEM to be computationally inexpensive when employed in multi-particle processes, the forces and torques caused by particle interaction are calculated by simplified models or equations. There exist a number of force models which mostly allow particles to have deformation. The deformation is modelled as an overlap between particles. In the general case of an assembly of many particles, the contact force model is applied at each contact and the vectorial sum of these contact forces is determined to yield the resultant contact force acting on that particle (Cundall and Strack, 1979). There has been extensive work in the literature in order to develop accurate and/or computationally efficient models based on theories of contact mechanics to be employed in DEM simulations. Mostly these models are developed for spherical contacts based on Hertz theory. The contact models can be divided into four categories: elastic, elasto-plastic, elastic-adhesive and elasto-plastic-adhesive models (for more information on these models the reader is referred to Zhu et al. 2007).

The overlap between two particles, relative to the surface orientation of the objects, creates a normal and a tangential spring at the initial contact point. The motion of the bodies is determined by the compression and elongation of these imaginary springs.

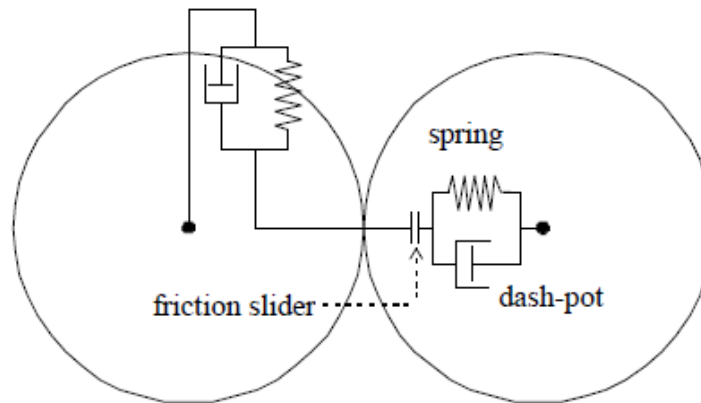


Figure 2.11: Diagram of the linear spring-dashpot soft-sphere model (Hoomans, 1996)

In the case of non-spherical particles, the consideration of contact forces between particles is much more complex. Two approaches have been proposed to handle such particles. The more basic approach treats a non-spherical particle as a collection of spherical particles (Gallas and Sokolowski, 1993; Pelessone, 2003; Bertrand et al., 2005). The main benefit of this technique is that it can be used to treat particles of very complicated structure, and it only requires a contact model for the spherical particle. In the second approach, the particles are considered to be of a certain shape such as cylinder, ellipsoid, and polygon. The occurrence of particle interaction between two such adjacent particles is calculated by solving the underlying mathematical equations (Langston et al., 2004). This latter technique is more precise; however it is more computationally expensive. The contact force model adopted in this work is one for spherical particles (Cleary and Sawley, 2002).

2.5.3.2 *Non-contact forces between particles*

For systems that contain relatively small particles and/or moisture, non-contact inter-particle forces can have a considerable influence on the packing and motion of particles. In DEM such forces are directly accounted for. Generally, three fundamental forces contribute to the non-contact forces: van der Waals, capillary (or liquid bridge) and electrostatic forces, which have the ability to act simultaneously or sequentially to different degrees.

The conventional Hertz contact theory describes the elastic deformation of bodies in contact, however does not consider the adhesion force brought about by van der Waals.

Hamaker (Hamaker, 1937) calculated the interaction force between a sphere and a semi-infinite body, by summarising all the possible individual molecular interactions, as follows (Seville et al., 2000),

$$F_{van} = \frac{A_H R}{12 d^2} \quad 2-15$$

where A_H is the Hamaker coefficient which is a material property related to the molecular properties of the particle with radius of R , and d is the separation distance between the two bodies.

A capillary force can form when there is surface tension at solid or fluid interfaces. γ . The attraction reaches a maximum for spherical particles that are completely covered by liquid. For such a case, the liquid bridge attraction force between two particles, F_{LB} , can be calculated as follow (Visser, 1989),

$$F_{LB} = 2\pi\gamma R \quad 2-16$$

where γ is the surface tension of the liquid and R is the radius of the two particles.

Finally, electrostatic forces can form as a result of tribo-electric charging or formation of a potential difference between particles. In the former case, charged particles attract neighbouring uncharged particles due to their own image charge. The attraction force can be calculated by the classical Coulomb equation (Visser, 1989),

$$F_{t_elec} = \frac{Q^2 \left(1 - \frac{d}{\sqrt{R^2 + d^2}} \right)}{16\pi\epsilon_0 d^2} \quad 2-17$$

where Q and R are the charge and radius of the charged particle, d is the separation distance between the two bodies, and ϵ_0 is the permittivity of the vacuum. In the latter case i.e. potential difference, particles with a different work-function can form a

potential difference when in close proximity. This attraction force can be calculated from the equation below (Visser, 1989),

$$F_{V_elec} = \frac{\pi\epsilon_0 R}{d} (\Delta V)^2 \quad 2-18$$

where ΔV is the potential difference formed by the contact. For a more detailed discussion on these force types the reader is directed to Comte-Bellot (1976). It is also worth noting that some DEM simulations incorporate a surface energy model as an alternative to explicitly calculating the electrostatic and van der Waals forces (Subero et al., 1999; Antony, 2000; Moreno et al., 2003).

For a more in depth review on the major theoretical developments and studies based on DEM the reader is referred to Zhu et al (2007) and Zhu et al (2008).

2.5.3.3 Contact forces between particles and wall

In theory, the removal of single particles from a wall by fluid turbulence is affected by the adhesive forces which in turn depend on the particle-to-substrate material composition, the humidity, the presence of electrostatic forces, gravity, the size and the shape of the particle as well as the substrate surface structure and the turbulent boundary layer (Zimon, 1982). The particle adhesion models to describe the contact of a sphere to another sphere are also typically used for contact to a flat wall, such as JKR (Johnson et al. (1971)) and DMT (Derjaguin et al. (1975)). Focusing on the relationship between the particle and fluid near the wall, it is difficult to calculate the displacement of fluid in this region due to its acceleration from particles approaching the wall (Figure 2.12). It is therefore crucial that this region is well resolved.

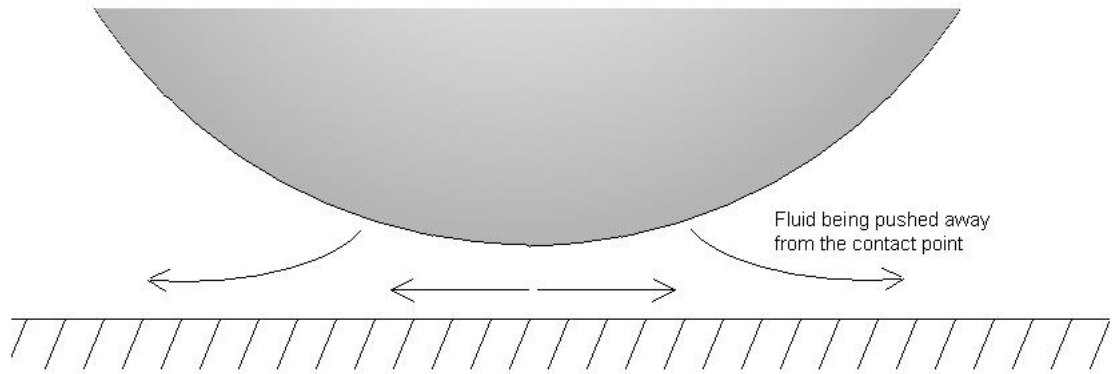


Figure 2.12: Fluid behaviour between a wall and an approaching particle (Pasol et al., 2005)

Particles can approach the wall from any direction, for that reason necessary to consider separately their parallel and normal components with respect to the wall reference frame. The decomposition of the 3D-vector of the particle velocity into the wall's local reference frame is defined by its projection on the vector normal to the surface and its projection on the plane tangential to the surface, as illustrated in Figure 2.13. It is therefore possible to express the motion of the particle relative to the wall as the sum of a velocity vector orthogonal to the wall and a velocity vector parallel to the wall. Based on this, the linear nature of the Stokes' equation allows the drag forces arising from various velocity components to be superimposed.

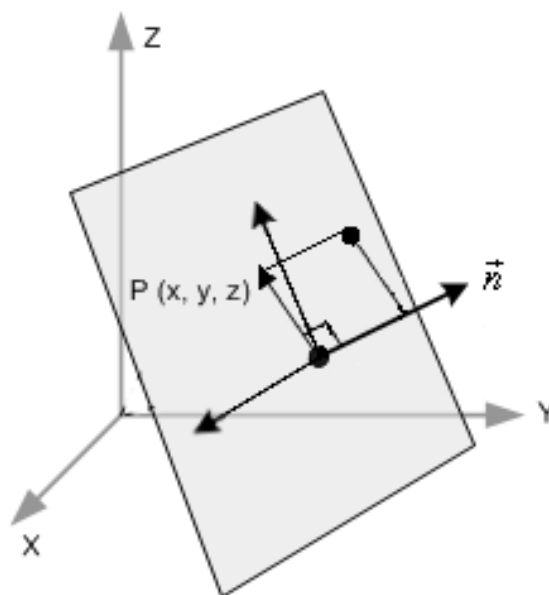


Figure 2.13: Principles of 3D projection (Chaumeil and Crapper, 2013)

2.6 Review of Numerical and Experimental Studies in Turbulent Bounded Flow

In single-phase flow, the simplest and best understood flow configurations are channels, pipes and ducts with many experimental and numerical studies available in open literature. The problem becomes significantly more difficult however, if particles are introduced into such a flow field (i.e. two-phase flow).

The overall aim of this research is to gain insight on particle interaction and agglomeration in turbulent channel flow using numerical methods. Experimental data can serve as validation to the numerical models used and also highlight areas needed for improvement. For that reason, this section gives a review of relevant experimental studies on single- and two-phase flow conducted in channels and does not provide any literature on other geometries.

In the context of numerical studies, the accuracy of LES can also be gauged by comparing against DNS data. Therefore, single-phase and two-phase DNS studies in channel flow are of relevance and briefly covered. Moreover, this review is mostly concerned with two-phase flow studies in which particle-particle interactions have been accounted for with emphasis on particle agglomeration. Such studies are limited; therefore in this case, RANS, LES and DNS are all of high value to this work. All reviewed literature, has been presented in a chronological layout.

2.6.1 Single-Phase Experiments

Experimental turbulence measurements for channels at high Reynolds number are rather limited and lag behind pipe and boundary layer flow studies. In a review paper on many of the experimental studies of turbulent channel flow, Zanoun et al. (2009), mentioned that the geometrical considerations associated with achieving well resolved measurements at high Reynolds number has greatly limited experimental work in this respect. For example, the combination of high aspect ratio and development length make achieving an extremely high Reynolds number in a channel flow facility much more costly than for a pipe flow. To explain further, consider experimental channel and pipe flow facilities with the same working fluid and identical height and diameter. The high aspect ratio needed for a channel flow facility to maintain nominally two-dimensional flow conditions (i.e., $W/H > 7$, where W is the channel width and H is the

height (Monty, 2005)) requires at least an order of magnitude larger volumetric flow rate to attain the same Reynolds number as the pipe flow facility. For that reason, there is less experimental work published on the understanding of high Reynolds number turbulent channel flow compared to pipe and duct flow. Noteworthy experimental works in turbulent channel flow are provided in the table below.

Table 2-1 Selected studies on liquid–solid/gas–solid channel flows

Reference	Reynolds number (bulk)	Reynolds number (centre-line)	Reynolds number (shear)	Technique
Laufer (1948)	62,000		1,500	
Comte-Bellot and Craya (1965)	230,000		4,800	
Patel and Head (1968)	1,000 – 10,000			HWA
Kreplin and Eckelmann (1979)		2,800 – 3,850		
Wei and Willmarth (1989)	40,000		1000	LDV
Niederschulte et al., 1990		2, 850 – 3,220		
Durst and Kikura (1995)	2,500 – 9,800		87 – 293	
Monty and Chong (2009)			> 1000	HWA
Schultz and Flack (2013)	10,000 – 300,000		350 – 6100	LDV

2.6.2 Two-Phase Experiments

In most of the experimental work in two-phase flow, the main focus of research is on flow turbulence modulation by particles. One of the earlier studies in horizontal channel flow is that of Lourenco et al. (1983), the work focussed on the modification of the gas velocity profiles by the particle phase and the effects of gravity. Kulick et al. (1994) investigated a downward directed gas–solid flow in a channel, which used a sophisticated feeding system to ensure a homogeneous dispersion of the particles. Small particles with different densities were used to observe turbulence reduction over a range of particle Stokes numbers. Although, the experiments were not accurate with regard to wall boundary conditions; as the test section was constructed from two different materials. According to Sommerfeld (2000) a channel flow is dominated by wall collisions, therefore, a change in wall material can significantly affect the results, which was later shown by numerous works using advanced computational approaches, such as large eddy simulation (e.g. Yamamoto et al. 2001). Sommerfeld and Huber (1999) conducted measurements in a narrow horizontal channel. The aim of the study was to obtain experimental data for the validation of a Lagrangian wall collision model with

wall roughness effects, by using different wall materials. A chopped Ar:ion laser was used to measure the change in particle velocity during a wall collision process based on the streakline technique. Both spherical and non-spherical particles were used. The statistical averaged parameters for up to 5,000 single events allowed an improvement and detailed validation of the proposed stochastic wall collision model (Sommerfeld and Huber 1999). Kussin and Sommerfeld (2002) used PDA to obtain detailed measurements of air and particle velocity in a developed particle laden horizontal channel flow. The velocity profiles and turbulence spectra for the streamwise velocity component showed modulation of turbulence fluctuations by particles. In addition to the effect of particle size and mass loading on turbulence modulation, the influence of wall roughness was analysed. It was clearly shown that increasing wall roughness also results in stronger turbulence dissipation due to two-way coupling. Lain et al. (2002) used a PDA approach to perform measurements in a horizontal channel flow with different particle diameters and mass loading ratios.. The data was required for the validation of numerical calculations based on a four-way coupled RANS-LPT approach.

A number of experiments in horizontal channel flow (Tanie`re et al. 1997; Kaftori et al. 1998; Kiger and Pan 2002; Wu et al. 2006; Li et al. 2010b) revealed that, even for $0.72 \times 10^{-6} < \phi_v < 2.3 \times 10^{-4}$, the presence of particles still leads to significant turbulence modulation. It is worth mentioning here that, more recently, advanced techniques such as PIV approaches have been used to investigate channel flows, see for example Lelouvetel et al. (2009) and Hout (2011). Advances in experimental techniques have also made it feasible to measure particle agglomeration. Wang et al. (2011) used a PDA technique to measure thermophoretic deposition of polydispersed particles in a gas-solid turbulent flow through a vertical channel. Their results showed that the particle concentration in the near wall region was much higher than that in the bulk flow region which was nearly uniform. The effects of turbulent diffusion and particle agglomeration on the particle deposition were studied. The high particle concentration in the near wall region due to turbulent diffusion was important for thermophoresis and particle agglomeration, although, the turbulent deposition was quite low. The particle agglomeration was analysed based on the experimental data, considering the effects of temperature and particle concentration. In a polydisperse system, the particle agglomeration had important effects on the particle deposition. Some noteworthy experimental studies on particle-laden flows in channels are summarised in Table 2-2.

There are also number of experimental studies on particle agglomeration in other geometries such as cyclones see for example, Paiva et al. (2010), Cheng (2012), Haig et al. (2014).

Table 2-2 Selected studies on liquid–solid/gas–solid channel flows

Reference	u (m/s)	ρ_p (kg/m ³)	d_p (mm)	Technique	ρ_f/ρ_p	ϕ_p ($\times 10^{-4}$)	Agglomeration
Matsumoto & Saito (1970)	7 & 10	1040 2500 8700	0.94 0.5 & 0.95 0.51	Visualisation			
Lourenco <i>et al.</i> (1983)	6 – 13	2400	0.25 & 0.5	LDA			
Sommerfeld (1992)	8.6	2500	0.45 & 0.11	LDA			
Kulick <i>et al.</i> (1994)	10.5	300 2500 8700	0.1 & 0.5 0.1 & 0.5 0.1 & 0.5	LDA			
Taniere <i>et al.</i> (1997)					2,100 1,200	0.05 0.05	
Kaftori <i>et al.</i> (1998)					1.03	0.95 – 1.9	
Sommerfeld & Huber (1999)	5 – 15	2500 2400	0.1 & 0.5 0.2	Streak Technique			
Kussin & Sommerfeld (2002)	10 – 25	2500 2400	0.06 – 1.0	PDA PIV			
Kiger and Pan (2002)					2.6	2.3	
Lain <i>et al.</i> (2002)	19.5 & 14	2500	0.04 & 0.1	PDA	1,563		
Sommerfeld and Kussin (2004)	20	2450	0.06 – 0.625	PDA			
(Wu <i>et al.</i> , 2006)					877	0.0072 – 0.48	
Wang <i>et al.</i> (2011)				PDA			✓
Li <i>et al.</i> (2012)					0.5 – 0.025		
Barth <i>et al.</i> (2014)				PIV			

In two-phase pipe flow, one of the earlier experimental studies was conducted by Friedlander & Johnstone (1957), in which the deposition of suspended particles in turbulent gas flow was investigated. Their results showed that the inertia effect of the turbulent eddies dominated particle transport. Other early experimental studies on two-phase pipe flow include those of; Postman & Schwendiman (1960), Wells & Chamberlain (1967), Yoder & Silverman (1967), Sehmel (1968), Farmer *et al.* (1970) and Ilori (1971). Experimental investigations using more advanced and less intrusive techniques include that of Tsuji & Morikawa (1982), Tsuji *et al.* (1984), Varaksin *et al.* (1998), Varaksin *et al.* (1999), Caraman *et al.* (2003), Boree & Caraman (2005), and

Obligado et al. (2011). There have been relatively little studies conducted in two-phase duct flow, with the majority of work being focused on pipe and tube flows. Important early experimental studies on two-phase duct flow include those of Alexander & Coldren (1951), Chamberlain (1967), and Sehmel (1971, 1973). For information and a more complete review on experimental studies on particle-laden duct flows the reader is directed to Sippola (2002) and Sippola and Nazaroff (2004).

2.6.3 Single-Phase Numerical Studies

One of the first DNS studies of fully developed turbulent channel flow was conducted by Kim et al. (1987) for a Shear Reynolds flow of 180. Followed by Kuroda et al. (1989) for a slightly lower Reynolds number of $Re_\tau = 150$. Kawamura and co-workers (Kawamura et al., 1998, Abe et al., 2001, Abe et al., 2004a, Abe et al., 2004b) have performed DNS studies for $Re_\tau = 180 - 1020$. The continuing rapid increase in computational power has made possible the simulation of wall bounded turbulent flow at appreciably high Reynolds numbers with a large computational domain, since much attention is paid to a large-scale motions (LSM) in the outer region, see Liu et al. (2001); Iwamoto et al., 2002; del Álamo and Jiménez, 2003; del Álamo et al., 2004; Abe et al., 2004; Hoyas and Jiménez, 2006, Jiménez et al. 2010. It is worth mentioning that for lower Reynolds number flows; the near-wall streaky structures are more elongated compared to those in high Reynolds number flows. Therefore, the DNS of a low Reynolds number flow requires a larger computational domain to capture the near-wall streaky structures and the LSM. Noteworthy works on low Reynolds number channel flow include for example, Bewley et al. (2001), Chang et al. (2002), Iwamoto et al. (2002), Högberg et al. (2003), Tsukahara (2014). Additionally, in pipe flow, recent DNS simulations have been carried out up to shear Reynolds numbers of 1,000 – 2,000 by Satake et al., 2000, and Chin et al. (2014), and El Khoury et al. (2014).

2.6.4 Two-Phase Numerical Studies

Studies wherein computational approaches have been applied to turbulent bounded flow are reviewed. The significant findings are discussed, with focus on the microdynamics such as flow structure and particle–particle, particle–fluid and particle–wall interaction forces. This review does not cover all applications and publications due to its diversity;

instead it aims to show that DEM is an effective approach for particle scale research of particulate systems and points out some of the major accomplishments.

2.6.4.1 RANS

In the area of two-phase flow; a bridge (overlap) has emerged between particle scientists and multiphase flow experts. This is because particle scientists have recently introduced CFD to DEM and multiphase flow experts have even more recently incorporated particle-particle interactions in their models. It is important to point out that, particle scientists usually refer to four-way coupled approaches as ‘two-way coupled CFD-DEM’.

Most of the computational studies that involve particle-particle interactions and agglomeration in two- and multi-phase flows have been conducted using RANS, with the majority being application based. Although, there are a number of studies, available in open literature, that have investigated simple geometry (e.g. channel and pipe flow) using four-way coupled RANS approaches. However, most of these have not taken into account particle agglomeration and are therefore only listed here: Lun and Liu (1997), Zhao et al. (2010), Alvandifar et al. (2011), Laín and Sommerfeld (2012), Pan et al. (2011a), Azimian et al. (2014), Laín (2014), and de Souza et al. (2014). Studies that incorporate particle agglomeration are of greater value to this work and are discussed below.

Marshall (2007) used a one-way coupled RANS-DEM approach to examine particle aggregate formation and particle capture by walls in laminar channel flow. The work provides a detailed investigation of the fundamental mechanics leading to adhesion of particle aggregates to channel walls, which involved a combination of aggregate capture, aggregate deformation by particle rolling and shearing of aggregates from the wall. Cases with different adhesion potential, particle sizes and flow Reynolds number were examined, for both mono- and poly-dispersed systems. The results revealed the importance in the deposition process of particle-particle interaction by showing that aerosol channels with previously deposited particles and agglomerates had a higher capture rate of incoming particles. Larger deposited agglomerates increased floc re-suspension (Li and Marshall, 2007). Zhao et al. (2010) carried out a numerical simulation of fully developed hydrodynamics of a two-dimensional channel using a

two-way coupled RANS-DEM approach. The solution to the established model was incorporated in the commercial CFD package of FLUENT. The residence time distribution (RTD) of solids was computed by tracking the displacements of all particles in the flow direction. The results showed a rather wide RTD for the solids in the upward flow and a sharp peak in downward flow, this was in agreement with previous experimental findings. The ensemble averaging of transient dynamics also showed reasonable profiles of solids volume fraction and solids velocity, and their dependence on particle density. Azimian et al. (2014) adopted a RANS-DEM approach to investigate fully developed turbulent flow through a channel with an obstacle. Simulations were carried out using the commercial discrete element method (DEM) software, EDEM, coupled with the CFD package, FLUENT. The velocity profiles of single phase and particulate flow were validated by their own LDA experimental data. Laín (2014) used a Reynolds stress turbulence model accounting to perform numerical computations in horizontal gas-particle flows emphasizing the importance of elementary processes, such as particle collisions with rough walls and inter-particle collisions, on the predicted two-phase flow variables and pressure drop along the channel. For the calculation of particle motion all relevant forces (i.e., drag, slip-shear and slip-rotational lift and gravity), inter-particle collisions and particle-rough wall collisions were considered. The agreement of the computations with the experiments of Sommerfeld and Kussin (2004) was found to be satisfactory for pressure drop and mean and fluctuating velocities of both phases as well as for the normalised particle mass flux. Tomac and Gutierrez (2014) adopted a RANS-DEM approach to investigate the effects of fluid lubrication on solid particle flow and transport in slurries at high solids concentrations. The approach incorporated a new user-defined contact model that accounted for particle lubrication and was implemented in the commercially available two-dimensional Particle Flow Code (PFC2D). It was found that the balance of fluid drag, related to the pressure drop in the channel and slurry properties (such as fluid viscosity, particles volumetric concentration, particles size and channel size substantially) contribute to the particle agglomeration in the absence of gravity.

In pipe flow, most of the works using full coupling or CFD-DEM involve the modeling of plug flow, which assumes there is no boundary layer adjacent to the inner wall of the pipe. The plug flow model has many practical applications and can be applied to systems with high solid concentrations and low gas velocities. An advantage of the plug

flow model is that no part of the solution of the problem can be perpetuated "upstream". Therefore, by knowing the initial conditions, it is possible to calculate the exact solution to the differential equation (no further iteration is required). Fraige and Langston (2006) used RANS-DEM to investigate horizontal pipe flow. Their studies provide an outline on the effects of material properties on flow characteristics, and potential intricacies found in RANS-DEM. Kuang et al. (2008) studied the microscopic and macroscopic structures of slug flow. Their results showed that slug movement is strongly influenced by particle-fluid and particle-wall interactions in the wall-normal direction, and that particle-particle interactions cause the slug to sweep particles upwards in the settled layer. Naturally, the magnitudes of these interaction forces increased with gas and solid flow rates. Ebrahimi et al. (2014) used RANS-DEM and LDA to investigate dilute particle-liquid flow in a horizontal pipe. Simulations were carried out by two-way coupling the commercial software's FLUENT and EDEM. From the simulation investigations it was concluded that the inclusion of the Magnus lift force had a crucial influence, with observed particle distributions in the upper part of the conveying line reproducible in the simulation only by implementing the Magnus lift force terms in the model equations. In vertical pipe flow, RANS-DEM studies have shown that for systems of low particle concentration and high gas velocities, the particles tend to be dispersed throughout the pipe cross section. Whereas for high solid concentrations and low gas velocities, the particles have a tendency to form clusters and move in the form of a dense plug (Kawaguchi et al., 2000b; Lim et al., 2006a; Zhang et al., 2008; Chu and Yu, 2008). Such flow patterns are commonly known as the dispersed, transition, and plug flow regimes, respectively, and show good agreement with the experimental results of Zhu et al. (2003). Han et al. (2003) produced work that showed particle breakage and attrition are unavoidable phenomena that influence the conveying characteristics and the quality of particulate materials. Additionally, Watano (2006) showed that charged powders are further affected by particle-particle-wall collisions. Some of the more recent works on fully coupled RANS studies in pipe flow include those of Sturm et al. (2009), Narayanan and Lakehal (2010), Pan et al. (2011b), Zhou et al. (2010), Hilton and Cleary (2011), Stratton and Wensrich (2011), Kuang et al. (2013), Alletto and Breuer (2013), Zhang et al. (2014).

Studies that investigate particle agglomeration in two-phase flow through other geometries are also of relevance to this work. Wang and Rhodes (2004) conducted one

of the earliest CFD-DEM studies that considered a wide range of inter-particle forces in a fluidized bed. Limtrakul et al. (2007) developed a mathematical model based on DEM to simulate the hydrodynamic behavior in a vibrated fluidized bed. The cohesive force in this study was Van der Waals (VdW) force calculated by Hamaker's theory (Hamaker, 1937). The effects of particle type, amplitude and frequency of vibration and superficial gas velocity were considered in their study. Yang et al. (2008) conducted a numerical study using DEM in which the agglomeration of fine particles was calculated based on the van der Waals attraction. The work investigated agglomerate structure, packing density, coordination number and tensile strength. Tong et al. (2010) used a RANS-DEM approach to investigate powder dispersion with applications in dry powder inhalers (DPI). In their study, agglomerates of different particle sizes and poly-dispersities were dispersed in a cyclonic flow at different flow velocities. It was shown that the dispersion was governed by particle-wall impacts and particle-particle adhesion. The influence of air flow on the dispersion and dispersion mechanism of DPI was further investigated by Yang et al. (2013). The authors investigated the effects of air flow on the detachment process for carrier-based DPIs. A coupled RANS-DEM approach was used to explore both gas-particle interactions and particle-particle adhesion. The effects of air velocity, work of adhesion and initial positions of particles were examined and a mechanism governing the detachment performance was proposed. Calvert et al., 2011 and Calvert et al., 2013 used DEM coupled to a continuum model to investigate the aerodynamic dispersion of cohesive clusters with different particle surface energies and size, respectively. The authors found a strong relationship between cluster dispersion and particle surface energy and cluster size. Hou et al. (2012) used CFD-DEM to investigate the micromechanics of different flow patterns in fixed, expanded and fluidised beds. The authors set out to establish the relation between macroscopic and microscopic aspects, formation of a stable expanded bed and the correlation between coordination number and porosity. Chaumeil and Crapper (2013) adopted a two-way coupled RANS-DEM approach by coupling FLUENT and EDEM to model agglomeration and deposition on a constricted tube collector of colloidal size particles immersed in a liquid. The ability of this method to represent surface interactions allowed the simulation of agglomeration and deposition at the particle scale. This DEM approach was initially applied to simulate the aggregation of suspended nanoparticles by Peng et al. (2010). The effects of various particle-to-collector size ratios, inlet fluid flow-rates and particle concentrations were examined

and it was found that deposition efficiency is strongly dependent on the inter-relation of these parameters. Mansourpour et al. (2014) employed a two-dimensional RANS-DEM approach coupled with the equations of energy to simulate the agglomeration process at high temperatures in an air-polyethylene fluidized bed. The inter-particle cohesive force was calculated based on solid bridging by the viscous flow. The influence of gas velocity on agglomerate size was investigated, and it was shown that the rate of formation of large agglomerates is decreased with an increase in gas velocity. Brosh et al. (2014) utilised a RANS-DEM approach by coupling ANSYS FLUENT to a DEM code to investigate a spiral jet mill. The work investigated the agglomeration, fatigue and breakage of particles due to particle-particle and particle-wall interactions. The predictions of the numerical simulations with and without VdW forces were compared with experimental data.

Most of the numerical investigations in two-phase flow are based on RANS combined with statistical turbulence models. RANS is not always capable of providing reliable predictions for practically relevant flows, where complex phenomena such as curved streamlines, secondary flow regions and transition are involved. Consequently, the prediction of particle dispersion and deposition using a Lagrangian random-walk eddy-interaction model or similar methods to track the particles in the flow field was sometimes found to not be accurate enough. Therefore, over the past few years there has been a drive towards a methodology which in general is more appropriate for the prediction of fluid turbulence including complex flow phenomena, i.e., LES. Among the different geometries of wall bounded turbulent two-phase flows encountered in industry, it is beneficiary to investigate two-phase channel and pipe flows as a first step towards more complex flow configurations. LES is very computationally demanding and this demand is further increased with predicting the particulate phase, especially if additional physical effects such as the fluid-particle interaction as well as particle-particle collisions are accounted for. Because of the considerably high computational costs, very few attempts have been made to simulate particle agglomeration in particle-laden turbulent flows.

2.6.4.2 LES

Studies where four-way coupled approaches have been used to investigate fully developed particle-fluid flows are of major relevance to this work. That being said,

studies involving one- and two-way coupled DNS and well resolved LES approaches are also of relevance.

To the best of the author's knowledge there are no LES or DNS papers on the agglomeration of particles in turbulent bounded flows. Although, there are LES and DNS studies on the breakup of agglomerates by fluid turbulence (see for example Nishiura et al. (2010), Shimosaka et al. (2012), and Babler et al. (2014)). There are a limited number of papers in open literature where four-way coupled LES and DNS approaches (without agglomeration) have been used to investigate bounded flows. These studies are more focused on the influence of particle-particle collisions on the fluid and particle phase characteristics. Recent work on four-way coupled flows, as considered herein, includes that of Alletto and Breuer (2012) who used LES to predict a particle-laden turbulent flow at high mass loading downstream of a channel and combustion chamber. The influence of fluid-particle interactions (two-way coupling) and particle-particle collisions (four-way coupling) were investigated in detail. A deterministic collision model was considered based on virtual cells, where only adjacent particles were taken into account in the search for potential collision partners. Mallouppas and van Wachem (2013) similarly used LES to simulate the behaviour of interacting particles in a turbulent channel flow. The importance of individual physical phenomena occurring in particle-laden flows was investigated through a series of simulations that were fully four-way coupled. The simulation results demonstrated that rough walls and inter-particle collisions have an important effect in redistributing particles across the channel, even for very dilute flows. Li et al. (2014) used LES-DEM to simulate particle-laden two-phase channel flow. The particle velocity, shear stress, and turbulence intensities were calculated, and distributions of slip velocity and feedback force were analysed to reveal the interactions between particles and the continuous fluid phase. Their results showed that inter-particle collisions significantly alter the velocity of particles within the near-surface region of the boundary layer. Other noteworthy four-way coupled LES studies in channel flow include, Yamamoto et al. (2001), Geurts (2011), Breuer and Alletto (2012), and in other geometries such as fluidised beds these include, Zhou et al. (2004), Gui et al. (2008), Berrouk and Wu (2010), Fang et al. (2013), Luo et al. (2013) and Yang et al. (2014). In other geometries, Laín (2014) described a three-dimensional Eulerian-Lagrangian calculation of confined horizontal gas-particle flows emphasising the importance of elementary processes, such

as particle collisions with rough walls and inter-particle collisions, on the predicted two-phase flow variables and pressure drop along a duct. de Souza et al. (2014) adopted an LES-LPT approach with the goal of better understanding the interactions between particles and fluid in a vertical conical diffuser. The authors showed that, even at moderate mass loadings, particles can significantly affect the diffuser flow pattern, and reattach the otherwise separated flow under some conditions.

2.6.4.3 DNS

In the context of two- and multiphase turbulent bounded flows, the most recent studies using one- and two-way coupled approaches for dispersed particle regimes mainly focus on the influence of flow structures on particle motion, and the study of non-spherical particle shapes. Vinkovic et al. (2011) conducted a DNS-LPT investigation of incompressible turbulent channel flows to study the characteristics of ejections that surround solid particles. The behavior of particles in dilute turbulent channel flows, without particle collisions and without feedback of particles on the carrier fluid, was studied using relatively high Reynolds number DNS. Zhao et al. (2010) used a two-way coupled DNS-LPT approach to investigate turbulence modulation and drag reduction by spherical particles in channel flow. Andersson et al. (2012) also used DNS to study torque-coupling and particle-turbulence interactions, with a number of other works by the same authors considering the modelling of particle stress, particle spin, and particle suspensions in two-way coupled gas-solid turbulent channel flows. There has been very little work done in these areas, in particular for pipes and ducts (Fairweather and Yao, 2009).

In an ideal DNS-DEM, the fluid phase is resolved at a scale similar to particle gaps, where the particles are taken as discrete moving boundaries (Hu, 1996). A notable advantage is that combined weak formulation is used to model the particle–fluid system. Moreover, DNS has the ability to generate in depth data of hydrodynamic interactions between the two phases (Pan et al. 2002). Yet, this model does not have the capacity to efficiently handle particle collisions. Granting, there are ongoing studies to devise new principles and algorithms for the direct numerical simulation of particle interactions within turbulent flow. Contrary to classical approaches which rely on the assumption of a particle ballistic displacement within a time step and are thus severely limited to small time steps, Mohaupt et al. (2011) developed a new method, in a one-way coupled

setting, that allowed the use of much larger time steps and could be applied also for very small particle diameters which are typical of colloids. This method could be a satisfactory candidate for the numerical prediction, in the context of DNS of the fluid flow, of the agglomeration kernels of colloidal particles with acceptable total computational costs. In most DNS models, particle collisions are not modelled whatsoever; the simulation halts if the space between two approaching particles is lower than a predetermined small value (Pan et al., 2002). In modern models, a repulsive body force has been incorporated into the momentum equation to prevent collisions between particles (Glowinski et al., 2000; Singh et al., 2000). As a result, up to now, DNS has mainly been employed in particle-liquid flows where the hydrodynamic interaction is prevailing and the interaction between particles is nonviolent. This reduces its effective use in fluidisation systems where particle collisions and inter-particle forces are substantial. Computationally, the turbulent channel flow is the most studied using DNS mainly because of the minimalism of the boundary conditions. For this reason, fully resolved simulations of turbulent channel flow have been carried out at Re_τ up to 2000 (e.g., Hoyas and Jiménez, 2006) which are much higher than the Reynolds numbers reached for either pipe or boundary layer flow simulations.

In recent years, studies have been conducted in two-phase turbulent bounded flows using four-way coupled DNS approaches in different geometries; these studies are state-of-the-art and have been included in this review. Zhao and van Wachem (2013) used DNS with full four-way coupling to study the behaviour of ellipsoidal particle in channel flow. The trajectories of the ellipsoids were tracked by solving the translational and rotational equations of motion in a Quaternion framework and closed with hydrodynamic drag and torque laws. To specifically identify the effect of particle shape, simulations of single phase channel flow were compared to simulations with spherical particles and to simulations with ellipsoids. Ahmadi et al. (2010) adopted a DNS approach to simulate two-phase flows including particle-particle collisions and two-way coupling in a turbulent duct flow. Several simulations for different particle relaxation times and particle mass loading were performed, and the effects of the inter-particle collisions and two-way coupling on the particle deposition velocity, fluid and particle fluctuating velocities, particle normal mean velocity, and particle concentration were determined. It was found that when both inter-particle collisions and two-way coupling effects were taken into account in the simulations, the particle deposition velocity

increased. Chen et al. (2011) used DNS to investigate the behavior of inter-particle collision and its effects on multiphase flow in a three-dimensional gas–solid two-phase plane mixing layer. The deterministic hard-sphere model was used to describe the inter-particle collision. It was found that inter-particle collision occur frequently in the local regions with higher particle concentration of the flow field. The modifications of the mixed fluid thickness, the Reynolds stresses, and the mean stream-wise velocity of two phases due to inter-particle collision were quantitatively investigated. Yoshida et al. (2013) developed a DNS-DEM approach to predict the apparent viscosity of slurry flow. Shear-thinning behavior due to the collapse of agglomerates with increase in mean shear rate was observed for the case of a slurry with agglomerated particles. This behavior was caused by the existence of so-called immobile water in the agglomerates. The influences of the shape of aggregation and particle interaction on the apparent viscosity were investigated. Deen and Kuipers (2014) presented a novel simulation technique to perform direct DNS-DEM of fluid flow and mass transfer in a dense fluidised bed. The method was verified using well known empirical expressions for the Sherwood number. Vincent et al. (2014) utilised a direct numerical simulation (DNS) together with a Lagrangian volume of fluid (VOF) method to study particle flows in a vertical pipe. The authors developed a specific Eulerian volume of fluid method with Lagrangian tracking of the phase function and presented a strategy for handling particle collisions and lubrication effects. The numerical solutions were compared to existing theoretical and experimental results with good agreement found.

It should be mentioned that DNS continues to be used to study low Reynolds number flows. Therefore one of the main challenges for LES is to compute flows with high precision at sufficiently high Reynolds numbers to more closely replicate those conditions found in practical applications. For a detailed review of the advances in DNS for predicting two-phase flow, the reader is directed to Vincent et al. (2014).

The present capability of LES in Eulerian–Lagrangian investigations of dispersed flows are very much restricted by the modelling of the SGS turbulence effects on particle motion. These effects must be considered if one is to generate accurate data on the physics of particle dispersion as the LES cut-off filter eliminates the energy and flow structures from the turbulent flow field. In light of the literature, it is concluded that the effect of SGS turbulence on particle accumulation at the near-wall cannot be recreated

by reconstructing the right amount of fluid and particle velocity fluctuations. However, LES-DEM can still be used as an alternative to DNS; the consequence is a lack of resolution of flow which can lead to the effects of the small scales of fluid turbulence not being captured, in particular in the near wall region. Most importantly, these effects are negligible when dealing with large Stokes number particles ($St > 25$) and can be neglected.

2.7 Conclusion of the Literature Review

The review has highlighted the importance of inter-particle collisions and their effects on fluid and particle phase characteristics. However, none has considered in detail the conditions that favour the agglomeration of particles. The dynamics of particle-laden fluid flows include a number of important aspects that dictate whether particle agglomeration will occur, affecting in turn particle dispersion and deposition. These include factors such as the instantaneous particle velocity, and the size, concentration, collision frequency and surface properties of the particles. As a result, many complications arise when analysing the underlying mechanisms responsible for agglomeration. The coupling of LES and DEM is an effective approach that is capable of providing insight into these mechanisms as well as a predictive method applicable to many practically-relevant flows. Moreover, the LES-DEM approach is much more computationally efficient than DNS and more competent in capturing particle physics compared to RANS or TFM.

3. Numerical Methodology of the LES-DEM Approach

3.1 Introduction

The aim of this chapter is to present the governing equations and numerical solution methods used in predicting the behaviour of two-phase flow of interest to this thesis. Here, the fluid phase is calculated using LES embodied in the commercial code FLUENT 14.5 which is capable of accurately predicting complex dynamic flow phenomena. The flow solutions are coupled to an LPT-DEM in EDEM 2.5 to predict the particle-phase. For additional information the reader is referred to the citations given.

3.2 Fluid-Phase Modelling

The basis for modelling a fluid flow arises from the mathematical statements of the conservation laws of physics; conservation of mass, energy and momentum. The derivations of these equations for a Newtonian fluid over a finite control volume are generally known as the Navier-Stokes equations. Solving these equations provide information on a number of flow characteristics in a variety of reference frames and also serve as accuracy checks for experimental, numerical, and asymptotic methods. These equations are well documented in any textbook on fluid dynamics. The conservation equations for mass and momentum can be written in Cartesian tensor notation as follows (Bird et al. 1960):

$$\text{Mass:} \quad \frac{\partial \rho}{\partial t} + \frac{\partial(\rho u_i)}{\partial x_i} = 0 \quad 3-1$$

$$\text{Momentum:} \quad \rho \frac{\partial u_i}{\partial t} + \rho u_j \frac{\partial u_i}{\partial x_j} = -\frac{\partial p}{\partial x_i} - \frac{\partial \tau_{ij}}{\partial x_j} + \rho g_i \quad 3-2$$

The stress tensor for a Newtonian fluid is given as:

$$\tau_{ij} = -\mu \left(\frac{\partial u_i}{\partial x_j} + \frac{\partial u_j}{\partial x_i} - \frac{2}{3} \frac{\partial u_l}{\partial x_l} \right) \delta_{ij} \quad 3-3$$

where the Kronecker delta, $\delta_{ij} = 1$ if $i = j$ and $\delta_{ij} = 0$ if $i \neq j$

3.3 Large Eddy Simulation

3.3.1 Filtering Operation

In LES, only the largest and most energetic scales of motions are directly computed, whilst the small scales are modelled (Smagorinsky, 1963).

$$f = \bar{f} + f_{SGS} \quad 3-4$$

Any function is therefore decomposed using a localised filter function such that filtered values only retain the variability of the original function over length scales comparable to, or larger than, that of the filter width Δ , with:

$$\bar{f}(x) = \int_D f(x') G(x, x'; \bar{\Delta}) dx' \quad 3-5$$

where D is the entire domain and G is the filter function. The filter function determines the size and the structure of the small scale turbulent motions. Common filter functions include the Gaussian and the “sharp cut-off”, however, in this work a top-hat filter was used (Germano, 1992) as this fits naturally into a finite-volume formulation. This takes the form:

$$G(x; x') = \begin{cases} \frac{1}{\bar{\Delta}^3} & \text{for } |x_i - x'_i| < \frac{\bar{\Delta}}{2} \\ 0 & \text{otherwise} \end{cases} \quad 3-6$$

3.3.2 Governing Equations

This decomposition is then applied to the Navier-Stokes equations, for an incompressible Newtonian fluid with constant properties, bringing about terms which represent the effect of the sub-grid scale (SGS) motion on the resolved motion. The governing equations are:

$$\frac{\partial \bar{u}_i}{\partial t} + \frac{\partial \bar{u}_i \bar{u}_j}{\partial x_j} = -\frac{1}{\rho} \frac{\partial \bar{p}}{\partial x_i} - \frac{\partial \tau_{ij}}{\partial x_j} + \frac{\partial}{\partial x_j} \left(\nu \frac{\partial \bar{u}_i}{\partial x_j} \right) + f_i \quad 3-7$$

$$\frac{\partial \bar{u}_i}{\partial x_i} = 0 \quad 3-8$$

where u_i , p and ν are the velocity components, the pressure and the kinematic viscosity, respectively. The term f_i denotes a source term (momentum sink) resulting from the particulate phase and the overbar ($\bar{\quad}$) denotes the resolved scales. The filtering of the non-linear convective term in the momentum equation, equation 3-7, gives rise to the additional SGS stress tensor τ_{ij} which has to mimic the influence of the non-resolved small-scale turbulence on the resolved large scale turbulent eddies. The sub-grid scale stress τ_{ij} is defined by;

$$\tau_{ij} = \overline{u_i u_j} - \bar{u}_i \bar{u}_j \quad 3-9$$

3.3.3 Sub-Grid Scale Modelling

This stress, which results from the filtering operation in equation 3-9, is unknown and needs closure. In this work, a model based on the eddy-viscosity concept was used to compute the SGS from:

$$\tau_{ij}^a = \tau_{ij} - \frac{1}{3} \tau_{kk} \delta_{ij} = -2\nu_t \bar{S}_{ij} \quad 3-10$$

where τ_{ij}^a is the anisotropic (traceless) part of the stress tensor τ_{ij} , ν_t is the SGS eddy-viscosity, δ_{ij} is the Kronecker delta, and \bar{S}_{ij} is the resolved rate-of-strain tensor defined as $\bar{S}_{ij} = 1/2(\partial \bar{u}_i / \partial x_j + \partial \bar{u}_j / \partial x_i)$. It is now required to determine the SGS viscosity, ν_t . The trace of the stress tensor is added to the pressure forming a new pressure $P = \bar{p} + \tau_{kk} / 3$. The eddy viscosity ν_t itself is a function of the strain rate tensor \bar{S}_{ij} and the sub-grid length l , according to:

$$v_t = C_v \bar{\Delta}^2 |\bar{S}| \quad \text{with} \quad |\bar{S}| = \sqrt{2\bar{S}_{ij}\bar{S}_{ij}} \quad 3-11$$

where C_v is a model constant, $|\bar{S}|$ is the modulus of the rate-of-strain for the resolved scales, and $\bar{\Delta}$ is the grid-filter width given by $\bar{\Delta} = V^{1/3}$. The sub-grid scale stress is therefore,

$$\tau_{ij} - \frac{\delta_{ij}}{3} \tau_{kk} = -2C_v \bar{\Delta}^2 |\bar{S}| \bar{S}_{ij} \quad 3-12$$

This simple model is both economic and robust, however, the practical shortcoming is that it is limited to a single value of the model constant (C_v) which is not universally applicable to a wide range of flows. Germano et al. (1991) and subsequently Lilly (1992) proposed a dynamic procedure in which the Smagorinsky constant, C_v , is computed as a function of time and space based on the information provided by the resolved scales of motion. This requires a test filter ($\tilde{\Delta}$) to acquire the small scales of the resolved field. It is common to denote the test-filtered quantities by a tilde, and write the filtered Navier-Stokes equations as the test-filtered Navier-Stokes equations (Kim, 2004). The stress associated with the smallest resolved scales between the test-filter scale ($\tilde{\Delta}$) and the grid-filter scale ($\bar{\Delta}$) can be interpreted as the stress components, L_{ij} , which can be directly obtained from the resolved scales and used to calculate the model constant.

$$L_{ij} - \frac{\delta_{ij}}{3} L_{kk} = C_v (\alpha_{ij} - \tilde{\beta}_{ij}) \quad 3-13$$

$$\text{where } \alpha_{ij} = -2\tilde{\Delta}^2 |\tilde{S}| \tilde{S}_{ij} \quad \text{and} \quad \beta_{ij} = -2\bar{\Delta}^2 |\bar{S}| \bar{S}_{ij} \quad 3-14$$

Based on Lilly's suggestion, the model constant C_v is calculated by determining the value of C_v which reduces the square of the errors given by:

$$E = \left(L_{ij} - \frac{\delta_{ij}}{3} L_{kk} - C_v M_{ij} \right)^2 \quad 3-15$$

$$\text{where } M_{ij} = \alpha_{ij} - \tilde{\beta}_{ij} = -2 \left(\tilde{\Delta}^2 \left| \tilde{S} \right| \tilde{S}_{ij} - \bar{\Delta}^2 \left| \tilde{S} \right| \tilde{S}_{ij} \right) \quad 3-16$$

Taking $\partial E / \partial C_v$ and setting it zero gives:

$$C_v = \frac{L_{ij} M_{ij}}{M_{ij} M_{ij}} \quad 3-17$$

As a result, the model constant C_v calculated is a local value that varies in time and space, taking both negative and positive values. A negative C_v gives rise to a negative eddy-viscosity which is caused by the flow of energy from the sub-grid scale eddies to the resolved eddies (i.e. “back-scatter”) and considered an advantageous aspect of dynamic models. A very large negative eddy viscosity can, however, bring about numerical instability, giving rise to a high level of numerical noise or even divergence of the numerical solution. To prevent this, C_v is cut-off at zero. This is somewhat different to the conventional approach in which the total viscosity (laminar viscosity plus eddy-viscosity) is limited, therefore permitting a small negative SGS eddy-viscosity.

The dynamic approach requires a test filter. One deciding factor in selecting the test-filter is that it should be consistent with the grid-filter. To meet this condition, this work employed a top-hat filter as it fits naturally into a finite-volume formulation. Moreover, the test-filter ought to be applicable to unstructured meshes:

$$\tilde{\phi}(c_0) = \frac{1}{\sum_n V_i} \int_{V_{tot}} \bar{\phi} dv = \frac{\sum_i \bar{\phi}_i V_i}{\sum_i V_i} \quad 3-18$$

3.3.4 Boundary Conditions

3.3.4.1 Inlet Conditions

There are a number of methods available for specifying the inflow boundary conditions. In most cases the generation of the turbulent inflow is based on artificial inflow information from experimental data or RANS solutions. In this method, the turbulence intensity value specified at a velocity inlet for LES is used to randomly perturb the instantaneous velocity

field at the inlet. It does not specify a modelled turbulence quantity. Instead, the stochastic components of the flow at the inlet boundary are accounted for by superposing random perturbations on individual velocity components. To generate a time-dependent inlet condition, a random 2-dimensional vortex method is considered. With this approach, a perturbation is added on a specified mean velocity profile via a fluctuating vorticity field (that is, two-dimensional in the plane normal to the streamwise direction). The vortex method is based on the Lagrangian form of the 2-dimensional evolution equation of the vorticity and the Biot-Savart law. A particle discretization is used to solve this equation. These particles or “vortex points” are convected randomly and carry information about the vorticity field. For more detailed information on the algorithms used to model the fluctuating velocity at velocity inlet boundaries or pressure inlet boundaries, the reader is referred to the theory guide of ANSYS FLUENT.

In cases where the flow considered is temporally developing, the need for inflow conditions can be eliminated (Jones. et al., 2002). In the case of the work described in this thesis, and due to the simple nature of the geometry considered, periodic boundary conditions were implemented at the inflow and outflow boundary locations. Periodic boundary conditions imply that the computational domain is repeated infinitely, or that the flow is fully developed and statistically stationary in space. Implementation requires some prior knowledge of the structure of the flow field since the minimum domain length along the direction where the periodic boundaries are applied must correspond at least to the wavelength of the longest structure present in the flow field (Piomelli and Chasnov 1996).

Realistic inlet conditions (streamwise velocity, kinetic energy and dissipation rate) obtained from separate RANS simulations, were introduced in the present work and were allowed to develop until numerically stable and fully turbulent. It should be noted that unrealistic (“flat”) turbulent profiles at the inlet generate unrealistic turbulent eddies at the inlet.

3.3.4.2 Wall Boundary Conditions

In cases where the mesh is fine enough to resolve the laminar viscous sub-layer, natural no-slip conditions can be implemented, and the wall shear stress τ_w is obtained from the laminar stress-strain relationship:

$$z^+ = \frac{\rho u_\tau z}{\mu} \quad 3-19$$

where z^+ is the non-dimensional wall distance, z is the distance to the nearest wall and u_τ is the shear or friction velocity ($u_\tau = (\tau_w/\rho)^{1/2}$) at the node closest to the wall.

At high Reynolds numbers it is not practicable for a full resolution of the viscous sub-layer to be made, and an approximate boundary condition is adopted. It is assumed that the centroid of the wall-adjacent cell falls within the logarithmic region of the boundary layer, and the law-of-the-wall is employed:

$$z^+ = \frac{1}{k} \ln E \left(\frac{\rho \mu_\tau z}{\mu} \right) \quad 3-20$$

where k is the von Kármán constant and $E = 9.793$. If the mesh is such that the first near-wall point is within the buffer region, then two above laws are blended in accordance with a function suggested by Kader (1981).

In this work, an alternative near-wall approach has been used based on the work of Werner and Wengle (1993), who proposed an analytical integration of the power-law near-wall velocity distribution resulting in the following expressions for the wall shear stress:

$$|\tau_w| = \begin{cases} \frac{2\mu |u_p|}{\Delta z} & \text{for } |u_p| \leq \frac{\mu}{2\rho\Delta z} A^{\frac{2}{1-B}} \\ \rho \left[\frac{1-B}{2} A^{\frac{1+B}{1-B}} \left(\frac{\mu}{\rho\Delta z} \right)^{1+B} + \frac{1+B}{A} \left(\frac{\mu}{\rho\Delta z} \right)^B |u_p| \right]^{\frac{2}{1+B}} & \text{for } |u_p| > \frac{\mu}{2\rho\Delta z} A^{\frac{2}{1-B}} \end{cases} \quad 3-21$$

where u_p is the wall-parallel velocity, $A = 8$, $B = 1/7$ are the constants, and Δz is the near-wall control volume length scale.

3.3.5 Solution Procedure

ANSYS FLUENT (Version 14.5) solves the governing integral equations for the conservation of mass and momentum, and (when appropriate) for energy and other scalars such as turbulence and chemical species. A control-volume-based technique is used that consists of: 1- division of the domain into discrete control volumes using a computational grid, 2- integration of the governing equations on the individual control volumes to construct algebraic equations for the discrete dependent variables (“unknowns”) such as velocities, pressure, temperature, and conserved scalars, and 3- linearisation of the discretised equations and solution of the resultant linear equation system to yield updated values of the dependent variables. In this section, the special practices related to the discretisation of the momentum and continuity equations and their solution by means of the pressure-based solver are addressed. Information is given in the following sequence: spatial and temporal discretisation of the momentum, continuity and other scalar transport equations, evaluation of the gradients, pressure-velocity coupling, time-advancement algorithm, and multigrid method.

By default, the discrete values of the scalar are stored at the cell centre. Spatial discretisation is carried out using an upwind scheme, wherein the face values required for the convection terms are interpolated from the cell centre values. A second order accurate central differencing scheme is employed. It is well known that central-differencing schemes can produce unbounded solutions and non-physical wiggles, which can lead to stability problems for the numerical procedure. These stability problems are avoided using a deferred correction for the central-differencing scheme. The discretisation scheme described for a scalar transport equation is also used to discretise the momentum equations. A co-located variable storage arrangement is used, whereby pressure and velocity are both stored at cell centers. This requires an interpolation scheme to compute the face values of pressure from the cell values, and has been achieved by the PRESTO! (PREssure STaggering Option) scheme. The scheme uses the discrete continuity balance for a staggered control volume about the face to compute the staggered (face) pressure. For the discretisation of the continuity equation, in order to proceed further, it is necessary to relate the face values of velocity, to the stored values of velocity at the cell centers. Linear interpolation of cell-centered velocities to the face results in unphysical checker-boarding of pressure. Because of this arrangement, a procedure similar to that outlined by Rhie and Chow (1983) has been utilised to prevent checker-boarding. The

face value of velocity is not averaged linearly; instead, momentum-weighted averaging, using weighting factors (based on coefficients for the cells on either side of the face) is performed. Pressure-velocity coupling is achieved by deriving an additional condition for pressure by reformatting the continuity equation. The pressure-velocity coupling algorithm selected is Pressure-Implicit with Splitting of Operators (PISO). The scheme is based on the higher degree of the approximate relation between the corrections for pressure and velocity. LES is a transient simulation; and therefore the governing equations require discretisation not only in space, but also in time. Temporal discretisation involves the integration of every term in the differential equations over a time step. Here, a bounded second order implicit time integration scheme is used. The bounded variables include the turbulence kinetic energy, dissipation rate, and specific dissipation rate. Gradients are used for constructing values of a scalar at the cell faces, and for computing secondary diffusion terms and velocity derivatives. The gradient of a given variable is used to discretise the convection and diffusion terms in the flow conservation equations. The gradients are computed according to the least squares cell based method. In this method the solution is assumed to vary linearly. Gradient limiters, also known as slope limiters, are sometimes used to prevent spurious oscillations. They are not required, however, for the central differencing scheme.

The pressure-based solver uses an implicit approach for discretisation of the transport equation. The overall time-discretisation error is determined by both the choice of temporal discretisation (as mentioned earlier) and the manner in which the solutions are advanced to the next time step (time-advancement scheme). The segregated solution process by which the equations are solved one by one introduces splitting error. In order to control the splitting error, the selected approach for the time-advancement scheme is an iterative one. In the iterative scheme, all the equations are solved iteratively, for a given time-step, until the convergence criteria are met. Thus, advancing the solutions by one time-step normally requires a number of outer iterations as shown in Figure 3.1. With this iterative scheme, non-linearity of the individual equations and inter-equation couplings are fully accounted for, eliminating the splitting error. Initially, an adaptive time-step was chosen, based on the estimation of a truncation error of 0.01 associated with the time integration scheme. If the truncation error was smaller than a specified tolerance, the size of the time-step was increased, and vice versa. This process continued until a constant time-step value was reached which was subsequently implemented as a fixed value. The simulation time taken for 1s of run was approximately 30 days on a Dell Precision T5500 workstation utilising 12GB

installed memory and 8 processors. The code is parallel and uses the message passing interface HP-MPI. Time-averaged flow field variables were computed from running averages during the computations. Further information on the mathematical model employed, and the numerical solution algorithm and its application, may be found in the ANSYS FLUENT 14.5 theory guide.

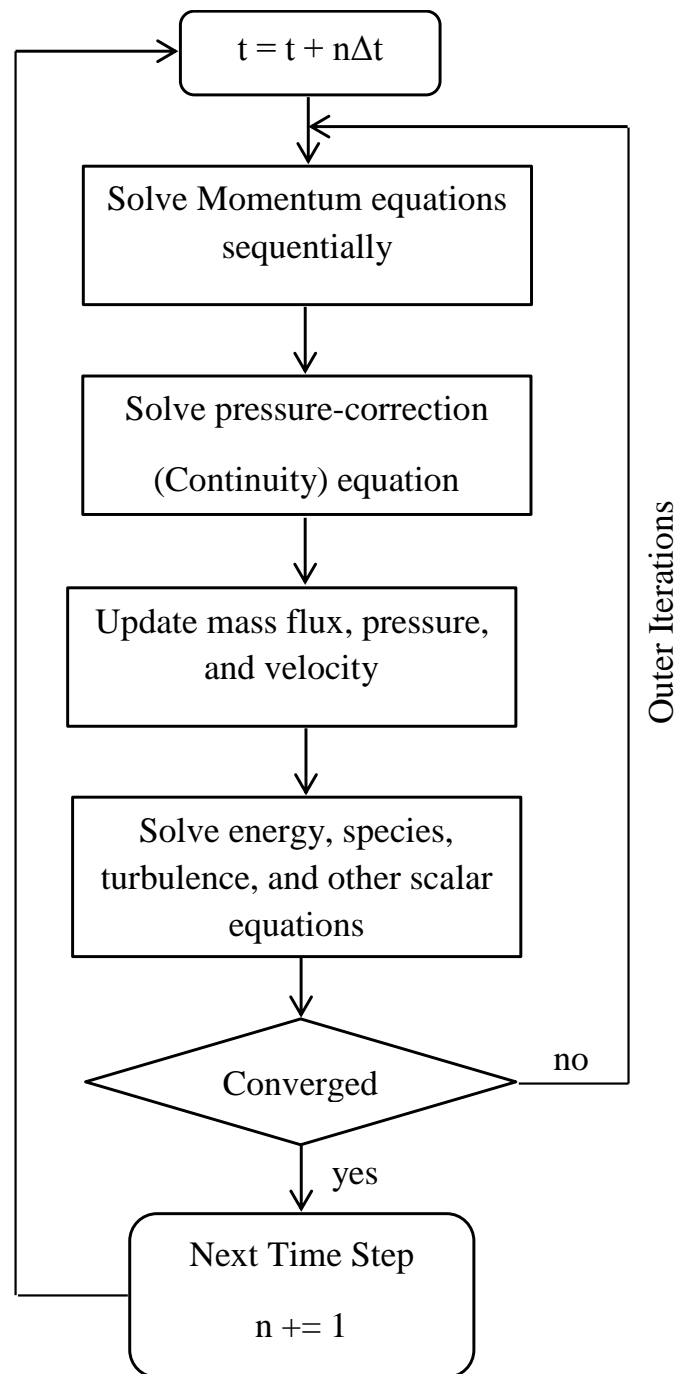


Figure 3.1 Overview of the iterative time advancement solution method for the Segregated Solver

A Gauss-Seidel point implicit solver has been used to rapidly remove local (high-frequency) errors in the solution, global (low-frequency) errors are reduced at a rate inversely related to the mesh size. This means, however, that for a large number of nodes, the solver stalls and the residual reduction rate becomes prohibitively low. Multigrid techniques allow global error to be addressed by using a sequence of successively coarser meshes. The solver contains a multigrid algebraic (AMG) method to accelerate solution convergence of the solver by computing corrections on a series of coarse grid levels.

3.4 Discrete Element Method

The ANSYS Fluent CFD code was coupled to the DEM-Solutions EDEM (discrete element method) software via a coupling interface in order to predict the particle-laden flows of interest. What follows is a description of the various elements of this coupled approach used in the present work.

3.4.1 Governing equations

The particles can have two types of motion: translational and rotational. Their paths are computed based on Newton's second law for the translational and rotational accelerations. This is achieved by integrating the accelerations over a time-step, with particle velocities and positions updated. The translational motion is calculated based on equation 3-22:

$$m \frac{d\vec{v}}{dt} = \vec{F}_g + \vec{F}_c + \vec{F}_{nc} \quad 3-22$$

where V is the translational velocity of the particle, m is the mass of the particle, \vec{F}_g is the resultant gravitational force acting on the particle, and \vec{F}_c and \vec{F}_{nc} are the resultant contact and non-contact forces between the particle and surrounding media or walls, respectively.

The rotational motion is calculated based on equation 3-23:

$$I \frac{d\vec{\omega}_p}{dt} = \vec{M} \quad 3-23$$

Where I is the moment of inertia, $\vec{\omega}_p$ is the angular velocity, t is time, $\vec{M} = -C_{fr} |\vec{F}_c| \vec{\omega}_p$ is the resultant contact torque acting on the particle and C_{fr} is the coefficient of rolling friction.

Figure 3.2 gives a schematic representation of these forces for particles a and b, showing the resultant normal and tangential forces acting on the particles, F_n and F_t , as well as the translational v and angular velocities ω_p , where α is the particle overlap, representing the deformation of the soft particles.

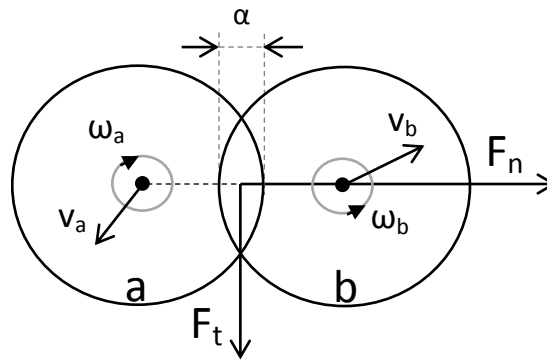


Figure 3.2. Schematic representation of the discrete particle collision model (after Deen et al., 2007).

Armenio and Fiorotto (2001) have shown that the only significant forces in these systems are the drag and buoyancy force. To understand the physics of turbulent dispersion in the most simplified setting, other forces acting on the particle, such as hydrostatic force, Magnus lift force, added mass force and Basset history force, have been neglected, their contribution being orders of magnitude smaller than that of the Saffman lift force (Armenio and Fiorotto, 2001). It is important to point out that, buoyancy was also neglected in simulations where the effect of gravity had not been considered. Brownian motion of the particles was also not considered since the particle sizes are large enough ($d_p \geq 1\mu\text{m}$) to permit the neglect of this molecular effect. In coupling the fluid dynamic and particle motion, particle rotation due to

fluid shear was also neglected on the grounds that this is only significant under high vorticity conditions. Furthermore, the aim was to minimise the number of degrees of freedom by keeping the simulations as simplified as possible whilst still retaining the realism required for practical applications; thus all particles were assumed to be spherical with equal diameter and density, and particles were assumed to be much heavier than the fluid ($\rho_p/\rho_f \gg 1$).

The shear induced Saffman lift force equation 3-27 was taken in account as it assumes non-trivial magnitudes in the viscous sub-layer, with the large velocity gradients in such regions inducing pressure differences on the surface of the particle, causing lift. This work used a modified spherical, free-stream drag for calculation of the force on the particles. All fluid parameters are taken from the fluid cell element which contained the centre of the DEM particle. This treatment is therefore only valid for particles of the same size as or smaller than a fluid finite-volume cell; or where the change in fluid parameters (velocity, density, viscosity, etc.) over the extent of a particle remains roughly constant. The governing equation for a spherical particle is:

$$m_p \frac{d\vec{v}}{dt} = 0.5C_D \rho_f A_p (\vec{u} - \vec{v}) |\vec{u} - \vec{v}| + (\vec{F}_L) \quad 3-24$$

where \vec{u} and \vec{v} are the fluid and particle velocity vectors, ρ_f is the fluid density, A_p is the projected particle area, \vec{F}_L is the lift force. The corresponding drag coefficient C_D depends on the particle Reynolds number Re_p given by Rowe and Enwood (1962):

$$C_D = \begin{cases} \frac{24}{Re_p} & Re_p \leq 0.5 \\ \frac{24}{Re_p} (1 + 0.15 Re_p^{0.687}) & 0.5 \leq Re_p \leq 1000 \\ 0.44 & Re_p > 1000 \end{cases} \quad 3-25$$

$$\text{where} \quad Re_p = \varphi \rho_f d_p |\vec{u} - \vec{v}| / \nu \quad 3-26$$

and d_p is the diameter of the particle's bounding sphere, and ε is the voidage/porosity of the fluid cell. The various specifications for C_D are required to extend the validity of the expression to cover a wide range of Re_p , and in particular to accommodate depositing particles.

The expression for the inertia shear lift was first obtained by Saffman (1965, 1968):

$$\vec{F}_{L,Saff} = 1.61d_p^2(\mu\rho_f)^{1/2}|\vec{\omega}_f|^{-1/2}[(\vec{u} - \vec{v}) \times \vec{\omega}_f] \quad 3-27$$

where the vorticity of the flow (also known as shear rate), $\vec{\omega}_f = \frac{d\vec{u}}{dt}$. However, this simple model requires the sheared flow to be quite slow, with the following conditions to be satisfied:

$$\begin{aligned} Re_s &= \frac{|\vec{u} - \vec{v}|d_p}{\nu} < 1 \\ Re_G &= \frac{|d\vec{u}/dy|d_p^2}{\nu} < 1 \\ Re_\Omega &= \frac{|0.5\vec{\omega}_f - \vec{\omega}_p|d_p^2}{\nu} < 1 \end{aligned} \quad 3-28$$

$$\text{where} \quad \xi = \frac{Re_G^{1/2}}{Re_s} > 1$$

Here Ω is the rotational speed of the sphere. Dandy & Dwyer (1990) found that the Saffman lift force is approximately valid at larger Re_s and small ξ . McLaughlin (1991) showed that the lift force decreases as ξ decreases. In order to overcome these constraints, Mei (1992) proposed the following two correlations for a finite, $0.1 < Re_s < 100$:

$$\begin{aligned} \frac{\vec{F}_{L,mei}}{\vec{F}_{L,saff}} &= (1 - 0.3314\eta^{1/2}) \exp\left(-\frac{Re_s}{10}\right) + 0.3314\eta^{1/2}, \quad (Re_s \leq 40) \\ \frac{\vec{F}_{L,mei}}{\vec{F}_{L,saff}} &= 0.0524(\eta Re_s)^{1/2}, \quad (Re_s > 40) \end{aligned} \quad 3-29$$

Nonetheless, the correlation still needs to satisfy a finite linear shear rate, $\eta = 1/2\text{Re}_s\xi^2$, which has to be $0.005 \leq \eta \leq 0.4$.

The particles are characterised by the relaxation time, defined as $\tau_p = \rho_p d_p^2 / 18\mu_f$, and the non-dimensional particle response time given by the particle Stokes number, $St = \tau_p^+ = \tau_p / \tau_f$ where τ_f is a characteristic time scale of the flow (defined as $\tau_f = \nu / u_\tau^2$, where the u_τ is the shear velocity). It is important to mention here that for the simulation results presented, the particles considered are large with relaxation times greater than the smallest fluid time scales, therefore the influence of the unresolved scales in LES on particle motion are negligible (Pozorski and Apte, 2009).

3.4.2 Interaction: fluid forces on particle

The particle time-steps required in solving the equation of motion are typically substantially smaller than the fluid time-steps in order to correctly capture any contact behaviour. The particles therefore do not move a significant distance in a single particle time-step. Typical ratios for the fluid:particle time-steps vary from 1:10 to 1:100. The fluid-particle coupling automatically adjusts the number of particle iterations carried out in order to match the fluid time-step, (τ_F) such that:

$$\tau_F = \sum_{\text{iterations}} \tau_p \quad 3-30$$

Note that in DEM there is no requirement for the time step, (τ_p), to be the same from one iteration to another.

3.4.3 Interaction: particle forces on fluid

The effect of particles on the continuous phase for volume fractions greater than 10^{-6} was taken into account, leading to a two-way coupled simulation as discussed earlier. The switch from one-way to two-way coupled regimes requires that the models used to calculate the drag and lift forces take into account the volume of particles found in each computational cell. The particle position is calculated at its centroid and its volume is returned as a scalar value. More

detailed information about particle shape can also be calculated from the particle sample points. The representation of particle volume is based on multiple sample points, generated using the Monte Carlo method. The method takes regular sample points within a box bounding a particle and keeps those points that lie within the particle's bounding surface, as illustrated in Figure 3.3.

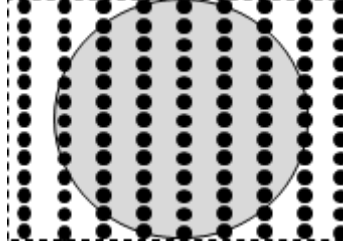


Figure 3.3. Sample points within the volume surrounding a particle.

Each point is then checked to determine which fluid computational cell it lies within. The solid volume fraction within a particular cell is then the percentage of the number of sample points that lie within that cell, given by:

$$\varepsilon_s = 1 - \varepsilon = \sum_{\text{particles}} \frac{n_c}{N} V_p \quad 3-31$$

where n_c is the number of sample points contained within the cell of particle p , N is the total number of sample points of the particle, and V_p is the volume of the particle. Sample points are generated for each of the particle types defined in the simulation. Using the position, orientation and scaling of the individual particles, the precise coordinates for the points representing each particle can be calculated. Provided no additional particle types are later added to the simulation, sample points need only be collected once, at the start of a simulation. Particles have external forces applied to them before the LPT executes a simulation-step, and up-to-date particle data are obtained and any force or torque applied to the particles during the simulation-step, prior to the LPT performing another simulation. Particle mass loading is considered through the momentum coupling terms of the continuous phase. The exchange of momentum between the two phases is achieved through the calculation of the momentum sink of the drag force that arises due to the relative velocity between the phases. An additional source term f_i representing the forces exerted by the

particles on the fluid is added to the filtered Navier-Stokes (equation 3-7). This momentum sink is calculated using:

$$f_i = \frac{-\sum_i^n \vec{F}}{V} \quad 3-32$$

Hence, the sink term is the summation of the drag and lift forces, \vec{F} , which are exerted on the fluid in that fluid cell, and V is the volume of the fluid solver finite-volume cell. A smooth source term distribution is achieved by using a tri-linear distribution of the contribution of the particles to the eight finite-volume cell centres surrounding the particle. Any further interactions between the phases are neglected, e.g. possible influences of the particles on the sub-grid scale stresses of the fluid are not taken into account. The reason for this is that when particle motion is computed using a well resolved LES velocity field, the approach is accurate for simulating gas-solid turbulent flow without any modelling of the sub-grid fluid velocity in the particle trajectory equation (Armenio et al., 1999). The sub-grid fluid turbulence scales will also hardly affect the instantaneous particle motion, and will have even less of an effect on the statistical properties, such as the mean particle concentration and the root-mean square of the particle velocity fluctuations (Kuerten, 2006). This is particularly the case for large particles (i.e. the $> 50\mu\text{m}$ particles considered herein) in low and moderate Reynolds number flow ($\text{Re}_\tau = 150 - 590$).

3.4.4 Interaction: particle forces on particle

At particle volume fractions greater than 10^{-3} the flow is no longer considered to be a dilute dispersed two-phase flow (Laín and Sommerfeld, 2008). In such flows, particle-particle collisions play an important role and must be accounted for, with this being commonly referred to as four-way coupling. One exception is for flows that include particles of relatively large Stokes number ($St \gg 1$); where for volume fractions less than 10^{-3} particle accumulation in the near-wall region is common and results in a considerable number of particle-particle interactions. In this work, the particle-laden flow was assumed to be dilute (particle volume fraction up to $\sim 10^{-4}$), and the method incorporated full coupling between the phases, i.e. interactions between particles were considered, and the flow and particles were

two-way coupled. Particle-wall collisions were assumed to be inelastic and described based on the coefficient of restitution.

The most computationally intensive part of DEM is locating the element pairs that are in close proximity to each other. Collision detection is carried out at every time-step, since particles change their mutual position in the succeeding time step. A smaller time-step requires an increase in contact detection and forces updates, and therefore a decrease in performance. This requires an efficient algorithm with a specific set of criteria to only check contact between particles that have a likelihood of interacting. The computational domain is divided into a uniform number of cubic elements with a size between 10 - 15 times larger than the particle radius. Each particle is assigned to the cell in which its centre point is located. Interaction is only checked between particles in the cell and neighbouring cells. Particle-particle interactions were modelled using the discrete element method incorporating the contact model of Herz-Mindlin with Johnson-Kendall-Roberts cohesion to allow the simulation of the Van der Waals forces which influence particle behaviour (Johnson et al., 1971). The approach only considered the attractive forces within the contact area, i.e. the attractive inter-particle forces are of infinite short range.

The Hertz-mindlin contact model has been used in order to prevent particles from interpenetrating each other, and to ensure that contact forces are transmitted properly between the different geometrical elements of the simulation. The contact force between two perfectly elastic spheres is resolved into normal and tangential (shear) components with respect to the contact plane,

$$\vec{F}_c = \vec{F}_n + \vec{F}_t \quad 3-33$$

Where F_c is the contact force, and F_n and F_t are the normal and tangential components of the contact force, respectively, and are given below,

$$\vec{F}_n = -\kappa_n \delta_n - \gamma_n \vec{v}_n \quad 3-34$$

$$\vec{F}_t = \begin{cases} -\kappa_t \delta_t - \gamma_t \vec{v}_t & \text{if } |k_t \delta_t| < |k_t \delta_t| C_{fs} \\ \frac{|k_t \delta_t| C_{fs} \delta_t}{|\delta_t|} & \end{cases} \quad 3-35$$

Where κ_n and κ_t are normal and tangential stiffness, v_n and v_t are the normal and tangential particle velocity, C_{fs} is the static friction coefficient and $\gamma_{n,t}$ are damping coefficients to the normal δ_n and tangential δ_t overlap, these are defined below

$$\delta_n = R_1 + R_2 - \|\vec{r}_1 - \vec{r}_2\|, \quad \delta_t = \int_t^{t+\Delta t} \vec{v}_t dt \quad 3-36$$

There are two stiffness's for an interaction in DEM, normal stiffness κ_n and shear (tangent) stiffness κ_t which are functions of the Young's modulus and Poisson's ratio of the particle material; however, in practice, their value is often chosen to lower computational costs as they are strongly related to the integration time-step, and their relation to the solid material property disregarded. In many DEM codes κ_t is often taken as a fraction of κ_n , however, in EDEM $\kappa_t = \kappa_n$ (DEM Solutions., 2014).

A more compound and theoretically comprehensive model to calculate force between two objects is the non-linear Hertz model (Di Renzo and Di Maio, 2004), where

$$\vec{F}_n = -\kappa_n u_n^{3/2} - \gamma_n u_n^{1/2} \vec{v}_n \quad 3-37$$

Because of its complex nature, however, this model is computationally expensive for DEM simulations of coarse flows that contain very high volume fraction of particles, and therefore is not used often in such flows.

From Hertz theory of elastic collision the total time of contact is given by:

$$t_h = 2.87 \left(\frac{m^*}{R^* E^* \vec{v}_z} \right)^{1/5} \quad 3-38$$

where m^* is related to the particle masses m_i by the equation

$$\frac{1}{m^*} = \frac{1}{m_1} + \frac{1}{m_2} \quad 3-39$$

where R^* is the equivalent radius, E^* is the equivalent Young's modulus and v_{12} is the relative velocity defines as,

$$R^* = \frac{R_1 R_2}{R_1 + R_2} \quad 3-40$$

$$E^* = \left(\frac{1-\nu_1^2}{E_1} + \frac{1-\nu_2^2}{E_2} \right)^{-1} \quad 3-41$$

and,

$$\vec{v}_{12} = \vec{v}_1 - \vec{v}_2 \quad 3-42$$

with the subscripts 1 and 2 representing the interacting particles 1 and 2. R is the particle radius, ν is the Poisson's ratio, and E is the Young's modulus of elasticity ($E = 2G(1 + \nu)$), and where G is the shear modulus.

JKR builds on the conventional Hertz model by incorporating an energy balance to extend it to cover two elastic-adhesive spheres. The contact area predicted by the JKR model is larger than that given by the Hertz model; this creates an outer annulus in the contact area which experiences tensile stress. This annulus surrounds an inner circular region over which a Hertzian compressive distribution acts (Thornton and Yin, 1991). When two spheres come into contact, the normal force between them immediately drops to a certain value ($8/9 f_c$, where f_c is the pull-off force (Thornton and Ning, 1998)) due to van der Waals attractive forces. The velocity of the spheres gradually reduces and some of the initial kinetic energy is radiated into the substrate as elastic waves. The loading stage is complete when the contact force reaches a maximum value and particle velocity drops to zero. In the recovery stage, the stored elastic energy is released and converted into kinetic energy causing the spheres to move in opposite directions. All the work done during the loading stage has been recovered

when the contact overlap becomes zero. At this stage, however, the spheres remain adhered to each other and further work (known as work of cohesion) is required to separate the surfaces. The contact breaks at a negative overlap, α_f , for a contact force $5/9 f_c$ (Ning, 1995). The pull-off force is the maximum tensile force the contact experiences and is given by (Johnson et al., 1971):

$$f_c = \frac{3}{2} \pi R^* \Gamma \quad 3-43$$

where Γ is the surface energy per unit area. The governing equation for the force-overlap is given by (Johnson, 1985):

$$\vec{F}_n = \frac{4E^* a^3}{3R^*} - (8\pi\Gamma E^* a^3)^{1/2} \quad 3-44$$

where a is the radius of overlap. The overlap α can be evaluated by (Johnson, 1985):

$$\alpha = \frac{a^2}{R^*} - \left(\frac{2\pi\Gamma a}{E^*} \right)^{1/2} \quad 3-45$$

The particle surface attractive force was altered by specifying the surface energy Γ with the amount of surface energy influencing the cohesion of the material.

The particles are treated as distinct elements which displace independently from one another and interact only at point contacts (Cundall and Strack, 1979). Particle motion in regions of high particle number density is affected not only by the forces and torques originating from contacts with its immediate neighbouring particles, but also by disturbances propagating from more distant particles. To avoid evaluation of the effects of disturbance waves, the combined DEM-LPT approach integrates fluid hydrodynamic forces and torques into the particle simulation on an individual particle level. When the DEM-LPT performs a time-step of the simulation, the external forces act upon the particles in addition to any collision forces. Figure 3.4 depicts the various stages of the DEM-LPT simulation loop and the point at which it interacts with the LES solver. As a result, any disturbance cannot propagate from each

particle further than its immediate neighbouring particles (Cundall and Strack, 1979). The speed of disturbance waves was approximated by Rayleigh surface wave propagation based on the physical properties of the discrete medium. The time must then be sufficiently less than the Rayleigh time-step in order to ensure realistic force transmission rates in the assembly and to prevent numerical instability (Ning and Ghadiri, 2006). The Rayleigh time-step is given by:

$$T_R = \frac{\pi R \left(\frac{\rho}{G} \right)^{1/2}}{0.16361\nu + 0.8766} \quad 3-46$$

where R is the particle radius, ρ is the density, G is the shear modulus and ν is Poisson's ratio for the particle. In practice, some fraction of this maximum value is used for the integration time-step. For dense systems (coordination numbers ≥ 4) a typical time-step of $0.2T_R$ has been shown to be appropriate and for less dense systems $0.4T_R$ is more suitable. In this work a time-step of $0.2T_R$ was selected. Since the time-step varies with different particle materials, for an assembly consisting of particles of different material types, the critical time-step should in general be the smallest among those determined for the different material properties.

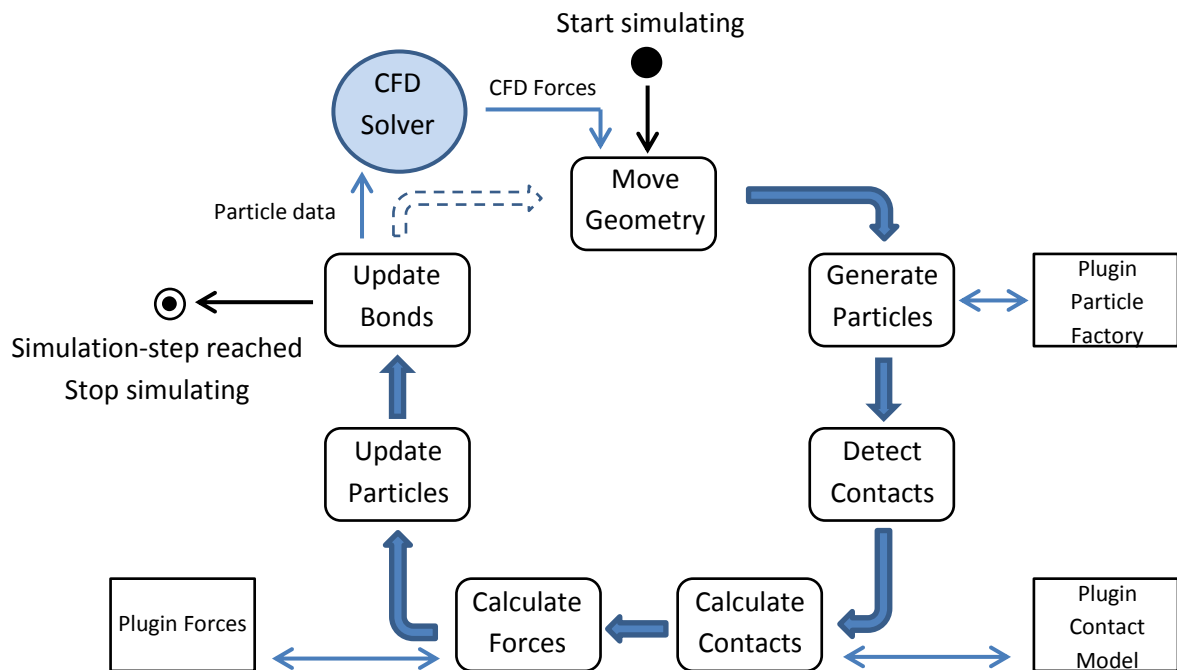


Figure 3.4. The LES-DEM-LPT solution cycle (based on DEM-Solutions, 2013).

During a coupled LES-DEM-LPT calculation (Figure 3.5), the LES solver and the DEM-LPT simulate in an alternating manner, with the LES solver first creating a fluid flow field into which particles are introduced. The LES solver simulates ahead in time and resolves the flow field of the continuous phase. When a stable solution is obtained, the flow field is passed to the coupling module, where the relative velocity between each particle and the surrounding fluid is calculated in order to obtain the drag force. The drag and lift forces acting on each particle are then passed to the DEM solver which updates the particle positions in a loop, until the end of the LES time-step is reached. The new particle positions are then handed back to the coupling module, which then updates the fluid cell porosities and calculates the momentum sink term for each cell. Based on this input, the LES solver iterates over the next time-step until the flow field again converges to a stable solution (Di Renzo et al., 2011; Favier et al., 2009). This alternating pattern continues until the simulation time has reached the specified end time, as shown in Figure 3.4. Due to the explicit time integration methods implemented in DEM it is common that multiple time-steps are required to simulate the same time period as a single time-step of an LES simulation. Therefore, the time-steps used in the two solvers are potentially different; however the simulation-steps are the same.

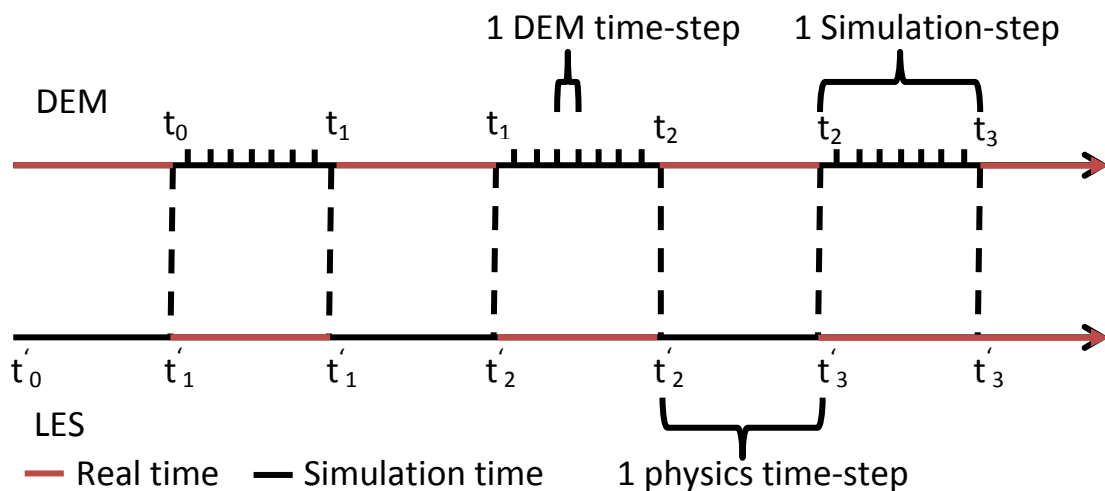


Figure 3.5. The alternating sequence of a coupled simulation (based on DEM-Solutions, 2013).

Each time the LES coupling interface sends a message to the DEM-LPT it blocks any further messages from being sent until the DEM-LPT returns a response. This synchronous behavior effectively pauses the LES solver until the DEM-LPT has calculated the required simulation

step. The sequence of a coupled simulation is shown in Figure 3.6, with the LES coupling interface relaying information on fluid forces and particle data between the two solvers. Once a coupling is successfully initialised between the DEM-LPT and the LES solver, the DEM-LPT is ready to start simulating (Steps 1-3). Simulation in the DEM-LPT commences when the LES solver sends fluid forces to apply to the particles in the simulation (Steps 5, 7, 9). If this is the first step of a simulation, and there are no particles to apply forces to, then this can be omitted before starting the LES-LPT simulation-step. After the DEM-LPT completes the simulation-step, it is possible to retrieve the new or updated particle information from the simulation. This information is then returned to the LES solver (Steps 6, 8, 10) in order to update the solver's variables and advance the simulation.

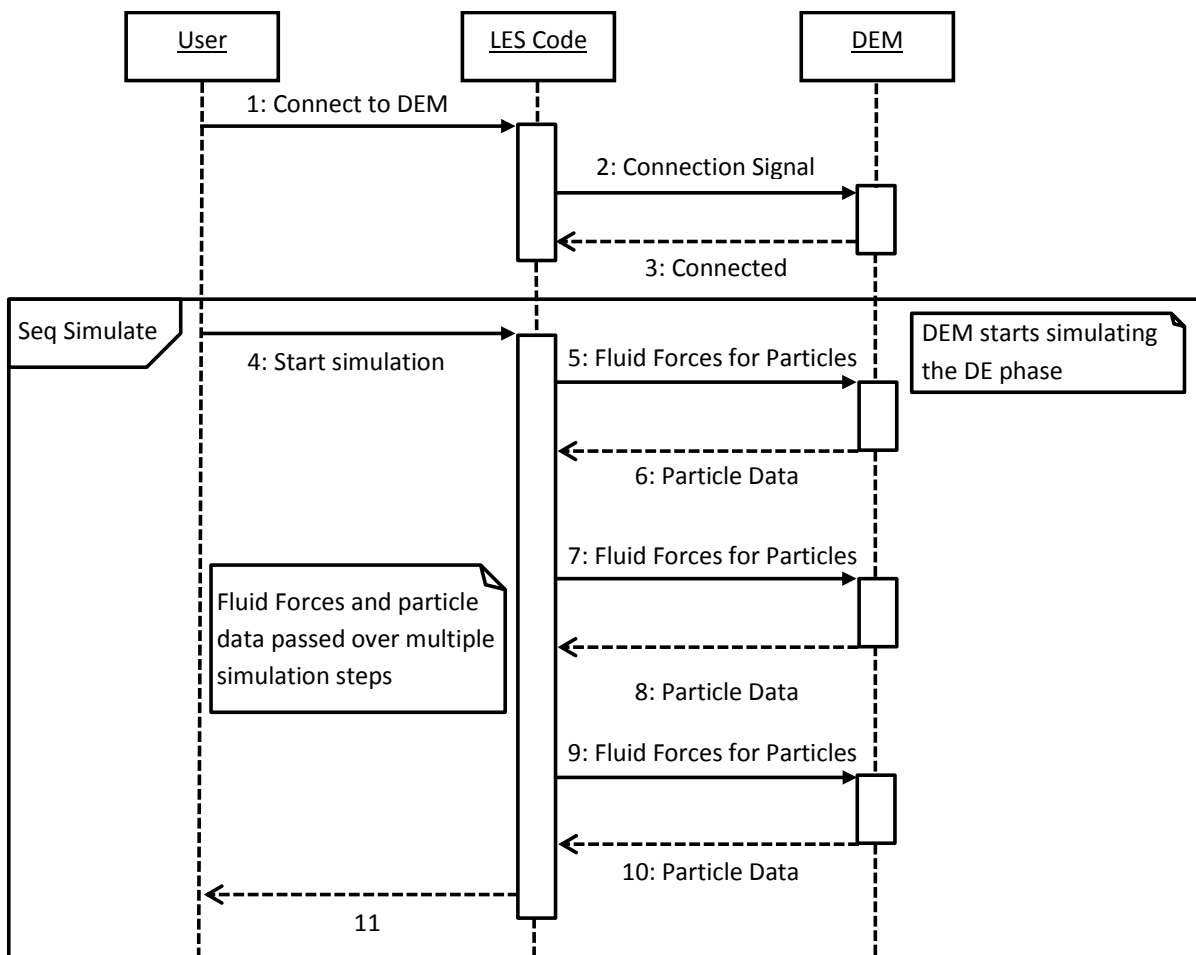


Figure 3.6. The coupled simulation sequence (based on DEM-Solutions, 2013).

4 Fluid-particle coupling and comparison

The treatment of discrete particles in the large turbulent scales of LES leads to questions in the assessment of the performance of the numerical methods used in the flow solver and on the accuracy of the interpolation scheme adopted to calculate the fluid velocity at the instantaneous particle location. All particles were individually tracked and their velocity calculated at the particle centre using interpolated fluid velocity values. In this framework, the appropriate parameters such as the grid resolution and the time-step size required for progression of the governing balance equations becomes critical.

Moreover, the level of fluid turbulence in wall bounded turbulent flow has an influence on particle-particle interactions and subsequent dispersion and deposition phenomena. Modelling this physical process is extremely important, particularly for techniques coarser than DNS. The difficulty is associated with the complicated interaction between non-homogenous turbulence structure in the wall-normal direction and the inertia of the particles. The small turbulent structures (i.e. eddies) are not solved by LES, eliminating the effect of small turbulent scales on tracked particles which may have an effect on their motion. It is therefore necessary to assess the mesh refinement and capability of the SGS model to predict accurately the selective response of different inertia particles. That being said, for the simulations presented, the particles considered were large with a relaxation time of greater order than the smallest fluid time scales, therefore the influence of the unresolved fluctuating velocities in the LES on particle motion was not important (Pozorski and Apte, 2009).

The aim is to predict the behaviour of particles in complex turbulent two-phase flow, with the potential to lead to physical insights on particle agglomeration and dispersion. This chapter starts out by assessing the capability of the LES approach within the FLUENT platform, in providing accurate predictions for single phase low Reynolds number, turbulent channel flow. It is important to mention here that commercial softwares for computational fluid dynamics, even though frequently exploited for high-Reynolds-number flows in complex geometries, have not yet been proven capable of predicting multiphase flows due to the lack of appropriate physical models for particle dispersion, re-suspension and deposition.

4.1 Flow Configuration and Initial Conditions

The flow into which particles were introduced was a turbulent channel flow of gas; Figure 4.1 gives a schematic diagram of the channel geometry and co-ordinate system. The flow is described by a three-dimensional Cartesian co-ordinate system (x , y and z) representing the streamwise, spanwise and wall-normal directions, respectively. The x , y , and z -directions correspond to the u_x , u_y , and u_z -velocity components, respectively. The boundary conditions for the momentum equations were set to no-slip at the channel walls and the instantaneous flow field was considered to be periodic along the streamwise and spanwise directions, with a constant mass flux through the channel in the streamwise direction maintained by a dynamically adjusted pressure gradient used to drive the flow. The rectangular channel considered was of dimensions $2h \times 2\pi h \times 4\pi h = 0.04\text{m} \times 0.13\text{m} \times 0.25\text{m}$. The length of the channel in the streamwise direction was sufficiently long to capture the streamwise-elongated, near-wall turbulent structures that exist in wall-bounded shear flows; such structures are usually shorter than ~ 1000 wall units (Robinson, 1991). Some variables reported in this work are in dimensionless form, represented by the superscript (+), and expressed in wall units, with the latter obtained by combining u_τ , ν and ρ .

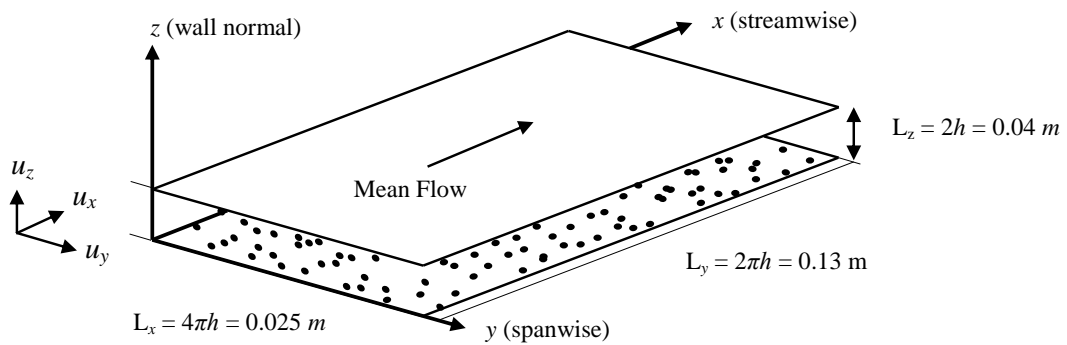


Figure 4.1 Schematic diagram of the channel geometry and coordinate system.

An example of the instantaneous streamwise velocity contours for both the fluid and particles predicted by the LES is given in Figure 4.2 (a). The velocity is seen to be at a maximum in the centre of the channel and decreases to a minimum towards the walls, due to the no-slip boundary conditions applied there. Figure 4.3 (a) shows a contour plot of the mean streamwise fluid velocity, whilst Figure 4.3 (b) gives a contour plot of the root-mean-square (rms) of the streamwise velocity fluctuation. In the latter, moving

away from the channel centre towards the walls, the values are seen to increase before reaching a minimum at the walls. Figure 4.4 provides a visual representation of the mesh used for the channel, a zoomed in section of the top corner shows how the non-uniform mesh becomes more refined towards the top wall.

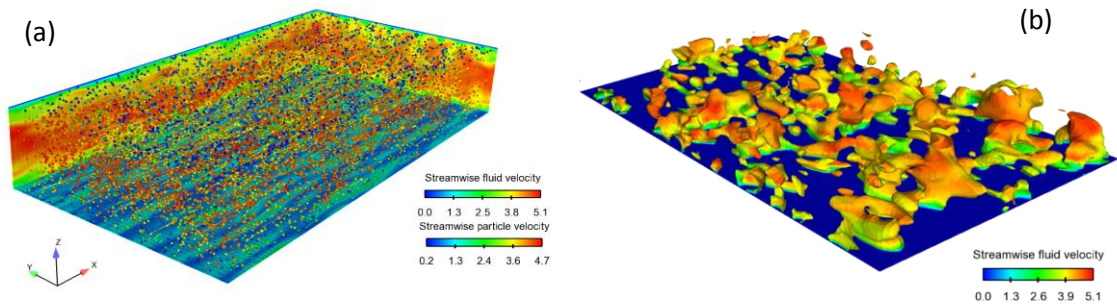


Figure 4.2 a) Contour plot of the instantaneous streamwise velocity, for the fluid u_x and particle v_x , in a rectangular channel flow, m/s. b) Iso-Contour plot of the instantaneous streamwise velocity, m/s

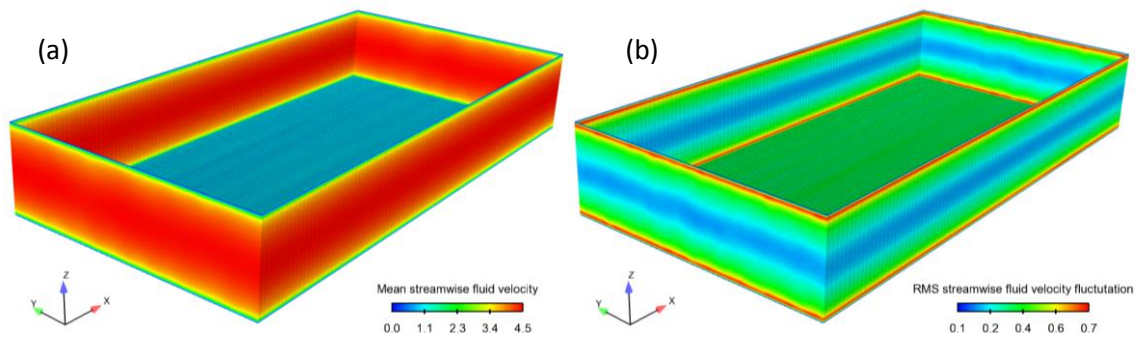


Figure 4.3 contour plots for the (a) mean streamwise velocity, U_x , m/s; (b) rms of streamwise velocity fluctuation, $u'_{x,rms}$, in a rectangular channel flow, m/s.

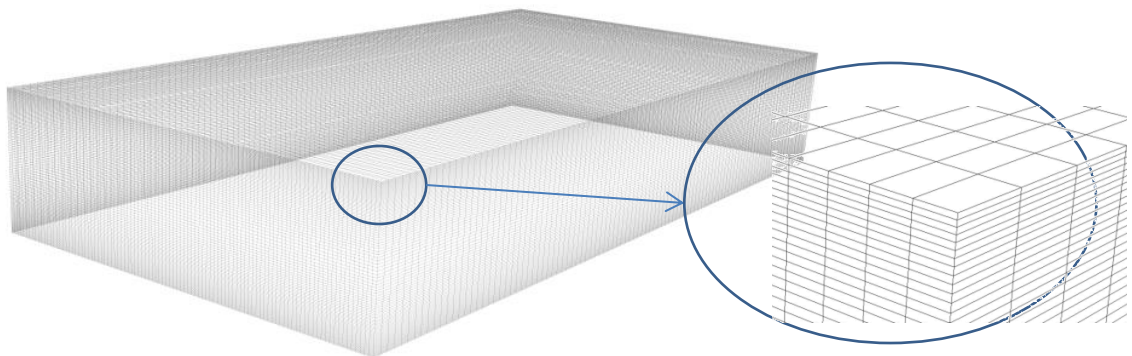


Figure 4.4 Mesh of channel and channel corner, left and right, respectively

4.2 Single-Phase Flow

Wall-bounded turbulent flows comprise of several regions, each with distinct flow characteristics, although frequently the flow is divided into an inner and outer layer. The inner layer encompasses the near-wall region, wherein the flow is considered to be unaffected by the geometry of the system. This means that flow quantities in the inner layer are alike in spite of the type of flow geometry (e.g. channel, duct or pipe). The outer layer, conversely, is dependent on the flow geometry. To make a quantitative comparison between the LES and DNS results, the flow solutions provided by both were scaled. For a smooth wall, suitable scaling parameters for the inner layer include the viscosity ν , and the friction velocity u_τ . Inner layer scaling then demands that the relationship given below holds for the mean streamwise fluid velocity, U_x :

$$U_x^+ = f(z^+) = U_x / u_\tau \quad 4-1$$

where U_x^+ is the non-dimensional mean streamwise fluid velocity, f is a universal function (independent of Reynolds number) and z^+ is the dimensionless distance from the wall. The mean velocity profile in a turbulent channel flow at high Reynolds number in the inner and outer layers may be represented using the expressions given by Von Karman (1930):

$$U_x^+ = z^+, \quad \text{if } 0 < z^+ < 5 \quad 4-2$$

$$U_x^+ = A \ln z^+ + B, \quad \text{if } z^+ > 30 \quad 4-3$$

The region near the wall can be divided into two sections, the viscous sublayer between $0 < z^+ < 5$ and the buffer layer between $5 < z^+ < 30$ where neither law holds; from $z^+ > 30$ the region goes on to the log-law region and the outer layer, where z^+ is the dimensionless distance to the wall. The above equations represent the analytical mean velocity profile given by the law of the wall, equation 4-2, and by the log-law, equation 4-3. The value of the constants A and B is an area of dispute due to the large amount of

scatter in values derived from experimental measurements. For fully developed flow at high Reynolds numbers, the average of all experimental data suggests that $A = 2.5$ and $B = 5$, whereas for low Reynolds number flow, the constant B acquires a value of 5.5 (Kim et al., 1987).

The choice of dynamic sub-grid scale model was based on sensitivity studies carried out using different sub-grid scale models and also sensitivity studies in the literature for the same code, for example (Abdilghanie et al., 2009). Sensitivity studies were also carried out using different SGS models, grid distributions, numbers of computational nodes, numerical method discretisation schemes and time step size (see Appendix). It is important to mention that the minimum grid size is limited by particle size. In tandem to that for the final grid arrangements, selected turbulence statistics were not found to be independent of grid resolution due this restriction, and possibly an increased expense in computational power and run times even without this restriction. There are two reasons to the minimum cell size criteria, the drag forces on the particle are calculated based on the fluid velocity found in the cell containing the particle centroid and the maximum volume fraction of the DEM phase in any cell is limited to 0.95 for numerical stability reasons. Therefore, if this criterion is not met, the LES solver has difficulty converging on a solution or convergence for each time-step will take a very large number of iterations (i.e., numerical instability). As a consequence, the simulations do not provide detailed flow information near the wall boundary. Based on the nonuniform Cartesian grid employed, $81 \times 80 \times 80$, the minimum grid resolution was $\Delta z^+ = 3.00$ and $\Delta y^+ = 23.6$ wall units in the wall-normal and spanwise directions, respectively, and $\Delta x^+ = 47.1$ in the streamwise direction. A second simulation using an increased total number of non-uniformly distributed nodes, $100 \times 100 \times 100$, was also used to give better resolution near the floor of the channel. This used a minimum grid resolution of $\Delta z_{\min}^+ = 2.40$ and $\Delta y^+ = 18.8$ wall units in the wall-normal and spanwise directions, respectively, and $\Delta x^+ = 37.7$ in the streamwise direction. To save computational effort, the coarse grid was employed for general analysis, with the more refined simulation used to give detailed flow information near the wall boundary. The dimensional integration time-step used for the fluid and particles was $\Delta t = 1.0 \times 10^{-5}$ and 5.2×10^{-7} s, respectively.

The fluid flow is air and is assumed to be incompressible and Newtonian with fluid density and kinematic viscosity set to $\rho_f = 1.3 \text{ kg m}^{-3}$ and $\nu = 15.7 \times 10^{-6} \text{ m}^2 \text{ s}^{-1}$,

respectively. The shear Reynolds numbers Re_τ used in the simulations were 150, 300 and 590 corresponding to bulk Reynolds numbers of $Re_b \sim 2100, 4200$ and 8260 , respectively, based on the channel half height, h . The shear velocity $u_\tau = 0.118, 0.235$ and 0.463 m/s for the 150, 300 and 590 shear Reynolds number flows, respectively.

In this sub-section some of the most relevant statistics for the fluid phase are presented and discussed to benchmark the performance of the LES approach. It is important to mention here that all fluid velocity statistics presented in this thesis refer to a fully developed flow. This point is achieved, when the first- and second-order moments (specifically, the mean streamwise velocity, rms values for all three directions and the Reynolds stresses) remain constant with time. To achieve smooth profiles the fluid statistics have been both spatial- and time-averaged over 100's of thousands of time steps. It is always beneficial to compare numerical work against experimental data, however, in its absence the work has been compared to DNS. The results generated by the LES for the fluid phase were compared using DNS predictions for shear Reynolds flows of $Re_\tau = 150, 300, \text{ and } 590$ (Marchioli et al., 2008, Marchioli and Soldati, 2007, and Moser et al., 1999, respectively).

4.2.1 Shear Reynolds number 150

Figure 4.5(a) shows the mean fluid velocity profile in the streamwise direction, U_x^+ , for $Re_\tau = 150$ plotted in semi-logarithmic form as predicted by LES, together with DNS results and the analytical profiles. Altogether five DNS data sets have been used (these include Marchioli et al., 2008 (UUD hereinafter), Kuerten, 2006 (TUE hereinafter), Arcen et al., 2006 (HPU hereinafter), Goldensoph, 2006 (ASU hereinafter), Cargnelutti and Portela, 2007 (TUD hereinafter)). The LES results show the anticipated symmetric behaviour for a fully developed flow and follow the general trend of the DNS, providing reasonable agreement overall. The LES clearly predicts the viscous sub-layer to a high degree of accuracy and quantitatively tends towards equation 4-2 as this region is approached. Good agreement with DNS results in this region is therefore indicative of the accuracy of the SGS model. It is seen that the LES slightly over predicts the DNS in this region, although the log scale used emphasises any discrepancies close to the wall and therefore highlights any differences. The logarithmic law given by equation 4-3 is shown for the region $z^+ > 30$, based on the values suggested by (Kim et al., 1987), with

the LES results seen to over predict this analytical profile and the DNS results, although the various approaches come in line at the centre of the channel. In this region of the channel, the flow characteristics are dominated by large energetic scales of motion and, given that these scales are directly computed by the LES, the predicted profile should match the DNS, with the differences observed due to the lack of resolution in the LES. Overall, however, the streamwise mean velocity generated by the LES is in acceptable agreement with the DNS.

Figure 4.6(a-c) give the rms of the non-dimensional fluid velocity fluctuation ($U'_{i,rms}^+$) for $Re_\tau = 150$ in the streamwise ($i = x$), spanwise ($i = y$) and wall-normal ($i = z$) directions. Results are in good agreement with the DNS for the $U'_{x,rms}^+$ component, with the positions of the peak and minimum values of this profile at the channel centre predicted well. The $U'_{y,rms}^+$ and $U'_{z,rms}^+$ profiles follow the trend of the DNS, although qualitative and quantitative differences are observed in some regions. For the $U'_{y,rms}^+$, an over prediction by the LES increases throughout the buffer layer where it reaches a maximum before decreasing towards the log region. For $U'_{z,rms}^+$, this difference increases throughout the log region where it reaches a maximum, before decreasing towards the outer layer. Agreement between the LES and DNS in the channel centre and close to the walls is good for all the profiles given in Figure 4.6.

Lastly, Figure 4.5(b) shows the time-averaged $U'_x U'_z$ component of the Reynolds stress tensor for $Re_\tau = 150$. Again, the LES profile follows that of the DNS and predicts the location of the minimum in the profile with good accuracy. Quantitatively, the buffer layer and log-law region DNS results are slightly over predicted, with this discrepancy being largest at the peak in the profile. Overall, agreement between the LES and DNS results of Marchioli et al. (2008) is satisfactory.

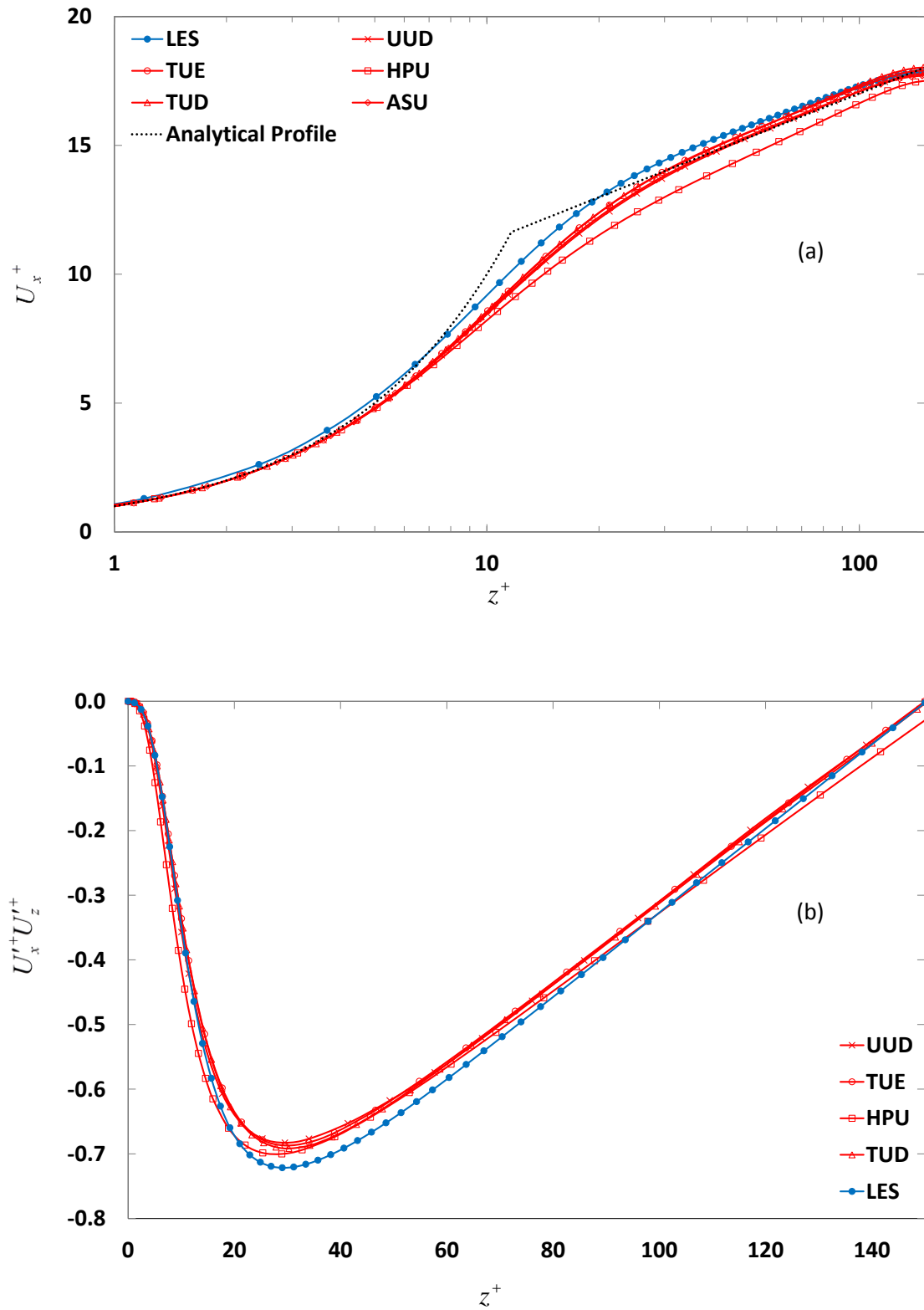


Figure 4.5 (a) Mean streamwise fluid velocity; (b) Fluid Reynolds stress component.

Closed blue symbols: LES; open red symbols: DNS ($Re_\tau = 150$).

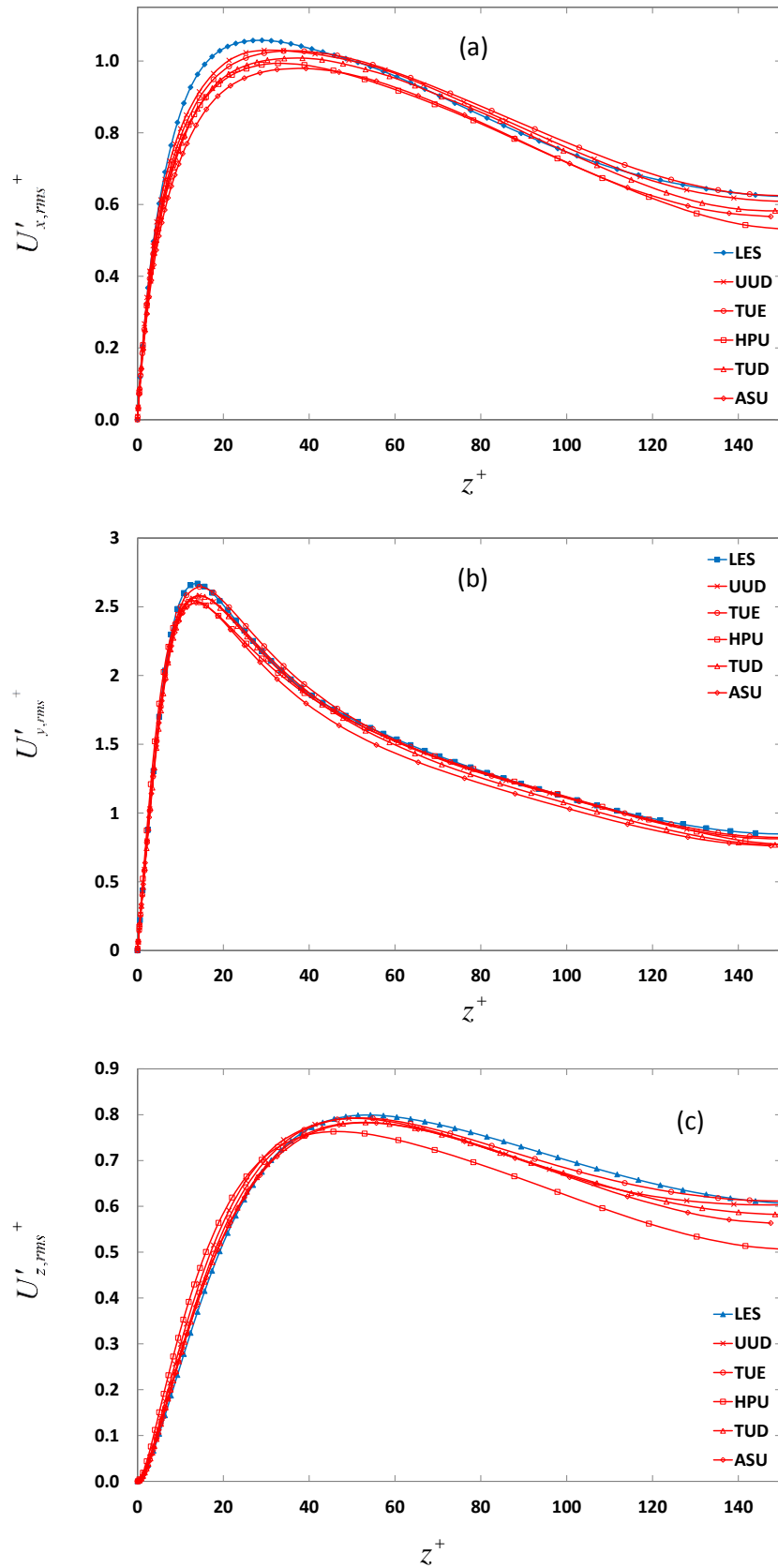


Figure 4.6 Root mean square of fluid velocity fluctuation (a) streamwise rms component; (b) spanwise rms component; (c) wall-normal rms component. Closed blue symbols: LES; open red symbols: DNS ($Re_\tau = 150$).

4.2.2 Shear Reynolds number 300

Figure 4.7(a) shows U_x^+ for $Re_\tau = 300$, plotted in semi-logarithmic form for LES, DNS results and the analytical profiles. The LES results match the general trend of the DNS, providing reasonable agreement overall. The LES provides accurate predictions in the viscous sublayer and quantitatively tends towards equation 4-2 as this region is approached. The LES slightly over predicts the DNS in the buffer region. The logarithmic law is given by equation 4-3, the LES results over predict this analytical profile and the DNS results, although the various approaches come in line at the channel centre. Overall, however, the streamwise mean velocity generated by the LES is in acceptable agreement with the DNS.

Figure 4.7(b) gives $U'_{i,rms}^+$ for $Re_\tau = 300$ in the streamwise, spanwise and wall-normal directions. Results are in good agreement with the DNS for the $U'_{x,rms}^+$ component, with the positions of the peak and minimum values of this profile at the channel centre predicted reasonably well. Further scrutiny of the results, however, shows an over prediction in the region $10 < z^+ < 106$, with the discrepancy being greater in regions of higher turbulence. It is well established that in relation to DNS results, LES streamwise velocity fluctuations are over predicted to some degree, some models minimize this discrepancy by employing eddy-viscosity models that incorporate proper near-wall damping. This under prediction is found in combination with different numerical methods, such as high order finite volume method and also spectral discretization approaches (Kuerten and Vreman, 2005). The $U'_{y,rms}^+$ and $U'_{z,rms}^+$ profiles also follow the trend of the DNS, although qualitative and quantitative differences are observed in some regions. For $U'_{y,rms}^+$, an under prediction by the LES increases from the buffer layer into the log region where it reaches a maximum before decreasing towards the channel centre. For $U'_{z,rms}^+$, this difference increases from the wall and throughout the viscous sub-layer region into the buffer layer where it reaches a maximum, before decreasing towards the outer layer. These under predictions may be minimised by increasing the number of computation cells (i.e. resolution), although based on the criteria defined by Piomelli and Balaras (2002), the mesh is fine enough to generate ‘well-resolved’ LES predictions of channel flow. A coarse mesh can bring about a non-linear accumulation of simulation errors caused by the interaction between discretization and subgrid modelling errors (Geurts and Fröhlich, 2002, Meyers et al.,

2003, Meyers et al., 2005). These effects are sufficiently small and do not interfere with the purpose of this work. Agreement between the LES and DNS in the channel centre is good for all the profiles given in the figure, and close to the wall for $U'_{x,rms}^+$ and $U'_{y,rms}^+$.

Lastly, Figure 4.7(c) shows $U'_x U'_z$ for $Re_\tau = 300$, again, the LES profile follows that of the DNS and predicts the location of the minimum in the profile with good accuracy. Quantitatively, the buffer layer and log-law region DNS results are slightly under predicted, with this discrepancy being largest at the peak in the profile. Overall, agreement between the LES and DNS results of Marchioli and Soldati (2007) is satisfactory.

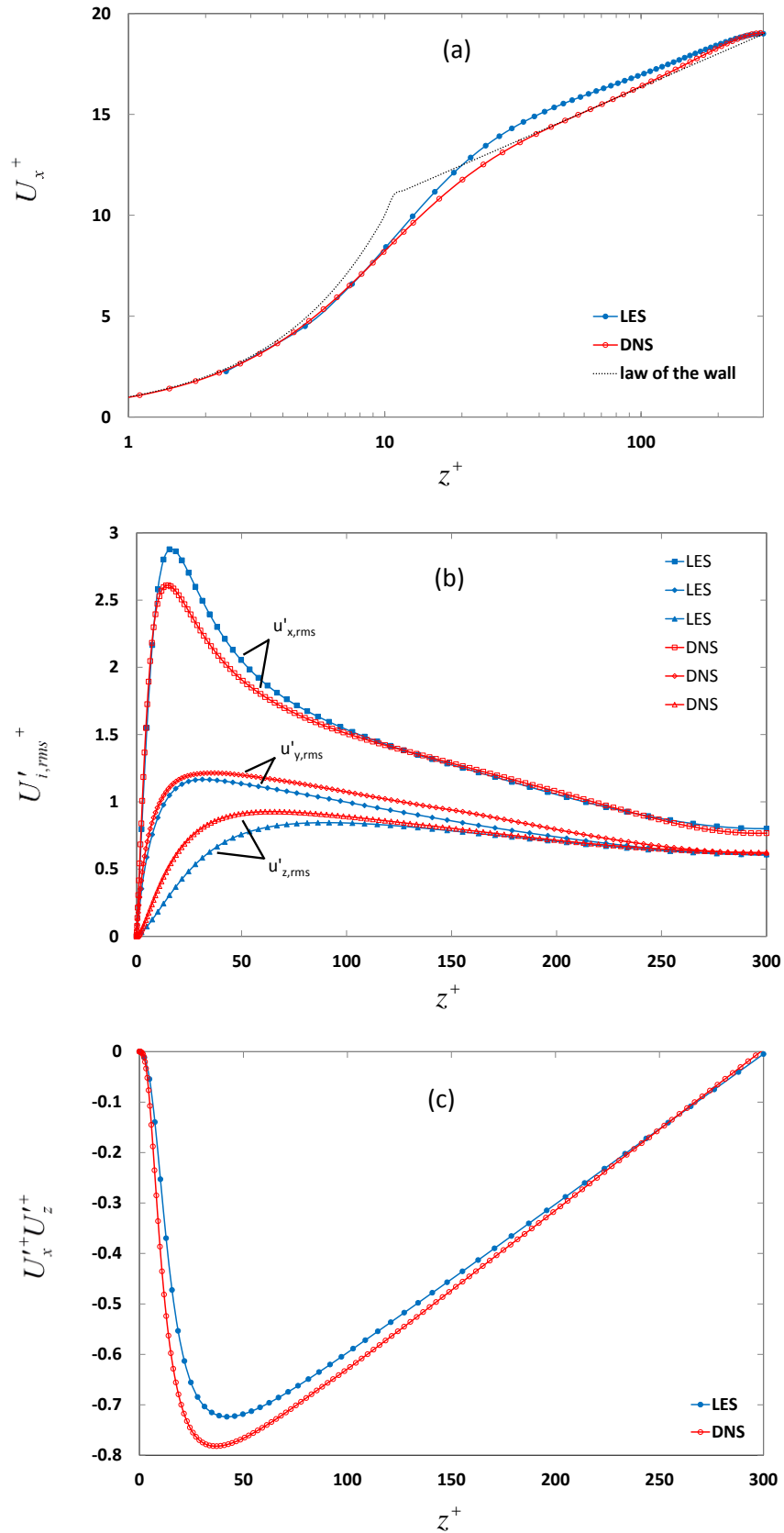


Figure 4.7 (a) Mean streamwise fluid velocity; (b) Root mean square of fluid velocity fluctuation; (c) Fluid Reynolds stress component. Closed blue symbols: LES; open red symbols: DNS ($Re_\tau = 300$).

4.2.3 Shear Reynolds number 590

Figure 4.8(a) shows U_x^+ for $Re_\tau = 590$, plotted in semi-logarithmic form for LES, DNS results and the analytical profiles. The LES results show similarity in terms of general trend (qualitative) of DNS, providing moderate agreement overall. Although in terms of magnitude (quantitative), the LES under predicts the viscous sublayer and only qualitatively tends towards equation 4-2 as this region is approached. The LES over predicts the DNS in the buffer region. The logarithmic law is given by equation 4-3, the LES results over predict this analytical profile and the DNS results, although the various approaches come in line at the channel centre. Overall, however, the streamwise mean velocity generated by the LES is in satisfactory agreement with the DNS. Figure 4.8 (b) gives $U'_{i,rms}^+$ for $Re_\tau = 590$ in the streamwise, spanwise and wall-normal directions. Results are in reasonable agreement with the DNS for the $U'_{x,rms}^+$ component, with the positions of the peak and minimum values of this profile at the channel centre predicted reasonably well. Further scrutiny of the results, however, shows an over prediction in the region $12 < z^+ < 143$ and an under prediction between $143 < z^+ < 540$. The $U'_{y,rms}^+$ and $U'_{z,rms}^+$ profiles also follow the trend of the DNS, although yet again qualitative and quantitative differences are observed in some regions. For both the $U'_{y,rms}^+$ and $U'_{z,rms}^+$, an under prediction by the LES increases from the wall and throughout the viscous sub-layer region into the buffer layer where it reaches a maximum, before decreasing towards the channel centre. Agreement between the LES and DNS in the channel centre is good for all the profiles given in the figure, and close to the wall for $U'_{x,rms}^+$.

Lastly, Figure 4.8 (c) shows $U_x^+ U_z^+$ for $Re_\tau = 590$, once more, the LES profile follows that of the DNS and predicts the location of the minimum in the profile with good accuracy. Quantitatively, the entire profile is under predicted, bar the channel walls and centre-line, with this discrepancy being largest at the peak in the profile. Overall, agreement between the LES and DNS results of Moser et al. (1999) is acceptable.

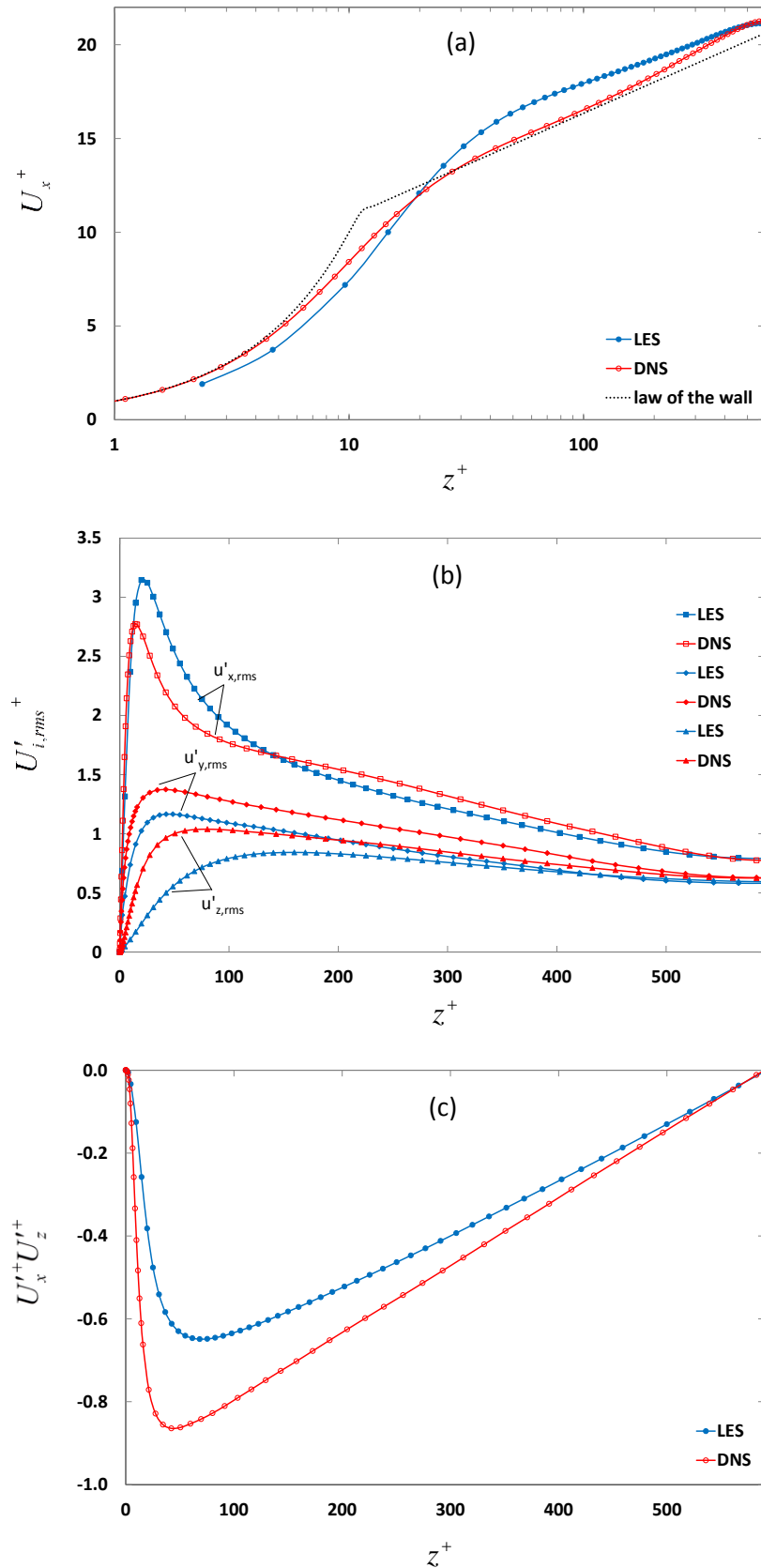


Figure 4.8 (a) Mean streamwise fluid velocity; (b) Root mean square of fluid velocity fluctuation; (c) Fluid Reynolds stress component. Closed blue symbols: LES; open red symbols: DNS ($Re_\tau = 590$).

4.2.4 Conclusion on single phase

To conclude the results dedicated to fluid statistics, a commercial LES code has been employed to investigate the turbulent flow field in a straight channel of rectangular cross section for $Re_\tau = 150$, $Re_\tau = 300$, and $Re_\tau = 590$. The results have been compared, with the computational data of Marchioli et al. (2008), Marchioli and Soldati (2007) and Moser et al. (1999), respectively. The agreement between the LES and DNS profiles is indeed satisfactory, in particular for the lower Reynolds number flows. This study confirms that the proposed simulation approach faithfully captures the turbulent velocity field within the channel flow. Differences observed in the first and second-order moments of the fluctuating fluid velocity field are, of course, due solely to the numerical method employed by the LES flow solver for large scales and SGS model used for small scales, and to the accuracy of grid discretization. Extension of the simulations to include particles should therefore produce reliable predictions for the particle-laden flows of interest.

4.3 Two-Phase Flow

In this section the fluid and particle velocity statistics are investigated in two different fully coupled particle-laden flows through a channel. These include: flow 1 – two-way coupled with ‘non-adhesive’ particle-particle interactions and flow 2 – two-way coupled with ‘adhesive’ particle-particle interactions. In sub-Section 4.3.1, turbulence modulation of the gas phase due to the presence of particles is quantified, by comparing the fluid velocity statistics of flow 1 with that of clean fluid flow. Furthermore, turbulence modulation of the gas phase by particle-particle adhesion (i.e. agglomeration) is quantified by comparing flows 1 and 2. In sub-Section 4.3.2, turbulence modulation of the particle phase by particle-particle adhesion is quantified by comparing the particle velocity statistics of flows 1 and flow 2.

The initial particle positions were distributed randomly throughout the channel, corresponding to an initially uniform wall-normal particle number density profile, with their initial velocity set equal to local flow velocities. The process of particle dispersion will not be sensitive to this initial condition if the long-term features of the motion are investigated. Particles were assumed to interact with turbulent eddies over a certain

period of time, that being the lesser of the eddy lifetime and the transition time. Particles that moved out of the rectangular channel in the streamwise and spanwise directions were re-introduced back into the computational domain using periodic boundary conditions. All of the particles used in this chapter have identical physical properties that approximately correspond to certain types of plastic such as polystyrene (Table 4-1). The surface energy, size and total number of particles considered, with the corresponding particle relaxation times, Stokes number, and other relevant parameters, are given in Table 4-2.

Table 4-1 Particle physical properties

Particle properties	
Particle density (kg/m ³)	1000
Shear modulus (MPa)	10
Poisson's ratio	0.25
Friction coefficient (static and rolling)	0.5 and 0.01
Restitution coefficient	0.5

Table 4-2 Particle parameters used in the simulations

<i>St</i>	Surface Energy / J m ⁻²	τ_p ($\cdot 10^{-3}$)	d_p / μm	Particle Number	Volume Fraction ($\cdot 10^{-6}$)	Re_τ
216	0; 0.05	61.2	150	20,000	28	300

It is important to mention here that all fluid and particle velocity statistics presented in this thesis refer to a fully developed flow and steady state for particle distribution, respectively. To ensure the reproducibility of results, it is required to define precisely the computational procedure used in computing particle statistics. In this work, particle velocity statistics were calculated by averaging over wall-parallel fluid slabs distributed non-uniformly along the wall-normal direction. Large particle concentration gradients are common close to the walls; therefore, the slabs were specified smaller than the wall-normal grid spacing of the numerical simulation, the minimum thickness allowed at the wall was limited by the particle radius. A density-weighted approach was used to sample particle statistics; in which the value of the selected variable (velocity, velocity fluctuation, for instance) was summed for all particles in a sampling volume, created by wall-parallel fluid slabs as described later, and averaging by the particle number in that sampling volume. Furthermore, to achieve smooth profiles the particle statistics have been time-averaged over 100's of thousands of time steps. For conciseness, the analysis is limited to the first- and second-order moments of both phases (specifically the mean streamwise velocity and the rms values for all three directions), to the Reynolds stresses

and to the particle concentration profiles. In the case of the particle concentration profiles and deposition rates however, particle statistics were calculated by averaging over uniformly distributed wall-parallel fluid slabs. A particle is considered to be in the slab where its particle centre is located.

4.3.1 Effects of particles and agglomeration on fluid velocity statistics

Sampling of the particle statistics can only commence after a statistically-steady state for the particle distribution is reached. For that reason the process of particle segregation was monitored over time. Figure 4.9 (a) shows the time evolution of the maximum value of particle number density n_p^{max} near the wall. The reason for observing this quantity is down to the concentration near the wall taking longest to reach a steady state. The binning procedure used for obtaining n_p^{max} is as follows. Initially the channel cross section is divided into 1568 uniform slabs equal to the particle radius, next the number of particles within each slab is divided by the volume of that slab at each time step to get the local concentration $n_p = n_p(s)$; next, the maximum value of n_p amongst all slabs is selected n_p^{max} , lastly, this value is normalised by the total number of particles and channel volume n_p^{total} . The particle number density distribution will be > 1 in cross sectional regions of the channel where particles tend to accumulate and ≈ 1 in regions where particles are uniformly dispersed. It is seen that initially, the particles accumulate at the walls at a high rate up to approximately $t^+ \approx 400$ ($t = 0.11$ s), followed by a gradual asymptotic convergence towards a mean value (represented by the horizontal dashed lines) reached at $t^+ \approx 1240$ (0.35 s). The time required for the fluid to reach fully developed flow corresponds to a developing-length of approximately 80 channel heights, based on the channel bulk velocity $U_x^+ \approx 16$. Moreover, run times for particles to reach a steady state can be significantly longer than the fluid. The long run times show the difficulty in collecting information on fully developed fluid-particle two-phase flows.

Particle concentration increases in the near wall region due to particles being transported by the effect of the wall-normal fluctuation velocity to regions where its value is low. The particle slip velocity and gradient of the fluid velocity are high close to the walls, and therefore particles are entrained due to the effects of the force from the velocity gradient. The driving mechanisms in close proximity to the wall, accountable

for an increase in particle concentration in the near-wall accumulation region can be summarised as follows, initially, the segregation of particles leads to the formation of coherent clusters in areas of the buffer layer where in-sweeps can entrain them. Once entrained in a sweep, the particles undergo a net drift directed toward the near-wall accumulation region, where particle numbers reach a maximum. In the physical situation under analysis, the main mechanism capable of causing such drift is turbophoresis (Narayanan et al., 2003; Marchioli et al., 2003). When particles are in the accumulation region, which is located deep in the viscous sublayer, they either deposit at the wall or are re-entrained into the main flow via ejections. Particle deposition takes place via two mechanisms (Portela et al., 2002; Narayanan et al., 2003): particles of high momentum can pass through the accumulation region and deposit by impaction directly at the wall; otherwise, particles of large residence time, can deposit under the influence of turbulent fluctuations at the wall, where the fluctuations value is zero, and are more effective in pushing particles to the wall because of turbulence non-homogeneity. The effectiveness of these two mechanisms is subject to particle inertia.

The particle velocity at the wall has also been monitored with time as shown in Figure 4.9 (b); the point in time at which steady state is reached for velocity corresponds with that of the position. However due to adhesive particles being used in the simulations, a steady state is also required for particle agglomeration. Figure 4.9 (c) shows the number of contacts between particles B with time t^+ . Contacts are the impacts occurring between particles at data write-out points, i.e., the contacts are in progress when the write-out takes place. The contact has an associated force and position that are discrete values. If two particles stay in contact with each other for some time e.g. over four write-out points, four contacts will be stored and each of these may have a different force and position. The results show that B nears to reaching an asymptote at $t^+ \approx 5300$ (1.5 s). For that reason time averaging of the particle statistics was commenced from this point onwards. The value of B at the end of the simulation is 1946.

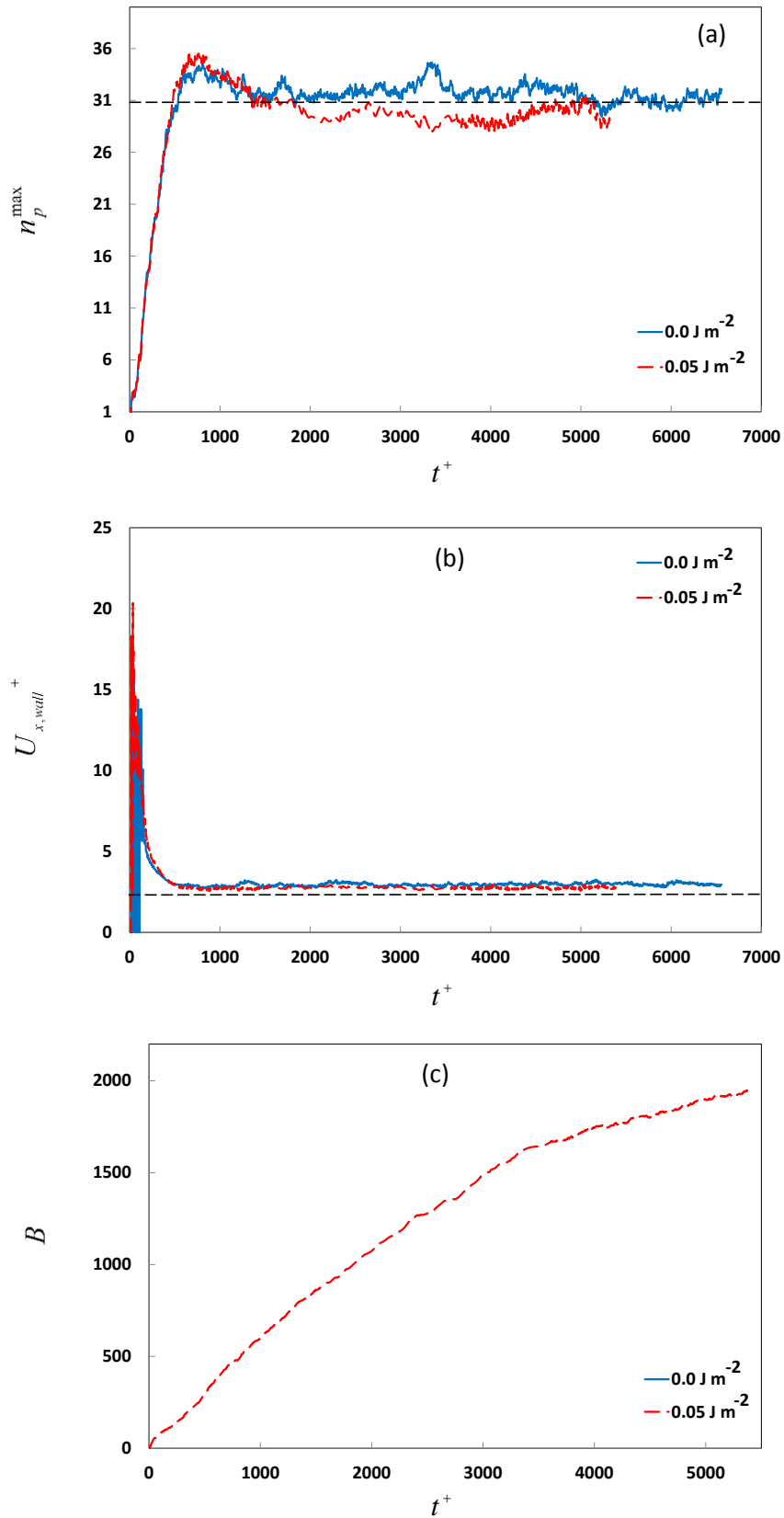


Figure 4.9 (a) Maximum value of particle number density at the wall, n_{pmax} ; (b) Mean streamwise fluid velocity at the wall, $U_{x,wall}^+$, Number of contacts, B , formed between particles as a function of time t^+

In this work, the effects of particles on SGS stress is not considered, therefore, the results provide information about turbulence modulation only at large scales. The results focus on interaction between large scale eddies and particles. Figure 4.10 (a) shows the U_x^+ for single-phase and fully coupled two-phase flows with 0.0 and 0.05 J/m^2 particles. It seems as though the fluid mean velocity has not been affected by the presence of particles for low mass loading $\phi_{p,m} = 0.022$. Comparing against the single flow, it is observed that the particles have no noticeable effect on the mean flow. Figure 4.11 (b) gives the logarithmic profile, where no effects on the fluid phase are also observed. Although not shown here, the results were symmetrical about the channel centerline. In particle-fluid flow, large-scale coherent structures are known to develop; therefore, longer time averaging is required to remove statistical error. Symmetry between the time-averaged results in the two channel halves is the first independent indication of statistical convergence. The long run times required to reach statistical convergence is due to the particle relaxation time τ_p .

Figure 4.11 (a) shows $U'_{i,rms}^+$, overall, the turbulence modulation by these particles slightly diminishes the magnitude of the streamwise, spanwise and wall-normal rms components. The difference between the single phase and two-phase flows is seen in the buffer layer, where it increases exponentially towards the peaks. These results generally correspond to the observations of existing experimental work. Although, it is difficult to directly compare these results with experimental data, unless all parameters have been set equal to the experimental set up, such as inlet conditions, volume fraction, and particle physical and chemical properties. The results from the simulation agree with the experimental work of Kulick et al. (1994) for channel flow, where smaller particles diminished all components of the rms. It is noted, however, the particles in the experiment were of smaller size (50 – 90 μm) and at higher volume fractions. The work also corresponds with LES of Yamamoto et al. (2001), who for similar volume fractions (10^{-4}) also observed damping of the fluid and particle statistics due to the effects of inter-particle collisions. The experimental work of Tsuji et al. (1984) involved larger particles (200 – 3000 μm) at higher volume fractions in pipe flow, the 200 μm particles were also found to reduce the rms values in the pipe cross section. For larger particles, however, all components of the rms were enhanced throughout the pipe. It is worth mentioning that rms's are somewhat more sensitive to the subgrid scale model in two-

phase flow compared to single-phase flow. This may be related to a lower magnitude of the fluctuations.

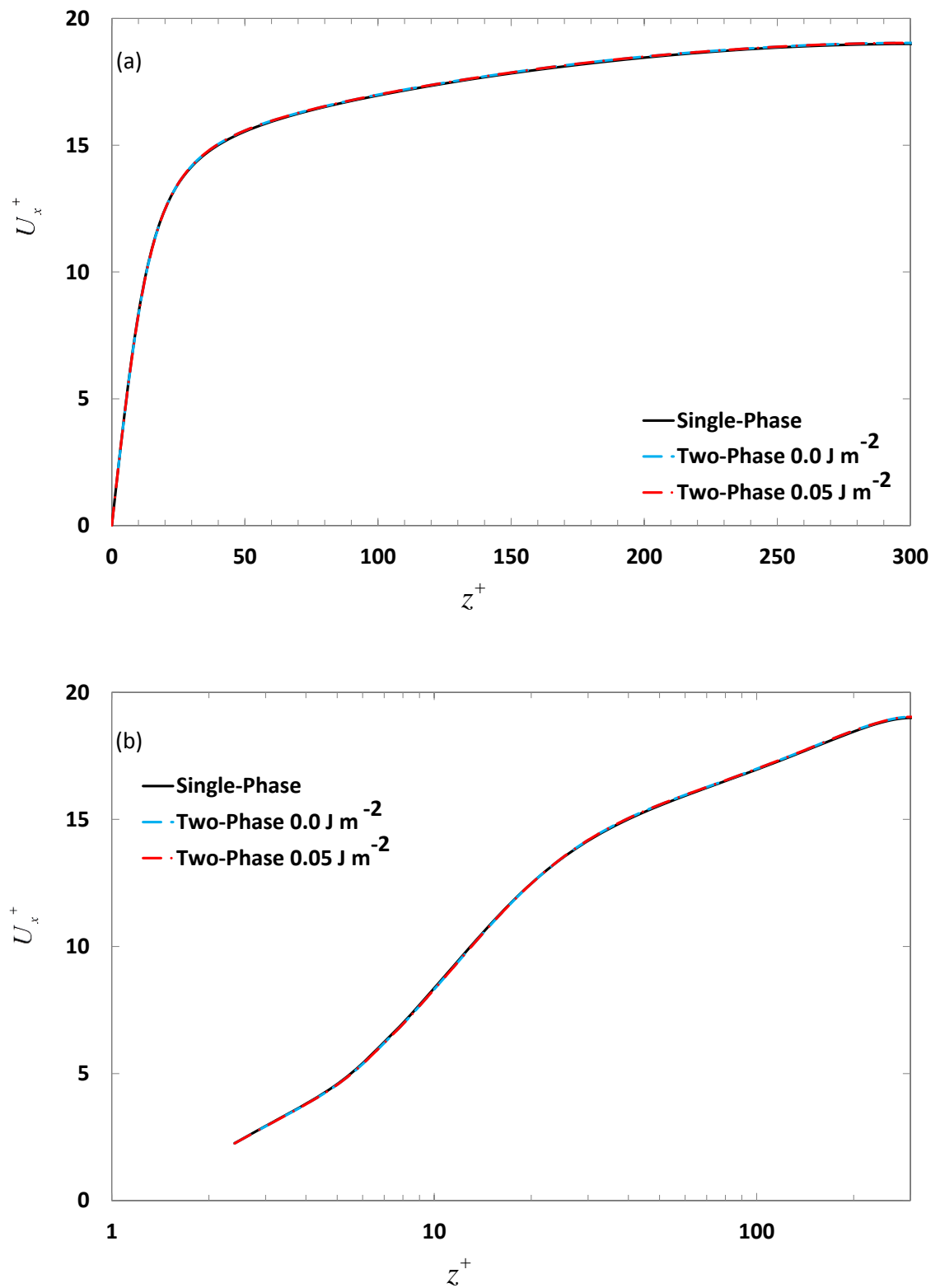


Figure 4.10 Non-dimensional mean streamwise fluid velocity, U_x^+ : (a) linear and (b) logarithmic ($Re_\tau = 300$).

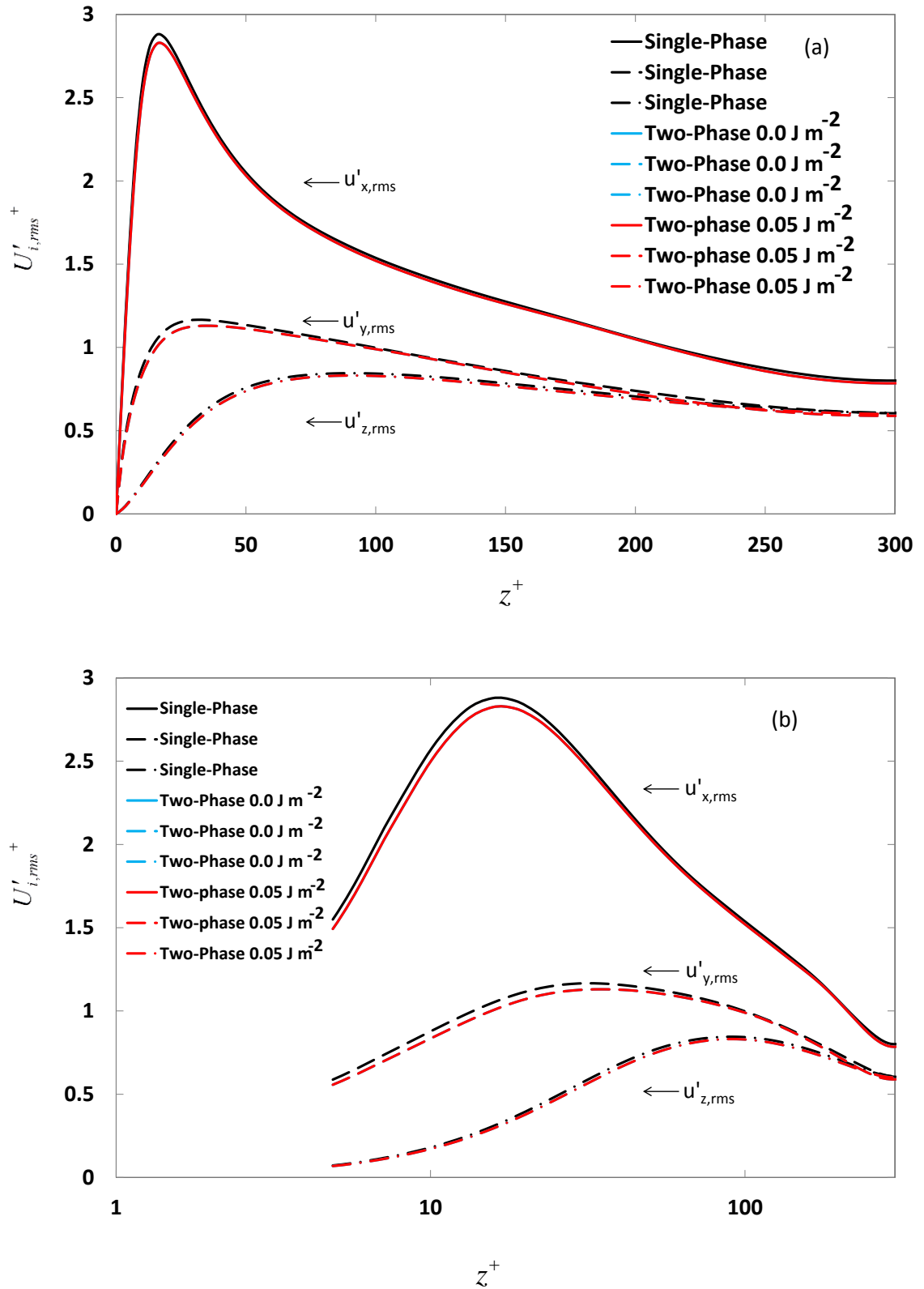


Figure 4.11 Root mean square of fluid velocity fluctuation, $U'_{i,rms}^+$; (a) linear and (b) logarithmic ($Re_\tau = 300$).

Ideally, the grid resolution for LES should be sufficient to resolve the bulk of the turbulent kinetic energy. If this is achieved, LES is most weakly dependent on the selected subgrid-scale model. In FLUENT, the mixing length for the subgrid scales L_s and the subgrid-scale eddy viscosity $\nu_t = \mu_t / \rho$ are used to create an estimate for the subgrid-scale or subtest kinetic energy $k_s = \nu_t^2 / L_s^2$. It can also be compared against the total turbulent kinetic energy, usually if less than 5% the solution is considered to be well resolved. Figure 4.12(a) shows the k_s of fluid for the single phase and two-phase flows. The results clearly show that particle inertia does have an effect on k_s . Figure 4.12(b) gives the same plot in log form, where it is seen that both two-phase flows are lower than the single phase flow between $0 < z^+ < 40$ and slightly over between $60 < z^+ < 250$. The discrepancy is relatively large; it is seen to begin from just outside the buffer region and increase towards the walls. These results indicate that the fluid velocity in the boundary layer is magnified by the forces of the particle exerted on the fluid. It is also noted that there is no difference between the two-phase flows containing 0.0 and 0.05 J m⁻² particles due to similar mass and momentum transfer. Therefore, although there is negligible effect of particles on the mean fluid velocities of the resolved scale, there is a prominent effect on the subgrid-scale velocities. Specifically, these 150 μ m particles dampen k_s in regions of high fluid turbulence and high particle concentrations close to the wall.

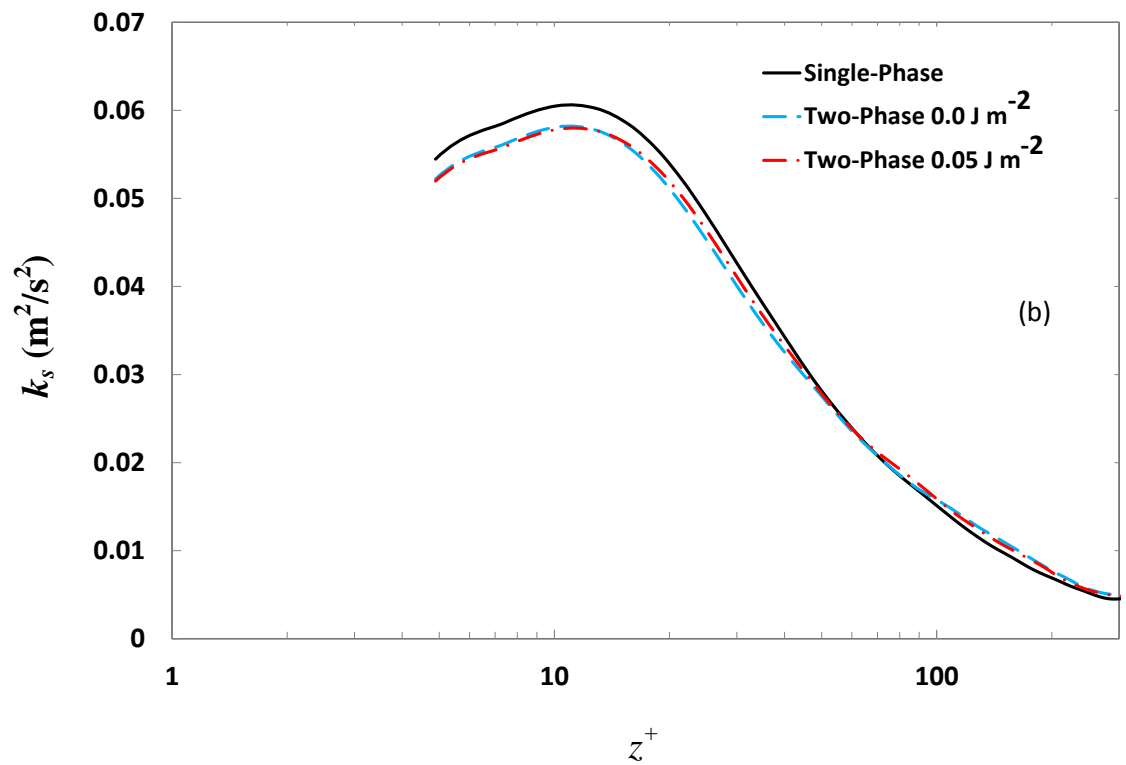
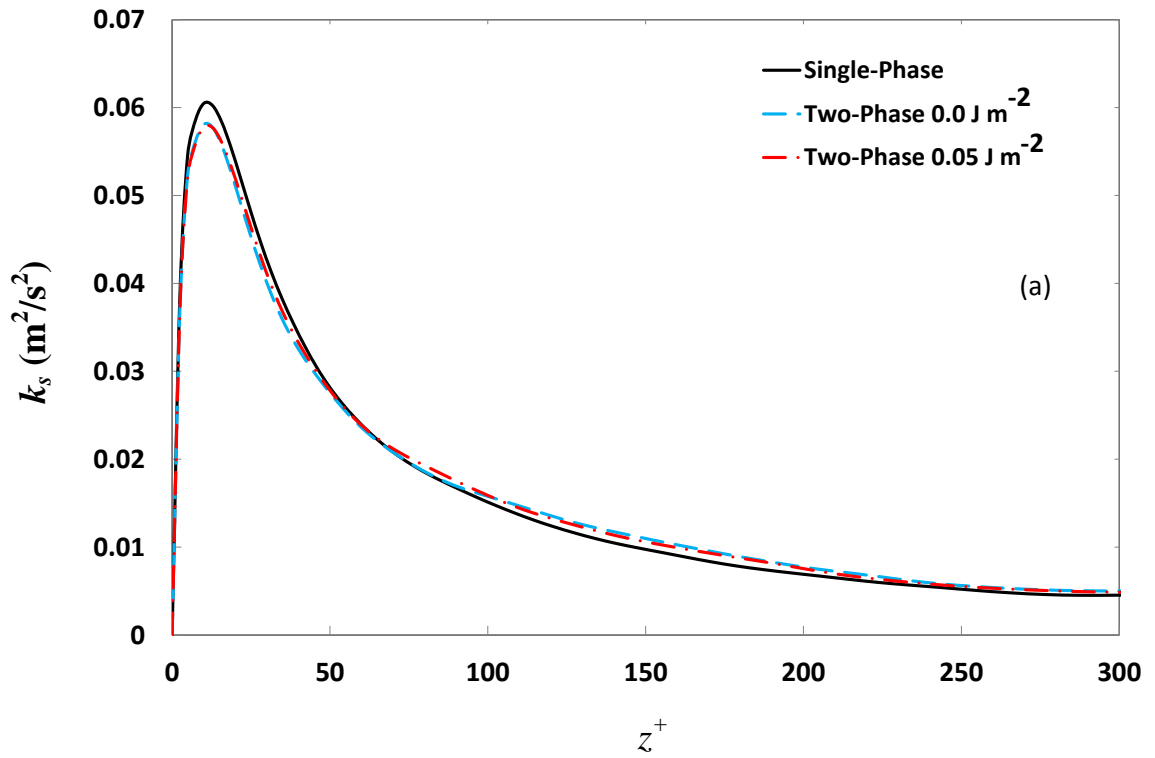


Figure 4.12 Subgrid-scale kinetic energy of fluid, k_s ($\text{Re}_\tau = 300$).

4.3.2 Effects of particle-particle contacts on particle velocity statistics

In this sub-section, the work quantifies the effects of particle-particle contacts on particle behavior. To achieve this, results from both simulations that contain cohesive and non-cohesive particles (0.05 and 0.0 J m^{-2}) are contrasted against each other. Figure 4.13(a) gives the mean streamwise velocity profiles for both flows. The results do not display any differences between the 0.0 and 0.05 J m^{-2} systems. This is also the case for the log-profile given in Figure 4.13(b). It is seen that the particle velocities near the channel walls do not reach zero. These results are in line with the experimental data of Righetti and Romano (2004) for horizontal channel flow: particle velocity is greater than fluid velocity near the wall $z^+ < 15$ and lower than fluid velocity in the outer layer.

Figure 4.14(a) shows the rms of particle velocity fluctuation and Reynolds stress for the two flows. There are some differences observed between the flows with 0.0 and 0.05 J m^{-2} particles. In particular for the $V_{x,rms}$, where the values are seen to diverge towards the channel centreline. Although, it is difficult to draw a definitive conclusion on whether these are waves in the profiles or discrepancies. Figure 4.14(b) shows the scaled particle-to-fluid rms's, it takes into account the effects of particles on both the fluid and particle phase characteristics. The results show that there is a large difference in particle and fluid turbulence at the wall for the wall-normal ($V_{z,rms}$) component followed by the streamwise ($V_{x,rms}$). Moreover, this difference in fluctuation for the $V_{z,rms}$ continues throughout the channel. In two-way coupled flows, the decrease in streamwise particle velocity due to friction between the particle and wall on impact is captured. Furthermore, the incorporation of inter-particle collisions means that particle collisions can increase fluctuation intensity in the wall-normal direction, by converting velocity from the streamwise to this direction. These effects are altered with differences in post collision velocities.

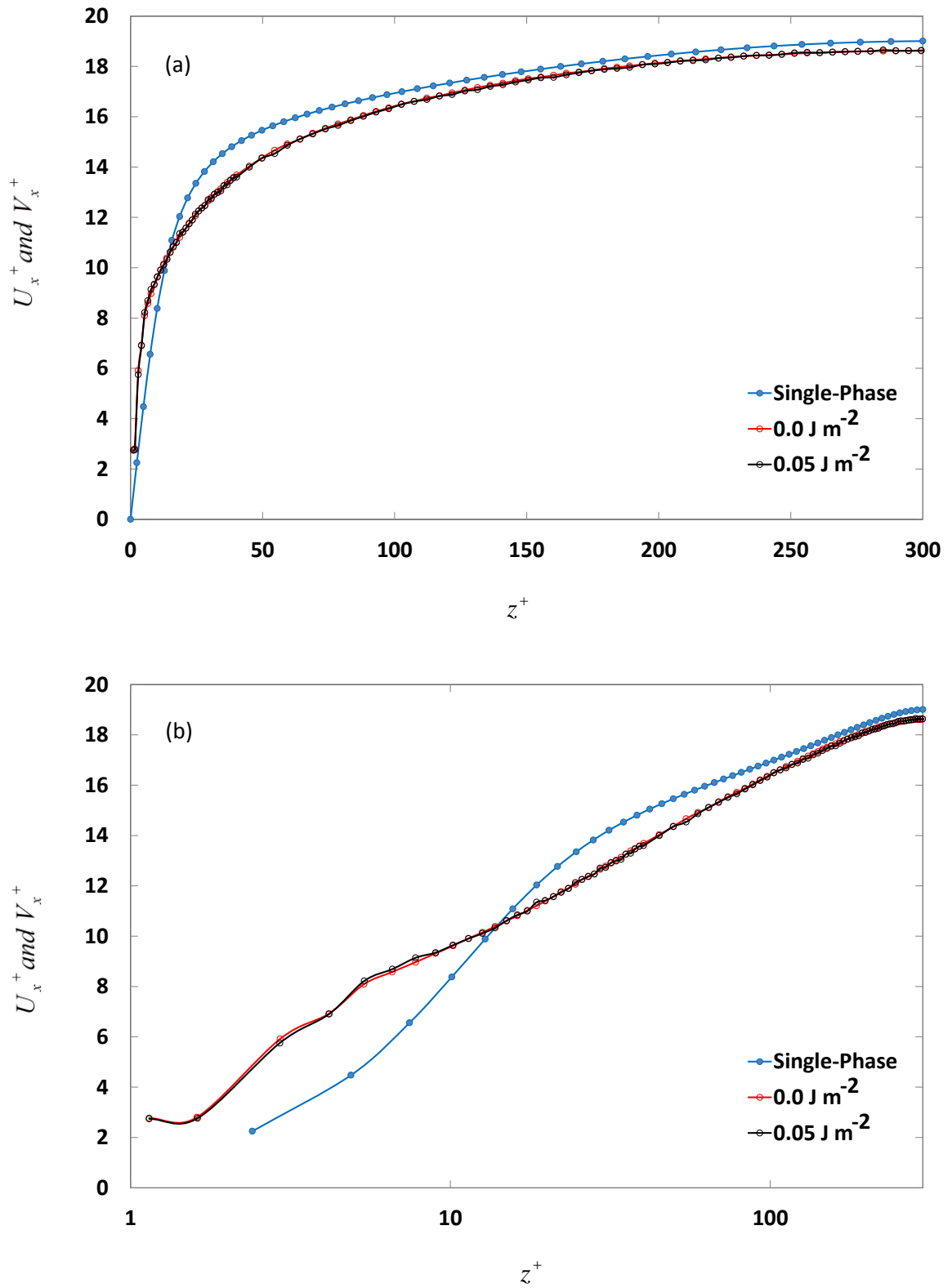


Figure 4.13 Non-dimensional mean streamwise particle velocity: (a) linear and (b) logarithmic ($Re_\tau = 300$).

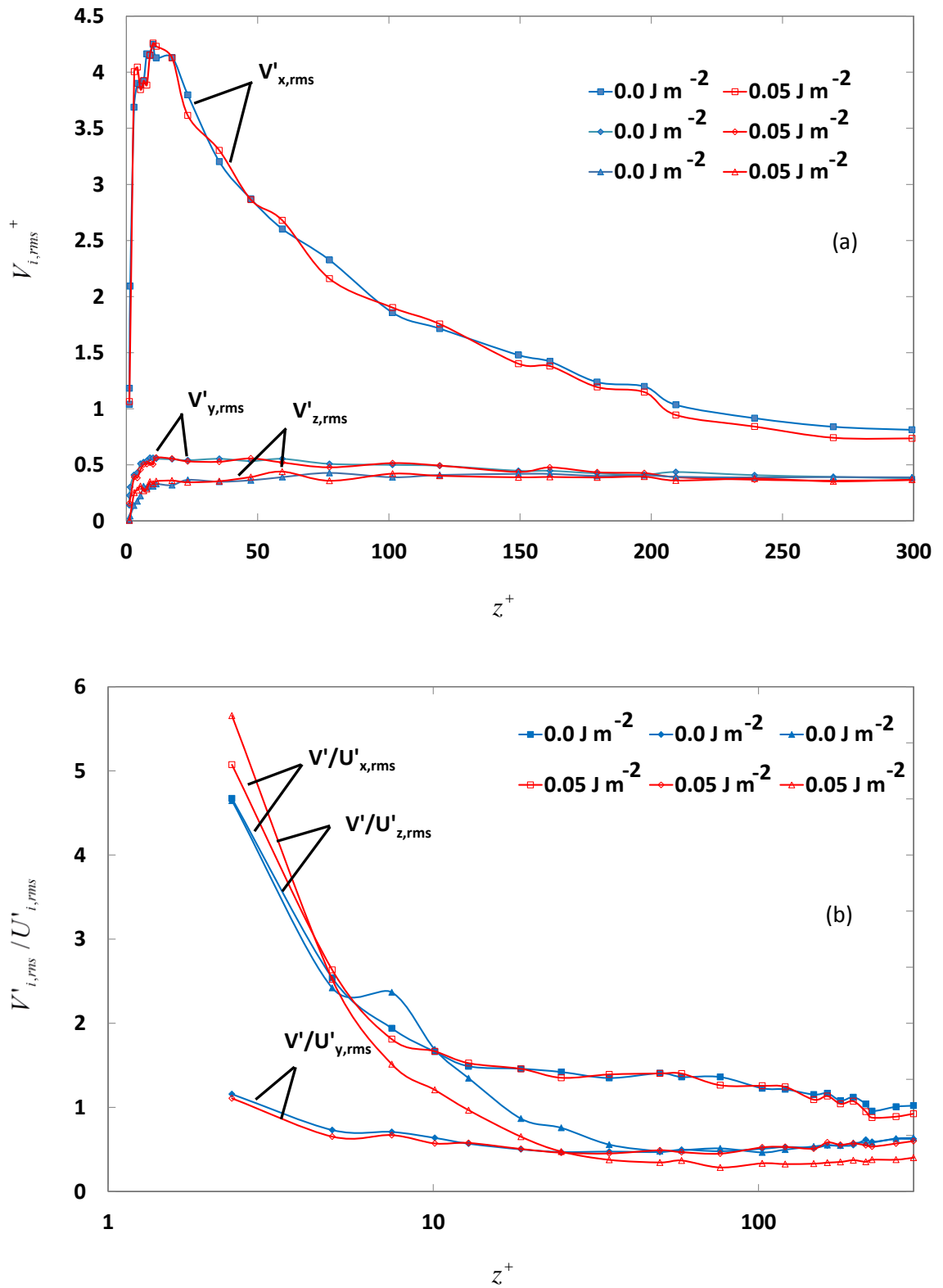


Figure 4.14 (a) Root mean square of particle velocity fluctuation; (b) Scaled particle-to-fluid velocity rms ratios, $V'_{i,rms}/U'_{i,rms}$, at $Re_\tau = 300$.

Figure 4.15 shows the particle number density n_p and collision number density $n_{collisions}$ profiles in the wall-normal direction, at the end of the simulation $t^+ = 5373$ (1.52 s) for 0.0 J m^{-2} and 0.05 J m^{-2} particles. The collisions are complete impacts, when two elements collide it will register as one collision, regardless of how long the elements stay in contact for. The value n_p is in effect the concentration and its calculation including binning procedure have been discussed earlier; this calculation also applies to $n_{collisions}$. The n_p profiles clearly show a uniform particle distribution at the channel centre corresponding to a flat profile centered on $n_p \approx 1$, where the particle density increases towards the walls with the magnitude decreasing with particles surface energy. The turbophoretic effects of the system are evident; the particle volume fraction is more than 14 times higher at the channel walls ($z^+ < d_p$) in relation to the channel centre. It is worth mentioning that particle accumulation near the walls is sensitive to the precise flow regime, for different particle sizes and volume fractions turbophoresis can be negligible. Comparing the two flows, the particle concentration at the walls compared to the mean concentration is about 17 and 16 times higher for the 0.0 J m^{-2} and 0.05 J m^{-2} simulations, respectively. Therefore, these results prove that particle bond formation does not necessarily lead to an increase local particle concentration. From the fluid statistics discussed earlier, it has been established that particle agglomeration for this particular mass loading is not sufficient enough to significantly dampen or amplify the fluid turbulence any further, and therefore would not alter the rate and/or magnitude of turbophoresis. The dissimilarity in these values is either because of a difference in the number of collisions and/or particle agglomerates have higher inertia and thus respond differently to turbophoretic effects. The collision number density profiles show that particles interact most frequently in regions of high concentration at the walls, and regions of high turbulence near the walls. The collisions frequency profile has been sampled throughout the simulation ($t^+ = 0 - 5373$ s). The collision density is 40% higher at the walls for the 0.0 J m^{-2} and could be the dominant factor for a higher concentration in this region due to post collision energy loss.

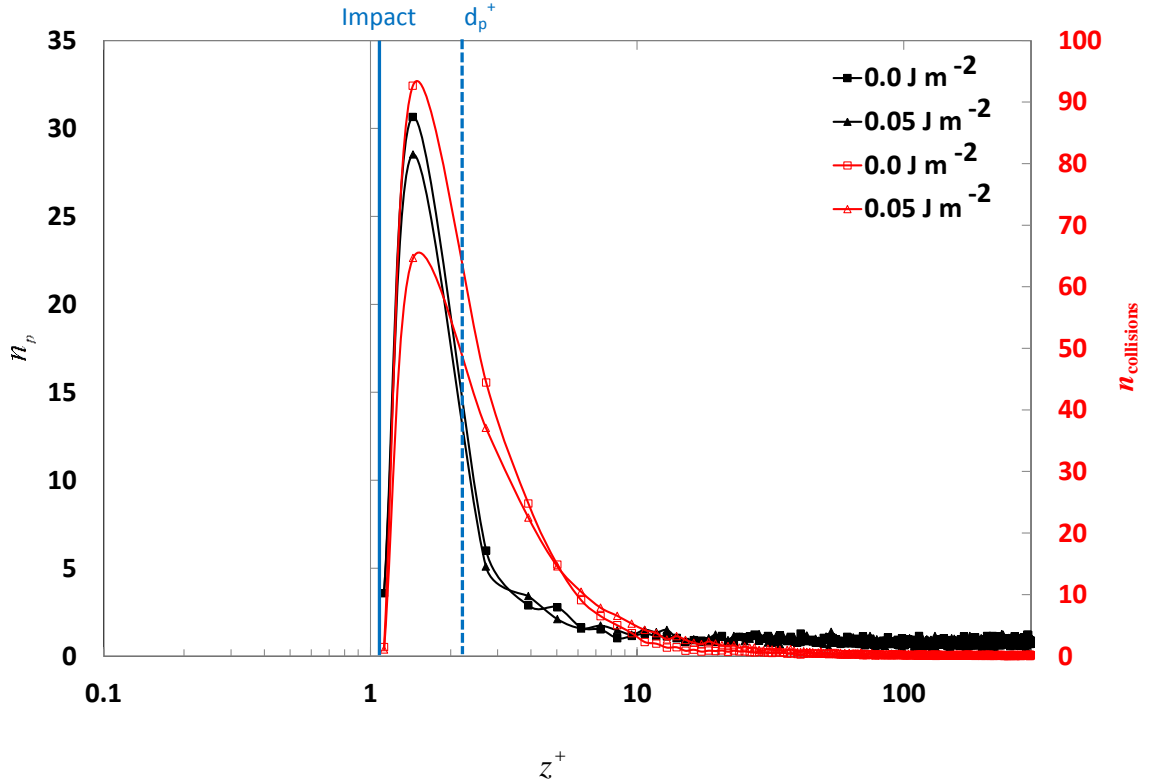


Figure 4.15 Particle number density, n_p , and total number of collisions, $n_{collisions}$, profiles in wall-normal direction at $t^+ = 5303$ (1.5 s). The vertical solid blue line indicates the position of contact between the particles and wall (impact); the vertical dashed line gives a visual indication of the particle size in wall units (d_p^+).

From earlier work, it is known that for turbulent channel flows particle locations close to a wall correlate with instantaneous regions of low velocity along the streamwise direction, with the particles avoiding regions of high velocity, with the former defined as areas of lower-than-mean streamwise velocity (Pan and Banerjee, 1996). Two-way coupled studies however, have reported an opposite trend. The work of Yamamoto et al. (2001) revealed that in fully coupled systems particles with large inertia are distributed nearly uniformly and are not affected by the small-scale turbulence structure of the gas phase. Moreover, particle concentration in the near-wall region is low because the inter-particle collision disperses particles in the wall-normal direction and no streaky particle distribution is observed. Figure 4.16 shows simultaneous visualisations of instantaneous particle distribution at the wall (thickness⁺ ~ 4) and fluid streamwise velocity distribution in the wall-parallel plane at $z^+ \sim 4$. They highlight the correlations between spatial assembly of particle distribution and fluid turbulence in the near-wall region (i.e. viscous sub-layer). For 0.0 J m^{-2} particles, the streamwise fluid velocity distribution

(Figure 4.16 (a)) has a streaky structure. In Figure 4.16 (b), in contrast to the fluid velocity, the particles are distributed almost uniformly and no streaky particle distribution is observed. In the case of particles with contacts (Figure 4.16 (c, d)), streamwise fluid velocity distribution again shows a streaky structure, however, particle concentration is slightly higher in random regions of the channel floor where the particles have formed large agglomerates. Further scrutiny of the results, yet again shows that there is no visible correlation between the particle concentration and regions of high or low velocity (turbulence structure). In the results shown, where inter-particle collisions have been accounted for, the structure of particle distribution is stretched in the streamwise and spanwise directions. It is a direct result of the inter-particle collisions dispersing particles in the wall-normal and spanwise directions. This corresponds with the experimental observations by Fessler et al. (1994); where particle clouds were elongated in the spanwise direction.

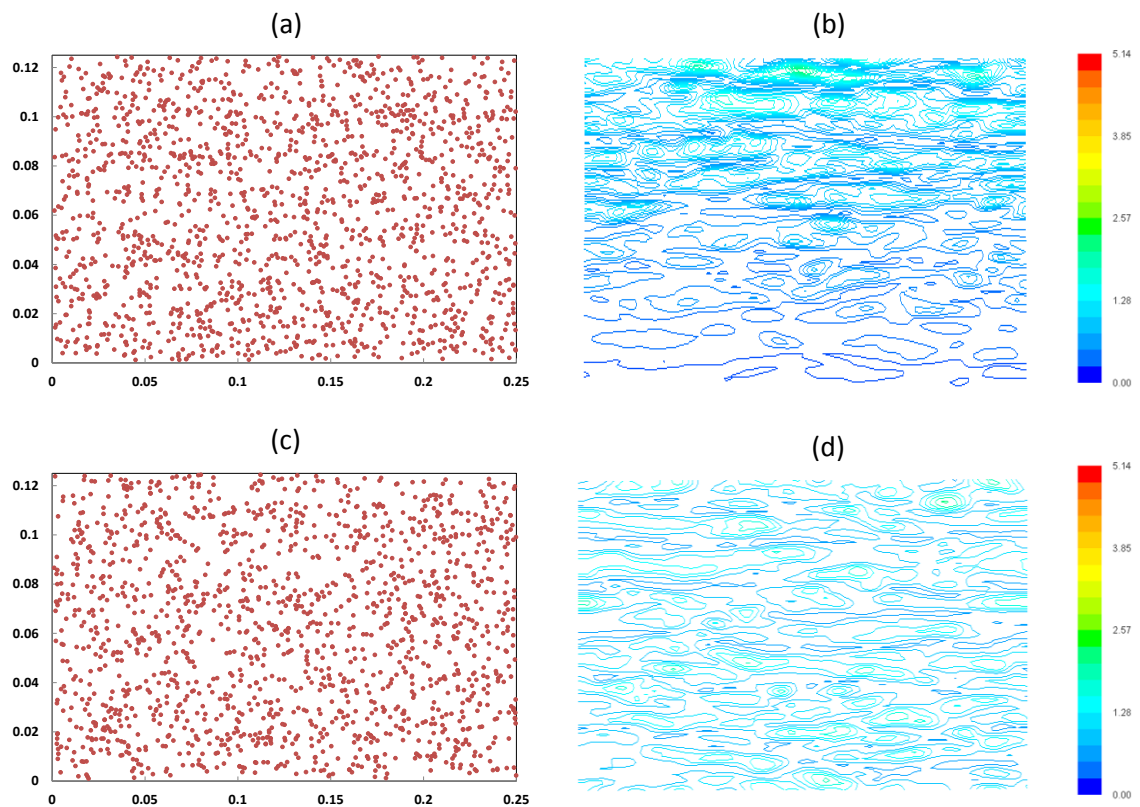


Figure 4.16 Instantaneous distribution of particles and gas streamwise velocity on the wall-parallel plane in the near-wall region (particle at $z^+ = 0 - 4$, fluid at $z^+ = 4$): a) 0.0 J m^{-2} , particle; b) 0.0 J m^{-2} , fluid velocity; c) 0.05 J m^{-2} , particle; d) 0.05 J m^{-2} , fluid velocity.

Following the comparison of particle concentration and collisions as a function of their location, it is necessary to consider the statistical correlation between particles and fluid velocity in different regions of the channel. Figure 4.17 shows probability density functions of particle streamwise and wall-normal velocity in the viscous sublayer ($0 < z^+ < 4$), buffer layer ($5 < z^+ < 30$), and outer layer ($100 < z^+ < 300$). Where U_i is the instantaneous streamwise gas velocity at the particle position; the velocities are normalised by the maximum. The data sets have been sampled at well separated time steps (0.01s). In the viscous sublayer, there is no difference for the distribution of streamwise and wall-normal velocities (Figure 4.17a,b). In the buffer layer, the streamwise profiles deviate from the peak towards higher velocities (Figure 4.17c). In the case of the wall normal (Figure 4.17d), the 0.05 J m^{-2} velocity profile is slightly lower between about $0.01 - 0.03 \text{ m s}^{-1}$. These results show that the cohesive particles have a lower maximum streamwise velocity in the buffer layer. In the outer layer (Figure 4.17e), the cohesive particles are seen to have lower minimum and maximum velocities. Furthermore, there is a large deviation between the central region of the profiles, this suggests that relative velocity between single particles and particle agglomerates widens in this region. For the wall normal (Figure 4.17f), the particles velocity distributions are similar for both particles.

To quantify the amount of preferential concentration which in this case is related to the degree of agglomeration, an approach from Eaton and Fessler (1994) has been adopted which examines the deviation of the number density distribution from the Poisson distribution. The Poisson distribution is given by $e^{-\lambda} \lambda^k / k!$, where n_p is the number density and λ is the mean number density. The number density follows the Poisson distribution when particles are evenly distributed. However, the number density distribution broadens when particle clouds are formed. The number density was calculated in 7.3 mm^2 cells; these cells were constructed by taking the channel as one uniform section from wall to wall; and dividing it into 90 and 45 sections in the streamwise and spanwise directions, respectively. Figure 4.18 shows the calculated number density distribution and Poisson distribution for the same number of particles. The vertical axis represents the frequency of the particle number density normalised by the total number of cells and the horizontal axis k represents the number of particles in a cell. The results were calculated by using data from time steps separated by 0.01 s intervals. In Figure 4.18, the number density distribution of the 0.0 and 0.05 J m^{-2}

particles generally follow the Poisson distribution. However, there are quantitative differences that suggest the particles are not distributed completely uniformly throughout the channel. For the 0.05 J m^{-2} particles, in relation to both distributions, the distribution function is lower and widened by the formation of particle agglomerates. This is indicative of higher particle number density in certain cells and therefore shows the degree of particle agglomerate in the system. Therefore these results show that the system with cohesive particles is less dispersed.

It is important to mention that this evaluation method used to calculate number density depends on the cell size. Eaton and Fessler (1994) gauged the extent of preferential concentration in particle clouds for different cell sizes by the parameter $D = (\sigma - \sigma_{\text{pois}})/\lambda$, where σ and σ_{pois} are the standard deviations for the calculated number density distribution and Poisson distribution, respectively. If the cell is significantly larger than a particle cloud or very small where it cannot contain many particles, the particle distribution is effectively random and the number density distribution approaches the Poisson distribution. Thus, $D \approx 0$ when the particles are distributed randomly and D is at a maximum when the cell size is similar in size to the particle clouds. It would be ideal to show the change of D for varying cell size, and select the cell size (Δ) where D is a maximum. However, such sensitivity tests are outside the scope of this thesis has been left to further.

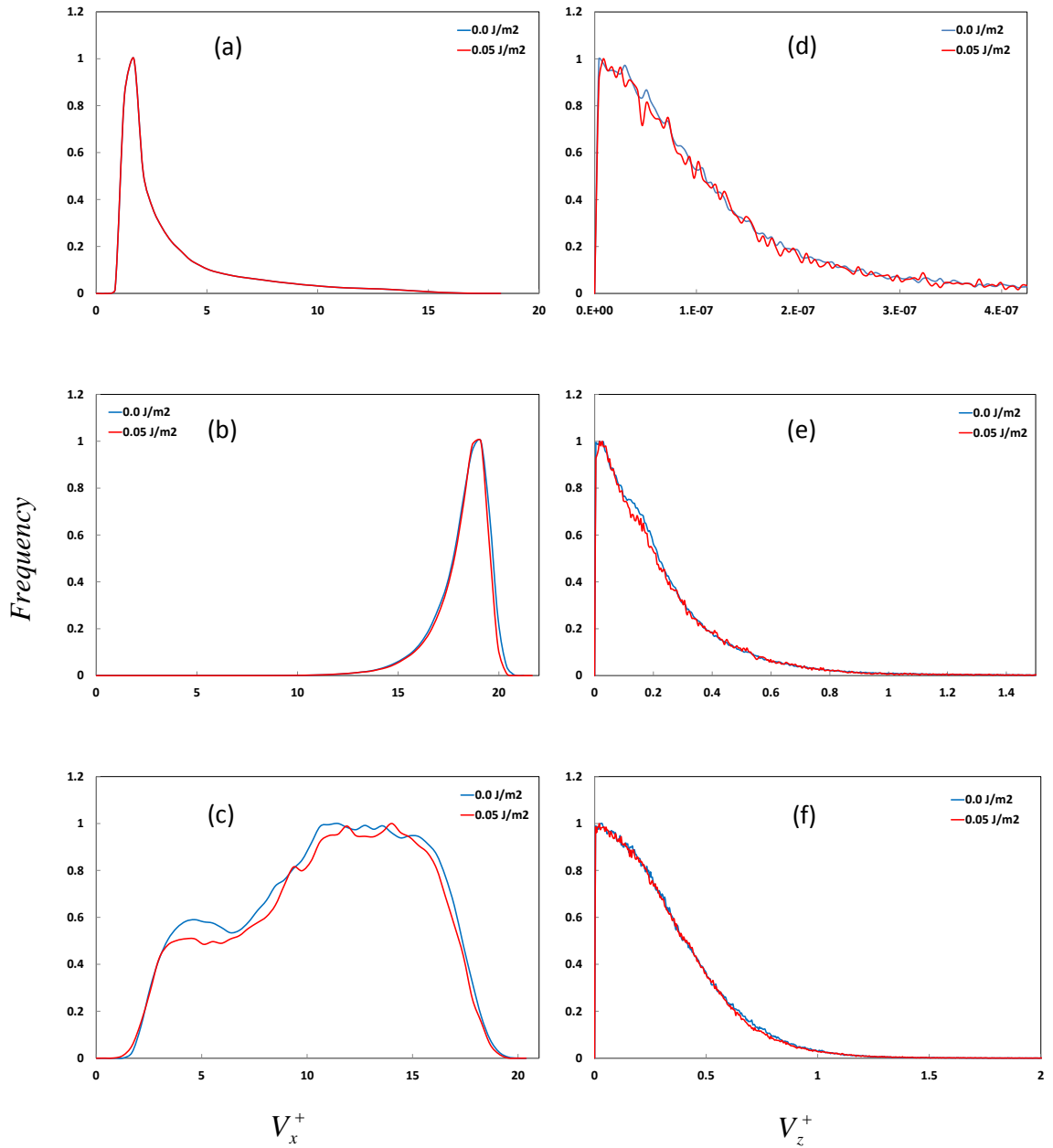


Figure 4.17 Probability density function of particle streamwise (left) and wall-normal (right) velocity: (a,d) $0 < z^+ < 4$; (b,e) $5 < z^+ < 30$; (c,f) $100 < z^+ < 300$ ($t^+ = 1,400 - 5373$).

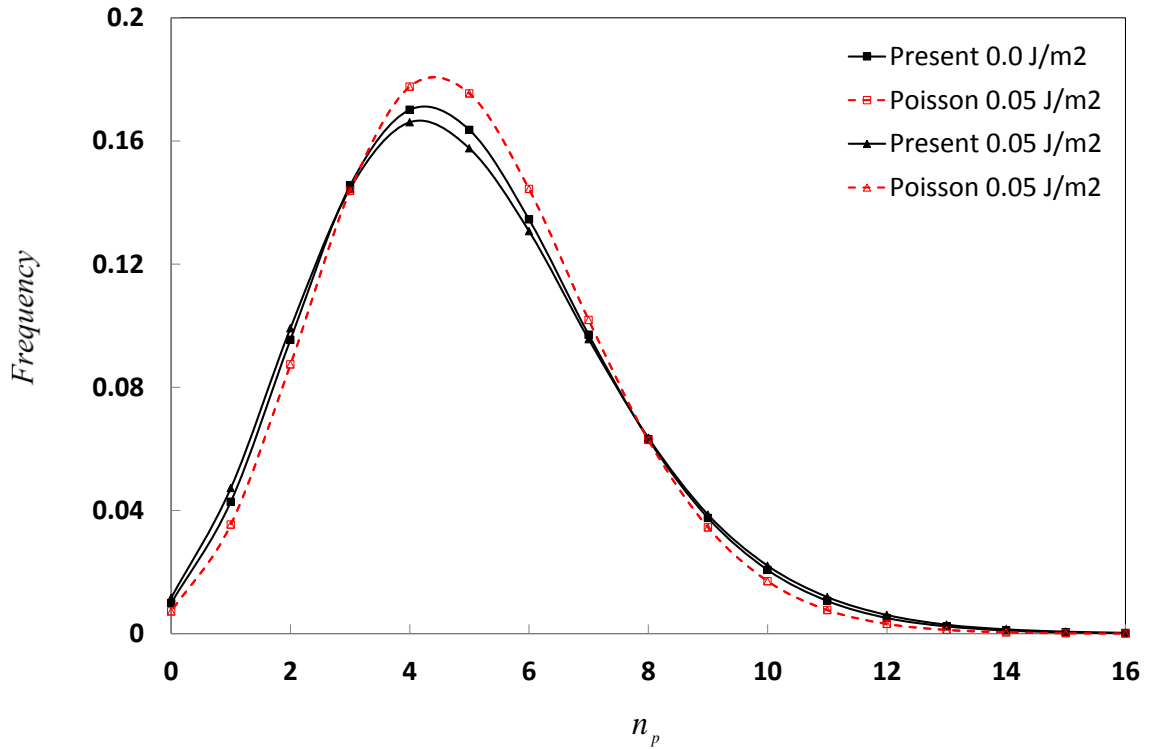


Figure 4.18. Particle number density distribution and Poisson distribution. The horizontal axis n_p represents the number of particles in a cell and the vertical axis represents the frequency of the particle number density normalized by the total number of cells ($t^+ = 1,400 - 5373$).

To better understand the mechanism of particle and agglomerate dispersion in channel flow, dynamic analysis was used to calculate the magnitude of the streamwise and wall-normal components of the drag and lift forces. Figure 4.19(a and b) show the mean streamwise and wall normal profiles for the particle coupling forces as a function of time, respectively. The coupling force is the summation of the lift and drag forces acting on the particle, and can be used to quantify the drift of particles in the channel, and specifically towards and away from the walls. It is important to highlight that the drag forces are calculated from the slip velocity between the fluid and particle $U_i - V_i$ (see LPT in methodology). Results are given for three different regions in the channel, these include the viscous sublayer ($0 < z^+ < 5$), buffer layer ($5 < z^+ < 30$), and outer region ($100 < z^+ < 300$). In Figure 4.19(a), generally, there is an initial sharp decrease in streamwise coupling force that transgresses to a profile that is constant on average with time. The results show quantitatively similar behaviour for the 0.0 and 0.05 J m⁻² particles. The profiles reach an asymptote at $t^+ \approx 810$ in the viscous and buffer layer, and at $t^+ \approx 270$ in the outer layer. Furthermore, the largest differences in the initial and

final values of the coupling force are seen in the viscous sublayer, followed by the buffer and outer layers, respectively. This is because particles are introduced with the local velocity of the fluid; the ones that remain in the outer layer quickly adjust to the fluid velocity. However, the particles that migrate towards the walls experience a decrease in velocity caused by the fluid velocity gradient in that direction. Also, the exaggerated wavelike profile for the buffer layer, in relation to the others, indicates the higher level of turbulence in this region. In Figure 4.19(b), profiles of the wall-normal coupling force show a similar trend to that seen for the streamwise (Figure 4.19(a)). However, further scrutiny of the results shows that $F_{z,coupling}$ in the buffer layer does not change with time. This suggests that the wall-normal velocity of the particles does not decrease until they enter the viscous sub-layer. By comparing the coupling force in the streamwise (Figure 4.19(a)) direction against the wall-normal (Figure 4.19(b)), it is possible to determine which fluctuation component is more responsible for particle-particle collisions. Although the wall-normal profiles have a lower magnitude compared to the stream-wise profiles, they exhibit more unsteadiness in all three regions and in particular in the buffer layer where the rate of agglomeration is the highest. Therefore, it is the wall-normal fluctuation that is the main driving force in particle-particle collisions. Furthermore, the wavy profile of the viscous sublayer suggests that the particles are driven to the walls by turbophoresis and rebound off the wall with a velocity in the opposite direction. The ejections and sweeps, and particle-particle collisions at the walls are also partly responsible for particle expulsions normal to the wall plane.

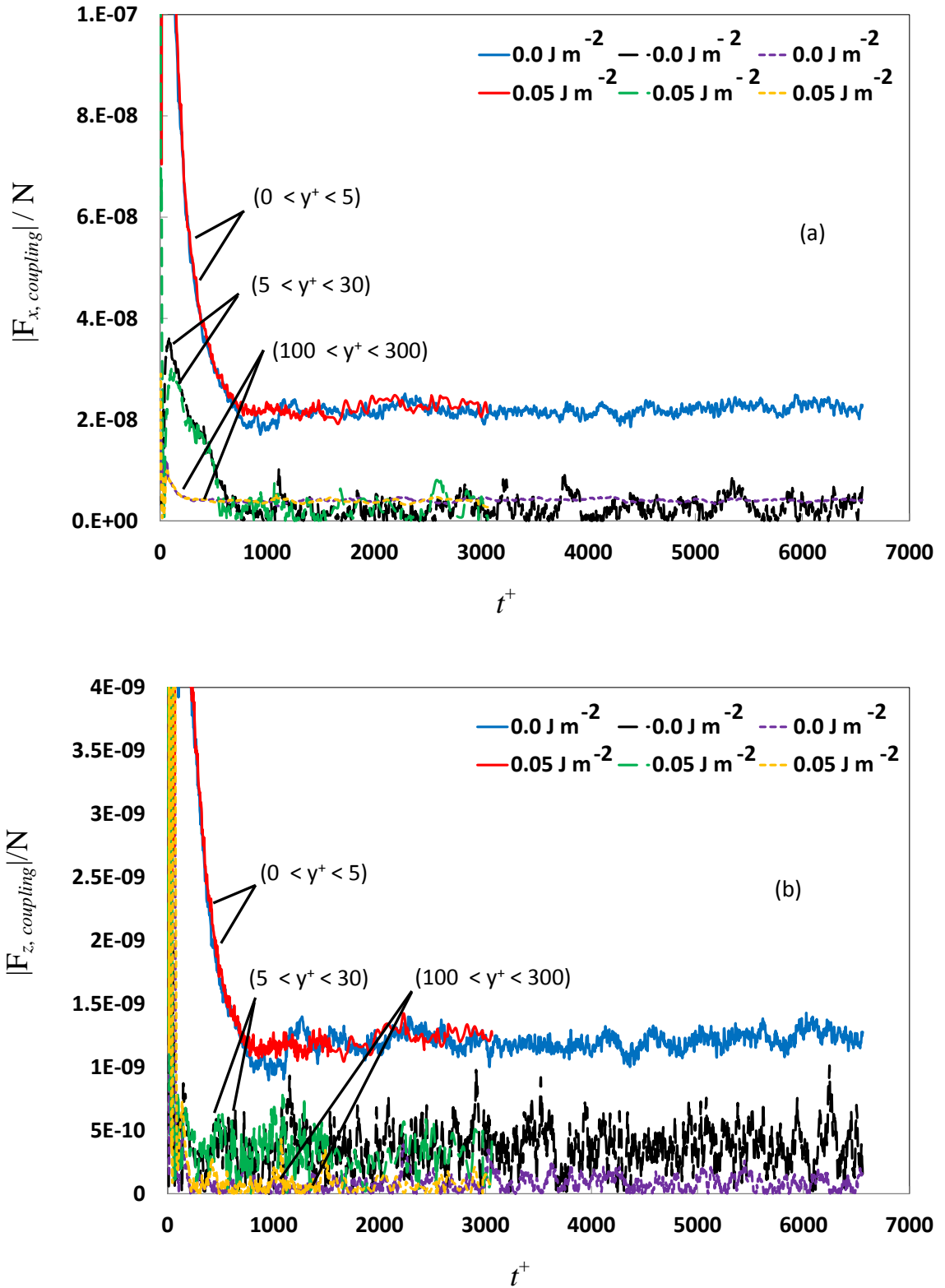


Figure 4.19 Absolute Coupling Forces $F_{i,coupling}$ (Drag and Lift) on Particles for three different regions in the channel with time t^+ : (a) Streamwise, (b) Wall-normal.

Figure 4.21(a,b) and Figure 4.22(a,b) show the mean streamwise and wall normal profiles for the particle coupling forces as a function of distance from the wall, respectively. The force coupling results in Figure 4.19 showed that most of the particle activity is at the earlier time steps of the simulation; therefore, when comparing the dispersing characteristics of the particles and agglomerates, the data has been sampled separately early into the simulation. Results have been time-averaged for the developing phase $t^+ = 0.0 - 1237$ ($t = 0.0 - 0.35$ s) and steady state $t^+ = 1237$ onwards ($t > 0.35$). In Figure 4.21(a,b), generally, the magnitude of $F_{x,coupling}$ increases towards the walls, this shows that the resistance of the particles to the fluid increases in this direction. This increase is seen for two separate sections resulting in two separate peaks. These peaks are at the edges of the viscous sub-layer ($z^+ \approx 4$) and buffer layer ($z^+ \approx 30$), the latter being lower in magnitude. The peak at $z^+ \approx 4$ is located in the region where the profile is negative ($z^+ \approx 0 - 15$). This signifies that some of the particles are being pushed backwards by the swirling fluid turbulence as they approach the walls. These particles will have a very high individual value of $F_{x,coupling}$, causing the average value to be negative. This does not mean that the majority of the particles are moving counter to the flow direction in this region. Comparing the developing and steady state profiles, moving away from the centre-line, they increase to peak values of around 10 and 18 nN at $z^+ \approx 30$, respectively. Both profiles then decrease to almost 0 nN at $z^+ \approx 15$. After which, the profiles continue to decrease to -47 and -65 nN at $z^+ \approx 4$ before increasing at the walls, respectively. $F_{x,coupling}$ is greater for the developing phase below $z^+ \approx 15$. This is because earlier into the simulation, the particles that drift into the near wall region have higher momentum and therefore see more resistance from the low velocity fluid in that region. In Figure 4.22(a,b), moving away from the centerline, generally, the magnitude of $F_{z,coupling}$ fluctuates about its axis up to $z^+ \approx 15$. From here it decreases to a minimum value at $z^+ \approx 4$ before rising again. Comparing the developing and steady state profiles, an increase in divergence is seen with magnitude, where the values reach minimums of -2.9 and -2.4 nN, respectively. The negative values designate that some of the particles are moving counter to the flow, i.e. towards the channel centre. This agrees with the findings from Figure 4.19(b) and further confirms that particles are rebounding off the wall. Again, it is important to stress that $F_{z,coupling}$ is very high for such particles and leads to a negative average, and does not mean that all particles are moving away from the walls in this region. Figure 4.20 shows particle position and corresponding contours of the coupling force for 0.05 J m^{-2} particles in the channel cross section. The

percentage distribution for wall-normal coupling force in the top and bottom half of the channel is also given for the start of the simulation ($t^+ = 35$). The wall-normal coupling force acts equally in both directions about the channel centerline ($z^+ = 300$), where 52 % of the particles are moving towards the walls. It is this additional 2% that results in particle accumulation at the walls.

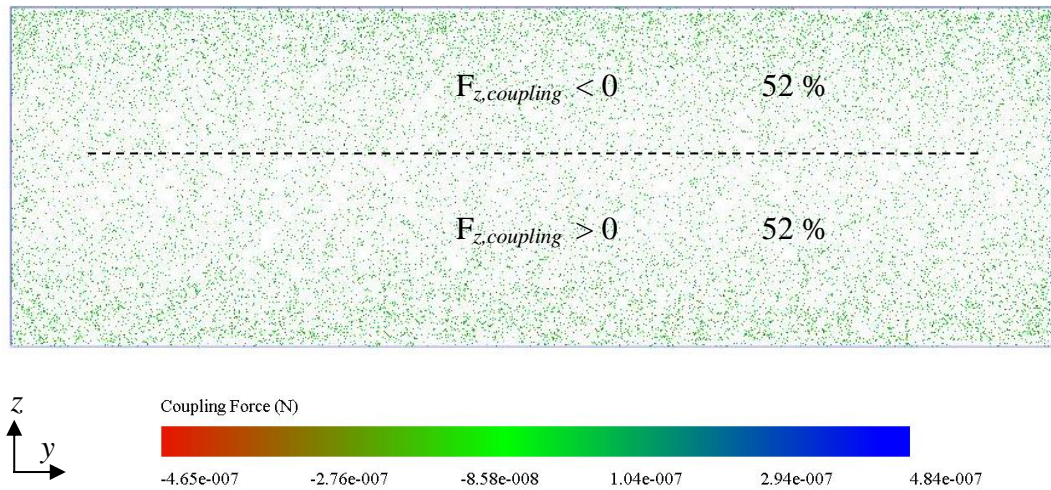


Figure 4.20 Contours of the Coupling Force for 0.05 J m^{-2} particles in the channel cross section; and corresponding percentage of distribution for wall-normal coupling force at time $t^+ = 35$ (0.001s).

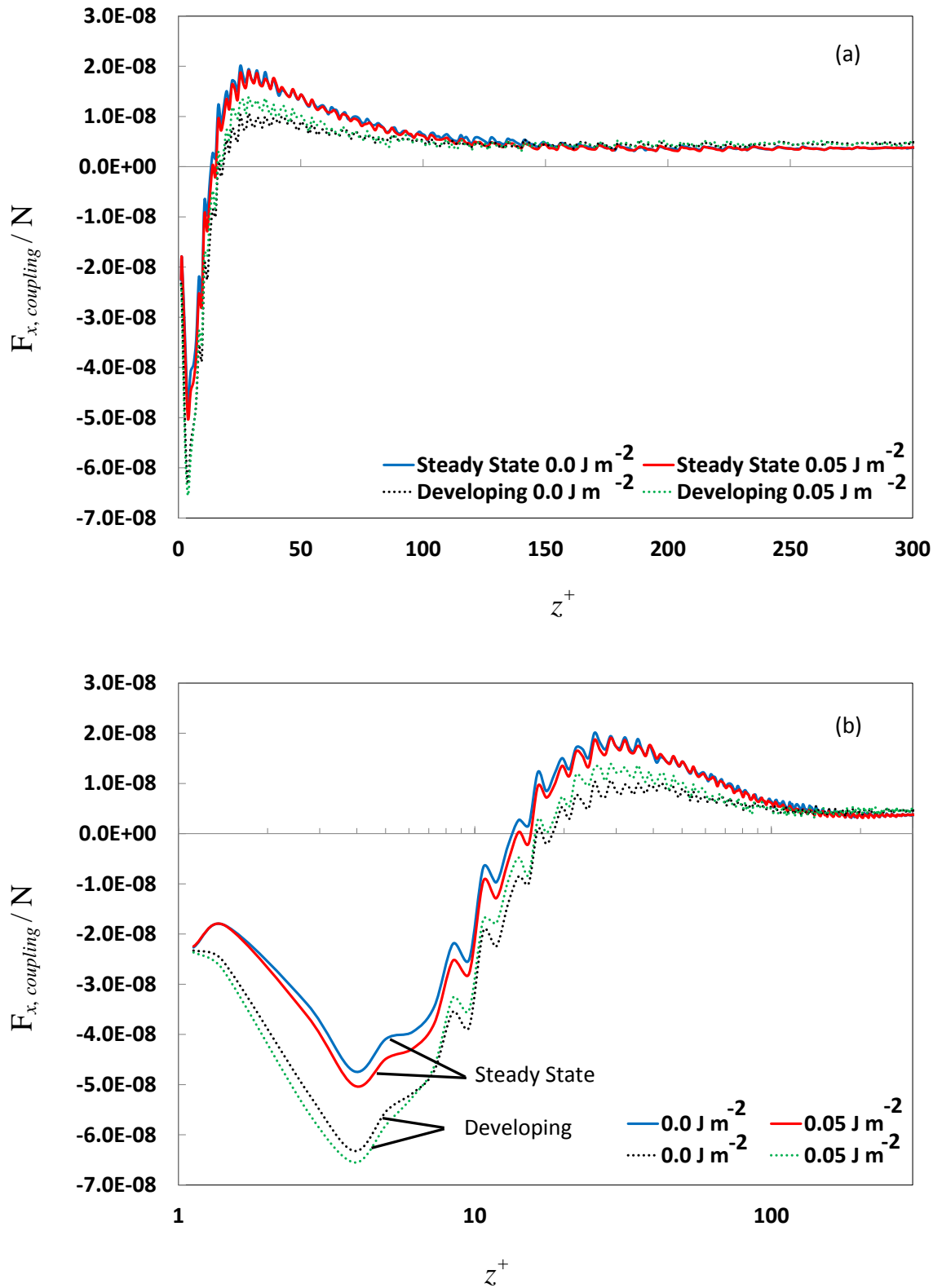


Figure 4.21 Streamwise component of Coupling Forces $F_{x,coupling}$ (Drag and Lift) on Particles in wall-normal direction z^+ : (a) linear, (b) logarithmic

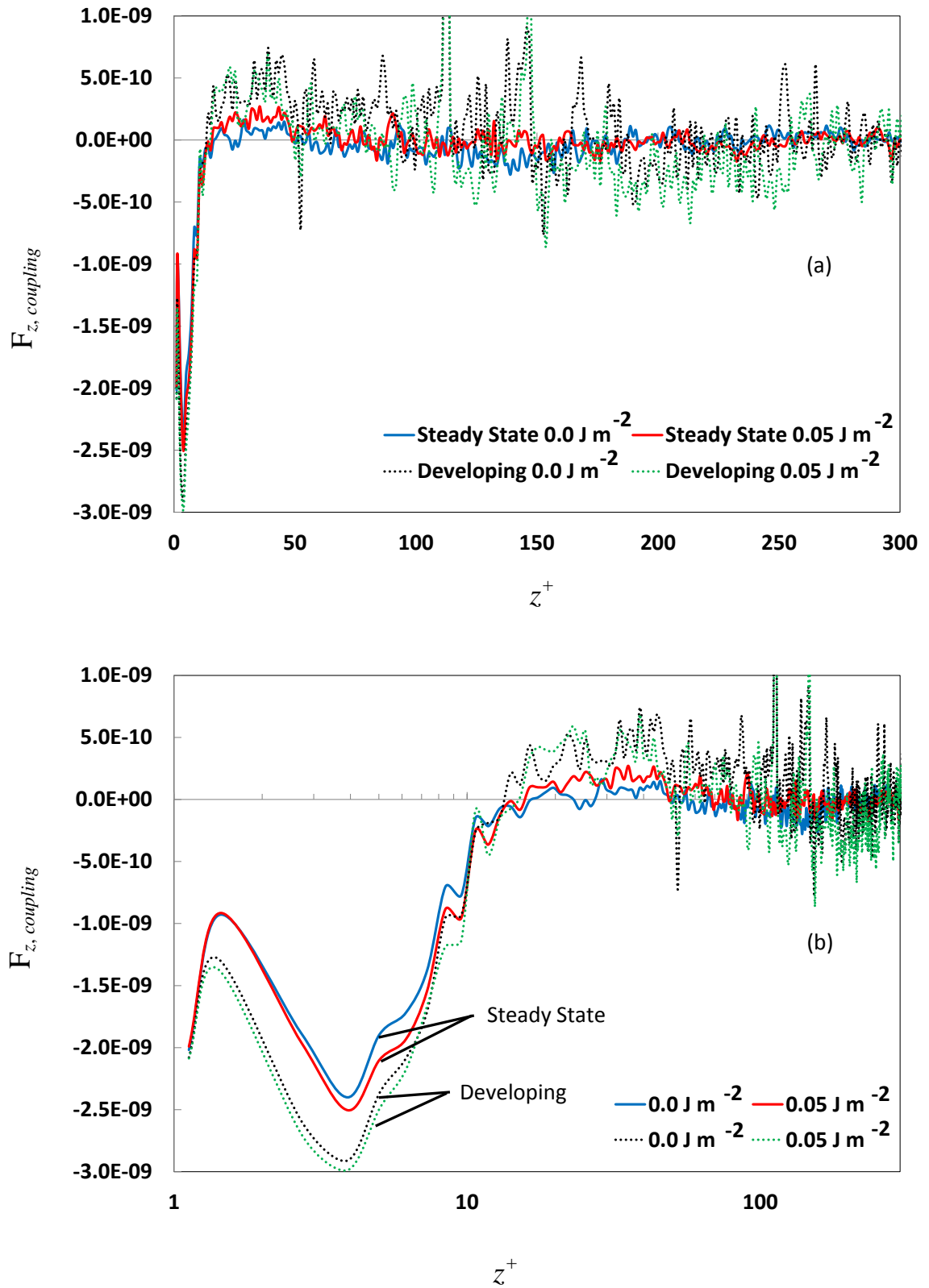


Figure 4.22 Wall-normal component of Coupling Forces $F_{z,coupling}$ (Drag and Lift) on Particles in wall-normal direction z^+ : (a) linear, (b) logarithmic

It is difficult to differentiate between the 0.0 and 0.05 J m⁻² profiles in Figure 4.19 and Figure 4.21. For that reason the average streamwise and wall-normal components of the coupling force $F_{i,coupling}$ are given in Table 4-3 and Table 4-4 for the viscous sublayer ($z^+ < 5$), buffer layer ($5 < z^+ < 30$), and outer region ($100 < z^+ < 300$), respectively. The results are given for the developing phase ($t^+ = 0.0 - 1237$) and at steady state ($t^+ = 5373$). For the 150 μm particles, generally, the coupling force in the streamwise direction (Table 4-3) is larger than the wall-normal direction (Table 4-4) by at least one order of magnitude, indicating that the motion of these particles is greater dominated by the drag force in the streamwise direction. This explains why these particles are well dispersed and take a long time to reach a steady state, as previously discussed. For the 0.0 and 0.05 J m⁻² particles, the overall values of $F_{x,coupling}$ (Table 4-3) are similar in the developing stage, this is also the case at steady state. Although, some differences are seen in the three different regions of the channel, where for the 0.05 J m⁻² particles, $F_{x,coupling}$ is up to 5 % higher in the buffer layer and outer region. Although these differences in $F_{x,coupling}$ are small, they do reduce the particle velocity distribution which is reflected in Figure 4.17. In Table 4-4, for the 0.0 and 0.05 J m⁻² particles, the overall value of $F_{z,coupling}$ in the developing phase are similar. Yet again however, dissimilarities are seen in the different regions of the channel. For cohesive particles (0.05 J m⁻²), in the buffer layer and outer region, $F_{z,coupling}$ is 9 and 14 % higher, respectively. This also suggests that agglomeration in the developing phase affects the results. Naturally the steady state profiles have a lower $F_{i,coupling}$ compared to the developing stage. Yet, the proportional increase in $F_{z,coupling}$ for cohesive particles is greater. Specifically, for the 0.05 J m⁻² particles the overall $F_{z,coupling}$ is higher which is mainly attributable to the 23% increase in the buffer layer.

Table 4-3 Comparison of Effect of Main Forces (Drag and .Lift) on Particles (Streamwise)

State	SE (J/m ²)	Drag and Lift (nN)			
		Streamwise			
		$0 < z^+ < 4$	$5 < z^+ < 30$	$100 < z^+ < 300$	All
Developing	0.0	40.9	16.4	4.45	6.96
Developing	0.05	42.9	17.2	4.46	7.04
Steady	0.0	30.6	16.8	4.13	7.25
Steady	0.05	31.8	17.1	4.18	7.26

Table 4-4 Comparison of Effect of Main Forces (Drag and Lift) on Particles (Wall-normal)

State	SE (J/m ²)	Drag and Lift (nN)			
		Wall-Normal			
		$0 < z^+ < 4$	$5 < z^+ < 30$	$100 < z^+ < 300$	All
Developing	0.0	2.22	0.58	0.25	0.36
Developing	0.05	2.29	0.62	0.29	0.36
Steady	0.0	1.81	0.34	0.07	0.11
Steady	0.05	1.84	0.44	0.08	0.13

4.4 Conclusion to fluid-particle coupling and comparison

This section has presented large-eddy simulation results of particle-laden turbulent flow in a horizontal channel. The results generated by the LES for the fluid phase were compared against DNS predictions for shear Reynolds flows of $Re_\tau = 150, 300,$ and 590 . Overall, the LES showed good agreement with the DNS, with the mean velocities and rms of fluctuating velocity components similar to those of the DNS. The particle phase behaviour was also compared with one-way coupled DNS results, with the LPT incorporated in the commercial code giving results that were in reasonable agreement with those derived on the basis of the DNS.

In the rectangular channel flow, fluid turbulence effects govern the dispersion of inertial particles. Shearing at the walls magnify drag, in particular in the wall normal direction, thereby affecting the wall-normal distribution and segregation rate of particles. The fluid turbulence dominates the behaviour of $150 \mu\text{m}$ ($St = 216$) particles, causing them to be distributed throughout the flow. Because of their high inertia however, these particles do not fully track the flow and consequently concentrate at the walls. The results show full coupling, even at very low volume fractions of approximately 10^{-5} , are capable of having some effect on the characteristics of the fluid and particle phase. Moreover, the velocity fluctuations in all three directions were increased.

In terms of the effects of particle agglomeration on the particle velocity statistics, no clear effects were noticed. However, agglomeration does effect the dispersion and segregation near the walls. The concentration and corresponding number of collisions for cohesive particles are less in this region compared to non-cohesive particles. Moreover, the components of $F_{i,coupling}$ are seen to increase with particle surface energy

and the agglomerates are more influenced by the wall normal velocities and their fluctuations which are responsible for particle drift towards and away from the walls. What's more, the largest differences for particle coupling force between the two particles are in regions of high turbulence (buffer layer) and high velocity (outer region), yet again confirming the results of Figure 4.17. Therefore, there is an effect of particle agglomeration on concentration and velocity distribution. It is important to echo that particle agglomeration results in higher inertia; this lowers the ability of agglomerates to track the flow which potentially leads to more collisions and further agglomeration.

5 Sensitivity Studies on Particle Dispersion and Agglomeration

Prior to discussing the results in this section, it is worth noting that the particle runs (intentionally) are not at steady-state aiming, as they are, at understanding the time-dependent agglomeration of particles.

The initial particle positions were distributed randomly throughout the channel, with their initial velocity set to zero and with the particles coming in-line with local flow velocities with time. Particles were assumed to interact with turbulent eddies over a certain period of time, that being the lesser of the eddy lifetime and the transition time. Particles that moved out of the channel were re-introduced into the computational domain using periodic boundary conditions.

All of the particles used in this chapter have identical physical properties (Table 5-1). The surface energy, size and total number of particles considered, with the corresponding particle relaxation times, Stokes number, and other relevant parameters, are given in Table 5-2. All particle sizes, surface energies, concentration, and shear Reynolds numbers used were 150 μm , 0.05 J m^{-2} , 20'000, and 300, unless stated otherwise. Particle and fluid densities were set to $\rho_p = 1000$ and $\rho_f = 1.3 \text{ kg m}^{-3}$, respectively, with the kinematic viscosity $\nu = 15.7 \times 10^{-6} \text{ m}^2 \text{ s}^{-1}$. The shear Reynolds numbers, $\text{Re}_\tau = hu_\tau/\nu$, used in the simulations were 150, 300 and 590 corresponding to bulk Reynolds numbers of $\text{Re}_b \sim 2100, 4200$ and 8260, respectively, based on the channel half height, h .

To ensure the reproducibility of results, the same computational procedure as Chapter 4 has been used in computing particle statistics.

Table 5-1 Particle physical properties

Particle properties	
Shear modulus (MPa)	10
Poisson's ratio	0.25
Friction coefficient (static and rolling)	0.5 and 0.01
Restitution coefficient	0.5

Table 5-2 Fluid and Particle parameters used in the simulations

Variable	St	$\Gamma / \text{J m}^{-2}$	τ_p ($\cdot 10^{-3}$)	d_p / μm	Particle Number	ϕ_p ($\cdot 10^6$)	Re_τ	ρ
Γ	216	0; 0.05; 0.5; 5	61.2	150	20000	28	300	1,000
Re_τ	54; 216; 837	0.05; 0.5	61.2	150	20000	28	150; 300; 590	1,000
ρ	25, 100, 216	0.0; 0.05		102	63607	28	300	250; 1000; 2159
d_p	100; 25	0.05	28.3; 7.11	102; 51	63607; 508850	28	300	1000
ϕ_p	216	0.05	61.2	150	5605; 71489	7.84; 100	300	1000

5.1 Effects of surface energy on particle agglomeration

This section investigates the effects of surface energy on particle agglomeration, four particles of different surface energies have been considered, with the corresponding particle relaxation times, Stokes number and other relevant parameters given in the top row of Table 5-2. The range of implemented surface energies covers non-cohesive particles (0 J m^{-2}), cohesive particles such as those with van der Waals attraction (0.05 J m^{-2}), very cohesive materials, for example when liquid bridges form (0.5 J m^{-2}), and extremely cohesive particles (5 J m^{-2}).

Figure 5.1 shows results for the number of particle contacts in the channel with time. Contacts are the impacts occurring between particles at data write-out points, i.e., the contacts are in progress when the write-out takes place. The contact has an associated force and position that are discrete values. If two particles stay in contact with each other for some time e.g. over four write-out points, four contacts will be stored and each of these may have a different force and position. The results clearly illustrate a general increase in the number of contacts with time due to the effects of flow turbulence in causing particle collisions; furthermore, the rate at which the particles form contacts increases with the particle surface energy, as would be anticipated. Agglomeration is first seen to occur at around $t = 0.001 \text{ s}$; here the particles have increased their velocity to an extent where the flow turbulence now causes particle-particle interactions. Further scrutiny of the results, for all the cases considered, shows that a linear increase in particle contact numbers then continues to about $t = 0.1 \text{ s}$, after which an increasing divergence is seen between the higher (5.0 and 0.5 J m^{-2}) and the lower (0.05 J m^{-2}) surface energy particles. For the 0.05 J m^{-2} particles the rate of contact formation

increases roughly linearly with time after an initial period. In the higher surface energy cases, however, the trend is exponential, indicating an ever increasing rate at which particle contacts form with time. This suggests that there is some mechanism that advantages the higher surface energy particles in the formation of agglomerates, other than the surface energy alone. In regions close to the channel centre, the particles are very dispersed and not likely to come into contact with each other. Therefore, the number of contacts formed is minimal and not significantly different for all surface energies. Towards the channel walls, however, the conditions favour particle agglomeration. In the buffer layer, the particle concentration is again low; nevertheless, the number of contacts formed is proportionally higher for particles of greater surface energy as the flow turbulence is sufficiently high to be effective in causing particle-particle collisions. Near the channel walls, high particle concentrations and low levels of flow turbulence lead to a further increase in the number of contacts formed as the particle kinetic energy is low and therefore ineffective in promoting particle separation after collision. Further analysis would be beneficial in order to quantify the relationship between the particle surface energy, the pull-off force and flow turbulence, and their impact on the formation of successful Van der Waals contacts. The dispersing behaviour of the particles and the regions in which particle contacts are formed is, however, discussed further below. At the end of the simulation ($t = 0.2\text{s}$), and for the 0.05, 0.5 and 5.0 J m⁻² surface energy particles, respectively, there are 265, 789 and 850 particle contacts in the flow. The greater surface energy of the 0.5 J m⁻² particles, as compared to the 0.05 J m⁻² particles, therefore gives rise to almost three times the number of contacts. However, a further increase of one order of magnitude in the surface energy to 5.0 J m⁻² does not result in an equivalent increase. This is indicative of the surface energy value nearing a threshold; hence, any further increase does not dramatically enhance particle agglomeration. From the above analysis, it is clear that the effects of flow turbulence are dominant in creating particle contacts, and that the particle surface energy is likewise a key factor in determining Van der Waals-induced particle agglomeration in the flow.

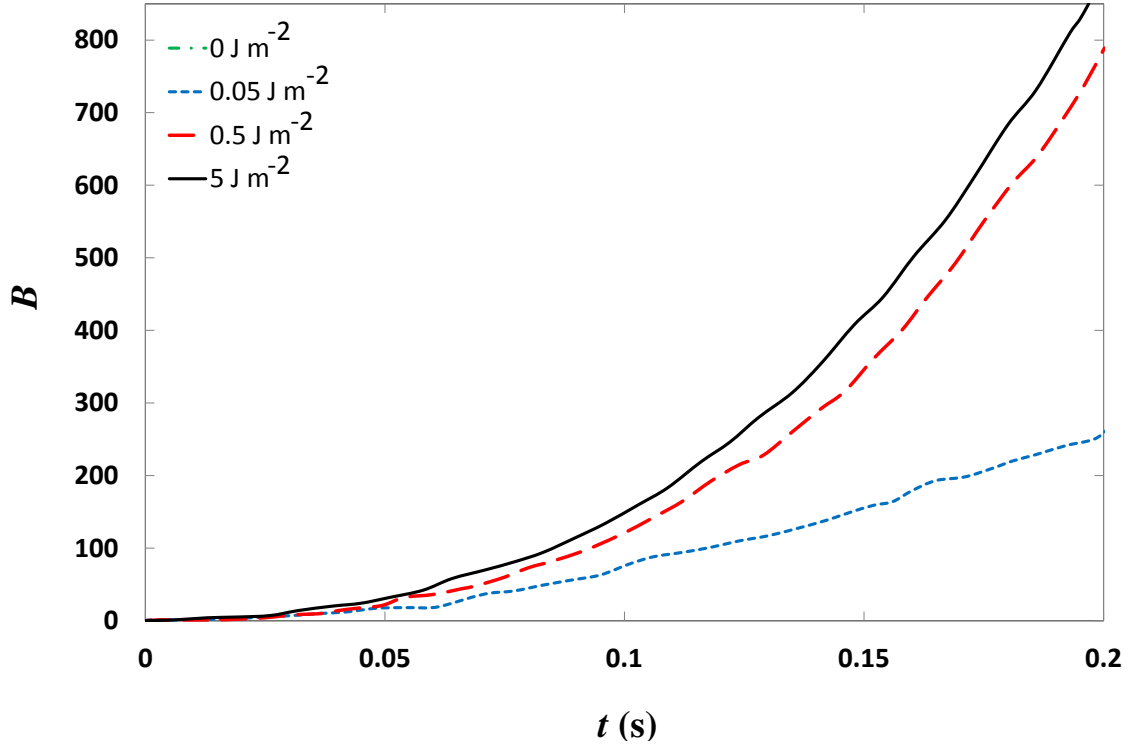


Figure 5.1. Number of contacts formed between particles, B , with time, t , for variations in particle surface energy

Figure 5.2 (a-c) shows the time dependent number of particles within the agglomerates, for all particle surface energies considered. The values have only been calculated for nine data outputs, and are therefore only representative of those time steps. In general, the number of single particles decreases gradually with time as the number of agglomerates increase within the simulation. For the single particles, there are initially 20,000, but this value begins to decrease at approximately $t = 0.015$ s in all cases and then follows a rapidly decreasing trend to 19,477 (for the 0.05 J m^{-2} surface energy particles), 18,667 (0.5 J m^{-2}) and 18,444 (5.0 J m^{-2}) at $t \approx 0.2$ s. It is clear that the rate of decline of the single particles increases with surface energy. The number of agglomerates is also inversely proportional to the number of single particles, with these agglomerates forming first at $t = 0.015$ s and increasing in number to final values of 260, 638 and 738 for the low, medium and high surface energy particles, respectively, at $t \approx 0.2$ s. In all cases the majority of the agglomerates are also duplets. For the low surface energy particles the triple and quadruple particle agglomerates first appear at $t = 0.105$ and 0.185 , although there are only 3 and 0 present in the channel, respectively, at the end of simulation due to particle agglomeration and breakage. The medium surface

energy particles first form triple, quadruple and quintuple agglomerates at $t = 0.105$, 0.075 and 0.135 , which increase to values of 30, 12 and 1 over the course of the simulation. Lastly, for the high surface energy particles the triple, quadruple, quintuple and sextuple particle agglomerates first appear at $t^+ = 0.105$, 0.105 , 0.165 and 0.185 and finish with values of 41, 10, 5 and 0 at $t = 0.2$ s. Over the simulation time considered, there are always far more double particles as compared to triple and larger agglomerates, and this difference was seen to increase further with time, with a longer simulation time clearly required before significant numbers of triple and larger particle agglomerates can be formed. Moreover, the higher surface energy particles show a greater propensity to form larger agglomerates in the time frame considered, as might be anticipated. This indicates that the stronger contacts between higher surface energy particles are more resistant to the effects of fluid drag, allowing larger particle chains to form in the system. Based on these trends, it is clear that with time the number of agglomerates and the size of the agglomerates will continue to increase, and that this will be greatest for the higher surface energy particles.

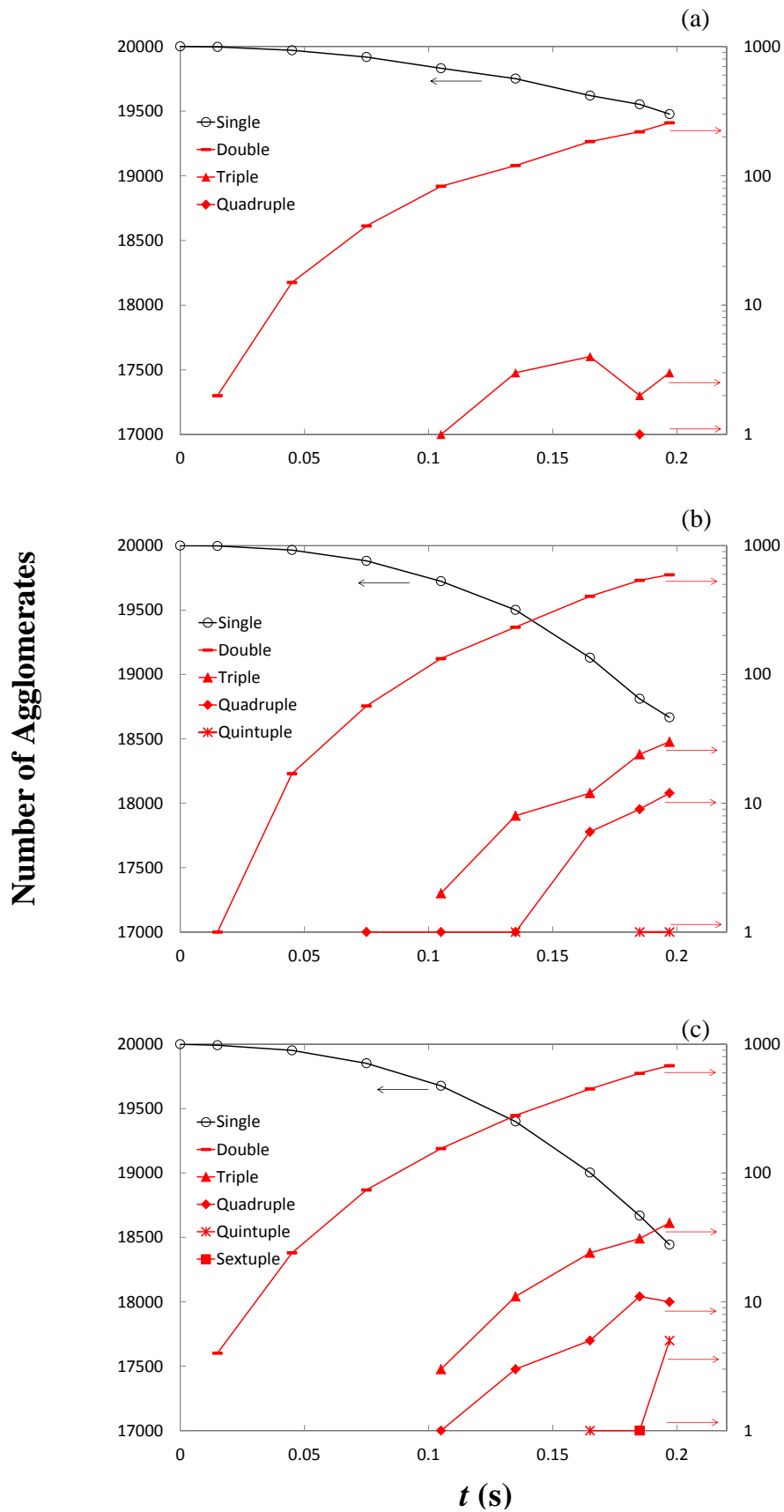


Figure 5.2. Variation of number of particle agglomerates with time, t , for surface energies of (a) 0.05 Jm^{-2} ; (b) 0.5 Jm^{-2} ; and (c) 5 Jm^{-2} . Black line: single particles; red lines: agglomerates.

Figure 5.3 shows the relationship between the instantaneous position of the particles and agglomerates in the wall-normal direction for all three particle surface energies, and their number in this direction at $t = 0.075, 0.135$ and 0.2 s. Results are shown for eight equally-spaced regions across half the channel height, with particle statistics combined within each of the regions of fluid considered. The location of each region of fluid is represented by a column and plotted in relation to the channel walls, where column 1 is the region adjacent to the upper and lower walls; these particular regions have a width that stretches over 38 wall units covering the viscous sub-layer ($y^+ < 5$) and the buffer layer ($5 < y^+ < 30$) within the near-wall region. The results show a general movement of particles and agglomerates (or particle count) towards the walls with time, indicated by column 1 which accounts for over $1/5^{\text{th}}$ of the total particle count by $t = 0.2$ s. Closer examination of the results reveals two opposing trends; a steady decrease in particle number from the centre of the channel (column 8) towards the walls up to and including region 2, followed by a dramatic increase in particle count adjacent to the walls. This indicates that particle numbers at the walls are directly related to the momentum of the particles prior to wall impact, such that higher velocity particles located in the centre of the channel move towards the walls but rebound off them with a high velocity, then travelling back into the central region of the channel. In contrast, particles that move towards the walls with a lower velocity have less momentum and after impact with the wall become entrained in the near-wall region.

Focusing on the agglomerates, the results clearly show an increase in their number towards the walls of the channel with time. For the lowest surface energy particles, at the channel centre, the fraction of the number of agglomerates to the total particle count is 0.00, 0.002, and 0.01 for times $t = 0.075, 0.135$ and 0.2 s, respectively, although these values are seen to increase towards the walls, where for the regions adjacent to the wall they increase to 0.005, 0.009 and 0.018. For the medium surface energy particles, at the channel centre, the fraction of the number of agglomerates to the total particle count is 0.00, 0.003 and 0.012 for times $t = 0.075, 0.135$ and 0.2 s, respectively, and for region 1 this value increases to 0.008, 0.028 and 0.066. When compared with the 0.05 J m^{-2} particles, the latter values are slightly higher at the channel centre and significantly higher at the walls. Lastly, for the highest surface energy particles, at the channel centre the fraction of the number of agglomerates to the total particle count is 0.00, 0.0038 and 0.007 for times $t = 0.075, 0.135$ and 0.2 s, respectively, with these values similar to

those observed for the 0.5 J m^{-2} particles. However, the rate of increase in the number of agglomerates close to the walls is seen to be higher; in region 1 these values are 0.013, 0.038 and 0.074 at the times noted.

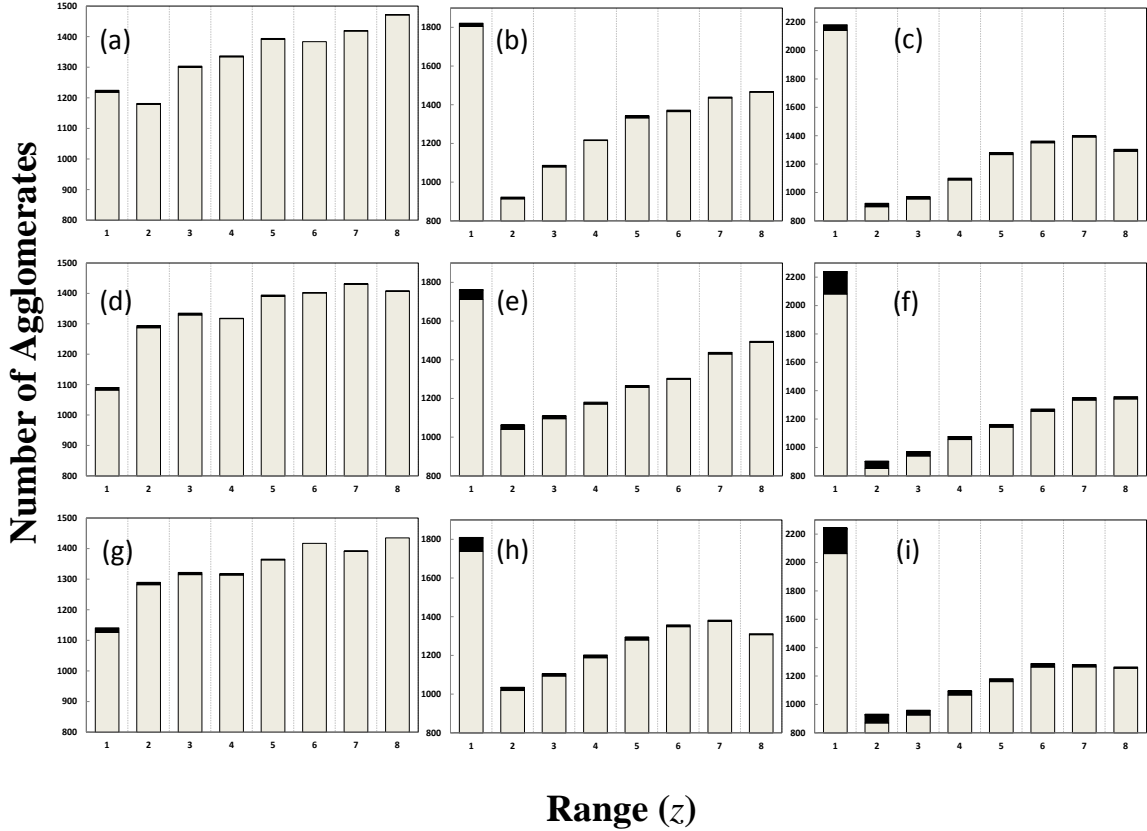


Figure 5.3. Agglomerate number distribution across the channel height for 0.05 J m^{-2} surface energy particles at (a) $t = 0.075$; (b) $t = 0.135$; and (c) $t = 0.2 \text{ s}$, for 0.5 J m^{-2} at (d) $t = 0.075$; (e) $t = 0.135$; and (f) $t = 0.2 \text{ s}$, and for 5 J m^{-2} at (g) $t = 0.075$; (h) $t = 0.135$; and (i) $t = 0.2 \text{ s}$ (□ single, ■ double-sextuple agglomerates).

The number of agglomerates also increases uniformly towards the walls, in contrast to the total number count, with the exception of the final near-wall regions where significantly increased numbers are found. Therefore, depending on the location of the agglomerates relative to the wall, two different mechanisms are responsible for their formation. Particle agglomeration near to the wall is therefore attributable to the high particle concentration in these regions, with the regions closest to the walls showing the highest particle count and number of agglomerates. In the remaining regions, particle agglomeration is enhanced in high fluctuating fluid velocity fields which lead to a high number of particle-particle interactions. These velocity fluctuations are typically at a

maximum 30 wall units away from the solid boundaries. This influence is indicated by the results for region 2, which contains the lowest particle count and yet the highest agglomerate number (bar those regions closest to the walls). It is important to mention that the simulations have not reached equilibrium and all of the results show a dynamic state of agglomeration.

Figure 5.4, shows the instantaneous location of individual particles and contacts B in the wall-normal direction for all cases given in the first row of Table 5-2 and their number n_p at each location, at time $t = 0.2$ s. This plot is more refined than those above; results are shown for equally spaced regions across half the channel height that are equivalent in size to the particle radius, with particle statistics combined within each of the bins of fluid considered. It is clear that the increase in contact number does not lead to an increase in particle number at those locations. As discussed above, generally the number contacts increases towards the walls and this is amplified with surface energy. In Figure 5.4 however, there is a sharp decrease in the number of particles and contacts at the wall. This is due to a low fluid velocity in that region which decreases the frequency of particle interactions. Comparing the number of contacts in regions of the channel that are characterised by different flow behaviour, starting close to the channel centre, ($250 < z^+ < 300$), the results show that the number of contacts is 12, 22 and 18, respectively, with these values increasing towards the walls, where for the buffer layer ($5 < z^+ < 30$) and viscous sub layer ($z^+ < 5$) regions they increase to an average of 28, 112 and 104, and 9, 46 and 69, respectively. Therefore, based on the total number of particle contacts present in those regions, particle agglomeration at the channel centre ($250 < z^+ < 300$) is highest for the medium surface energy particles, whereas close to the walls agglomeration is highest for the highest surface energy particles ($z^+ < 5$). Further away from the walls ($5 < z^+ < 30$) it is highest again for the medium surface energy particles. These results indicate, therefore, that particle surface energy is important in the formation of particle-particle contacts, as might be anticipated, although less effective in resisting contact breakage due to the effects of flow turbulence. This is due to flow turbulence increasing the pull-off force of the higher surface energy particles leading to their separation.

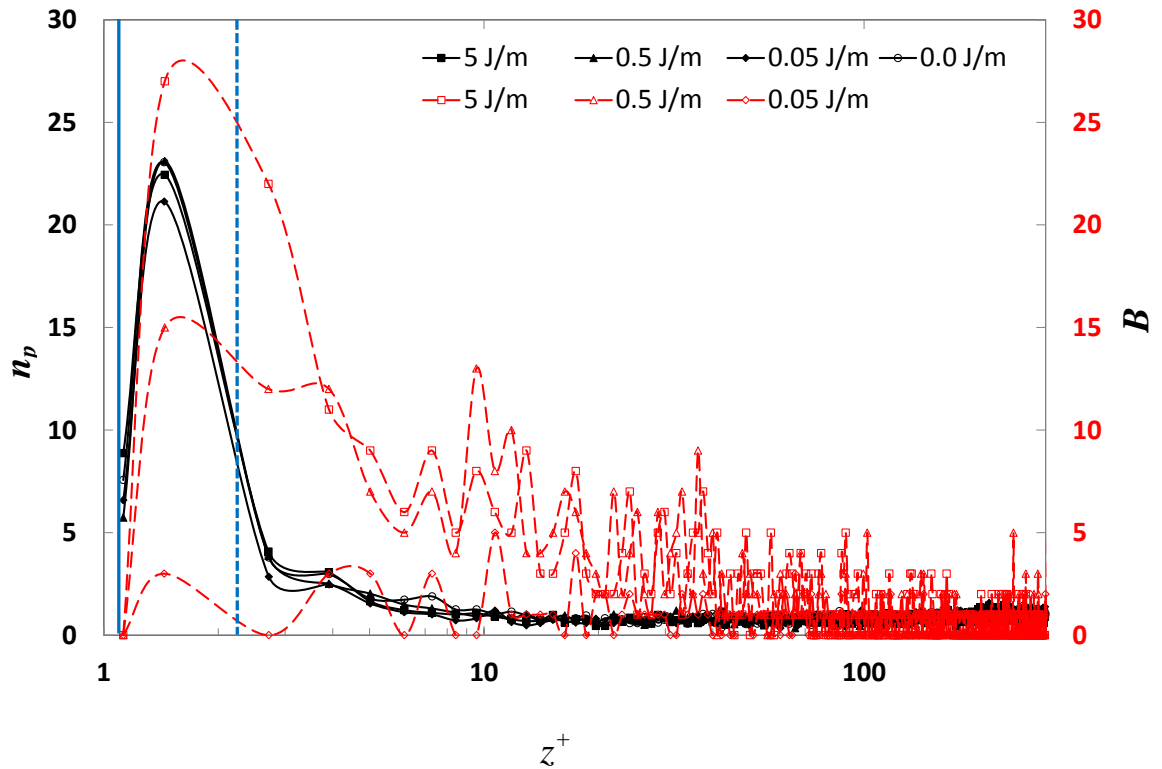


Figure 5.4 Particle local concentration, n_p , and particle-particle contact, B , number density profiles across the channel for variations in surface energy ($t = 0.2s$). The vertical solid blue line indicates the position of contact between the particles and wall (impact); the vertical dashed line gives a visual indication of the particle size in wall units (d_p^+).

It is important to highlight that not all particle-particle interactions lead to the formation of agglomerates. The contact forces between colliding particles are based on the concept of contact mechanics, which takes plastic deformation of particles into consideration. In the work presented only elastic deformation occurs, since the maximum stress does not reach the yield strength of the colliding particles (Bitter, 1963). The numerical model in EDEM predicts the critical sticking and removal velocities, which are important parameters in determining the formation of agglomerates. During the collision of particles a normal contact force F_n and a tangential contact force F_t are developed. The normal contact force acts in line with the particle centre of the colliding particles while the tangential contact force acts perpendicularly to the centre (see Figure 3.2). The contact force is defined by the collision phase and the relative velocity of the colliding particles. Collision between particles can be divided into two consecutive phases, the approach and the restitution phase. The approach phase ends when the two bodies have

a relative normal velocity equal to zero as a result of impact. According to Thornton and Ning (1998) the work required to break the contact between two particles is given by,

$$W_e = 7.09 \left(\frac{\Gamma^5 R^{*4}}{E^{*2}} \right)^{1/3} \quad 5-1$$

If energy losses due to elastic wave propagation are neglected, the only work dissipated during a collision is the work done in separating the surfaces, W_e . Therefore,

$$W_e = \frac{1}{2} m^* v_i^2 - \frac{1}{2} m^* v_r^2 \quad 5-2$$

If the rebound velocity ($v_r = 0$) then the impact velocity $v_i = v_s$, accounting for the coefficient of restitution, e , the critical velocity below which sticking occurs from Equations 5-1) and 5-2), the sticking criterion becomes,

$$v_s = \frac{1}{e_1 e_2} \left(\frac{14.18}{m^*} \right)^{1/2} \left(\frac{\Gamma^5 R^{*4}}{E^{*2}} \right)^{1/6} \quad 5-3$$

If $v_i > v_s$ then bounce occurs and Equation 5-2 may be written as,

$$1 = \left(\frac{v_r}{v_i} \right)^2 = \left(\frac{v_s}{v_i} \right)^2 \quad 5-4$$

The sticking velocity has been calculated using Equation 5-3 and values are shown in Table 5-3.

Surface Energy (J m^{-2})	0.05	0.5	5
Sticking Velocity (m s^{-1})	0.35	2.39	16.3

Figure 5.5 shows number of particle collisions and the corresponding normal component of the impact (relative) velocity for the four different surface energy particles 0.05, 0.5, and 5 J/m² between time $t = 0.19 - 0.2$ s. Collisions are complete impacts, when two particles collide it will register as one collision, regardless of how long the elements stay in contact for. The data is collected for the duration of the collision (e.g. total energy loss and normal force data). Collisions may occur in between write-outs and never register as contacts. The impact velocity normal of two particles in a collision is $v_{r1} - v_{r2}$; this value is calculated from the contact points and not the particle centres. The impact velocity is based on the physical properties of the particles in the flow which are identical in all four simulations, for that reason the results have only been shown for one of the cases (0.0 J/m²). In agglomerating systems the magnitude of the impact velocities may decrease until a steady state is reached total contact number. The data sampling should ideally start from this point onwards to be fully representative of the quantitative differences. However, this requires long run times and would not contribute considerably to this analysis. As can be seen in Figure 5.5 the impact velocities range from less than 0.002 m/s to a maximum of 3.1 m/s The velocity regions in which sticking occurs have been highlighted for different surface energies. Based on these cut-off points the number of successful collisions are 49, 188, and 193 for the 0.05, 0.5 and 5 J/m², respectively. Increasing the particle surface energy by one order of magnitude from 0.05 to 0.5 J/m², therefore results in almost an 8 fold increase in contact number. However, a further increase by the same order of magnitude to 5 J/m² only gives rise to approximately 2 times the number of contacts. This is because the number of collisions does not increase linearly with approach velocity. Moreover, it is seen that for a surface energy of 5 J/m², bounce cannot occur after collision; thus, any further increase will not result in the formation of additional contacts. From this analysis it is clear that the number of contacts formed is a function of the number of collisions in relation to the sticking velocity between the particles. To further understand the extent to which particle surface energy effects the mechanisms of particle agglomeration and dispersion, it would be beneficial to analyse in detail the contact breakage and post collision energies. This has not yet been carried out (as it is beyond the scope of this work) but can be looked up on as feasible extension to this analysis. The understanding of the data needs to be interpreted with this in mind.

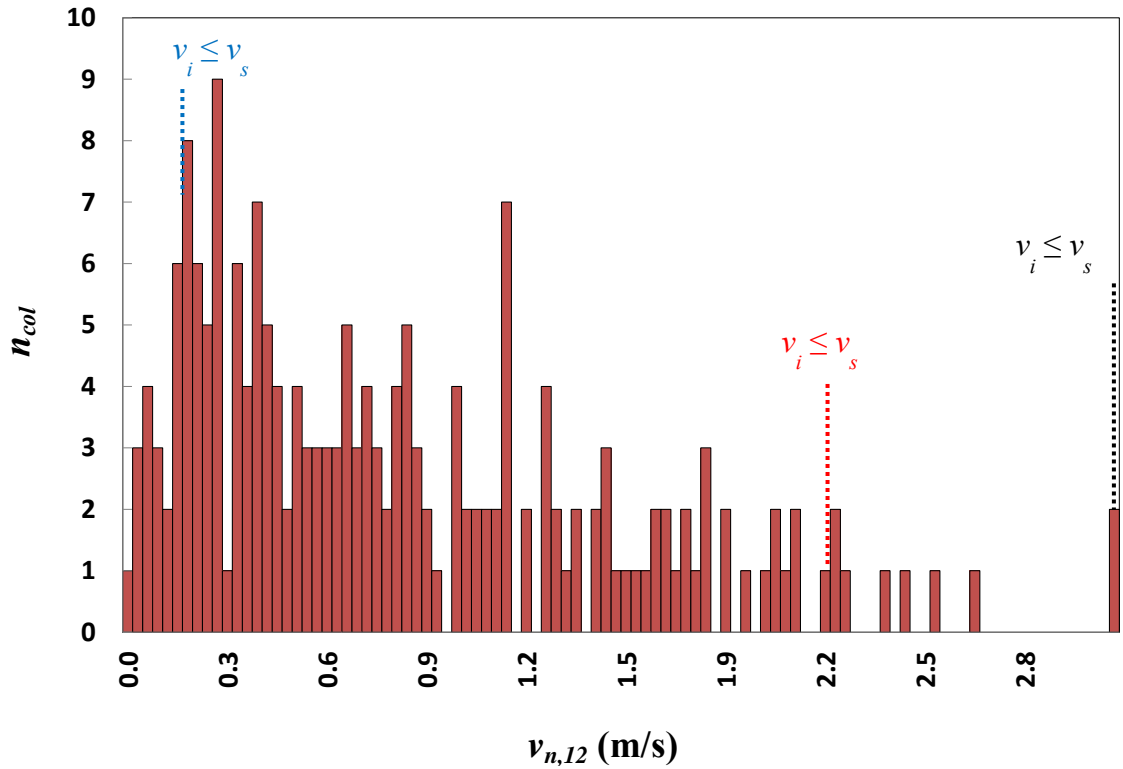


Figure 5.5 Number of particle collisions, n_{col} , and their relative velocity normal, $v_{n,12}$, for $Re_\tau = 590$ ($t = 0.19 - 0.2$ s). The vertical dotted blue, red, and black lines indicate the maximum sticking velocity for 0.05 , 0.5 and 5 J m^{-2} particles, respectively.

Figure 5.6 shows the time evolution of the maximum value of the particle number density, n_p^{max} , near the wall. The rationale for monitoring this quantity lies in the fact that the concentration close to the wall is the one that takes longest time to reach a steady state. The results clearly show that, starting from an initial distribution corresponding to a flat profile centered around $n_p^{max} = 1$, the particles accumulate at the walls at an approximately linear rate. The behaviour observed in Figure 5.6 is also consistent with previous LES and DNS results where turbophoresis is known to cause the accumulation of particles in near-wall regions, which in the present flow also enhances the rate of particle agglomeration in such regions.

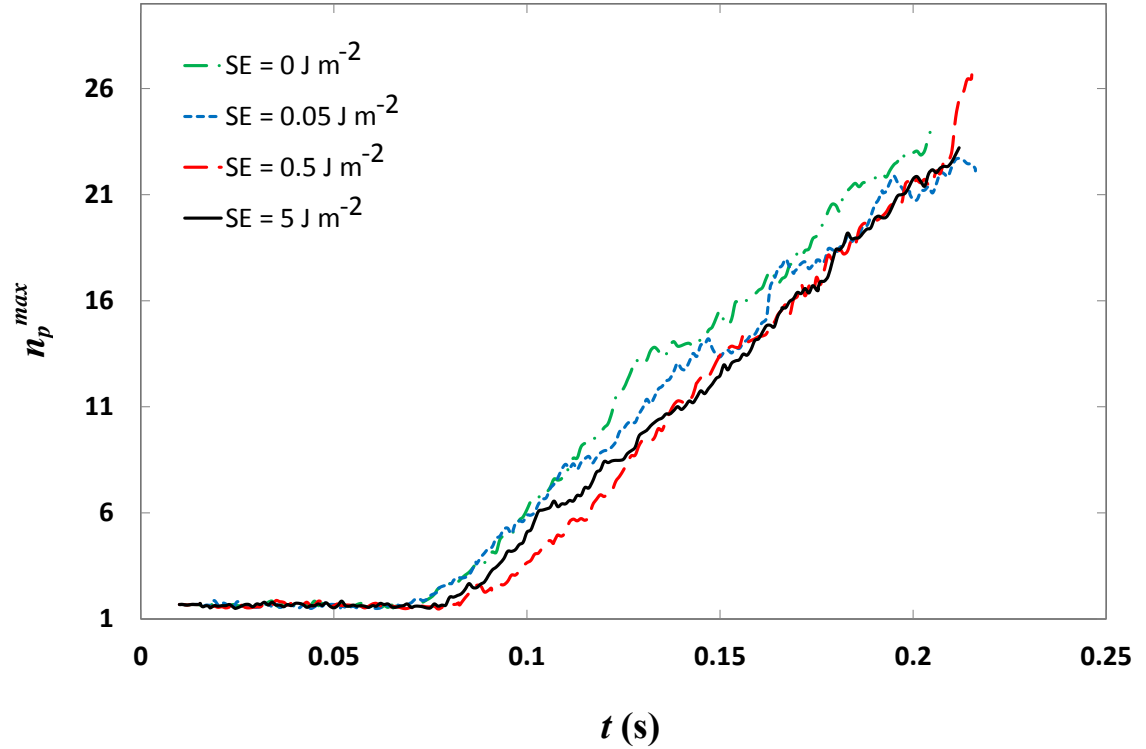


Figure 5.6. Maximum value of particle number density, n_p^{max} , at the wall as a function of time, t , for variations in surface energy.

5.2 Effects of Reynolds number on particle agglomeration

This section investigates the effects of turbulence on particle agglomeration, three different flow Reynolds numbers have been considered, these include $Re_\tau = 150$, 300 and 590. The particles with 0.05 and 0.5 $J m^{-2}$ surface energies have greater practical relevance and were therefore selected for further study, with the corresponding particle relaxation times, Stokes number and other relevant parameters given in the second row of Table 5-2.

Figure 5.7 shows the formation of particle contacts, for the three different flow Reynolds numbers. For all three shear Reynolds numbers containing 0.05 $J m^{-2}$ particles, initially the rate at which the particles form contacts increase linearly with Reynolds number. Further scrutiny of the results shows that agglomeration first occurs at $t \approx 0.005$, 0.001 and 0.003 s for the $Re_\tau = 150$, 300 and 590 flows, respectively, indicating a slower acceleration of the particles in the $Re_\tau = 150$ flow. The number of contacts formed in the $Re_\tau = 590$ flow is seen to diverge from the lower Reynolds

number flows and peaks at $t \approx 0.170$ s, after which the rate of contact formation declines slightly. However, this change in the rate of contact formation is not seen for the $Re_\tau = 150$ and 300 flows. Eventually, the contact numbers for the $Re_\tau = 300$ and 150 flows surpass that of the $Re_\tau = 590$ flow at $t \approx 0.162$ and $t \approx 0.197$ s, respectively. At the end of the simulation, and for the $Re_\tau = 150$, 300 and 590 flows, there are 215, 229 and 207 particle contacts, respectively. This behaviour suggests that the higher flow turbulence in the $Re_\tau = 590$ case is responsible for creating a larger number of particle-particle interactions compared to the $Re_\tau = 300$ and 150 flows. The subsequent decline in the rate of particle contact formation for the $Re_\tau = 590$ case is then indicative of an increase in the rate of particle contact breakage. This behaviour can be attributed to the initial conditions; as the particles accelerate and their velocity comes in line with that of the fluid, the greater flow turbulence causes the particles to encounter more fluid resistance (due to the drag forces acting in the opposite direction to the relative motion of the particle moving with respect to the surrounding fluid), with this increased resistance responsible for the increased rate of particle contact breakage in the higher Reynolds number flow.

For 0.5 J m^{-2} particles, the results clearly show an increase in the number of contacts with time due to the effects of flow turbulence on the particles; however, the rate at which the particles form contacts increases with the flow Reynolds number throughout the simulation. For all three shear Reynolds numbers, initially the rate of contact formation increases roughly linearly with time but then changes to an exponential profile. This is most apparent for the higher shear Reynolds number case. Agglomeration is first seen at approximately $t = 0.001$ s for the 300 and 590 Reynolds number flows and at $t = 0.01$ s in the case of the 150 Reynolds number flow. Here the particles have increased their velocity to an extent where the flow turbulence now causes particle-particle interactions. A linear increase in particle contact numbers then continues to about $t = 0.05$ s, after which an increasing divergence is seen between the various Reynolds number flows. As for the results of

Figure 5.1, this behaviour indicates a mechanism within the flow that advantages the particles exposed to higher Reynolds numbers in the formation of agglomerates. This occurs as a result of regions of high particle concentration and low particle mean velocity near the channel walls; in such regions the number of contacts formed is

proportionally higher for particles of higher Reynolds number as the particles migrate to these regions at a faster rate. Moreover, the increased shear in the high Reynolds number flows increases the intensity of these turbulent regions, and therefore the particle fluctuations and hence their interactions. Further analysis is desirable to establish a quantitative relationship between the particle fluctuating velocity and its impact on the formation of successful contacts. This along with the dispersing behaviour of the particles and the regions in which contacts are formed are discussed further below. For the $Re_\tau = 150, 300$ and 590 flows, respectively, there are 528, 635 and 1524 particle contacts in the flow at the end of the simulation. These figures further reflect that increases in the flow Reynolds number dramatically enhance turbulence, and as a result particle agglomeration. It is thus again clear that the effects of turbulence are significant in creating successful particle-particle contacts, and that the flow Reynolds number is a key factor in determining particle agglomeration.

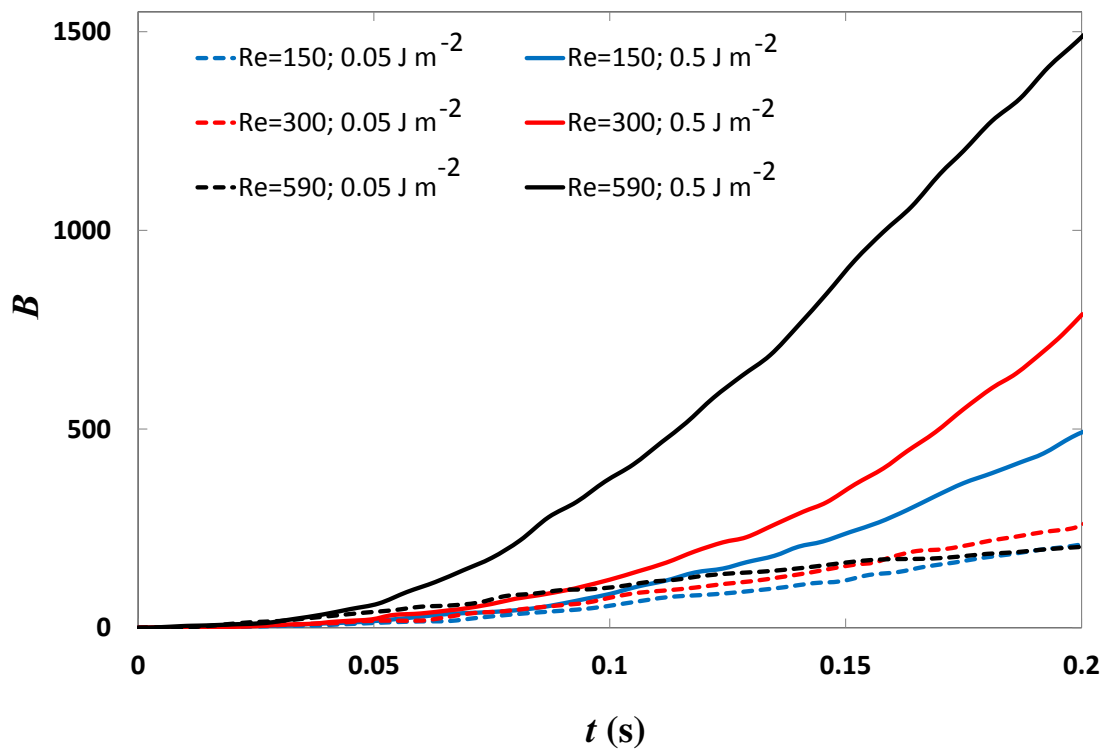


Figure 5.7 Number of contacts, B , formed between particles with time, t , for variations in flow Reynolds number.

Figure 5.8 (a-f) shows the instantaneous location of individual particles and contacts in the wall-normal direction for all cases given in the second row of Table 5-2, and their

number at each location, at time $t = 0.2$ s. Results are shown for 50 equally spaced regions across half the channel height, with particle statistics combined within each of the slabs of fluid considered. The columns for the number of contacts are plotted in relation to the channel walls, with column 1 adjacent to the lower and upper walls and column 50 at the channel centre. The effect of flow Reynolds number on particle agglomeration for low surface energy (0.05 J m^{-2}) particles is considered in the results for three Re_τ ; 150 (Figure 2(a)), 300 (Figure 2(b)) and 590 (Figure 2(c)). The results show a general movement of particles towards the walls and that for low surface energy particles, the level of turbulence in the $Re_\tau=300$ flow is the most effective in forming particle agglomerates. In the case of the medium surface energy (0.5 J m^{-2}) particles for $Re_\tau=150$ (Figure 2(d)), 300 (Figure 2(e)) and 590 (Figure 2(f)), overall, the results show a general movement of particles and also agglomerates towards the walls, indicated by columns 1 to 7 accounting for approximately 60% of the total particle contact count at all Re_τ . For $Re_\tau = 150, 300$ and 590 , around the channel centre (columns 47 to 53) the number of contacts is 20, 18 and 47, respectively, with these values increasing towards the walls, where for columns 1 to 7 they increase to total of 129, 203 and 249, respectively. In all three cases, particle agglomeration near to the wall can be attributed to the high particle concentration and the high turbulence levels in this region. Further scrutiny of the results shows that for the high Reynolds number flow, particle agglomeration is roughly double that of the other flows at the channel centre. This relationship also holds between the high and low Reynolds number flows close to the channel walls, although the number of agglomerates at $Re_\tau = 300$ is relatively closer to that of the $Re_\tau = 590$ case. The particle behaviour reflects the higher turbulence levels in the 590 flow, which drives the particles to regions of lower fluid velocity. Throughout the $Re_\tau=590$ flow, particle agglomeration is enhanced through high fluctuating velocities which affect a high number of particle-particle interactions, with peak levels approximately 30 wall units away from the solid boundaries. This effect is therefore most evident in the results for columns 2 and 3, which contain the highest agglomerate number, excluding those regions closest to the walls where particle concentrations are high. These results indicate, therefore, that flow Reynolds number is important in the formation of particle-particle contacts for high surface energies, as might be anticipated. Although, less effective for lower surface energies because of an increase in contact breakage due to the effects of flow turbulence.

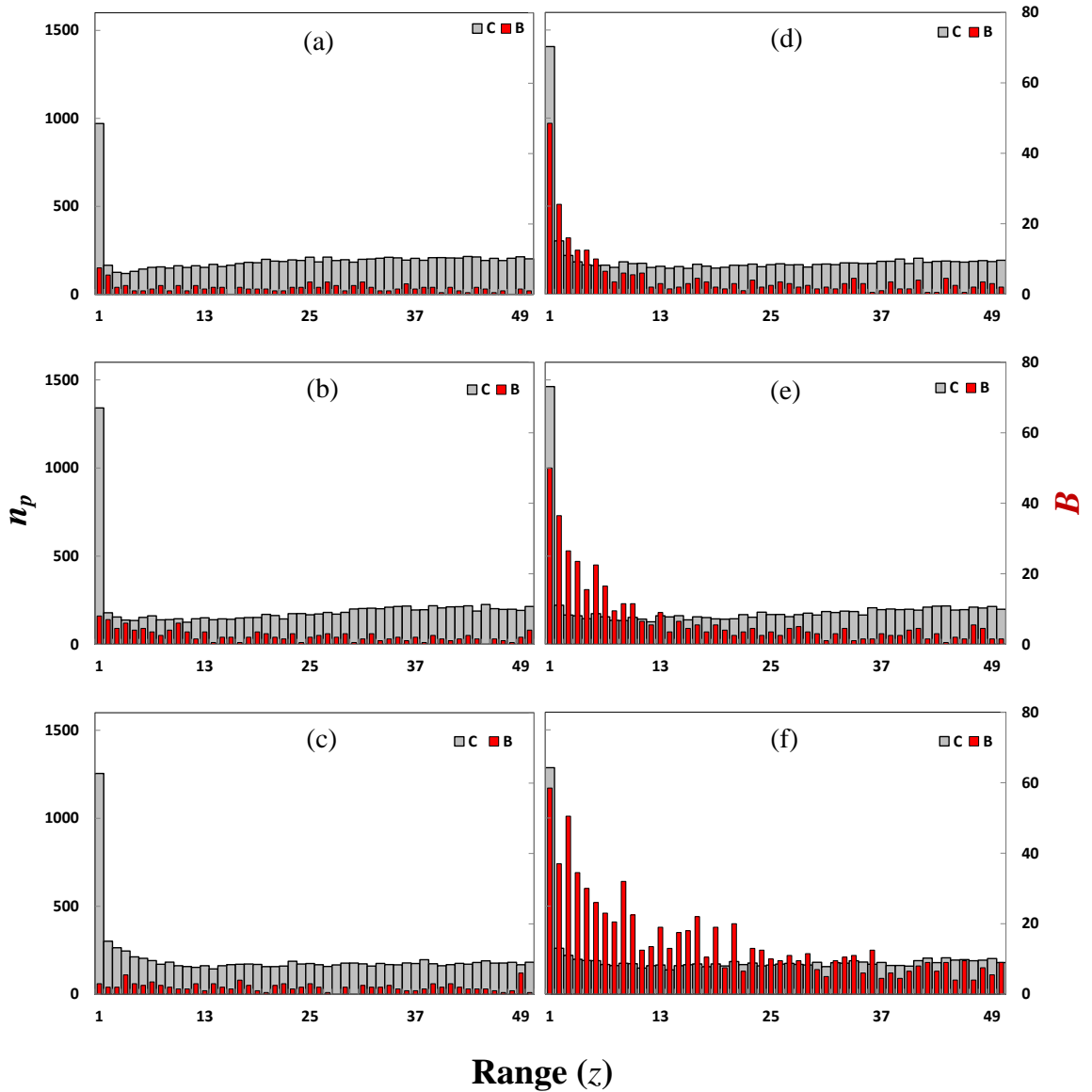


Figure 5.8 Particle contacts, B , and local concentration, n_p , distribution across the channel at $t = 0.2$ s for (a) $Re_\tau = 150$; 0.05 J m^{-2} , (b) $Re_\tau = 300$; 0.05 J m^{-2} , (c) $Re_\tau = 590$; 0.05 J m^{-2} , (d) $Re_\tau = 150$; 0.5 J m^{-2} , (e) $Re_\tau = 300$; 0.5 J m^{-2} , (f) $Re_\tau = 590$; 0.5 J m^{-2}

Figure 5.9 shows the instantaneous location of individual particles and contacts B in the wall-normal direction, and their number n_p at each location, at time $t = 0.2$ s. These plots are more refined than those above; results are shown for equally spaced regions across half the channel height that are equivalent in size to the particle radius. As already mentioned, generally the number of particles and contacts increases towards the walls. In the results of Figure 5.9 (a,b) however, a sharp decrease is seen in the number of particles and contacts at the wall. Further scrutiny of the results shows that the point at which particles and contacts accumulation peaks for the $Re_\tau = 150$, is further away from the wall compared to the other two flows. This is related to the fact that the

streamwise fluid velocity gradient is less steep towards the walls resulting in a wider boundary layer and the amplitude of the wall-normal turbulence intensity is lower.

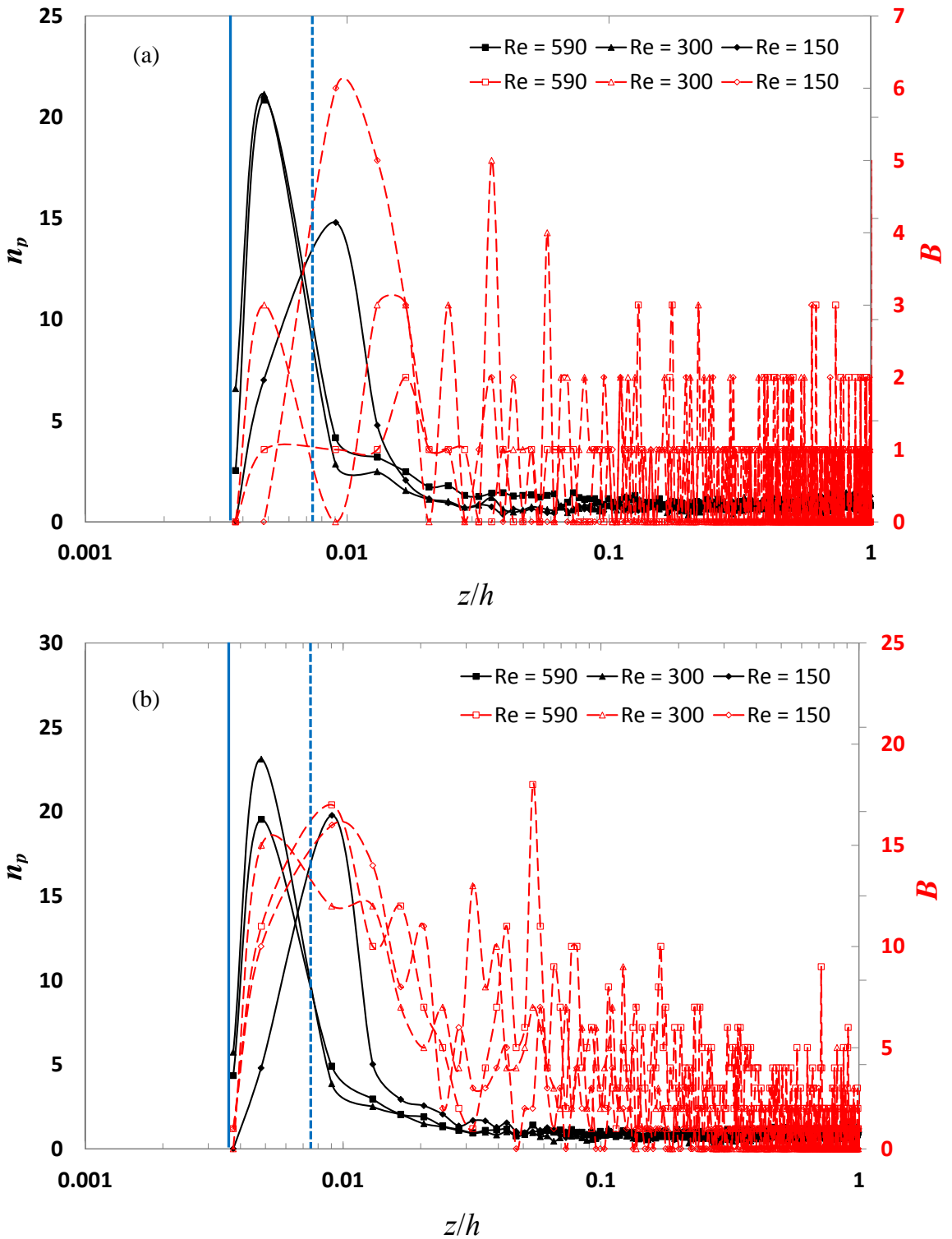


Figure 5.9 Particle number n_p and particle-particle contact number B density profiles across the channel at $t = 0.2\text{s}$ for (a) 0.05 J m^{-2} and (b) 0.5 J m^{-2} . The vertical solid blue line indicates the position of contact between the particles and wall (impact); the vertical dashed line gives a visual indication of the particle size in wall units (d_p^+).

Figure 5.10 shows the number of particle collisions and corresponding normal component of the relative (impact) velocity for $Re_\tau = 590$, between time $t = 0.19 - 0.2$ s. The relative velocity is based on the physical properties of the particles in the flow which are identical for all simulations, for that reason the results have only been shown for one of the cases (0.05 J/m^2). In Figure 5.10 the relative velocities range from less than 0.1 m s^{-1} to a maximum of 7.1 m s^{-1} . The velocity regions in which sticking occurs have been highlighted for different surface energies. Based on these cut-off points the number of successful collisions are 15, 227, and 317 for the 0.05 , 0.5 , and 5 J/m^2 particles, respectively. Increasing the particle surface energy by one order of magnitude from 0.05 to 0.5 J/m^2 , therefore results in a 55 fold increase in contact number. However, a further increase by the same order of magnitude to 5 J/m^2 only gives rise to approximately 5 times the number of contacts. This is because the number of collisions does not increase linearly with approach velocity. Furthermore, it is seen that for low surface energy particles (0.05 J/m^2), the number of collisions within the range required for sticking is very low compared to the higher surface energy particles (0.5 and 5 J/m^2) and narrates the low number of agglomerates formed.

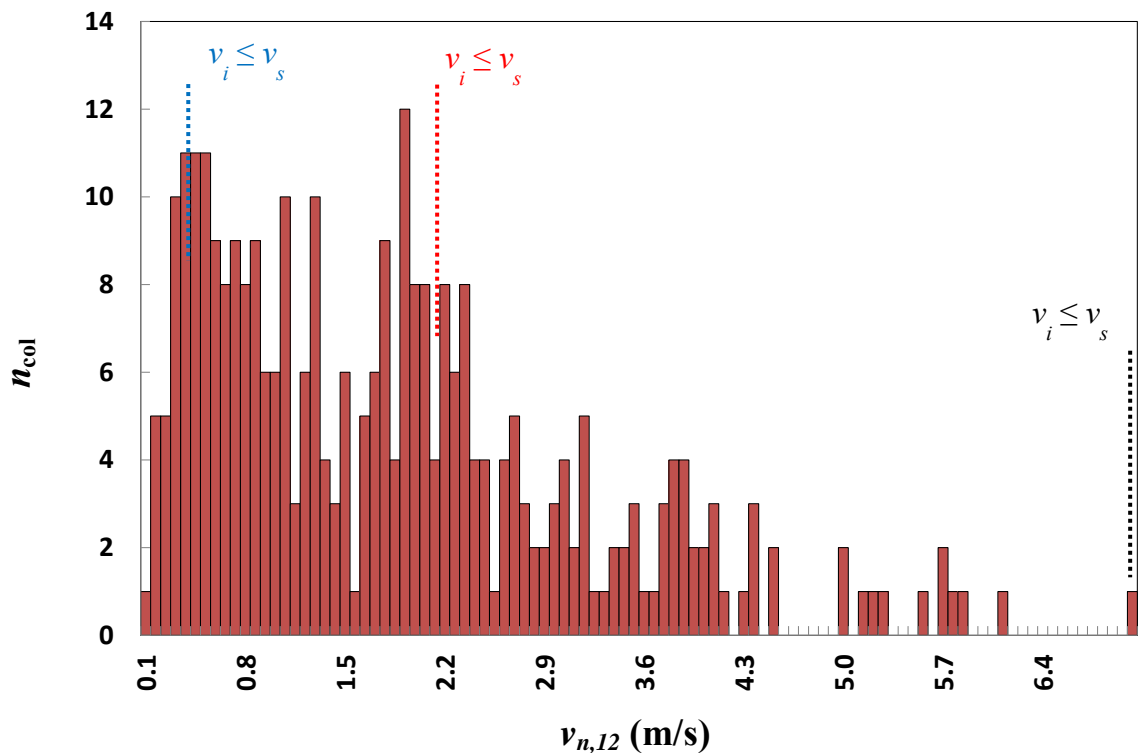


Figure 5.10 Number of particle collisions, n_{col} , and their relative velocity normal, $v_{n,12}$, for $Re_\tau = 590$ ($t = 0.19 - 0.2$ s). The vertical dotted blue, red, and black lines indicate the maximum sticking velocity for 0.05 , 0.5 , and 5 J m^{-2} particles, respectively.

Figure 5.11 shows V_x for all three shear Reynolds numbers, it is clear that the fluid mean velocity increases with flow Reynolds number. Figure 5.12(a-c) show the relationship between the instantaneous particle position in the wall-normal direction for all three Reynolds numbers, plotted against the particle fluctuating velocity magnitude in the wall-normal, spanwise, and streamwise directions, respectively, at time $t = 0.2$ s. The locations of the points are plotted relative to the lower wall. In the regions closest to the walls, the resultant of particle velocity fluctuations $V'_{i,rms}$ show peak values of approximately 0.2, 0.3 and 0.8 m s^{-1} with increasing Reynolds number. These results clearly illustrate the dramatic increase in fluctuating velocities with Reynolds number in regions where preferential agglomeration occurs. In the next zones moving away from the walls ($z/h = 0.01 - 0.11$), the peak fluctuating velocities (resultant) are about 0.4, 0.8, and 1.8 m s^{-1} . The range in particle velocity fluctuations in the highest Re_τ case demonstrates the significant influence of flow turbulence on particle agglomeration in both these regions. Relating the results of Figure 5.11 and Figure 5.12, the findings of section 5.1, the difference in particle agglomeration between the various Reynolds numbers in the latter zones can be attributed to a combination of both the particle mean velocity and the particle velocity fluctuation. Finally, at the channel centre, the particle velocity fluctuation peak values are 0.35, 0.7 and 0.8 ms^{-1} , for $Re_\tau = 150, 300$ and 590. In this region the fluctuations are seen to be low, thereby explaining the lower levels of particle agglomeration.

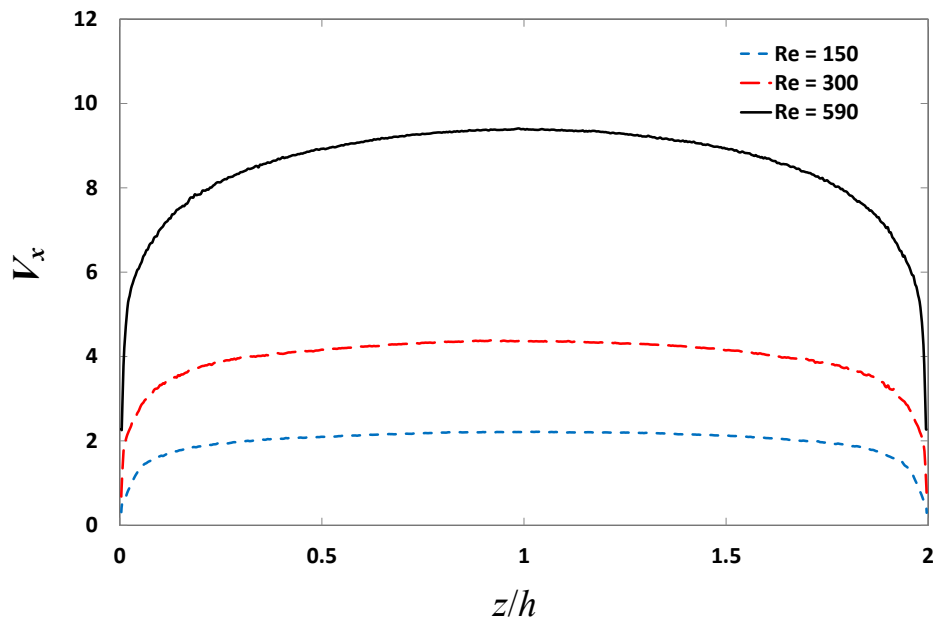


Figure 5.11 Mean streamwise particle velocity, V_x , as a function of the non-dimensional distance to the wall

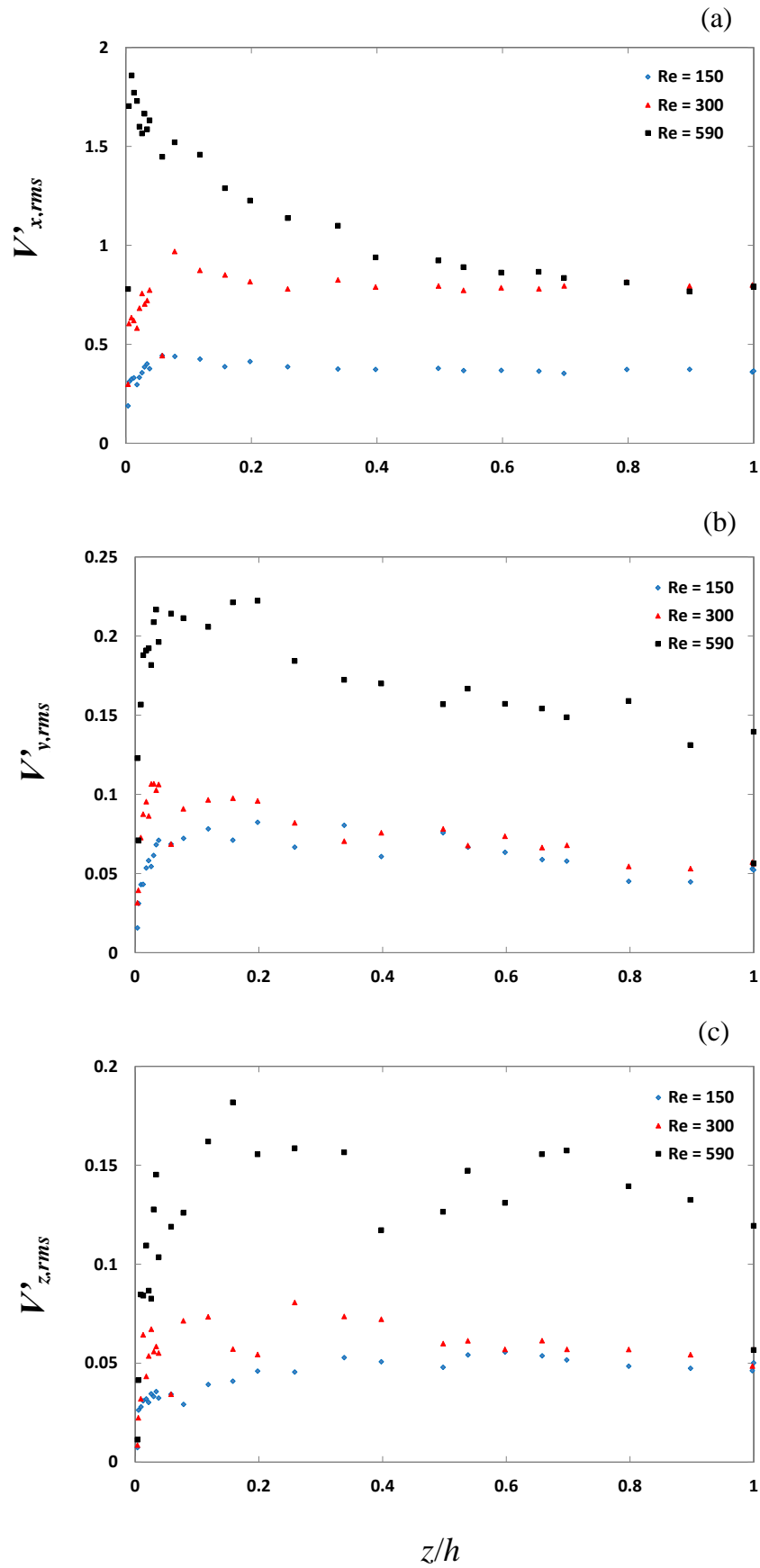


Figure 5.12 Instantaneous particle fluctuations for different shear Reynolds numbers (a) $V'_{x,rms}$, (b) $V'_{y,rms}$ and (c) $V'_{z,rms}$ ($t = 0.20s$).

Lastly, Figure 5.13 shows the time evolution of the maximum value of the particle number density, n_p^{max} , near the wall. The n_p^{max} for the $Re_\tau = 150, 300$ and 590 flows is seen to increase linearly to almost constant values at around $0.17, 0.19$ and 0.23 s, respectively. This behaviour suggests that the turbulence in the higher Reynolds number flows accelerates the particles at a faster rate in all directions (including towards the walls). Figure 5.14 (a-c) show contours of particle velocity in the streamwise direction for 0.05 J m^{-2} , at times $t^+ = 128, 304,$ and 707 . It is seen that particles accumulate near the walls and lose their velocity in this region with time.

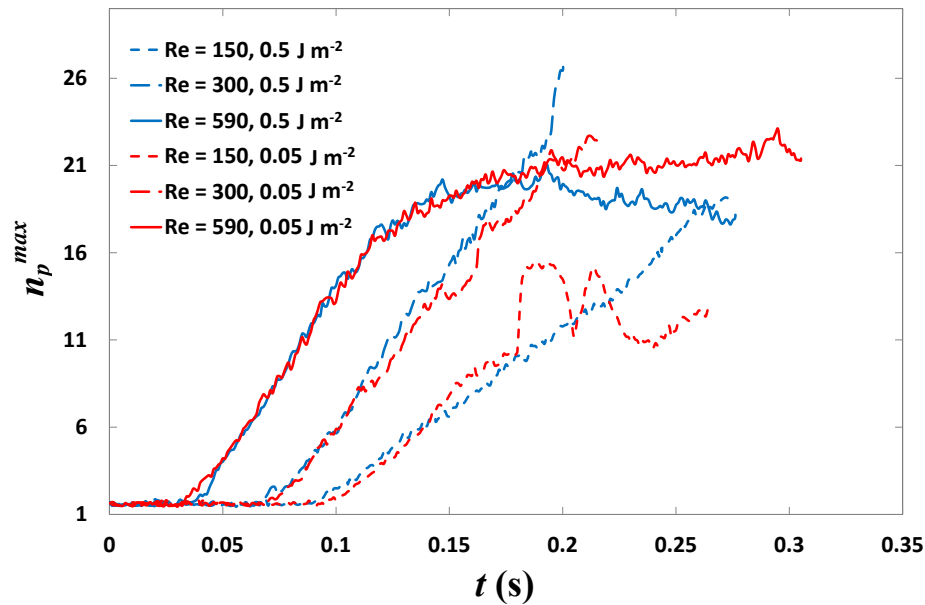


Figure 5.13 Maximum value of particle number density at the wall, n_p^{max} , as function of time t for variations in Reynolds number (0.05 and 0.5 J/m^2).

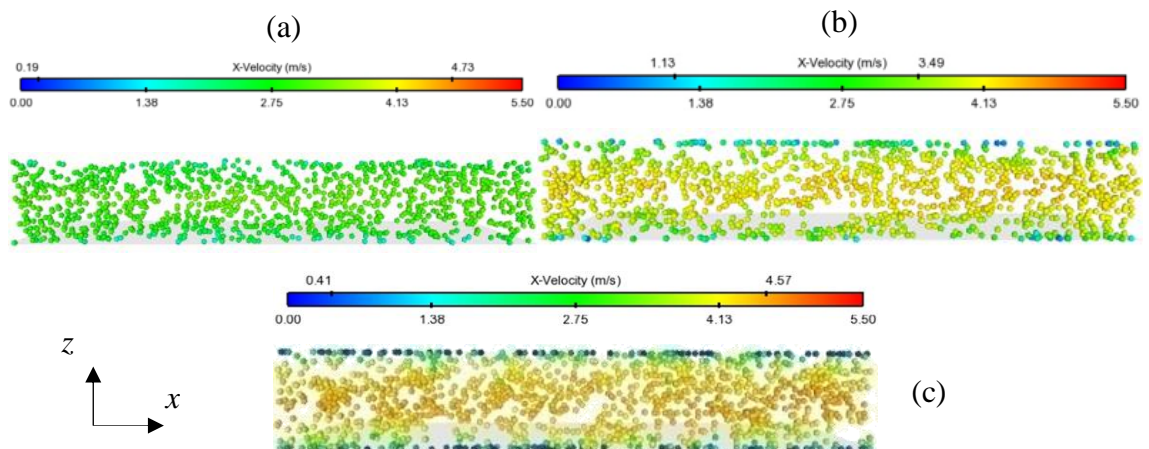


Figure 5.14 Contours of the streamwise velocity for 0.05 J m^{-2} particles in x - z plane, V_x (m/s) at time (a) $t^+ = 128$ (0.045 s); (b) $t^+ = 304$ (0.10 s); and (c) $t^+ = 707$ (0.20 s).

5.3 Effects of particle density on agglomeration

This section investigates the effects of particle density on particle agglomeration, three different particle densities have been considered, 250 kg m^{-3} , 1000 kg m^{-3} and 2159 kg m^{-3} , which correspond to particle Stokes 25, 100, and 216, respectively. Where, for an equal particle size and volume fraction of $102 \text{ }\mu\text{m}$ and 2.8×10^{-5} , the mass fractions are 2.8×10^{-6} , 1.1×10^{-5} and 2.4×10^{-5} , respectively. A surface energy of 0.05 J m^{-2} was selected for further study, with the corresponding particle relaxation times, and other relevant parameters given in the bottom row of Table 5-2.

Figure 5.15(a) shows particle contact formation for the three different particle densities mentioned earlier. For all particle densities, the rate of contact formation increases roughly linearly with time after an initial period. The results show an inverse relationship between particle density and the rate at which particle contacts form, indicated by the steeper gradient of the low density (250 kg m^{-3}) particles. Agglomeration is first seen to occur for these particles at around $t = 0.001 \text{ s}$, followed by the medium (1000 kg m^{-3}) and high (2159 kg m^{-3}) density particles at around $t = 0.002$ and 0.007 , respectively. For the low density particles, the number of contacts increases exponentially with time, whereas in the heavier particle cases the trend is more linear, indicating a lower rate of contact formation. This difference in contact formation can be caused by the differences in the rate of particle collisions. The lower density particles have lower St and therefore accelerate faster, and/or the greater mass of higher density particles could lead to the breakage of particle-particle contacts. Towards the end of the simulation, for the 250 , 1000 and 2159 kg m^{-3} particles, there are $3,690$, $2,232$ and $1,089$ particle contacts in the flow, respectively. Reducing the particle density by $\frac{1}{2}$ from 2159 to 1000 kg m^{-3} , for an equivalent volume fraction, therefore results in a 2 fold increase in contact number, although a further reduction of $\frac{3}{4}$ 250 kg m^{-3} gives rise to only just over $1\frac{1}{2}$ times the number of contacts. Therefore, a further reduction in particle density may not, however, necessarily lead to an increase in the number of particle contacts formed, as low density particles have low inertia and tend to track the fluid flow. From the above analysis, it is clear that the effects of flow turbulence are similar across all particle densities (or Stokes numbers), and that the particle density is likewise a key factor in determining particle agglomeration in the flow. To further understand the extent to which particle density affects the mechanisms of particle

agglomeration and dispersion, it would be beneficial to analyse in detail the particle collision frequency, the contact strength, and particle drag and dispersion, although some of this will be the subject of further work.

Figure 5.15(b) shows the cumulative number of particle-particle collisions for 1000 and 2159 kg m⁻³ particles. In general the rate of collisions continues to increase with time. At first, the profiles show exponential behaviour but then shift to linear further into the simulation. This exponential profile is indicative of the region in which the particles are accelerating to a constant bulk velocity. Naturally, the higher density particles respond slowly to fluid motion and therefore accelerate at a slower rate reaching a constant bulk velocity at a later time of $t \approx 0.17$ s compared to $t \approx 0.11$ s for the medium density particles. Comparing Figure 5.15(b) against Figure 5.15(a), the initial behaviour seen for particle-particle collisions is similar to that seen for contacts. Particle collisions occur for medium density particles prior to the high density particles, and the profiles are seen to diverge in the same manner with time. However, from around $t \approx 0.17$ s onwards, this divergence does not continue for collisions. Instead the rate of particle-particle collisions remains constant with time. This designates that more contacts are formed between lower density particles due to a higher rate of particle-particle collisions. However, the difference in contact formation is elevated by more frequent contact breakage for the higher density/mass particles.

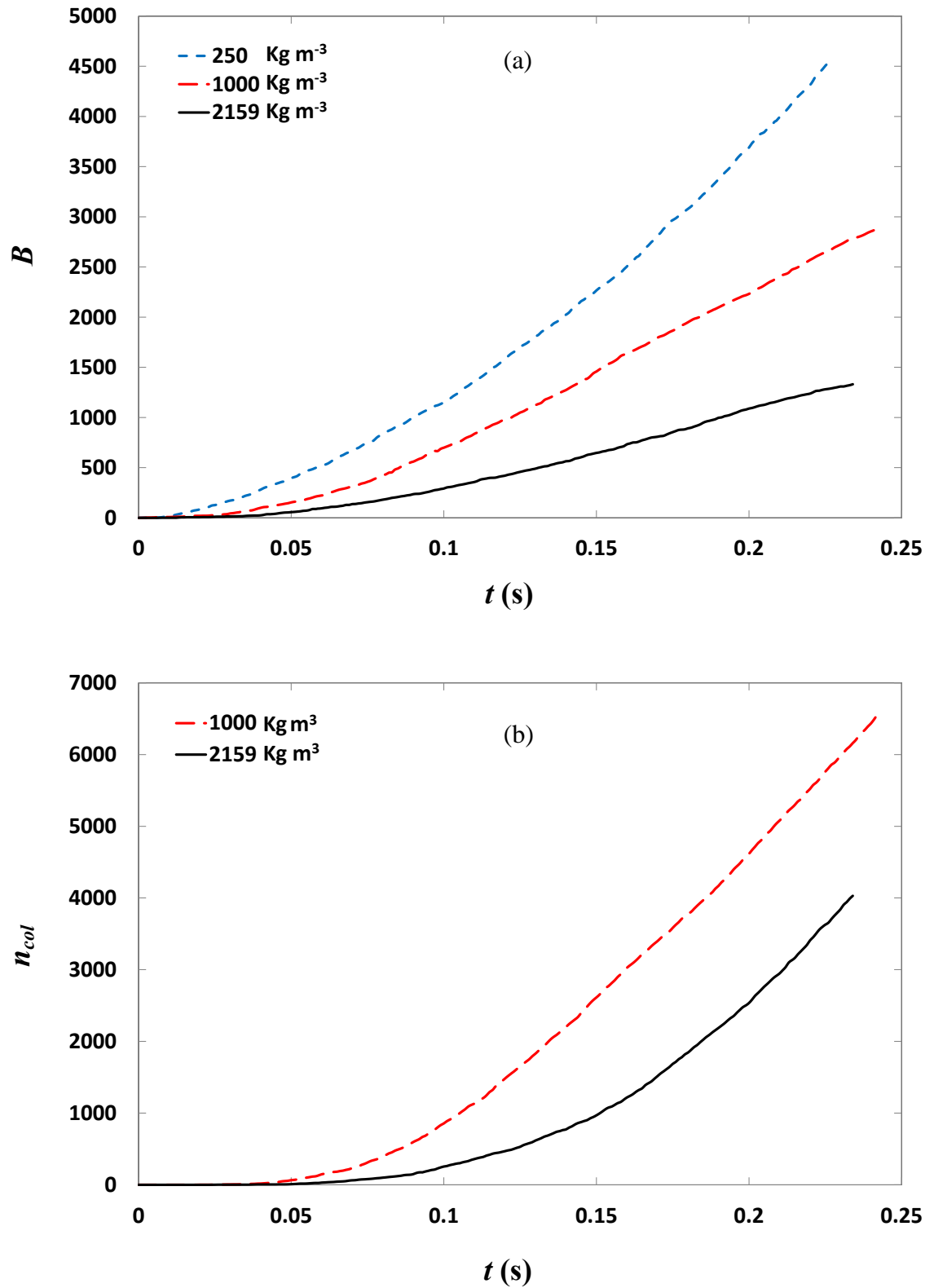


Figure 5.15 Number of contacts, B , (a) and cumulative collisions, n_{col} , (b) between particles with time, t , for variations in particle density.

Figure 5.16(a-c) show the instantaneous location of individual particles and contacts in the wall-normal direction for all cases given in the third row of Table 5-2, and their number at each location, at time $t = 0.2$ s. The plots have been generated using the same approach as Figure 5.8. For all particle densities 250 kg m^{-3} (Figure 5.16(a)), 1000 kg m^{-3} (Figure 5.16(b)), and 2159 kg m^{-3} (Figure 5.16(c)), overall, the results show a general movement of particles and also agglomerates towards the walls. For low, medium, and high density particles at the channel centre (column 50) the number of particles and contacts is 606, 627, and 710 and 11, 16 and 9, respectively, with these values increasing towards the walls, where for column 1 they increase to 7117, 4803, and 3489, and 550, 100 and 30, respectively. Therefore, the results show that for all particle densities, particle number and agglomeration is roughly similar at the channel centre. However at the walls, the particle number is seen to increase inversely with particle density. Moreover, there is an exponential increase in the number of bonds in relation to the number particles in this region. In all three cases, particle agglomeration can be attributed to the high particle concentration at the walls and the high turbulence levels near to the walls. These results indicate, therefore, that particle density is important in the formation of particle-particle contacts even for relatively low surface energy particles (0.05 J m^{-2}). The increased accumulation of lower density particles at the walls is either due to greater turbophoretic effects on such particles and/or more successful particle agglomeration promoting particle build up in this region. For that reason, in order to identify which of the two mechanisms is responsible, separate simulations have been run for the 250 , 1000 , and 2159 kg m^{-3} particles using zero surface energy particles (0.0 J m^{-2}).

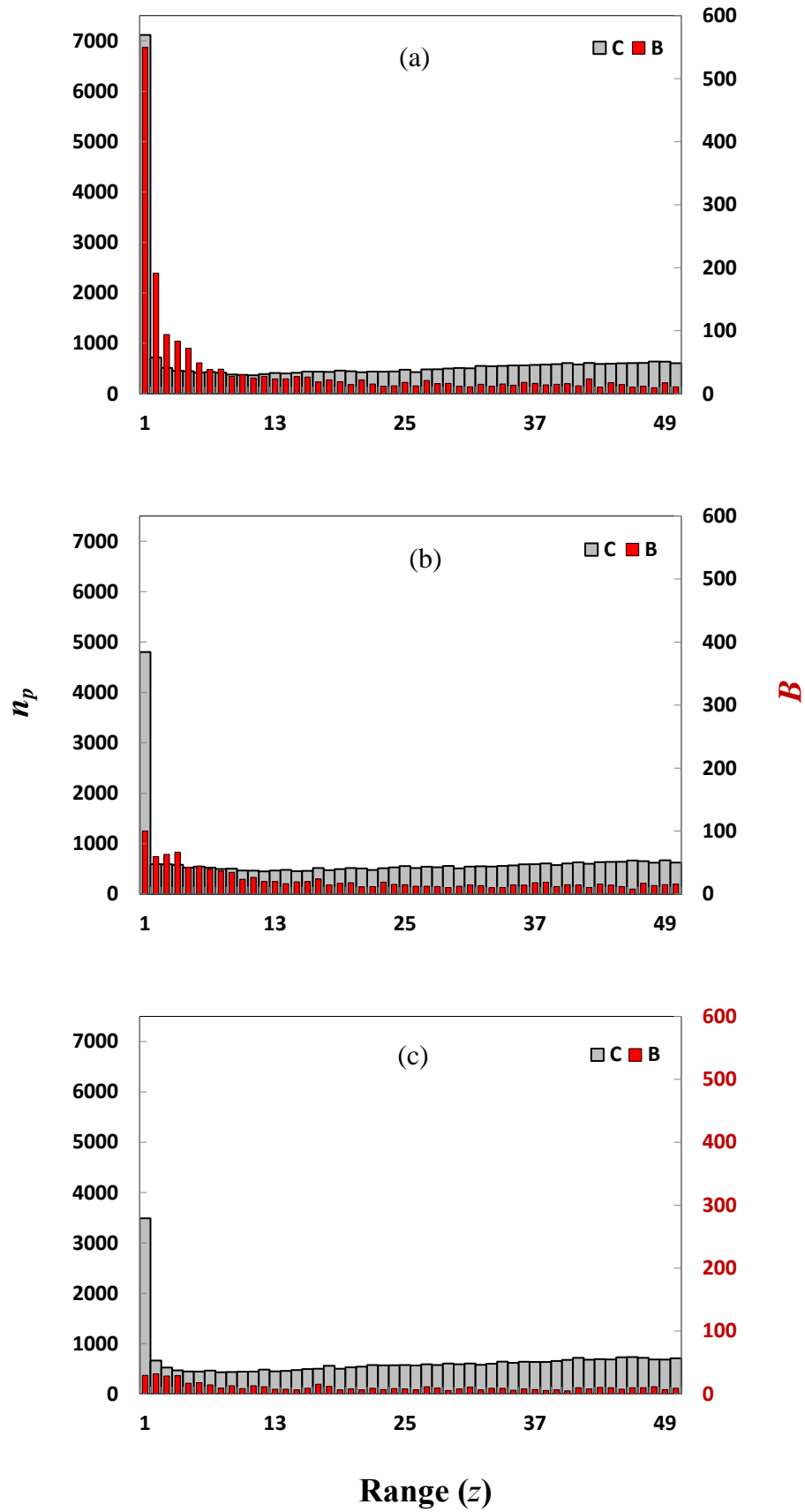


Figure 5.16 Contact, B , and local concentration, n_p , distribution across the channel at $t = 0.2$ s for (a) 250 kg m⁻³, (b) 1000 kg m⁻³, and (c) 2159 kg m⁻³.

Figure 5.17 shows the instantaneous location of individual particles in the wall-normal direction, and their number n_p at each location, at time $t = 0.2$ s. These plots are more refined than those above; results are shown for equally spaced regions across half the channel height that are equivalent in size to the particle radius. The results show that there is no relationship between particle surface energy and accumulation at the walls. Therefore, the enhanced increase in particle concentration in this region is solely due to the enhanced turbophoretic effects for lower density particles. Further scrutiny of the results in Figure 5.17 reveals that more low density (2159 kg m^{-3}) particles are in contact with the wall. This is due to their larger inertial effects; as a result these particles are less affected by fluid fluctuations and maintain their momentum towards the walls where they deposit. Furthermore, these particles are less likely to be removed from the walls by near wall phenomena such as ejections and sweeps. Figure 5.18 shows the number of present particle-particle contacts B and total sampled collisions $n_{collisions}$ in the wall-normal direction, at times $t = 0.2$ s and $t = 0 - 0.2$ s, respectively. The binning procedure used is the same as that in Figure 5.17. Generally the number of contacts increases towards the walls as already mentioned, in consort with the number of collisions.

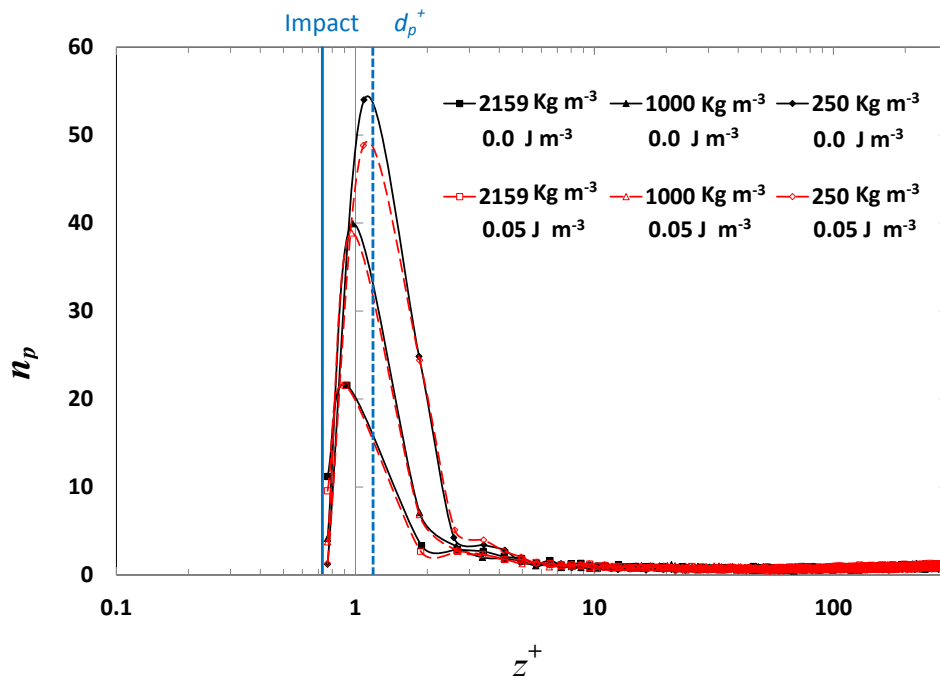


Figure 5.17 Particle number density, n_p , profiles in wall-normal direction, z^+ , at $t = 0.2$ s. The vertical solid blue line indicates the position of contact between the particles and wall (impact); the vertical dashed line gives a visual indication of the particle size in wall units (d_p^+).

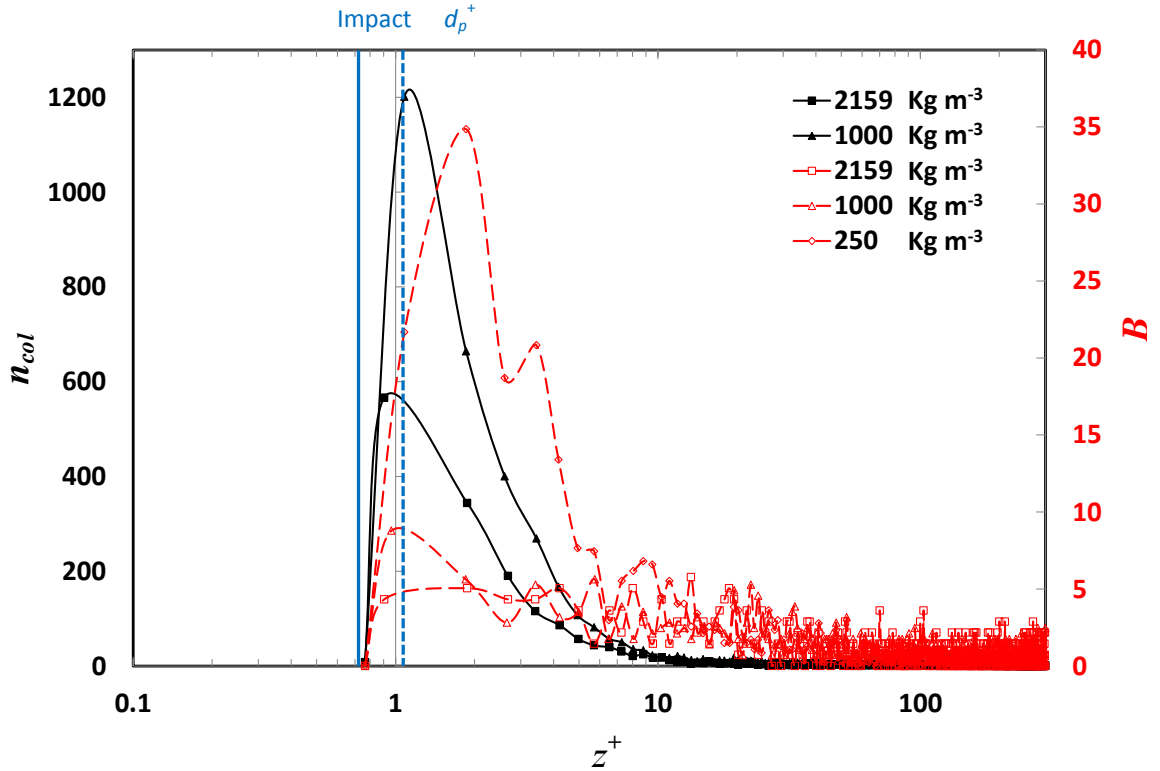


Figure 5.18 Particle-particle collision, n_{col} , and contact, B , profiles in the wall-normal direction for variations in particle density at $t = 0 - 0.2s$ and $t = 0.2 s$. The vertical solid blue line indicates the position of contact between the particles and wall (impact); the vertical dashed line gives a visual indication of the particle size in wall units (d_p^+).

Figure 5.19(a) shows the time evolution of the maximum value of the particle number density n_p^{max} near the wall. The n_p^{max} for the 250, 1000, and 2159 kg m^{-3} flows is seen to increase from around 0.02, 0.04 and 0.06 s, respectively, to almost constant values except for the 250 kg m^{-3} . This behaviour suggests that the flow turbulence accelerates the lighter particles at a faster rate in all directions (including towards the walls). The results also confirm that there is an inverse relationship between particle density and concentration build up at the walls. Moreover, due to this heightened particle drift, the lighter particles take longer to reach a steady state. Figure 5.19(b) shows three different regions close to the walls where the particles are accumulating, these include at the 1 - wall, 2 - viscous sublayer ($d_p - 5$) and 3 - buffer layer ($5 < z^+ < 30$). At the walls particle accumulation is seen to be similar. In the viscous sublayer however, the lower density (250 kg m^{-3}) particles increase in number at a faster rate compared to the medium (1000 kg m^{-3}) and high density (2159 kg m^{-3}). Finally in the buffer layer, particle accumulation is far greater for the high density particles; in fact particle number for the

low and medium density is none existent. This designates that the low and medium density particles are largely affected by fluid fluctuations, causing these particle to be pushed out of regions of high turbulence. Overall, in terms of particle distribution, it is clear that the fluid turbulence leads to different dispersion characteristics corresponding to particle Stokes.

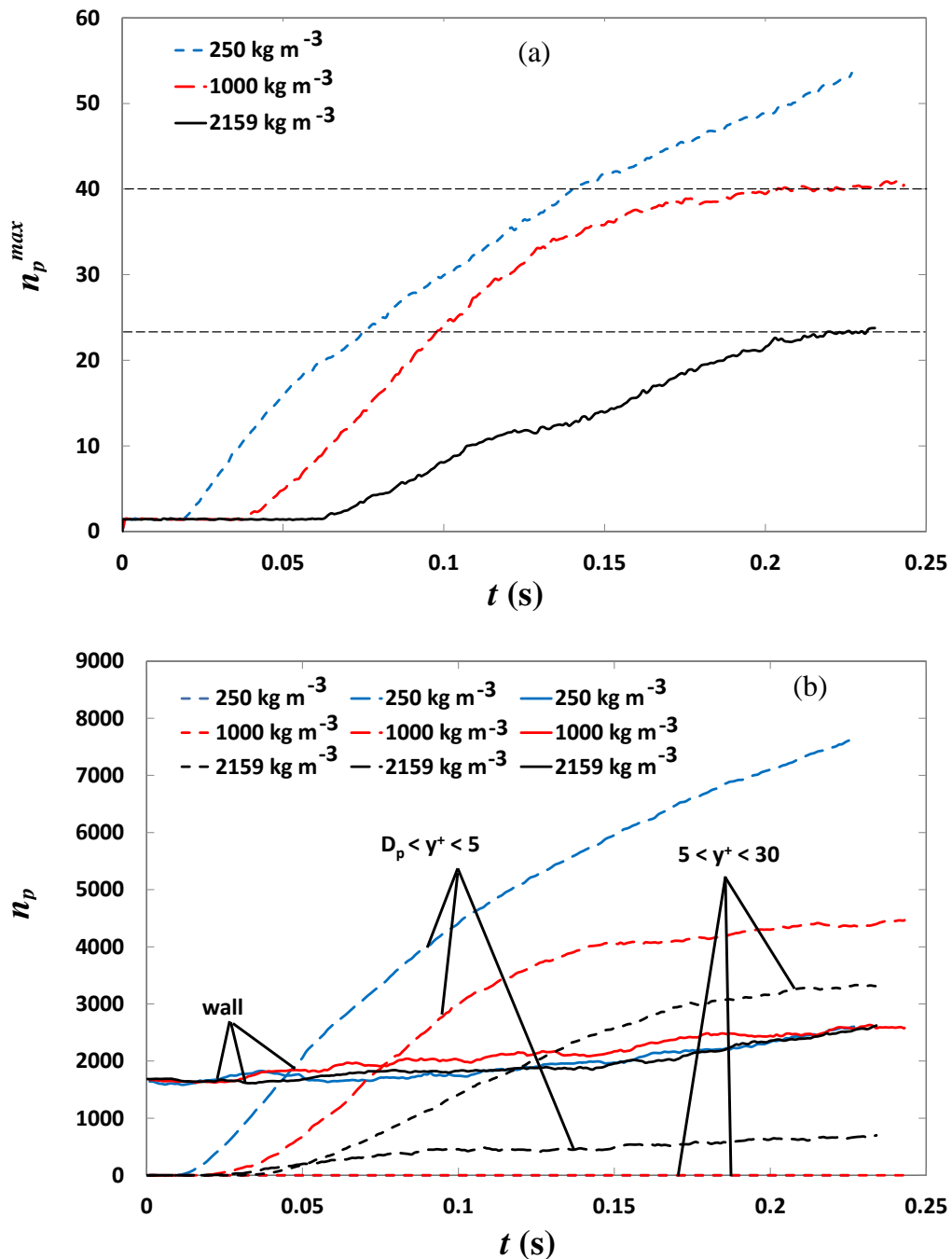


Figure 5.19. (a) Maximum value of particle number density at the wall, n_p^{max} , as a function of time, t , for variations in density; (b) Particle number, n_p , in three different regions of the channel with time.

Figure 5.20 shows the mean collision velocity between the particles and bottom channel wall v_n with time for medium (1000 kg m^{-3}) and high density (2159 kg m^{-3}) particles. In general, the collision velocities start off high before decreasing to a constant value with time. The initial high velocities are due to particles drifting towards the walls from regions of high velocity in the main body of the flow; this phenomenon decreases as steady state is reached. The medium density particles are the first to impact with the wall and at a higher v_n . This is because, as previously mentioned, lower density particles have a lower St , and therefore accelerate faster and better track the flow. Furthermore, for the high density particles, the width of the peak is larger this designates that these particles lose their momentum at a lower rate.

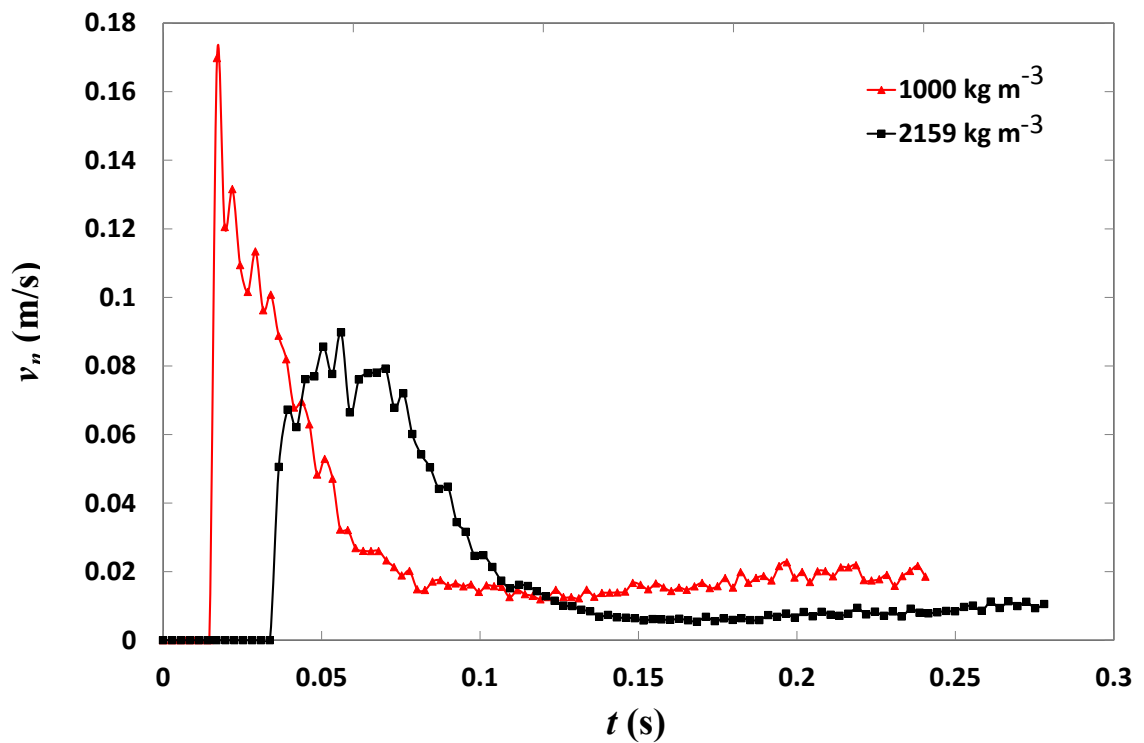


Figure 5.20. Mean particle relative (impact) velocity normal with the bottom wall, v_n , as a function of time, t , for variations in density.

Figure 5.21(a,b) show the number of particle-wall collisions and corresponding normal component of the relative (impact) velocity for 1000 and 2159 kg m^{-3} particles, respectively, between time $t = 0.0 - 0.2 \text{ s}$. The relative velocities range from less than 0.01 m s^{-1} to over of 0.18 m s^{-1} . Comparing the medium (Figure 5.21(a)) and high (Figure 5.21(b)) density results, there are more collisions for the high density particles below 0.01 m s^{-1} and less above this value. The greater number of higher velocity

particle-wall collisions for the medium density particles can be seen clearer in the zoomed in section of both figures.

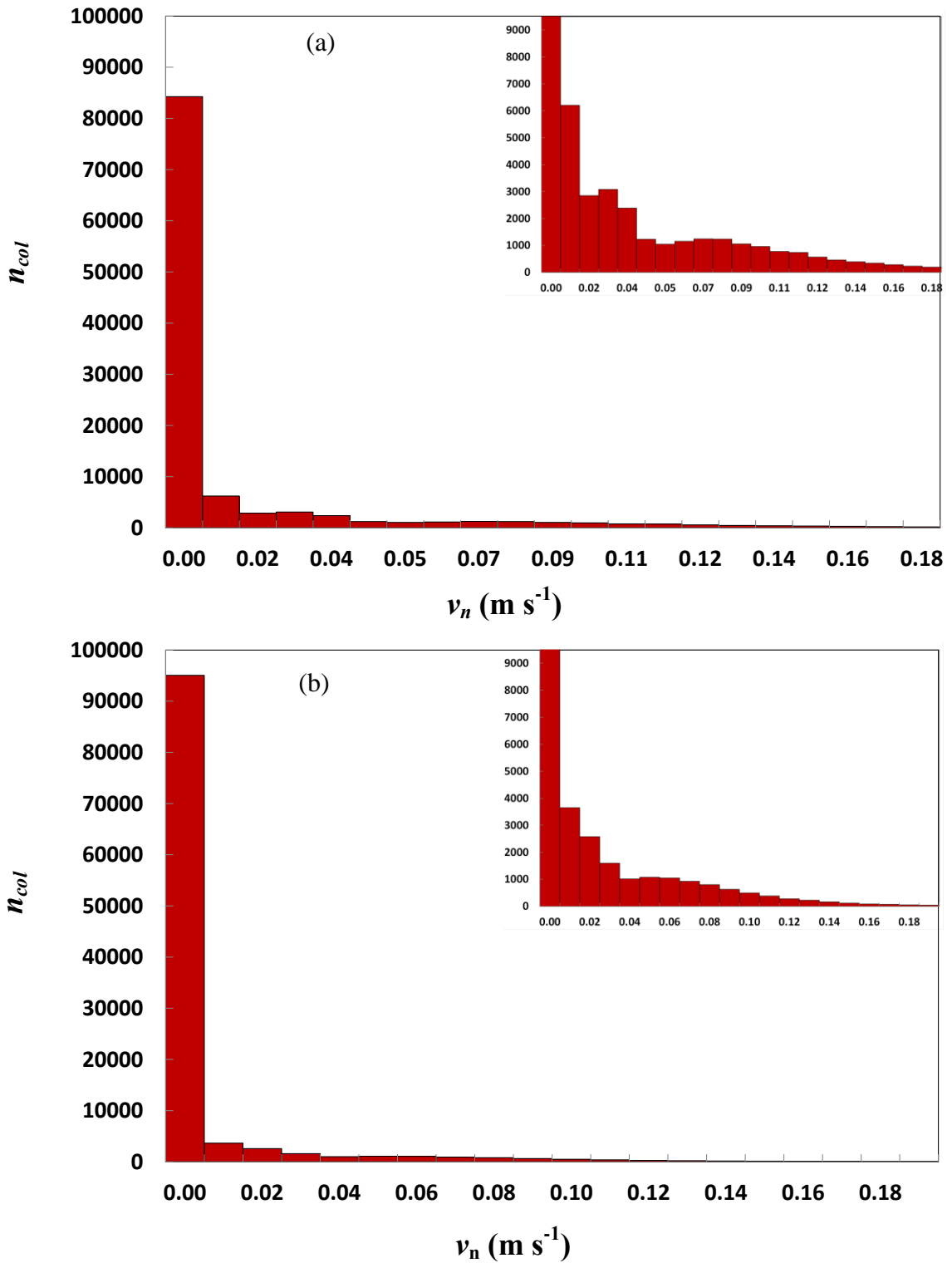


Figure 5.21 Total number of particle-wall collisions, n_{col} , and their relative velocity normal with the bottom wall, v_n , for (a) 1000 kg m^{-3} and (b) 2159 Kg/m^3 ($t = 0.0 - 0.2$ s).

Figure 5.22 shows the relative velocity normal as a function of distance to the wall for the 1000 and 2159 kg m⁻³ particles. In general, the relative velocity increases from the channel centre towards the walls. This behaviour can be attributed to more random particle behaviour in this direction.

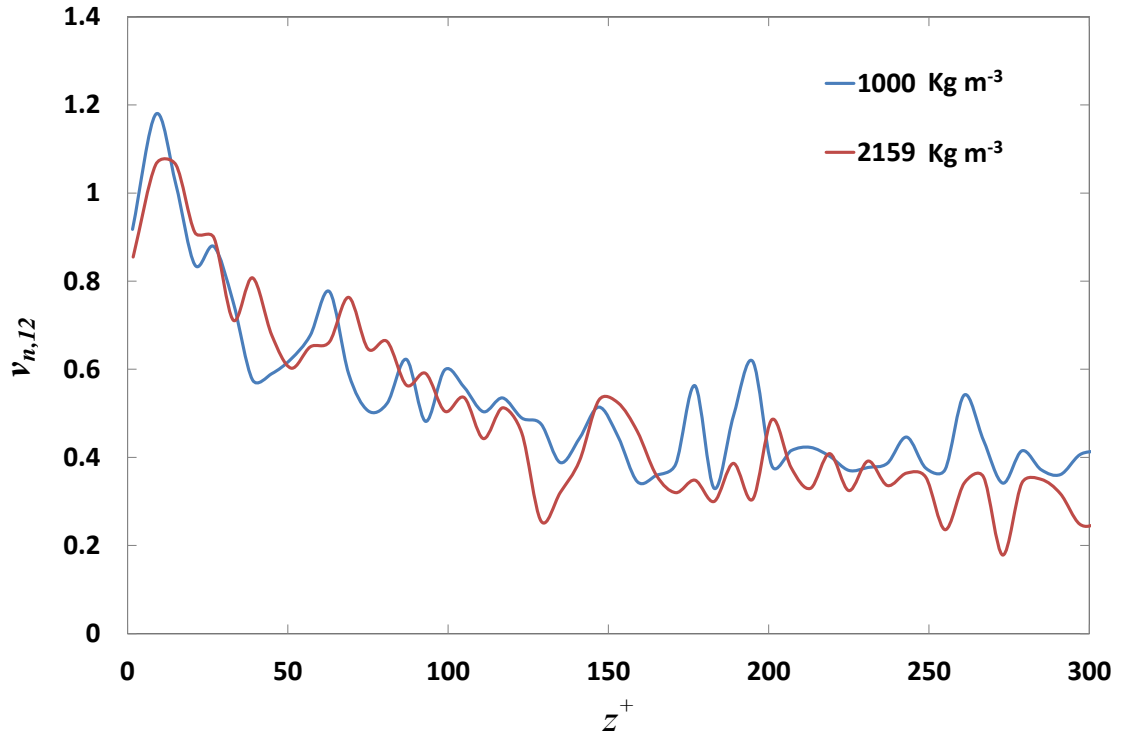


Figure 5.22 Relative velocity normal, $v_{n,12}$, as a function of distance to the wall, z^+ , for (a) 1000 kg/m³ and (b) 2159 Kg m⁻³ ($t = 0.0 - 0.2$ s).

Figure 5.23 shows the number of particle collisions and the corresponding normal component of the relative (impact) velocity for the different density particles, 1000, and 2159 kg m⁻³ between time $t = 0.0 - 0.2$ s. As can be seen in Figure 5.23 the impact velocities range from less than 0.01 m s⁻¹ to over 3.0 m s⁻¹. The velocity regions in which sticking occurs are given in Table 5-4 and have been highlighted for different surface energies. Based on these cut-off points the numbers of successful collisions are 2295 and 1059 for the 1000 and 2159 kg/m³. These values match the number of particle-particle contacts in Figure 5.14. In this case increasing the particle density by 2 folds has resulted in a 2 fold increase in the contact number. Although, that this cannot be taken as a linear relationship as the number of collisions has also changed with density.

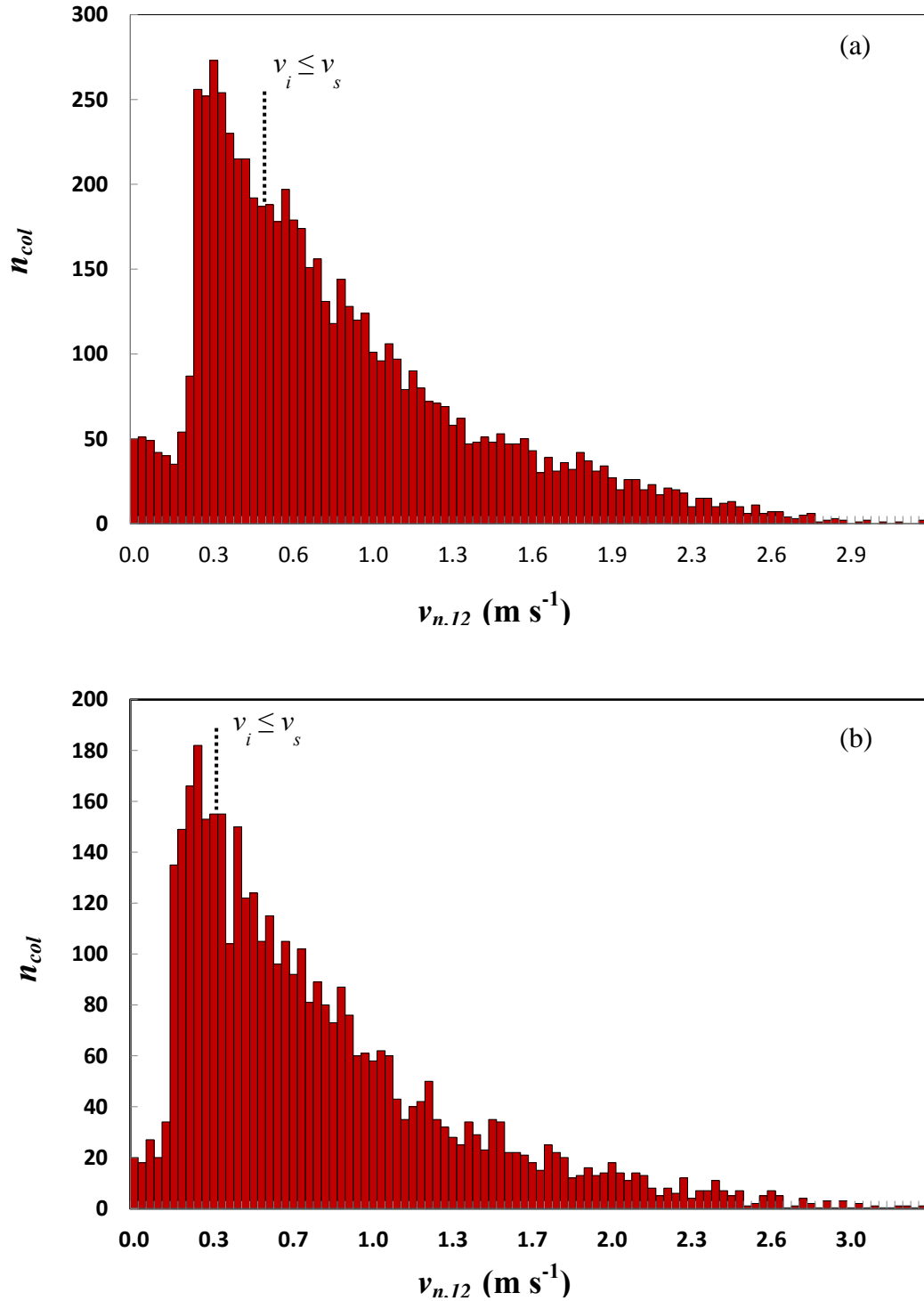


Figure 5.23 Total number of particle-particle collisions, n_{col} , and their relative velocity normal, $v_{n,12}$, for (a) 1000 kg m^{-3} and (b) 2159 kg m^{-3} . The vertical dotted black lines indicate the maximum sticking velocity for the particles ($t = 0.0 - 0.2 \text{ s}$).

Table 5-4 Sticking velocity of different density particles (0.05 J m^{-2})

Density (kg m^{-3})	249.9	1000	2159
Sticking Velocity (m s)	0.97	0.48	0.33

Figure 5.24 (a) shows the mean kinetic profile as a function of distance to the wall, $k_p = \frac{1}{2}m\bar{V}^2$, for 250, 1000, and 2159 kg m^{-3} particles. Figure 5.24 (b) shows the same profile plotted in semi-logarithmic form. The results show the anticipated symmetric behaviour for a fully developed flow, where k_p is maximum at the channel centre and decreases to a minimum at the walls. It is seen that the proportional difference in particle density (or mass) is also projected in the particle kinetic energy as expected.

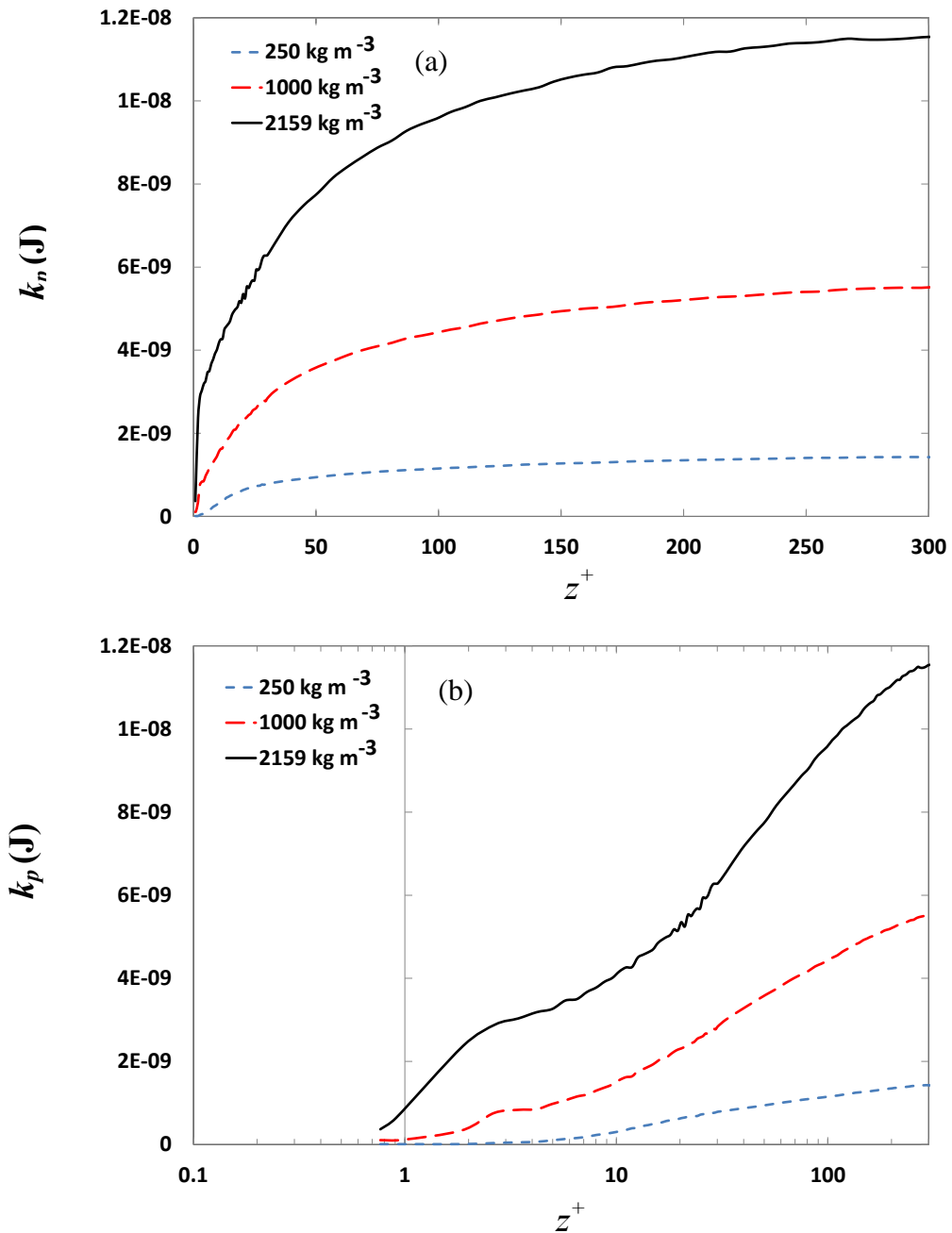


Figure 5.24 Mean particle kinetic energy, k_p , as a function of distance to the wall, z^+ , for variations in particle density: (a) normal, (b) log ($t = 2.0 - 2.2$ s).

Figure 5.25(a-c) show the mean streamwise $F_{x,\text{coupling}}$, wall normal $F_{z,\text{coupling}}$ and resultant $F_{r,\text{coupling}}$ forces plotted against the streamwise velocity V_x , wall-normal velocity V_z and kinetic energy k_p of the particles, respectively. The coupling force is the summation of all forces acting on the particle, in this channel flow it includes the fluid drag and Saffman lift force. In Figure 5.25(a), generally, $F_{x,\text{coupling}}$ is seen to increase linearly with V_x . Furthermore, $F_{x,\text{coupling}}$ increases with particle density. In Figure 5.25(b), there is yet again a general increase in $F_{z,\text{coupling}}$ with particle density. Further scrutiny of the results however shows that for the low density particles, $F_{z,\text{coupling}}$ remains stagnant with increasing V_z , and the medium and high density particles show a sharp increase in $F_{z,\text{coupling}}$ followed by an asymptote, before increasing again at higher velocities. An increase in drag force is representative of an increase in relative slip velocity, defined as the difference between the particle and local fluid velocity. Therefore, at higher velocities these particles are less capable of tracking the flow and this is more evident at higher density due to their higher inertia. The non-linear changes in $F_{z,\text{coupling}}$ are due to transfer of particle momentum from the streamwise component to the wall-normal in regions of high turbulence where particles exhibit random motion. Lastly, Figure 5.25(c) shows the relationship between the resultant of the coupling force $F_{r,\text{coupling}}$ and normalized particle kinetic energy K_p . The results are similar to Figure 5.25(a) since the streamwise velocity component makes the largest contribution to the resultant velocities used in $F_{r,\text{coupling}}$ and K_p . It is seen that, similar to the previous figures, the kinetic energy of low and medium density particles is very small compared to the high density,

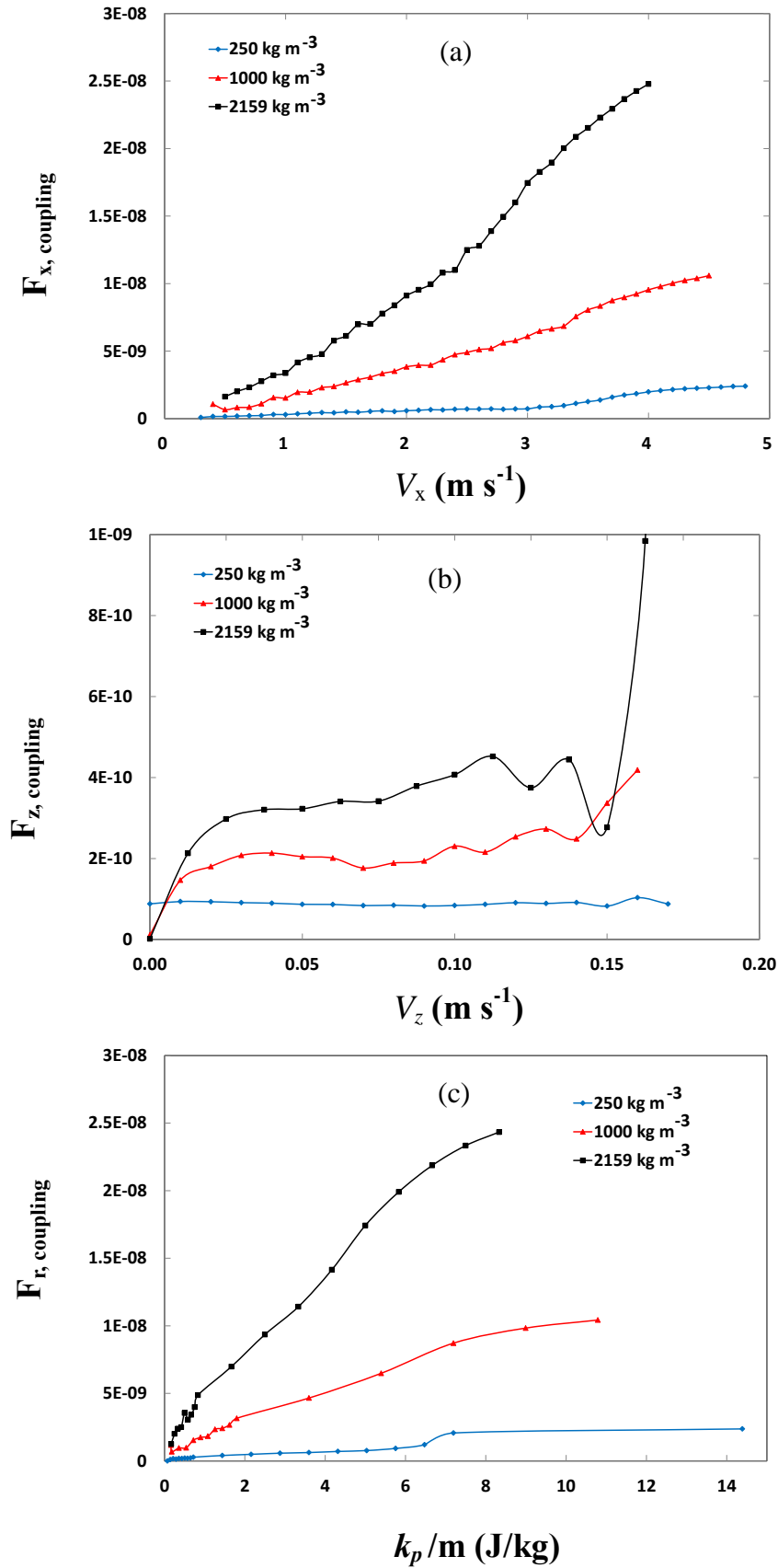


Figure 5.25 Mean particle coupling Forces $F_{i, \text{coupling}}$ (Drag and Lift) as a function of particle (a) Streamwise velocity V_x , (b) Wall-normal velocity V_z , (c) Kinetic Energy k_p

Figure 5.26(a,b) show the streamwise components of the mean particle coupling force as a function of distance to the wall. The concentration graphs showed that most of the particle activity is at the earlier time steps; therefore, when comparing the dispersing characteristics of the particles, the data has also been sampled early into the simulation. Results have been time-averaged for the developing phase $t = 0.01 - 0.2$ s and near to steady state onwards $t = 0.2 - 0.22$ s. In Figure 5.26(a,b), generally, the magnitude of $F_{x,coupling}$ increases from the channel centre towards the walls where it reaches a maximum in the viscous sublayer before decreasing at the walls. The profile is negative in the region $0 < z^+ < 15$, which signifies that some of the particles are being pushed backwards by the swirling fluid turbulence as they approach the walls. These particles will have a very high individual value of $F_{x,coupling}$, causing the average value to be negative. This does not mean that the majority of the particles are moving counter to the flow direction in this region. Comparing Figure 5.26(a) and Figure 5.26(b) it is seen that, throughout the channel cross section, $F_{x,coupling}$ is greater earlier into the simulation for all particle densities. This difference is most prevalent between $30 < z^+ < 100$ and increases with particle density. The results therefore suggest that there is a net drift of particles from the main body of the flow towards the walls early into the simulation which reduces once a steady state is reached. Further scrutiny of the results in Figure 5.26(a,b), shows that the coupling force does not reach zero at the walls for the medium and high density particles. Therefore, the higher density particles are less effected by the no slip wall conditions in the streamwise direction and have a more uniform velocity (smaller velocity gradient) across the cross section (due to their larger mass and therefore momentum, assuming the difference in velocity is not considerably high compared to the lower density particles. On that basis, it is possible to deduce that the low density particles are more effected by the shearing of fluid at the walls, causing particles in this region to slow down in the stream wise direction, however, this does not imply that the mean particle velocity in the channel centre is less for the lower density particles compared to the higher ones, instead, it suggests a larger velocity gradient exists for the smaller particles.

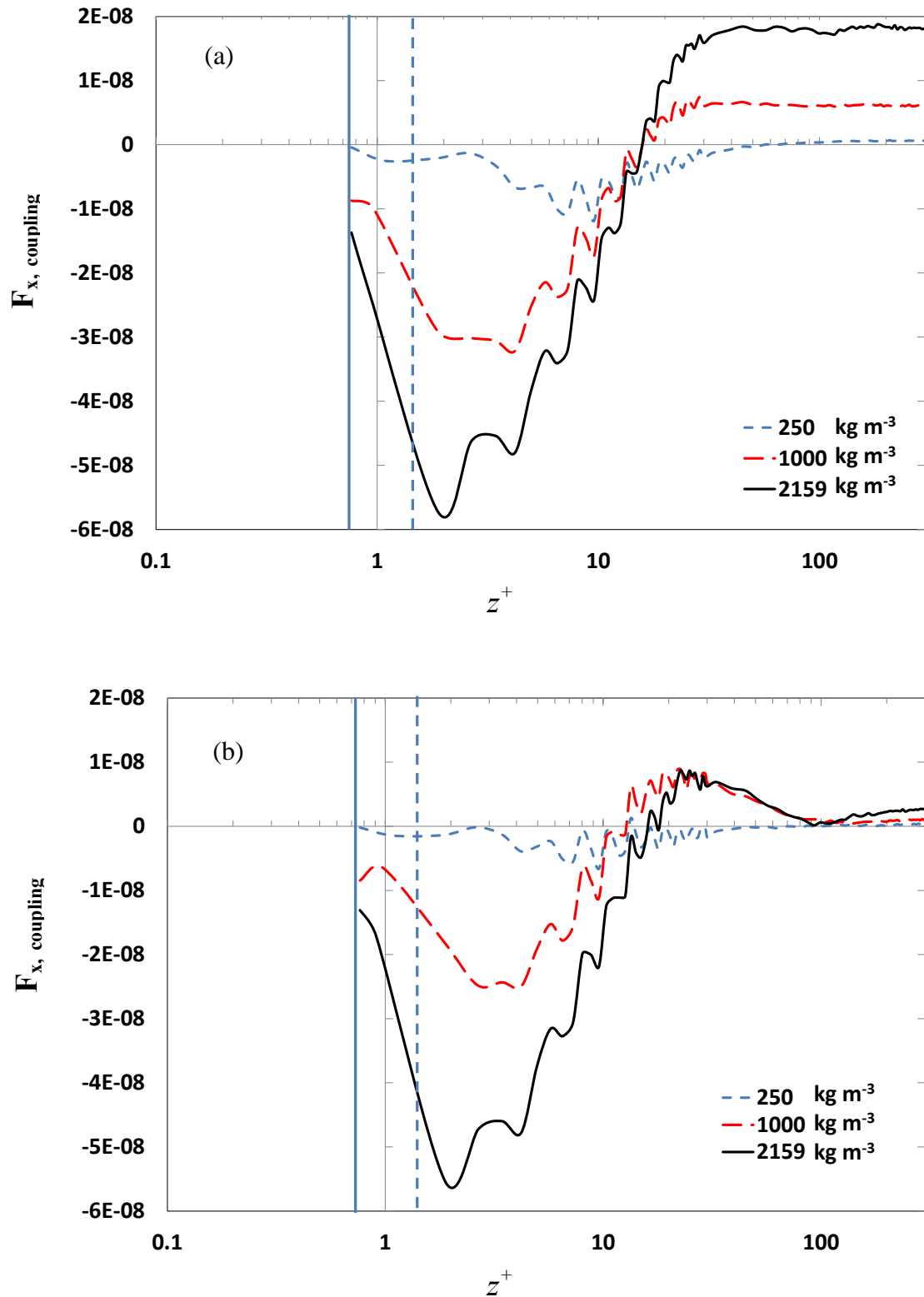


Figure 5.26 Streamwise Coupling Forces $F_{i,coupling}$ (Drag and Lift) on Particles as a function of distance to the wall, z^+ . (a) $t = 0.01 - 0.2 \text{ s}$, (b) $t = 0.2 - 0.22 \text{ s}$. The vertical solid blue line indicates the position of contact between the particles and wall (impact); the vertical dashed line gives a visual indication of the particle size in wall units (d_p^+).

In the case of the wall-normal component $F_{z,coupling}$; in Figure 5.27(a,b) the data has also been sampled early ($t = 0.01 - 0.2$ s) and late ($t = 2.0 - 2.2$ s) into the simulation, respectively. Comparing the earlier and later times, overall $F_{z,coupling}$ is again generally greater earlier in the simulation (Figure 5.27(a)). Such behaviour can be contributed to turbophoretic drift; the fluid transfers particles at a higher than mean velocity from the centre towards the walls, giving rise to a velocity component in that direction. Comparing $F_{z,coupling}$, for different particle densities, it is seen that higher density particles have a higher $F_{z,coupling}$ throughout the channel cross section. This suggests that the dispersing of particles towards the walls is faster for the low density particles due to less drag and confirms the behaviour shown by the mean particle deposition in the previous sections. Further scrutiny of the results shows that for the low density particles, moving away from the centerline and towards the walls, generally, the value of $F_{z,coupling}$ increases to just outside the buffer before decreasing to almost zero in the viscous sublayer and at the wall. Therefore, the particle velocities decrease in this region along with that of the fluid and particles do not rebound with a relatively high velocity off the walls. In the case of the medium and high density particles however, $F_{z,coupling}$ decreases to a very low value. The negative values indicate that some of the particles are moving counter to the flow, i.e. towards the channel centre after rebounding with the walls. Again, it is important to stress that $F_{z,coupling}$ is very high for such particles and leads to a negative average, it does not mean that all particles are moving away from the walls in this region. The mean relative slip velocities for all particle densities in Figure 5.27(b) are shown in Table 5-5.

Table 5-5 Comparison of effect of main forces (Drag and .Lift) on particles ($t = 0.2 - 0.22$ s)

ρ	Coupling Force (nN)		
	$ x $	$ y $	$ z $
250	0.38	0.004	0.003
1000	0.44	0.01	0.04
2159	1.34	0.04	0.006

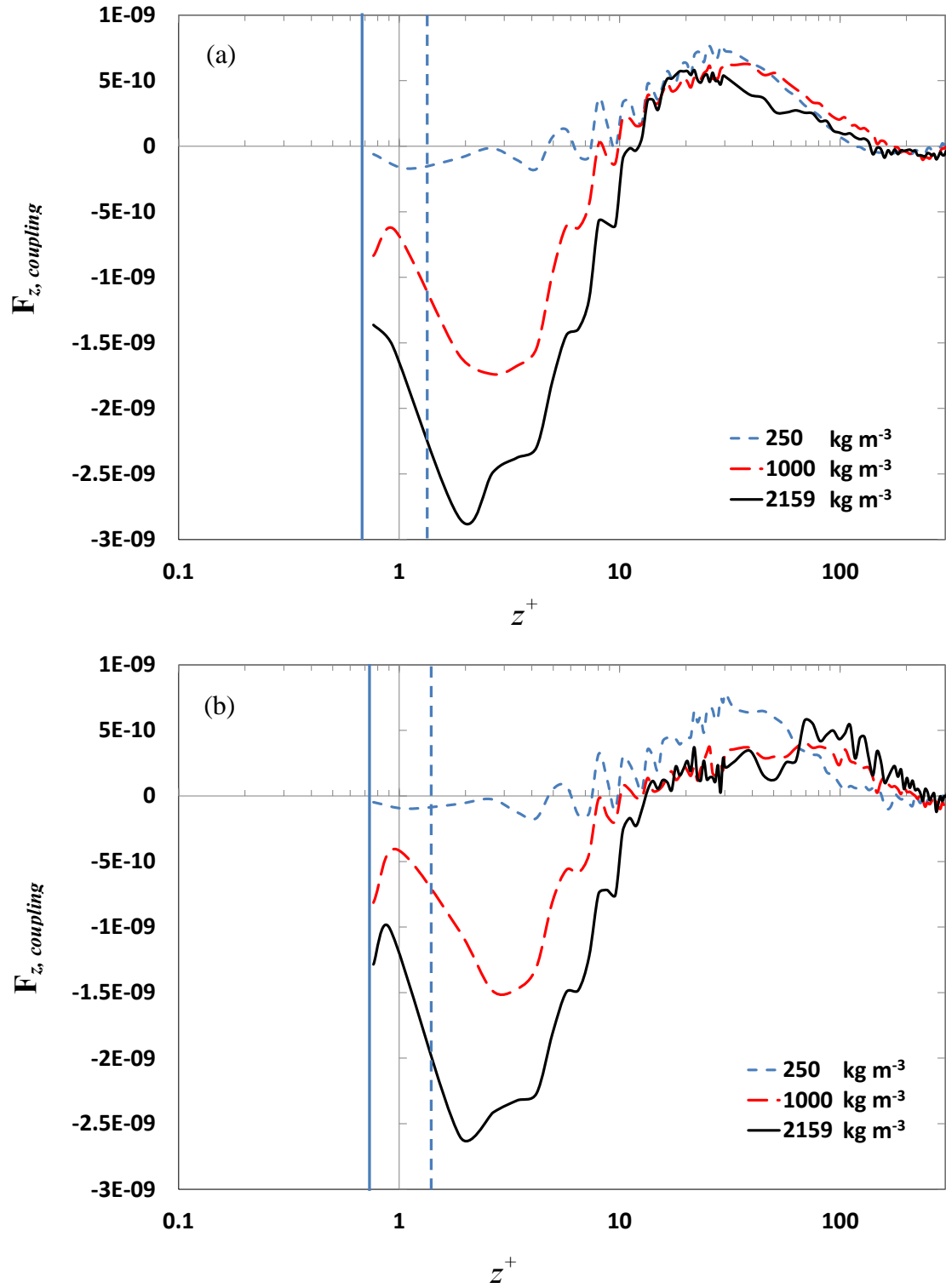


Figure 5.27 Wall-normal Coupling Forces $F_{z,coupling}$ (Drag and Lift) on Particles as a function of distance to the wall, z^+ : (a) $t = 0.01 - 0.2$ s, (b) $t = 0.2 - 0.22$ s. The vertical solid blue line indicates the position of contact between the particles and wall (impact); the vertical dashed line gives a visual indication of the particle size in wall units (d_p^+).

From previous works (such as Moreno-Atanasio (2012)) it is known that particle collisions (normal impact) diffuse particle kinetic energy. Moreover, this loss in kinetic energy can change for particles with different chemical and physical properties. Other works (e.g., Vreman et al. (2009)) have shown that particle collisions are directly responsible for differences in the mean velocities in two-phase flow. The loss in particle kinetic energy causes flattening of the particle mean velocity profile. Although, for such effects to be seen higher concentrations would be required than used in this work.

Figure 5.28 shows the normal $-E_n$, tangential $-E_t$ and total loss of energy $-E_T$ as a function of the relative (impact) velocity normal for the 1000 and 2159 kg m⁻³ particles. The normal and tangential energy loss is the energy lost during a collision due to the normal and tangential overlap, respectively. The total energy loss is obtained by summing these two values. The results show that generally energy loss increases with relative velocity. From closer analysis it is seen that both the normal and tangential energy losses are higher for the high density particles, and this discrepancy increasing with relative velocity. Furthermore, the difference is more prevalent for the normal energy. This can be explained as follows, the collisions between particles gradually reduce particle velocity. Part of the initial kinetic energy is radiated into the particles as elastic waves. Here, the contact forces reach a maximum value (maximum deceleration) and the particle velocities drop to zero. This is followed by a recovery stage; stored elastic energy is released and converted into kinetic energy and the particle moves with a rebound velocity in the opposite direction. A higher density contributes to greater particle momentum and therefore greater energy loss.

Figure 5.29 shows total, kinetic and rotational kinetic energy with time for the 1000 kg m⁻³ particles. The total energy is the summation of the potential, kinetic and rotational kinetic energy; the potential energy is zero in this system (due to the negligence of gravity and therefore has not been plotted). The kinetic energy is dependent on particle velocity magnitude and the rotational kinetic energy is dependent on particle-particle and particle-wall collision. In this system both energies have been initialised at zero. From the results of Figure 5.29, it is seen that the total energy and kinetic energy are similar, and are seen to increase exponentially before approaching an asymptote and reaching steady state at $t \approx 0.15$ s. This is indicative of the fluid flow increasing particle velocity. In the case of the rotational kinetic energy, this value remains almost constant

with time. This shows that the effects of particle rotation on particle movement are negligible.

Table 5-6 Comparison of effect of mean contact attributes on particles ($t = 0.2 - 0.22s$)

ρ	Contact Force (nN)								Overlap (nm)		Contact Vector (μm)
	F_n				F_t				α_n	α_t	
	$ x $	$ y $	$ z $	Mag	$ x $	$ y $	$ z $	Mag			
250	1.88	1.34	0.79	39.6	0.20	1.09	0.41	39.8	220	0.74	50.8900
1000	0.52	0.2	2.62	77.5	1.24	0.40	0.91	71.8	220	1.31	50.8902
2159	4.96	0.17	3.27	96.4	3.45	1.74	2.04	81.1	219	1.44	50.8903

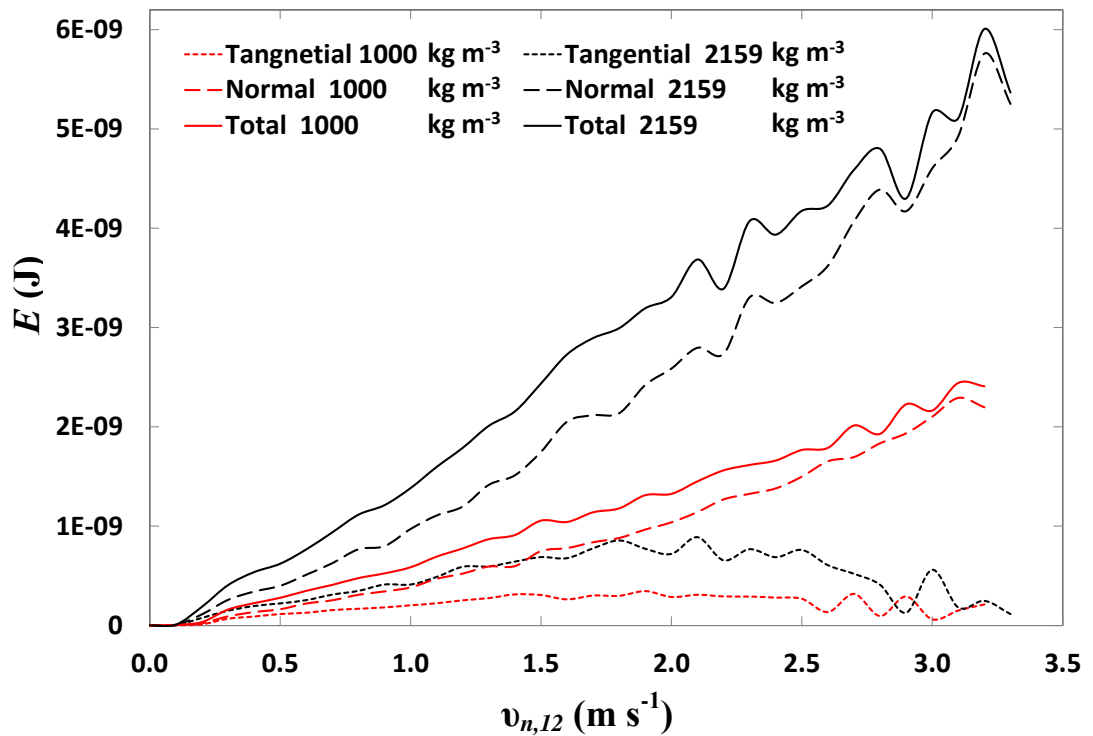


Figure 5.28 Loss of normal $-E_n$, tangential $-E_t$ and total energy $-E_T$ for the 1000 and 2159 kg m^{-3} particles as a function of particle relative velocity normal $v_{n,12}$.

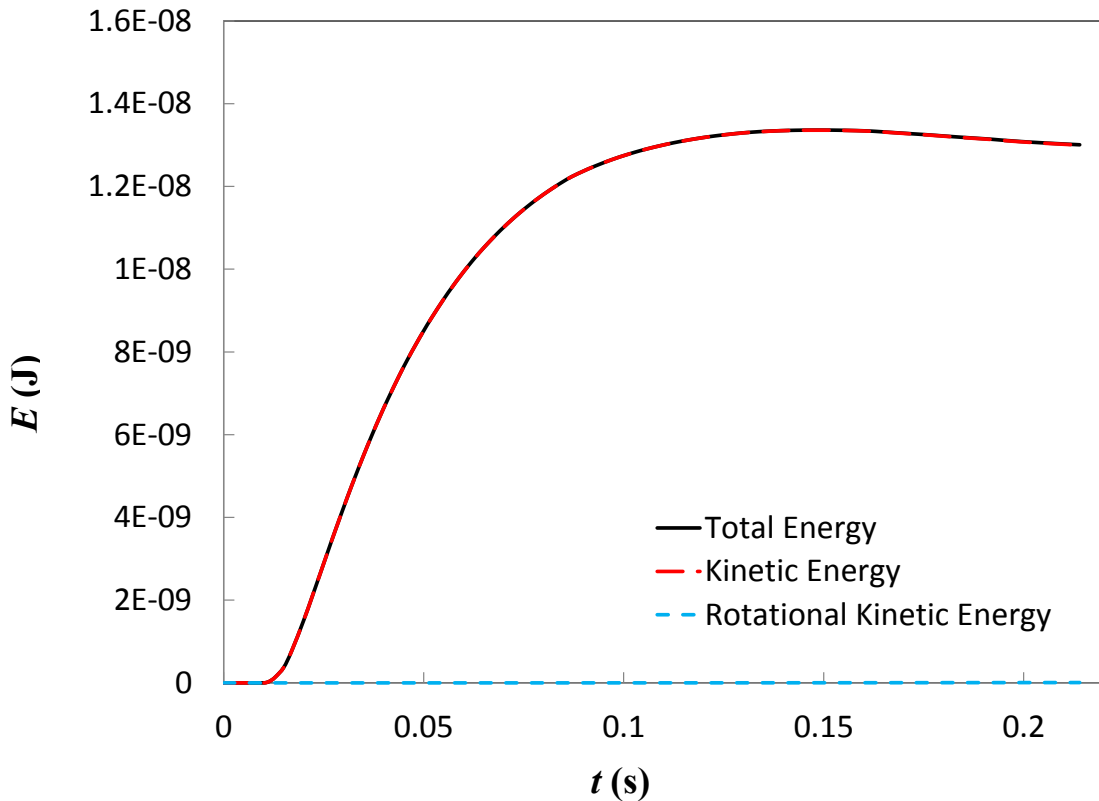


Figure 5.29 Rotational kinetic energy, kinetic energy k_p and total energy E_t for the 1000 kg m^{-3} particles as a function of time, t .

To quantitatively analyse the contacts between particles, the contact attributes have been time averaged from $t = 0.2 - 0.22\text{s}$ in the channel and are given in Table 5-6. A visual representation of these contact attributes is shown in Figure 5.30. These include the normal force, tangential force, contact vector, and normal overlap. When two contact radii overlap the contact force calculation is entered, however internally the physical radius of the spheres is used to calculate the magnitude of the contact force. Central aspects in contact mechanics are the pressures and adhesion acting perpendicular to the contacting bodies surfaces (known as the normal direction) and the frictional stresses acting tangentially between the surfaces. This work involves dispersed particle systems and is therefore mainly concerned with the normal direction of collision. The contact vector is the vector connecting the contact point to the center of the particle when two particles collide. In Table 5-6, generally, the magnitude of the normal and tangential contact forces increases with particle density. It is possible to compare these forces with that exerted onto the particle by the fluid to predict contact breakage in different regions of the channel. However this is outside the scope of this thesis and will be left to further work.

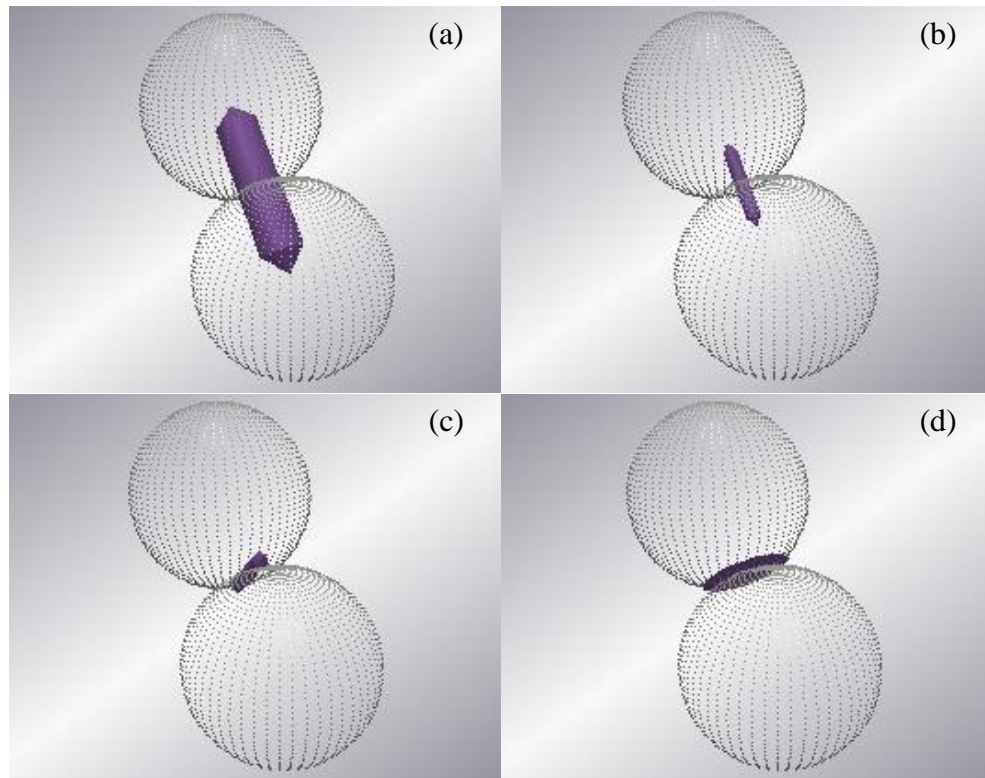


Figure 5.30 Virtual representation of the contact attributes (a) contact vector, (b) normal force, (c) tangential force, (d) normal overlap

5.4 Effects of particle size on agglomeration

This section investigates the effects of particle size on particle agglomeration, three different particle sizes have been considered, 51 μm , 102 μm and 150 μm , where for an equal volume fraction of 2.8×10^{-5} , there are 508,850, 63,607 and 20,000 particles in the flow, respectively. Again, a surface energy of 0.05 J m^{-2} was selected for further study, with the corresponding particle relaxation times, Stokes number and other relevant parameters given in the fourth row of Table 5-2.

Figure 5.31 shows particle contact formation for the three different particle sizes mentioned above. For all particle sizes, the rate of contact formation increases roughly linearly with time after an initial period. The results show an inverse relationship between particle size and the rate at which particle contacts form, indicated by the steeper gradient of the smaller particle results. Agglomeration is first seen to occur at around $t = 0.001 \text{ s}$ for all particle sizes. For the 51 μm particles, the number of contacts increases smoothly with time, whereas in the larger particle cases the trend is more

variable, indicating a higher rate of contact breakage. This difference in contact breakage is explained by the differences in particle numbers, the cubed power-law relationship between particle radius and the particle overlap region (see JKR adhesion contact model in section 3), the fact that smaller particles encounter less fluid drag, and lastly larger particles having greater momentum for the collision which could lead to the breakage of the contacts. At the end of the simulation, for the 51, 102 and 150 μm particles, there are 42,209, 2,247 and 229 particle contacts in the flow, respectively. Reducing the particle diameter one half from 150 to 102 μm , for an equivalent volume fraction, therefore results in a 10 fold increase in contact number, with a further reduction to 51 μm giving rise to more than 18 times the number of contacts. A further reduction in particle size may not, however, necessarily lead to an increase in the number of particle contacts formed, as very small particles have low inertia and tend to track the fluid flow. From the above analysis, it is clear that the effects of flow turbulence are similar across all particle sizes (or Stokes numbers), and that the particle size is likewise a key factor in determining particle agglomeration in the flow. To further understand the extent to which particle size affects the mechanisms of particle agglomeration and dispersion, it would be beneficial to analyse in detail the particle collision frequency, the contact strength, and particle drag and dispersion, although this will be the subject of further work.

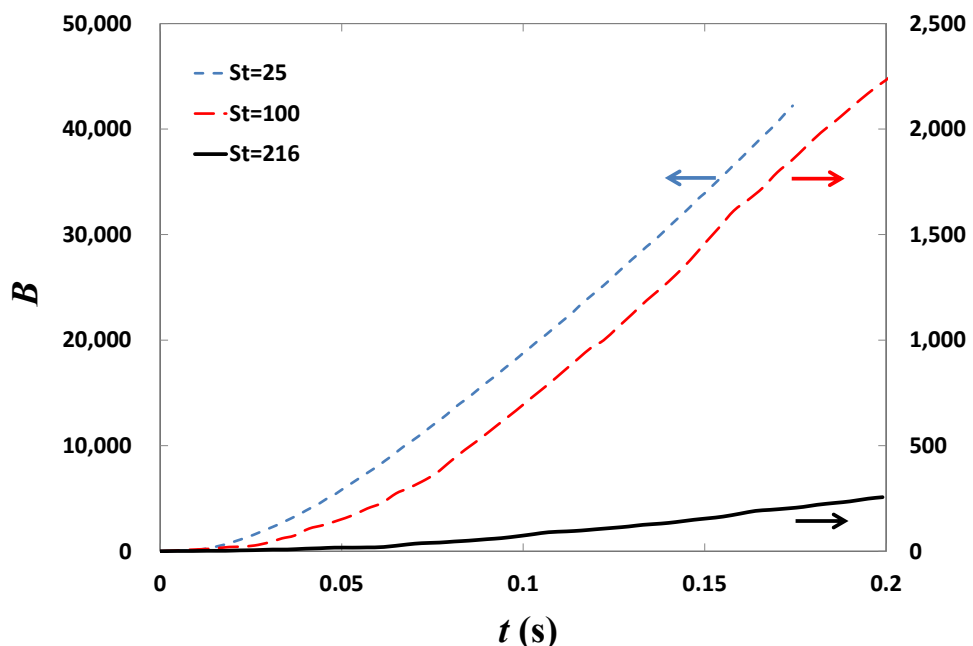


Figure 5.31 Number of contacts, B , formed between particles with time, t , for variations in particle size.

Figure 5.32 (a), (b) and (c) compare the instantaneous distribution of particle position and contacts for different particle sizes (i.e. 51, 102 and 150 μm) and a surface energy 0.05 J m^{-2} , at time $t = 0.2 \text{ s}$. Results are shown for 50 equally spaced regions across half the channel height, with particle statistics combined within each of the slabs of fluid considered. The columns for the number of contacts are plotted in relation to the channel walls, with column 1 adjacent to the lower and upper walls and column 50 at the channel centre. In order to compare the effects of different variables on particle agglomeration in flows with different particle concentrations, the local number of contacts, $B=B(s)$, has been normalised by the mean number of contacts, B_m . Furthermore, the local particle concentration $C=C(s)$, has been normalised against the concentration, C_0 , at an earlier time step of $t = 0.1 \text{ s}$ so that the results are independent of the initial conditions imposed on the particles. Again, a general increase in particle agglomeration is seen towards the channel walls. For the 51 and 102 μm particles, at the channel centre (column 50) the normalised number of bonds is 0.43 and 0.72, with these values increasing towards the walls at a high rate, where for columns 1 and 2 they increase to an average of 11.9 and 4.48, and 4.68 and 2.67, respectively. In contrast, the 150 μm particle bonds are more dispersed within the channel. The results therefore suggest that smaller particles have a greater propensity to form particle agglomerates throughout the channel, which is further aided by regions of high turbulence in the buffer layer and high particle concentrations at the walls. Figure 5.33 shows particle and contact number density profiles as a function of distance to the wall. These plots are more refined than Figure 5.32; results are shown for equally spaced regions across half the channel height that are equivalent in size to the particle radius. The results show that there are more 51 and 102 μm particles compared to the 150 μm particles

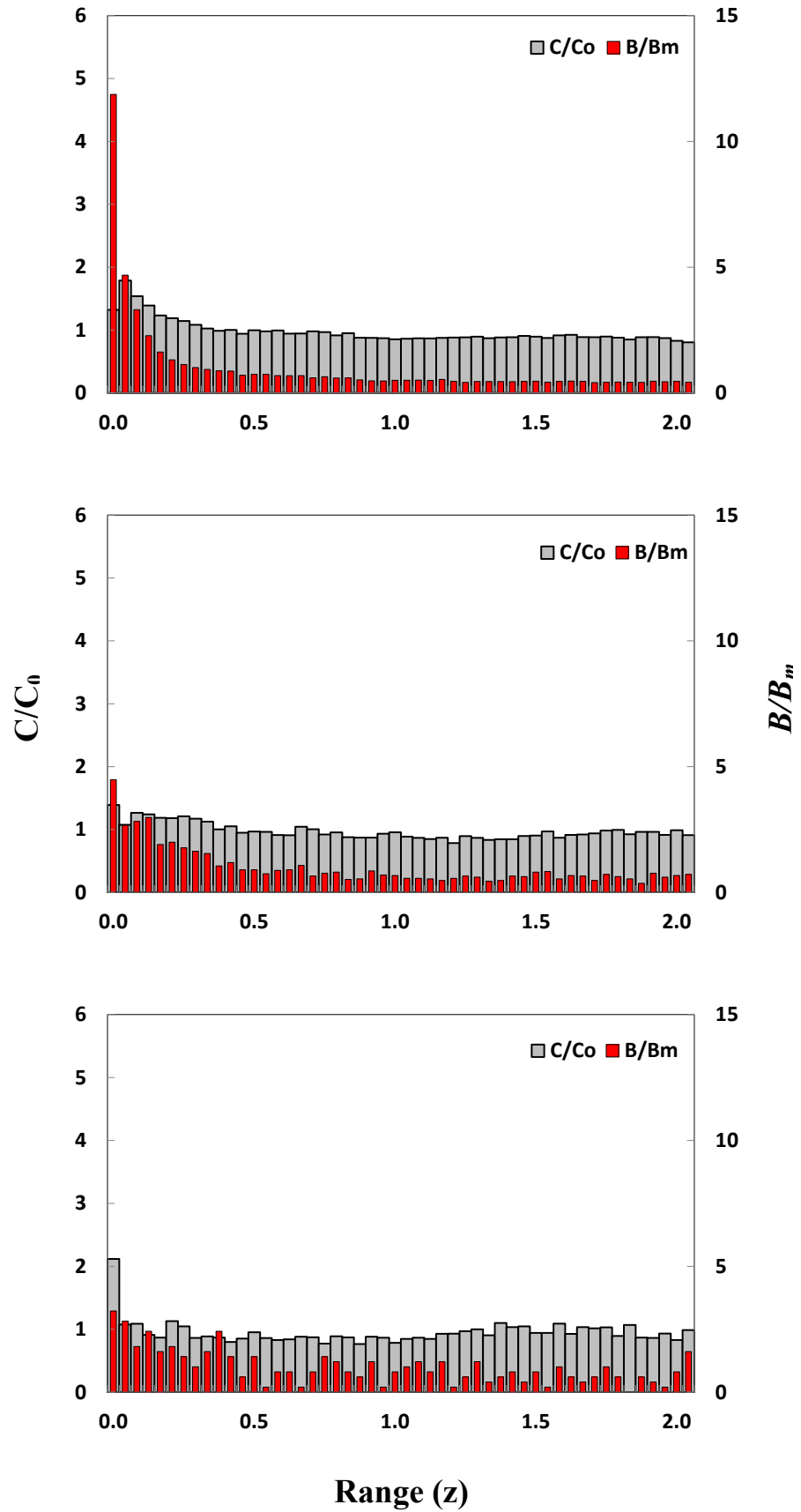


Figure 5.32 Contact, B/B_m , and particle concentration, C/C_0 , distribution across the channel at $t = 0.2$ s for (a) 51 μm, (b) 102 μm, and (c) 150 μm.

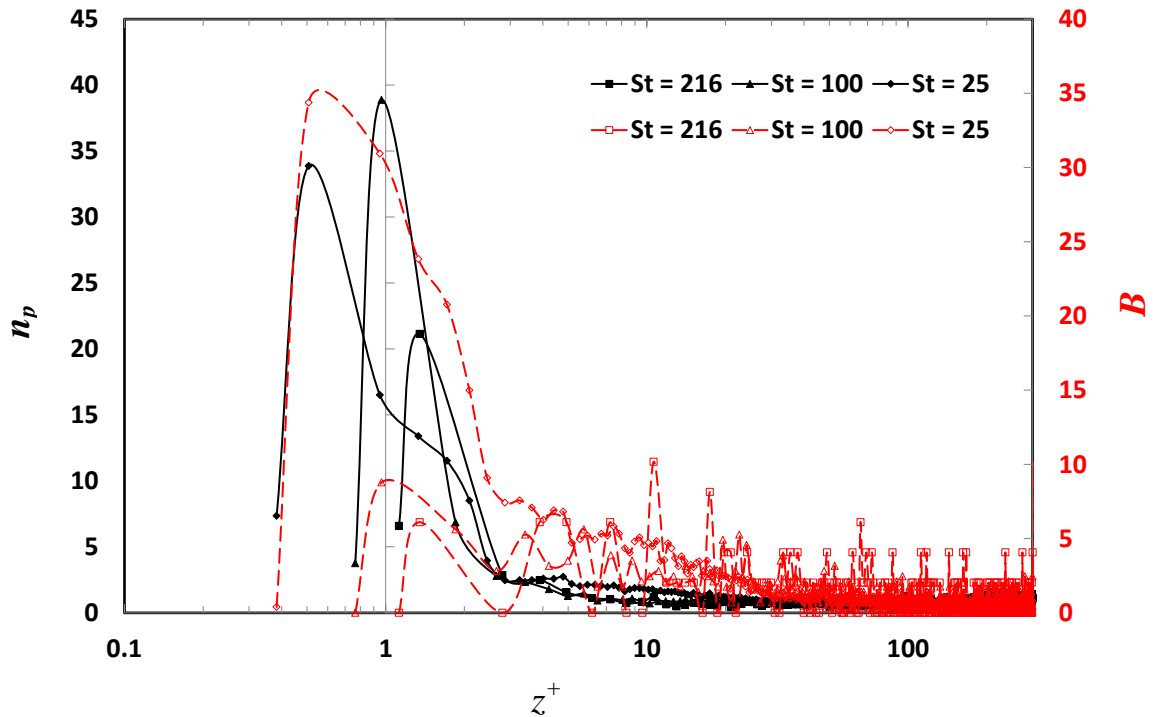


Figure 5.33 Particle, n_p , and particle-particle contact, B , number density profiles across the channel for variations in particle size ($t = 0.2s$).

Figure 5.34 shows number of particle collisions and the corresponding normal component of the impact (relative) velocity for 51 μm particles throughout the simulation ($t = 0.0 - 0.2$ s). The sticking velocities have been calculated for 51, 102 and 150 μm particles with a surface energy of 0.05 J m^{-2} (see Table 5-7). Based on this cut-off point the number of successful collisions are 15'876/25'115, 2'295/6'570, and 980/3'860 for these particles, which equals 25, 35, and 63 % respectively. Therefore, the likelihood that a collision will lead to a contact increases for smaller particle sizes. Decreasing the particle size by 1/3 from 150 to 102 μm , results in more than double the number of contacts. However, a further decrease by 1/2 gives rise to almost 7 times the number of successful collisions. This is due to an increase in both particle surface energy and particle number for smaller particles. Figure 5.35 shows the time evolution of the maximum value of the particle number density, n_p^{max} , near the wall. The results show that two competing effects are relevant, making the analysis more complicated, namely particle concentration and Stokes number.

Table 5-7 Sticking velocity of different sized particles

Diameter (μm)	51	102	150
Sticking Velocity (m/s)	0.86	0.48	0.35

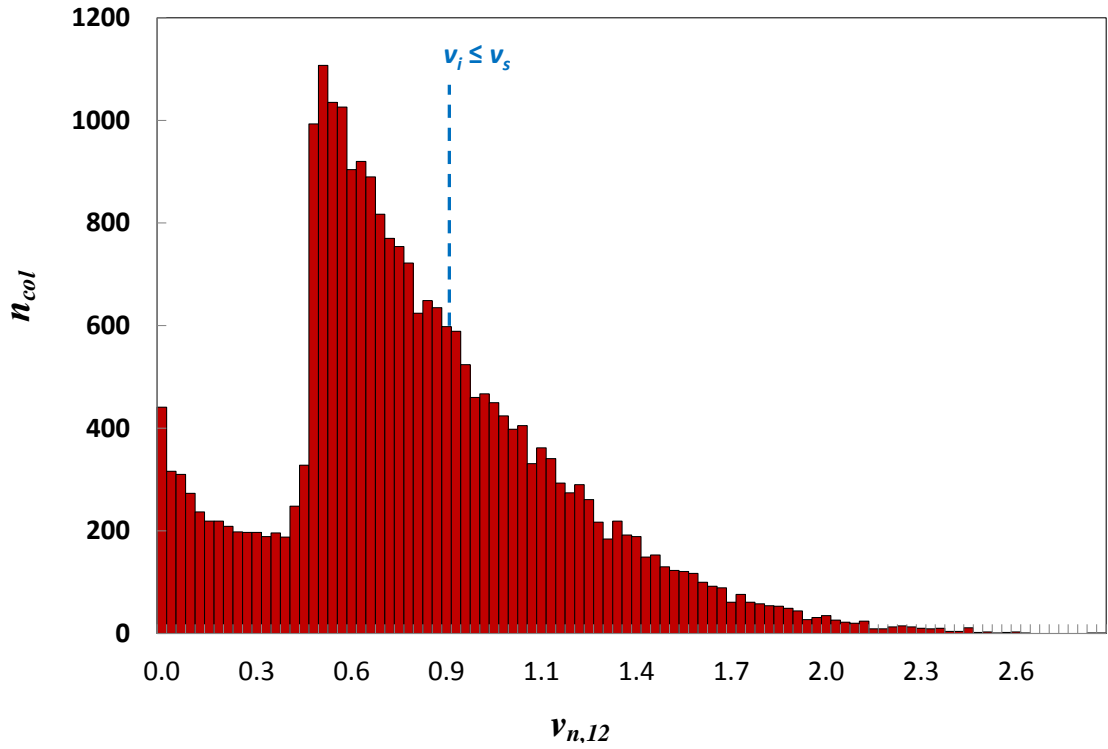


Figure 5.34 Number of particle-particle collisions, n_{col} , and their relative velocity normal, $v_{n,12}$ for $51\mu\text{m}$ ($t = 0.0 - 0.2$ s). The vertical dotted blue line indicates the maximum sticking velocity for a surface energy of 0.05 J/m^2 .

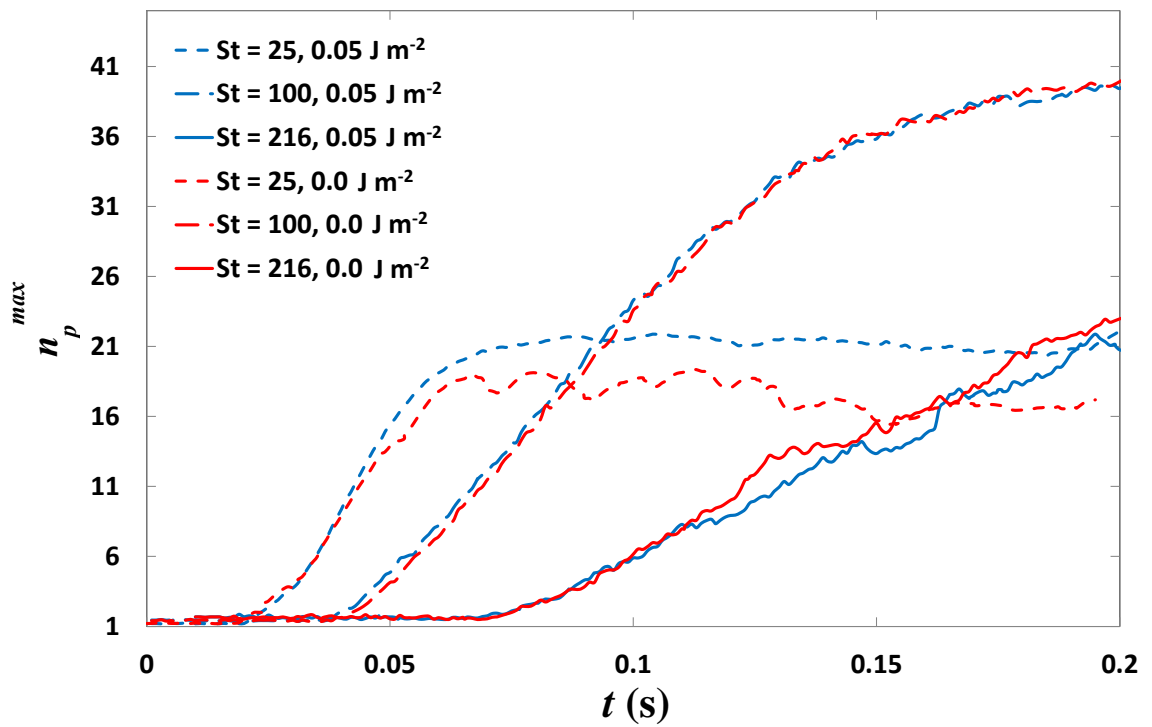


Figure 5.35 Maximum value of particle number density at the wall, n_p^{max} , as function of time, t , for variations in particle size.

5.5 Effects of particle concentration on agglomeration

This section investigates the effects of particle concentration on particle agglomeration, three different particle numbers have been considered, 5,605, 20,000 and 71,489, which correspond to volume fractions of 7.84×10^{-6} , 2.80×10^{-5} and 1.00×10^{-4} , respectively. A surface energy of 0.05 J m^{-2} was selected for this study, with the corresponding particle relaxation time, Stokes number and other relevant parameters given in the last row of Table 5-2.

Figure 5.36 shows particle contact formation for the three different particle numbers mentioned above. For all particle concentrations there is an increase in the number of contacts with time, with the rate at which the particle contacts form increasing with concentration. Agglomeration is first seen at approximately $t = 0.015$, 0.001 and 0.004 s for the 5,605, 20,000, and 71,489 particle numbers. This reflects that for low particle concentrations the particles have to disperse a greater distance before coming into contact. For the lowest concentration flow, the rate of contact formation remains consistent and almost linear with time. In the case of the medium and high concentrations, however, initially the rate of contact formation increases roughly linearly with time but then changes to an exponential profile at about $t = 0.02$ s, before reverting back to a linear relationship around $t = 0.07$ s. This is most apparent for the highest concentration case, where the trend shows a more evident transition from exponential to a very steep linear relationship, indicating that the flow accelerates the particles to an approximately constant bulk particle velocity. Closer examination of the results shows that the highest concentration flow diverges from the lower concentration cases at the very start of the simulation, with the divergence increasing as the particles increase in their velocity. This trend is again repeated at $t = 0.06$ s where the medium concentration flow deviates at an increasing rate from the low concentration case. For the low, medium and high volume fraction flows, respectively, there are 21, 265 and 2,675 particle contacts in the flow at the end of the simulation. These figures demonstrate that a three and a half fold increase in particle number dramatically increases the number of particle contacts. It is thus clear that the collision frequency in turbulent flows is not directly proportional to the particle concentration, i.e. an increase in particle number gives an exponential rise in the number of particle contacts.

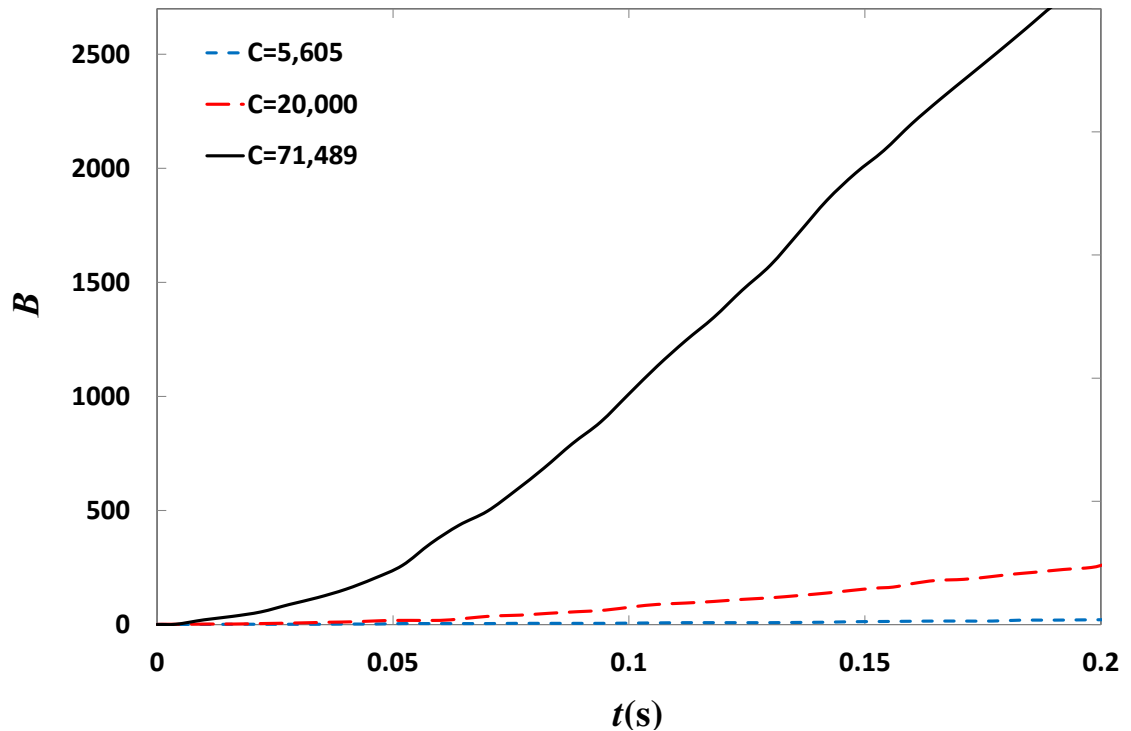


Figure 5.36 Number of contacts formed between particles, B , with time, t , for variations in particle concentration.

Figure 5.37 shows the instantaneous location of individual particles and contacts in the wall-normal direction for low surface energy particles (0.05 J m^{-2}) at low (5,605, Figure 5.37(a)), medium (20,000, Figure 5.37(b)), and high (71,489, Figure 5.37 (i)) concentrations, and their number at each location, at time $t = 0.2 \text{ s}$. Results are shown for 50 equally spaced regions across half the channel height, with particle statistics combined within each of the slabs of fluid considered. The columns for the number of contacts are plotted in relation to the channel walls, with column 1 adjacent to the lower and upper walls and column 50 at the channel centre. In order to compare the effects of different variables on particle agglomeration in flows with different particle concentrations, the local number of contacts, $B=B(s)$, has been normalised by the mean number of contacts, B_m . Furthermore, the local particle concentration $C=C(s)$, has been normalised against the concentration, C_0 , at an earlier time step of $t = 0.1 \text{ s}$ so that the results are independent of the initial conditions imposed on the particles. In the low concentration flow, particles form contacts in different regions of the channel and are well dispersed, whereas a large number of particles are segregated at the walls. A higher fraction of contacts are present closer to the channel walls, with columns 1-5 containing 14.3% of the total number of contacts. The medium concentration flow contains

particle-particle contacts that are more concentrated closer to the channel walls, with columns 1-5 accounting for 23.8% of the total number of contacts. Lastly, in the high concentration flow, particle contacts are again well dispersed, as seen in the lower concentration flow, where columns 1-5 contain 16.8% of the total number of contacts. This behaviour indicates that a very high concentration of particles damps the flow turbulence and/or slows down the rate of particle dispersion in the flow.

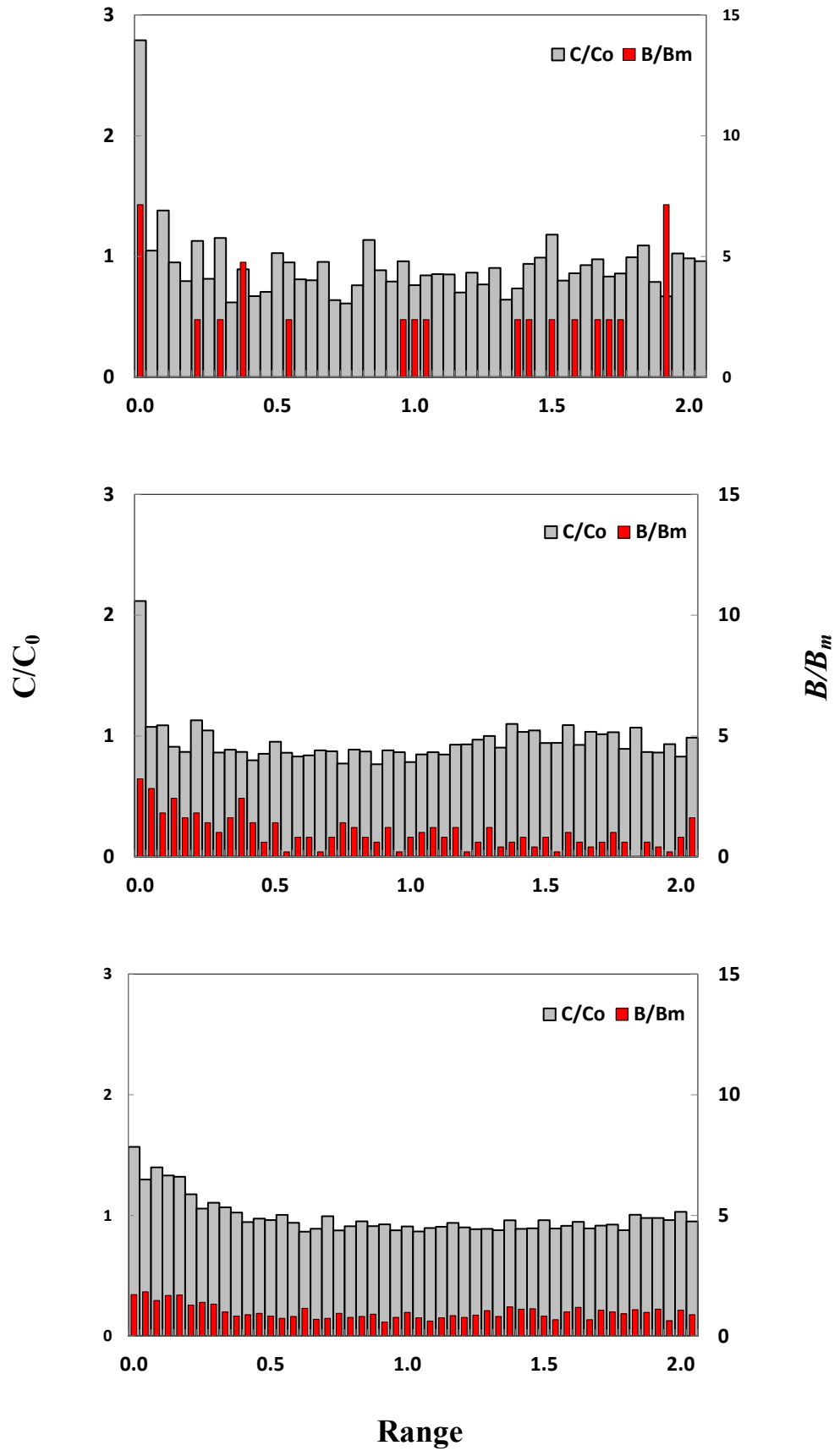


Figure 5.37 Contact, B/B_m , and particle concentration, C/C_0 , distribution across the channel at $t = 0.2$ s for (a) 5,605, (b) 20,000, (c) 71,489.

Figure 5.38 shows the time evolution of the maximum value of the particle number density, n_p^{max} , near the wall. The higher concentration flows (20'000 and 71,489) reach an asymptote earlier than the flow with the lowest particle concentration (5'605). This is mainly due to a large relative difference in particle number at the walls and in the main body of the flow for the lower concentration flow. Although, a high concentration of particles may damp the flow turbulence and/or lead to particles blocking each other and delaying particle drift. Turbulence modulation cannot be shown here, as it would require a very high run time.

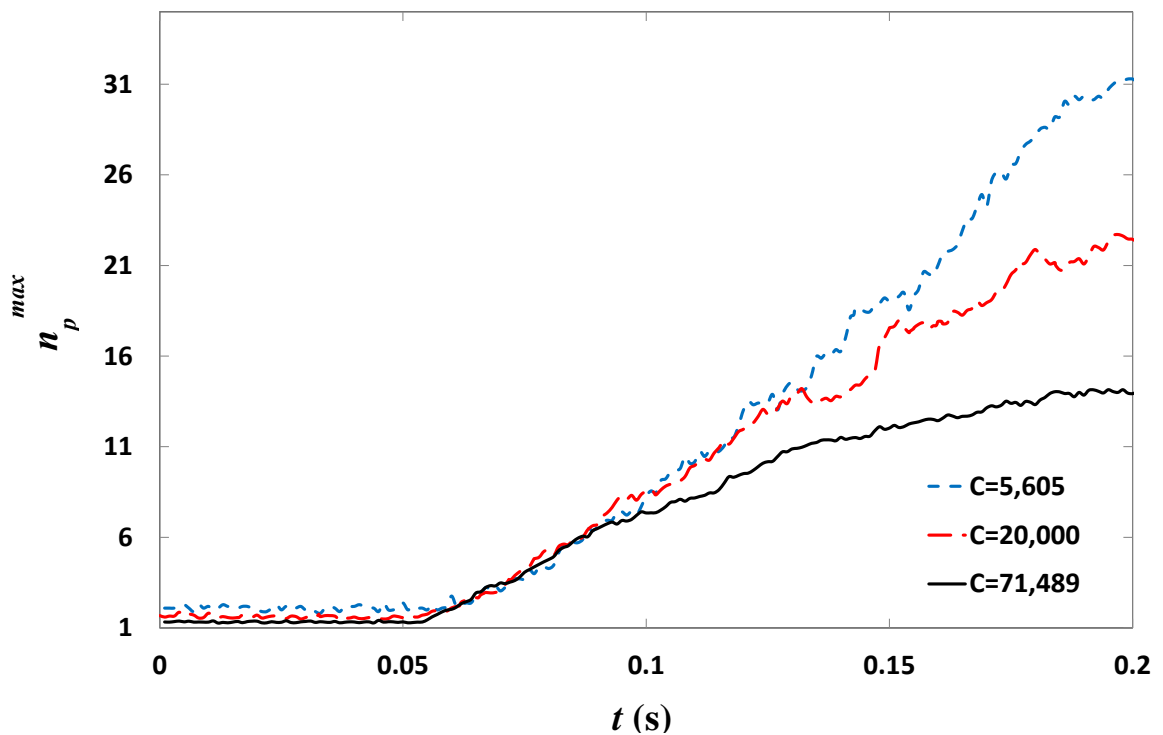


Figure 5.38 Maximum value of particle number density at the wall, n_p^{max} , as function of time, t , for variations in particle concentration.

5.6 Conclusions to sensitivity studies on particle dispersion and agglomeration

The work reported has focused on the prediction of those conditions that favour particle agglomeration and dispersion within turbulent channel flows using a fully coupled LES-DEM approach. Simulations have been carried out to investigate the effects of particle density, size and concentration on particle agglomeration. Furthermore, particles with different surface properties have been simulated in three channel flows with different

levels of flow turbulence, achieved by increasing the Reynolds number of the flow. It has been found that the turbulence structure of the flow dominates the motion of the particles, creating particle-particle interactions, with most of these interactions taking place at locations close to the channel walls and in regions of high turbulence where their agglomeration is aided both by the high levels of turbulence and the high concentration of particles. A positive relationship between particle surface energy, density, concentration and size, and agglomeration, was observed. Moreover, the results derived for the three Reynolds numbers considered show that the rate of agglomeration is strongly influenced for high surface energy particles by, and increases with, the intensity of the flow turbulence. In contrast, for lower surface energy particles, the rate of agglomeration diminishes with an increase in flow turbulence intensity.

6 Particle Dispersion, Deposition and Agglomeration

6.1 Effects of gravity on particle dispersion, deposition and agglomeration

This sub-section investigates the effects of gravity on particle agglomeration. This has been achieved by investigating two different horizontal channel flows; one which excludes gravity effects, and another in which the gravitational force is taken as 9.81 m s^{-2} acting in the downwards direction. A surface energy, size and density of 0.05 J m^{-2} , $150 \text{ }\mu\text{m}$ and 150 kg m^{-3} have been considered due to their practical implications, respectively, for a total number of 20,000 particles. Other physical properties have been kept constant with chapter 5 (see Table 5-1). All particles have been introduced at the local fluid velocity in this section and the following. To ensure the reproducibility of results, the computational procedure used in computing particle statistics has also been kept constant with the previous results chapters.

Figure 6.1(a) shows particle-particle contact formation for the two different channel flows mentioned above. For the zero gravity flow, the rate of contact formation increases roughly linearly with time. In the gravity system however, the number of contacts increase exponentially before approaching an asymptote and reaching steady state at $t^+ \approx 6,000$, indicating a higher rate of contact formation. Further scrutiny of the results shows that agglomeration is first seen to occur around the same time for both flows ($t^+ \approx 10$). At the end of the simulation ($t^+ \approx 7,948$), for the 0.0 and 9.81 m s^{-2} flows, there are 19,279 and 40,414 particle contacts in the flow, respectively. Therefore, the incorporation of gravity effects results in more than twice the number of contacts. Although, if the simulation is run further, this difference is likely to decrease with time as the contact number for the zero gravity flow hasn't reached steady state at the end of the simulation. From the above analysis, it is clear that the effects of flow turbulence are responsible for particle agglomeration in the flow. Moreover, this is magnified with the incorporation of gravity due to an increased local concentration in the bottom half of the channel. To further understand the extent to which gravity affects the mechanisms of particle agglomeration and dispersion, it is necessary to analyse the particle collision frequency, contact and collision locations, and phase coupling forces. Figure 6.1(b) shows the cumulative number of particle-particle collisions for the 0.0 and 9.81 m s^{-2}

flows. In general, the rate of pcollisions increases with time. For the zero gravity system this increase is linear, whereas for the gravity system an exponential increase is seen up to $t^+ \approx 5,000$, after which it starts to decay. This exponential profile is indicative of particle net deposition on the channel floor. Comparing the contacts (Figure 6.1(a)) against collisions (Figure 6.1(b)) the results exhibit similar behaviour to that seen for contact formation; the profiles are seen to diverge in the same manner with time. Closer analysis of the results however, shows that the difference between collision profiles is far greater, and this increases with time. It is therefore possible to deduce that the collisions in the zero gravity are more successful in forming particle-particle contacts.

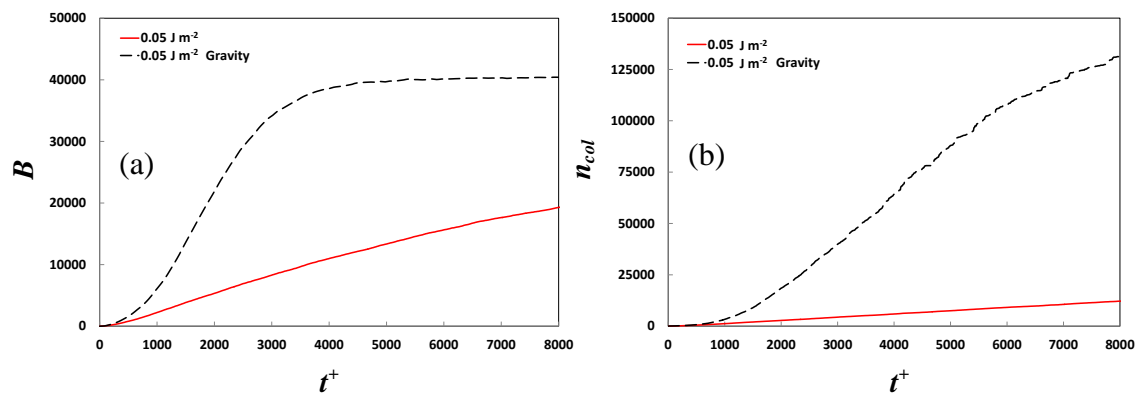


Figure 6.1 Number of contacts, B , (a) and cumulative collisions, n_{col} , (b) between particles as a function of time.

Figure 6.2(a,b) show the instantaneous location of individual particles in the wall-normal direction, and their number n_p at each location, at time $t^+ = 7,948$. Results are presented for equally spaced bins across the bottom half of the channel height that are equivalent in size to the particle radius. Generally, the particles are seen to accumulate at the bottom wall. For the zero gravity flow, moving away from the channel centre, the particles are uniformly distributed across the channel cross section up to $z^+ = 10$, after which they increase to a maximum $n_p = 964$ at $z^+ = 1.6$, before decreasing to 22 at the walls. In the case of the gravity system however, all are situated below $z^+ = 92$, from here this value increases to a maximum $n_p = 794$ at $z^+ = 12$, before decreasing to 379 at the walls. Therefore, unexpectedly, despite all particles being situated in the channel bottom half, there are fewer particles in the near wall region for the gravity case. Figure 6.3a,b show the number of particle-particle contacts B and total collisions n_{col} in the wall-normal direction, at times $t^+ = 7,948$ and $t^+ = 0 - 7,948$, respectively. The binning

procedure used is the same as that in Figure 6.2. Generally the number of contacts increases towards the walls in consort with the number of collisions which is related to the regions of high particle concentration seen in Figure 6.2(a,b). From further scrutiny of the results it is seen that for the gravity flow, although n_p and B align, n_{col} is shifted to the left. This may be as a result of different fluid shearing at the wall or particle-wall interactions.

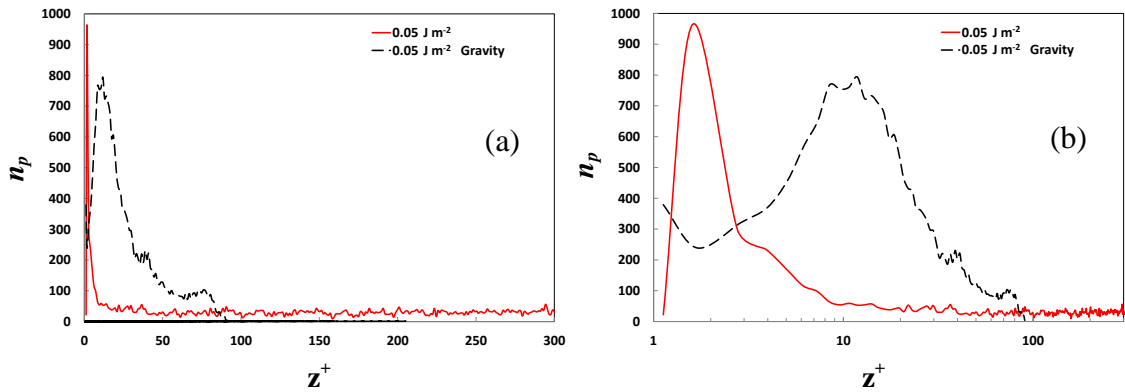


Figure 6.2 Particle number profiles, n_p , in wall-normal direction at time $t^+ = 7,948$ ($t = 2.25$ s): (a) linear, (b) log

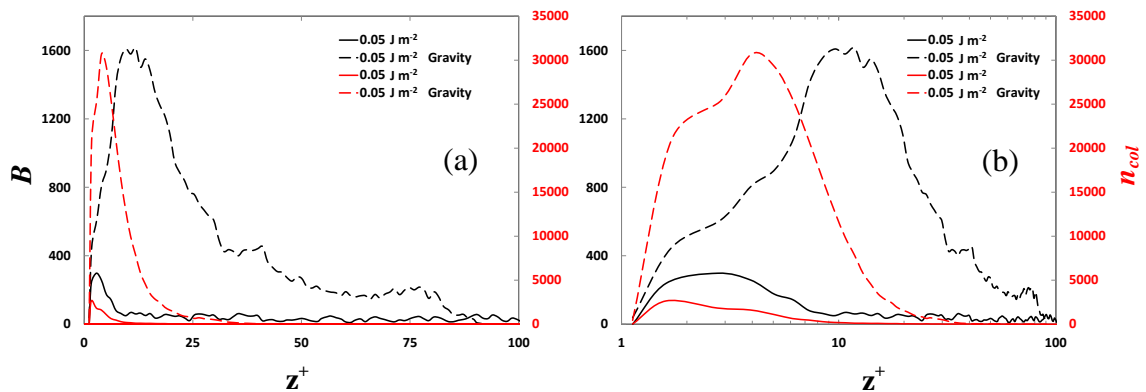


Figure 6.3 Particle-particle contact, B , and collision, n_{col} , profiles in the wall-normal direction for time $t^+ = 7,948$ and $t^+ = 0 - 7,948$, respectively.

In this section, force analysis has been used to calculate a summation of the main coupling forces ($F_{i,coupling}$) acting on the particles (gravity, lift, and drag) at steady state $t^+ = 7,948$. The results are given in Table 6-1 with the streamwise ($F_{x,coupling}$) and wall-normal ($F_{z,coupling}$) components shown for the channel flow. For the zero gravity system, there is not much difference between the two components of $F_{i,coupling}$ due to the negligence of gravity. Although their magnitudes are still relatively high, this suggests

the streamwise component of drag force dominates particle motion in the channel flow, whereas as the wall-normal component of drag force dominates particle drift. In the case of the gravity system however, $F_{z,coupling}$ is greater than $F_{x,coupling}$ by half an order of magnitude, suggesting that gravity dominates the motion of these particles. Comparing the results for the gravity and zero gravity system, it is found that $F_{i,coupling}$ is over one order of magnitude greater in both the streamwise and wall-normal directions. This occurrence can be contributed to the extent of particle agglomeration. The results indicate that the particles deposit at a relatively high velocity towards under the influence of gravity towards the channel floor, causing an increase in local concentration that promotes particle agglomeration. These agglomerates have high inertia, which results in the higher drag force reflected in the magnitude of $F_{x,coupling}$.

Table 6-1 Comparison of effect of the mean of main forces (Gravity, Lift, and Drag) on particles ($t^+ = 7,948$)

Gravitational Acceleration	Coupling Force (N)	
	$F_{x,coupling}$	$F_{z,coupling}$
0.0 m s^{-2}	4.24×10^{-11}	6.01×10^{-11}
9.81 m s^{-2}	7.45×10^{-10}	1.79×10^{-9}

6.2 Effects of surface energy on dispersion, deposition and agglomeration

In the previous sub-section (6.1), it was seen that for the system considered, the effects of gravity are significant on particle agglomeration. This sub-section investigates the effects of particle surface energy on agglomeration under the influence of gravity. Surface energies of 0.01 and 0.05 J m^{-2} have been considered with all other physical parameters and inlet and boundary conditions kept constant with section 6.1.

Results obtained when particles are introduced into the flow are shown in Figure 6.4, which gives a perspective view of instantaneous distributions of particles crossing (x, z) planes at various time instants. For low surface energy particles (0.01 J m^{-2} , Figure 6.4a-c), the effect of gravity leads to accumulation of particles within the lower half of the channel. Although, there distribution does not change much beyond $t^+ = 3,533$. At high particle surface energies (0.05 J m^{-2} , Figure 6.4(d-f)), however, the majority of particles are seen to deposit on the channel floor. In terms of the distribution of particles, the existence of competing gravitational and flow turbulence influences clearly lead to

different dispersion characteristics depending on particle surface energies, with gravity decoupling particle behaviour from the effects of flow turbulence structure which subsequently affects the particle wall-normal distribution and deposition rate, particularly for higher surface energy particles.

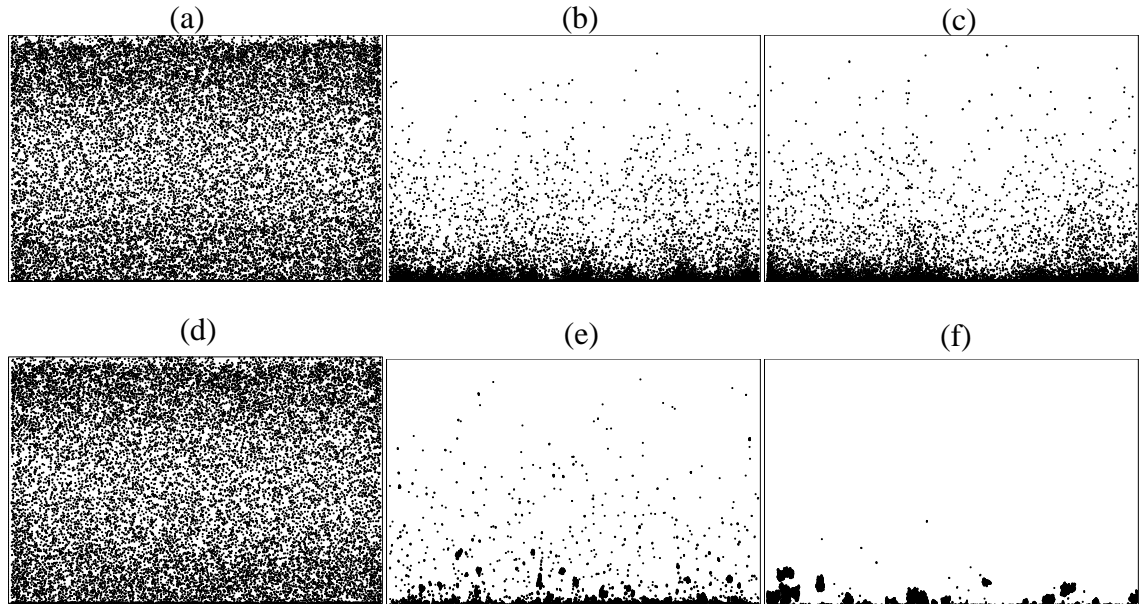


Figure 6.4 Instantaneous distribution of particles on (z, y) planes perpendicular to the streamwise direction: 0.01 J m^{-2} (a) $t^+ = 71$; (b) $t^+ = 3,533$; (c) $t^+ = 7,948$ and 0.05 J m^{-2} (d) $t^+ = 71$; (e) $t^+ = 3,533$; (f) $t^+ = 7,948$.

Figure 6.5a shows particle-particle contact formation for the 0.01 and 0.05 J m^{-2} surface energies. Generally, the number of contacts increases with time. For the 0.01 J m^{-2} particles, the rate of contact formation increases roughly linearly to an asymptote at around $t^+ = 2,575$. In the case of the 0.05 J m^{-2} particles however, the number of contacts increase exponentially before approaching an asymptote and reaching steady state at $t^+ \approx 6,000$, indicating a higher rate of contact formation. Further scrutiny of the results shows that agglomeration is first seen to occur around the same time for both surface energies ($t^+ \approx 10$). At the end of the simulation ($t^+ \approx 7,948$), for the 0.01 and 0.05 J m^{-2} particles, there are 3,078 and 40,414 particle contacts in the flow, respectively. Therefore, a fivefold increase in the surface energy results in the number of contacts increasing by one order of magnitude. From the above analysis, it is clear that the effects of surface energy are responsible for particle agglomeration in the flow. Moreover, this is increased with the incorporation of gravity due to an increased local concentration in the bottom half of the channel. To further understand the extent to

which gravity affects the mechanisms of particle agglomeration and dispersion, it is beneficial to analyse the particle collision frequency, particle dispersion and deposition rates, and particle and bond concentrations along the channel height. Figure 6.5b shows the cumulative number of particle-particle collisions for the 0.01 and 0.05 J m⁻² surface energies. The rate of collisions is seen to generally increase with time. For the 0.01 J m⁻² particles there is an initial exponential climb of particle collisions up to $t^+ = 1,547$ followed by a linear rate until the end of the simulation. For the 0.05 J m⁻² particles yet again the exponential increase and translation to a linear profile is seen, however, the rate of particle-particle collisions is lower compared to 0.01 J m⁻² particles. Moreover, the collision rate starts to decline at $t^+ = 5,945$, which will inevitably result in the number of collisions approaching a constant value.

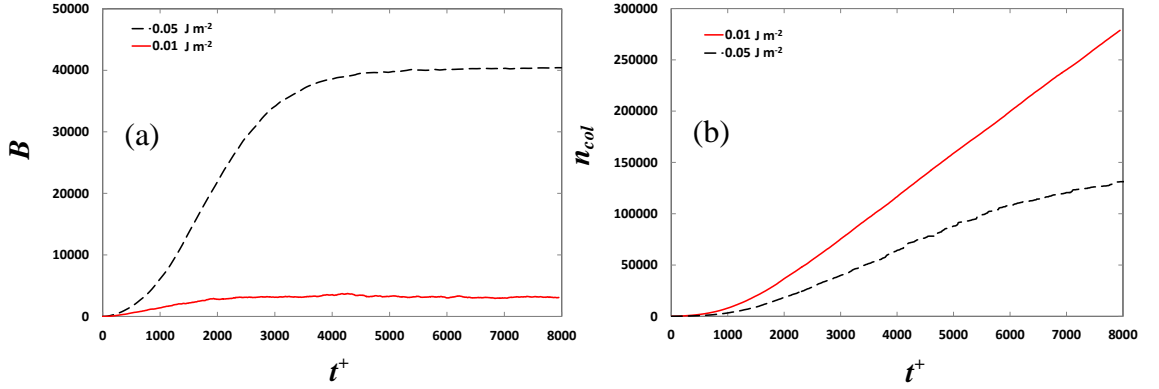


Figure 6.5 Number of contacts, B , (a) and cumulative collisions, n_{col} , (b) between particles as a function of time for variations in particle surface energy.

To investigate particle dispersion in the channel flow quantitatively, the dispersion function in the wall-normal, z , direction for particles distributed in the channel can be represented by the following equation:

$$D_z^+(t) = \left[\sum_{i=1}^{n_t} \frac{(z_{i(t)}^+ - z_{i(m)}^+)^2}{n_t} \right]^{\frac{1}{2}} \quad (6-1)$$

where n_t is the total number of particles in the computational domain at time t , $z_{i(t)}^+$ is the particle displacement in the wall-normal direction, and $z_{m(t)}^+$ is the mean value, both relative to the centre-line of the channel.

Figure 6.6(a) shows results for the time dependent particle dispersion in the wall-normal direction. The results clearly illustrate a general decrease in mean particle displacement with time due to the effect of gravity; furthermore, the rate at which the particles deposit increases with particle surface energy. For both the 0.01 and 0.05 J m^{-2} particles, the trends are very similar; the rate of deposition is seen to be significantly high and most particles deposit within $t^+ \approx 3,500$. After this point, the value of particle dispersion remains almost constant with time ($z_m^+ \approx -278$). Further scrutiny of the results, however, shows that for the 0.05 J m^{-2} particles, particle dispersion oscillates around this value much more in relation to the 0.01 J m^{-2} particles. It is also observed that the rate of particle deposition decreases as the particles approach the bottom of the channel. Therefore, physically further into the simulation, the particle velocity is lower than it was earlier, with the particles being in closer proximity to the floor. This is because the particles are subjected to a shear field flow and affected by the Saffman lift force in the wall-normal direction; the shear lift increases as the particles draw nearer to the floor brought about by the inertia effects in the viscous flow around the particle. The dispersion function is the standard deviation and on this basis a large dispersion function depicts a large dispersion of particles, and vice versa. Examination of the results presented in Figure 6.6b, reveals that for both the 0.01 and 0.05 J m^{-2} particles, the function decreases rapidly with time up to $t^+ = 2,830$. For the 0.01 J m^{-2} particles, from here onwards, the dispersion function remains constant ($D_x^+ \approx 53$). In the case of the 0.05 J m^{-2} particles, however, the dispersion function continues to decrease to $t^+ = 5,650$, and also remains roughly constant from this point onwards ($D_x^+ \approx 21$). From the above analysis, it is clear that although the 0.01 and 0.05 J m^{-2} particles show similar mean displacement, a higher proportion of the 0.01 J m^{-2} particles are at the channel floor, and at the same time these particles are more distributed across the channel height. Furthermore, the 0.01 J m^{-2} particles deposit forming a uniform bed in the spanwise direction. In the case of the 0.05 J m^{-2} particles, however, these particles have a higher tendency to form agglomerates, therefore, they almost all deposit towards the channel floor where they arrange themselves into large clusters. The differences between the 0.01 and 0.05 J m^{-2} particles in terms of particle dispersion and deposition can be attributed to the effect of gravity. These findings are in tandem with the qualitative results described earlier.

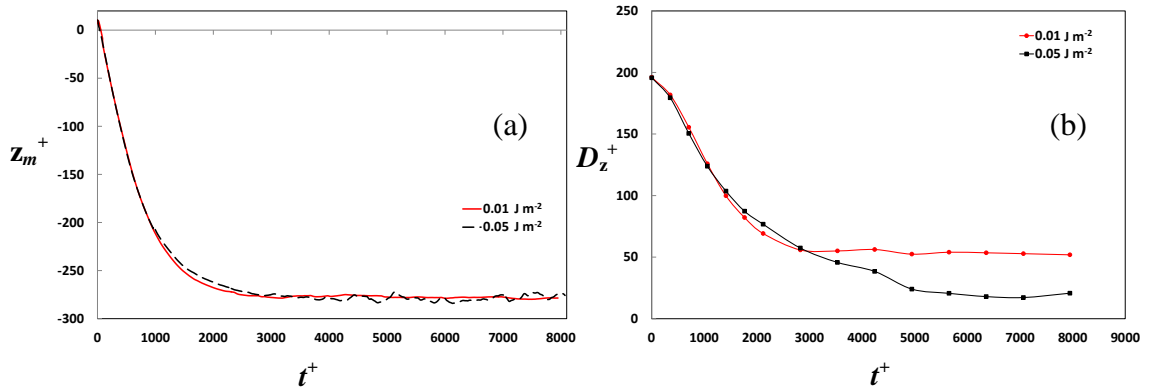


Figure 6.6 (a) Particle mean displacement and (b) dispersion function in the wall-normal direction with time for variations in surface energy.

To better understand the roles fluid turbulence and gravity play in the agglomeration and dispersion of particles in the channel, it is necessary to investigate the regions where the particle contact and collision locations are occurring. Figure 6.7(a,b) show the instantaneous location of individual particles in the wall-normal direction, and their number n_p at each location, at time $t^+ = 7,948$. Results are presented for equally spaced bins across the bottom half of the channel height that are equivalent in size to the particle radius. In general, the particles increase in concentration towards the bottom wall. For the 0.01 J m^{-2} surface energy, the particles are uniformly distributed between $49 < z^+ < 300$, from $z^+ = 49$ they increase linearly to a maximum ($n_p = 964$) at the wall. Whereas for the 0.05 J m^{-2} surface energy there are no particles present for $z^+ < 88$, and the concentration profile has a parabolic shape with a maximum ($n_p = 794$) at $z^+ = 11$. Moreover there are only 379 particles at bottom wall. The results, therefore, show that the 0.01 J m^{-2} particles are more successful in accumulating on the bottom surface of the channel compared to the 0.05 J m^{-2} . Figure 6.8a,b show the number of particle-particle contacts B and total collisions n_{col} in the wall-normal direction, at times $t^+ = 7,948$ and $t^+ = 0 - 7,948$, respectively. The binning procedure used is the same as that in Figure 6.7. Generally the number of contacts increases towards the walls in consort with the number of collisions which is related to the regions of high particle concentration seen in Figure 6.7. From further scrutiny of the results it is seen that for the 0.05 J m^{-2} particles, although n_p and B align, n_{col} is shifted to the left. This suggests that the particle agglomerates are moving in the upwards direction and away from the channel floor. Following this phenomenon it is necessary to analyse particle distribution, and particle-wall and particle-particle collisions in relation to particles velocities and their magnitude for different surface energy particles.

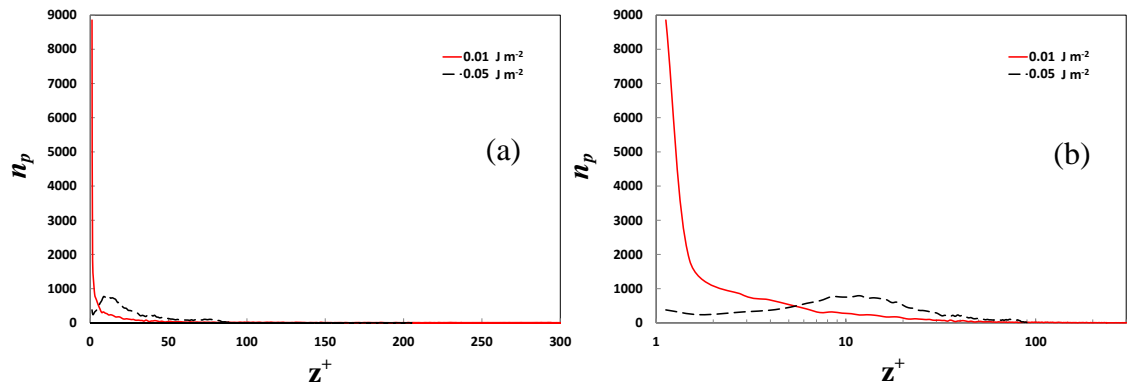


Figure 6.7 Particle number profiles in wall-normal direction, n_p , for variations in particle surface energy at time $t^+ = 7,948$ ($t = 2.25$ s): (a) linear, (b) log

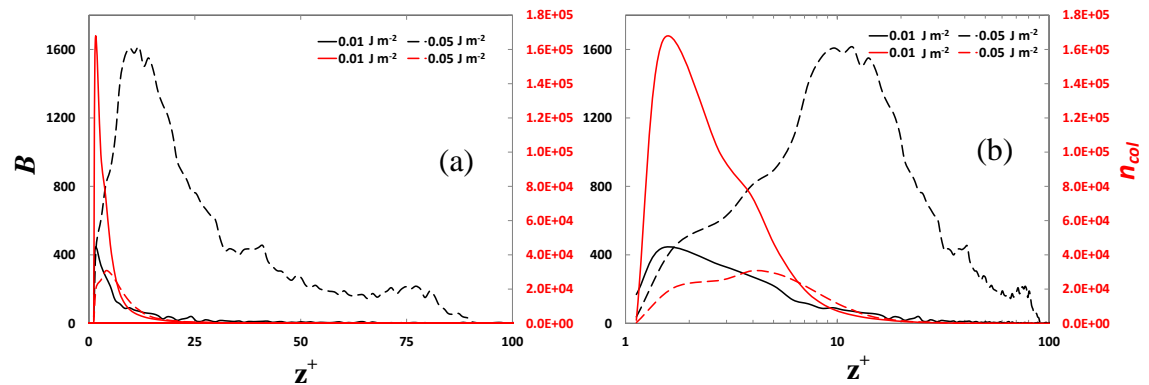


Figure 6.8 Particle-particle collision, n_{col} , and contact, B , profiles in the wall-normal direction for variations in particle surface energy at $t^+ = 0 - 7,948$ and $t^+ = 7,948$: (a) linear, (b) log

Figure 6.9a-f show the relationship between the instantaneous particle position in the wall-normal direction, for particle surface energies 0.01 and 0.05 J m^{-2} , and the distribution of velocity in this direction at three different times in the simulation, $t^+ = 71$, $3,533$, and $7,948$. The locations of the points are plotted in relation to the channel centre-line, with positive velocities indicating upward movement and negative downward movement. In Figure 6.9a ($t^+ = 71$), the 0.01 J m^{-2} particles are well dispersed along the wall-normal direction, with almost an equal number of particles situated above the centre-line (49 %), whereas, most of the particle velocities are associated with negative values (71 %). Therefore, indicating the importance of gravity effects on their distribution. Figure 6.9b once more illustrates the instantaneous distribution of particle position for the 0.01 J m^{-2} particles, but at the later time of $t^+ = 3,533$. The particles are no longer well dispersed with almost all particles located in the

lower half (99%), although, approximately half the particles have a positive velocity acting in the opposite direction to gravity (48%). This indicates that the particles are rebounding upwards off the channel floor ($z^+ = -300$). Lastly, in Figure 6.9c ($t^+ = 7,948$); there are no noticeable changes for the particle distribution and velocities in relation to Figure 6.9b. This behaviour indicates that agglomerate size has reached a threshold owing to fluid turbulence breaking the particle-particle contacts.

The results in Figure 6.9d-f show the instantaneous distribution of particle location and velocity for the 0.05 J m^{-2} particles in the same direction, again for $t^+ = 71, 3,533$ and $7,948$. In Figure 6.9d ($t^+ = 71$), similar to that seen for the 0.01 J m^{-2} particles (Figure 6.9a), the 0.05 J m^{-2} particles are well distributed in the wall-normal direction and their velocity is mostly negative. In Figure 6.9e ($t^+ = 3,533$), again similar to the 0.01 J m^{-2} particles (Figure 6.9d), virtually all particles are situated in the lower section of the channel (99%) and their velocity is almost symmetrical about $V_z^+ = 0$. Although in this case the 0.05 J m^{-2} particles are seen to move towards the channel bed in a very compact manner. In Figure 6.9f, when compared with the earlier time the particles are closer to the channel floor. Also, the particles velocity distribution is narrower with most of the particles (74%) having a positive velocity. For the 0.05 J m^{-2} particles, therefore, gravitational force causes them to move downward and hit the base of the channel and to rebound off it with an upward velocity. Moreover, because of their high cohesiveness this process significantly enhances particle agglomeration. Following the rebound, however, the effects of gravity overcome the motion of now particle agglomerates and draw them back towards the channel floor. This cycle then continues until the agglomerates completely settle down on the channel bed. From the above analysis, it can be concluded that the effects of both gravity and fluid turbulence are prominent in determining particle motion in a channel. For the low surface energy particles, the fluid turbulence and gravity are both influential in determining particle distribution and deposition. For high surface energy particles, gravity effects dominate particle movement and deposition.

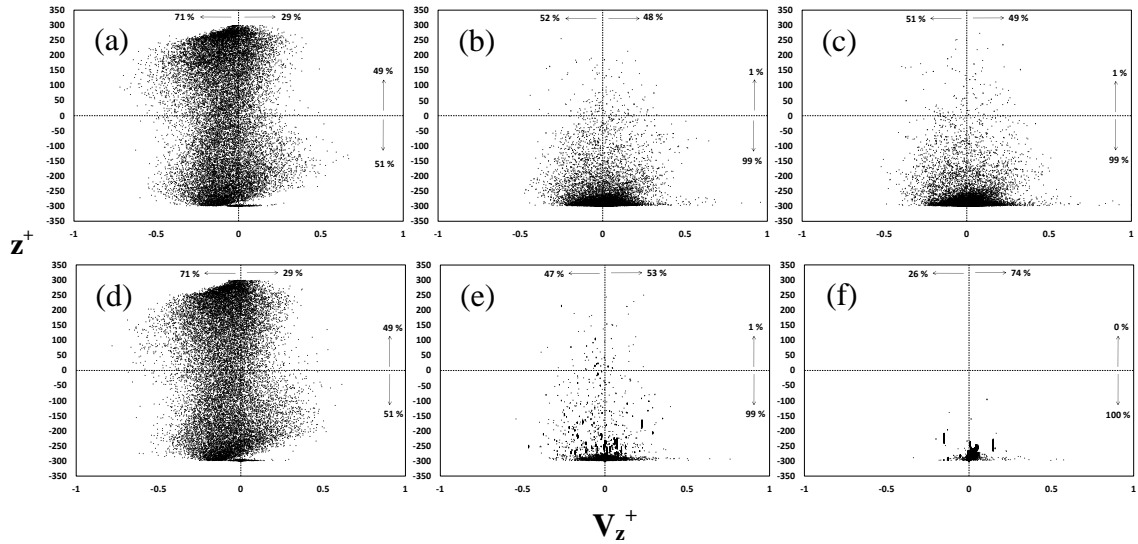


Figure 6.9 Instantaneous distribution of particle position and velocity a) 71; (b) 3,533; (c) 7,948 (0.01 J m^{-2}), (d) 71; (e) 3,533; (f) 7,948 (0.05 J m^{-2}).

Figure 6.10a shows the mean fluid streamwise velocity with time for the 0.01 and 0.05 J m^{-2} particles. The results show a general decrease in V_x^+ with time due to the effect of gravity. Initially the 0.0 and 0.05 J m^{-2} particles decrease at the same rate up to $t^+ = 407$, after this point the profiles diverge. As previously mentioned the exponential decay seen is indicative of particles slowing down when nearing the channel floor. From about $t^+ = 3,150$, for the 0.01 J m^{-2} particles, V_x^+ remains almost constant with time, whereas for the 0.05 J m^{-2} particles it increases. Figure 6.10b shows the mean fluid wall-normal velocity, for both surface energies V_z^+ is seen to initially increase in magnitude up to $t^+ = 96$, before decreasing to $V_z^+ = 0$ at about $t^+ = 3,150$. From here, for the 0.01 J m^{-2} particles, the behaviour is similar to that seen for the V_x^+ ; V_z^+ remains almost constant with time. In the case of the 0.05 J m^{-2} particles, however, V_z^+ does not increase as seen with V_x^+ , instead it oscillates very intensely around $V_z^+ = 0$.

In Figure 6.10c,d the mean fluid streamwise and wall-normal velocities are isolated for the particles at the bottom wall. The results show a general decrease in V_x^+ with time due to the no-slip boundary conditions imposed at the walls. In Figure 6.10c, for the 0.01 J m^{-2} particles, as they enter this region their velocity decreases to a constant value of about $V_x^+ = 1.18$ at $t^+ = 339$. The profile of the 0.05 J m^{-2} particles closely follows that of the 0.01 J m^{-2} until $t^+ = 1,430$, from this point the velocity increases causing it to diverge up to $t^+ = 3,550$ where it reaches an asymptote. Figure 6.10d shows that both surface energies lose their velocities early in the simulation and the 0.05 J m^{-2} profile

oscillates from mid-simulation onwards, these results are in accordance with the those discussed earlier;. This behaviour indicates that the high surface energy particle agglomerates are rolling on the bottom of the channel and increasing in size like a ‘snow ball effect’. The larger particle agglomerates see a higher streamwise velocity as they stretch further in the wall-normal direction.

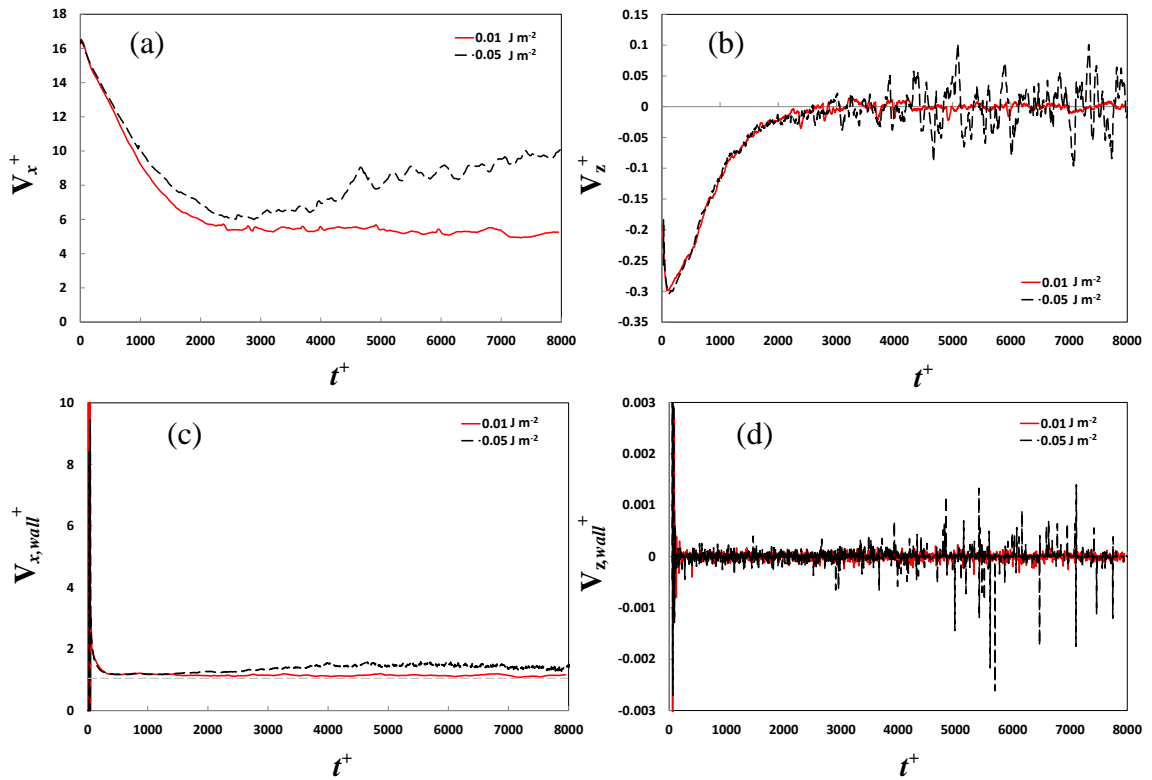


Figure 6.10 Mean particle velocity for (a) streamwise, (b) wall-normal (total); (c) streamwise and (d) wall-normal (wall), as a function of time.

Following the comparison of particle mean velocities, it is useful to consider the statistical correlation between particle concentration and fluid velocity in the channel. Figure 6.11 shows probability density functions of particle streamwise velocity throughout the domain for 0.01 and 0.05 J m^{-2} particles. Where V_x^+ is the instantaneous particle velocity; the frequency has been normalised by the maximum. The data sets have been sampled at well separated time steps (0.01s). Starting from the left axis, it is seen that there are more 0.01 J m^{-2} particles situated in regions of low fluid streamwise velocity ($V_x^+ < 2.2 \text{ m s}^{-1}$) compared to the 0.05 J m^{-2} . Although further scrutiny of the results reveals that only the 0.05 J m^{-2} particles actually reach zero. In contrast there are more 0.05 J m^{-2} particles for velocities between $2.2 < V_x^+ < 13.9 \text{ m s}^{-1}$. This is not the case however, at higher fluid velocities ($13.9 < V_x^+ < 21.4 \text{ m s}^{-1}$) where there are more

0.01 J m⁻² particles present. Relating the fluid velocities in Figure 6.11 to the mean velocity profile for $Re_\tau = 300$, it is possible to identify the regions that the velocities represent in the channel cross section. Based on this, the results indicate that there are more 0.01 J m⁻² particles in the low and high velocity regions of the channel, which correspond to the viscous sublayer and outer region. Whereas, there are more 0.05 J m⁻² particles in the mid-velocity regions which correspond to the buffer layer.

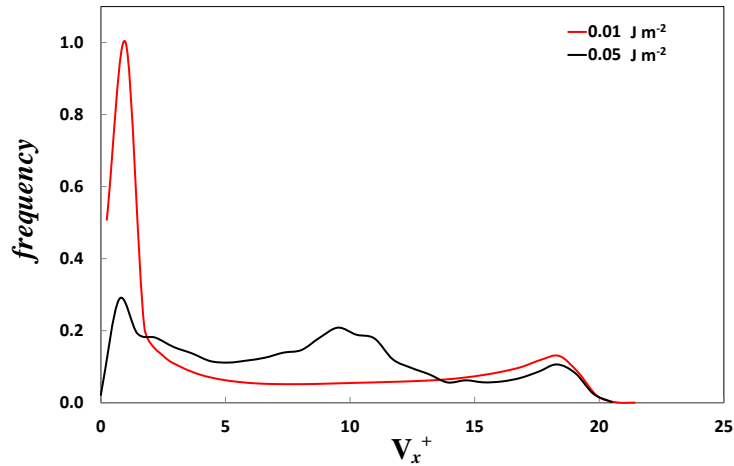


Figure 6.11 Probability density function of fluid streamwise velocity ($t^+ = 0 - 7,948$).

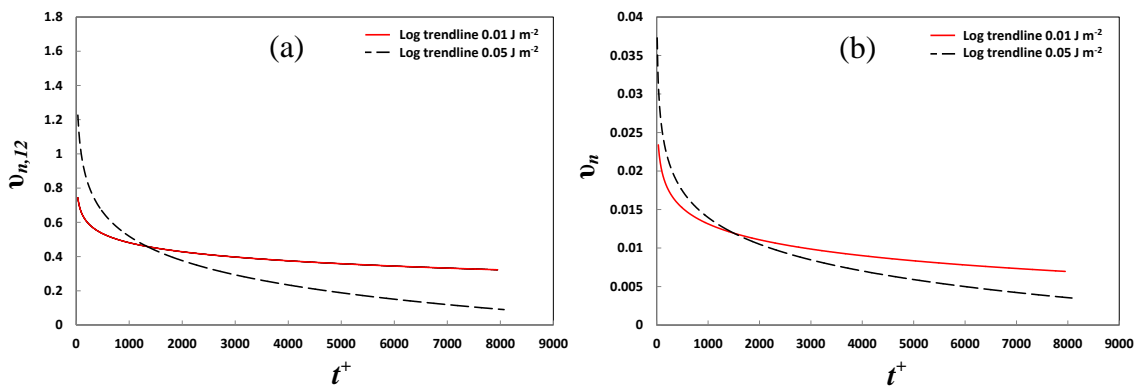


Figure 6.12. Mean relative (impact) velocity normal with time for (a) particle-particle, (b) particle-wall.

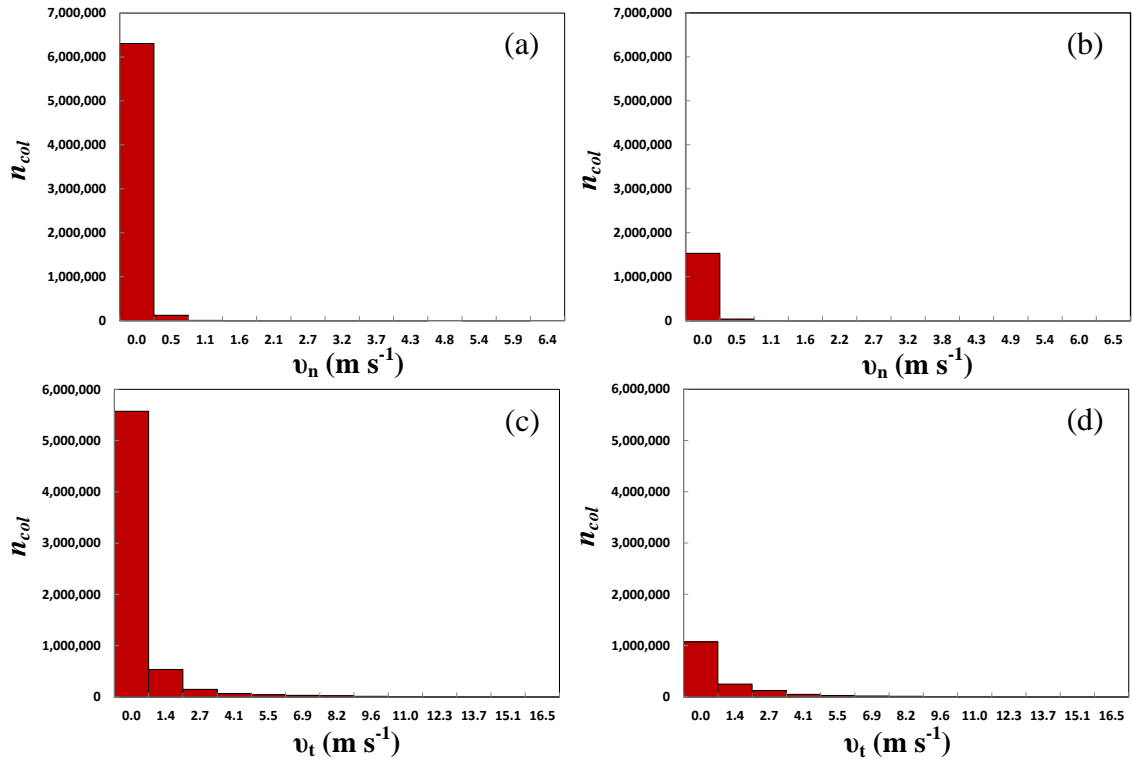


Figure 6.13 Total number of particle collisions and their relative (impact) velocity with the bottom wall for (a) 0.01 J m^{-2} ; (b) 0.05 J m^{-2} (normal), (c) 0.01 J m^{-2} ; (d) 0.05 J m^{-2} (tangential), at $t^+ = 0 - 7,948$.

Figure 6.12a,b show the mean collision velocity between particles and the bottom channel wall as a function of time for 0.01 and 0.05 J m^{-2} particles. In Figure 6.12a, the collision velocities generally decrease exponentially with time. Initially the 0.05 J m^{-2} particles have a higher mean impact velocity until $t^+ = 1,254$, after which it is higher for the 0.01 J m^{-2} particles. In Figure 6.12b, yet again it is seen that the initial mean impact velocity of the 0.05 J m^{-2} particles is higher than the 0.01 J m^{-2} particles up to $t^+ = 1413$ and less from this point onwards. Thus, the 0.05 J m^{-2} particles lose their velocities at a higher rate after wall impact. It is worth pointing out that v_n is less than $v_{n,12}$ due to the wall-normal lift force created by fluid shearing in the streamwise direction. These results confirm that particle agglomeration leads to the acceleration of particles moving downwards and de-acceleration of particles moving upwards. Figure 6.13a-d show the number of particle-wall collisions and corresponding relative (impact) velocity normal and tangential for the 0.01 and 0.05 J m^{-2} particles between $t^+ = 0 - 7,948$. The range of impact velocity normal and tangential is the same for the 0.01 (Figure 6.13a,c) and 0.05 J m^{-2} (Figure 6.13b,d) particles. On the other hand, in terms of collision number, it is almost three times higher for the 0.01 J m^{-2} particles. Figure

6.14a-d shows the number of particle-particle collisions and the corresponding relative (impact) velocity normal and tangential for the different surface energy particles between $t^+ = 0 - 7,948$. In general, yet again it is seen that there are more collisions for the 0.01 J m^{-2} particles across all impact velocities compared to the 0.05 J m^{-2} particles. The velocity regions in which sticking occurs are given in Table 6-2 and have been highlighted for different surface energies. Based on these cut-off points the number of successful collisions are 166,601 and 125,598 for the 0.01 and 0.05 J m^{-2} particles. It is important to mention that this does not take into account the contacts broken by fluid turbulence and agglomerates colliding with each other and the walls. These values match the number of particle-particle contacts and collisions shown in Figure 6.5.

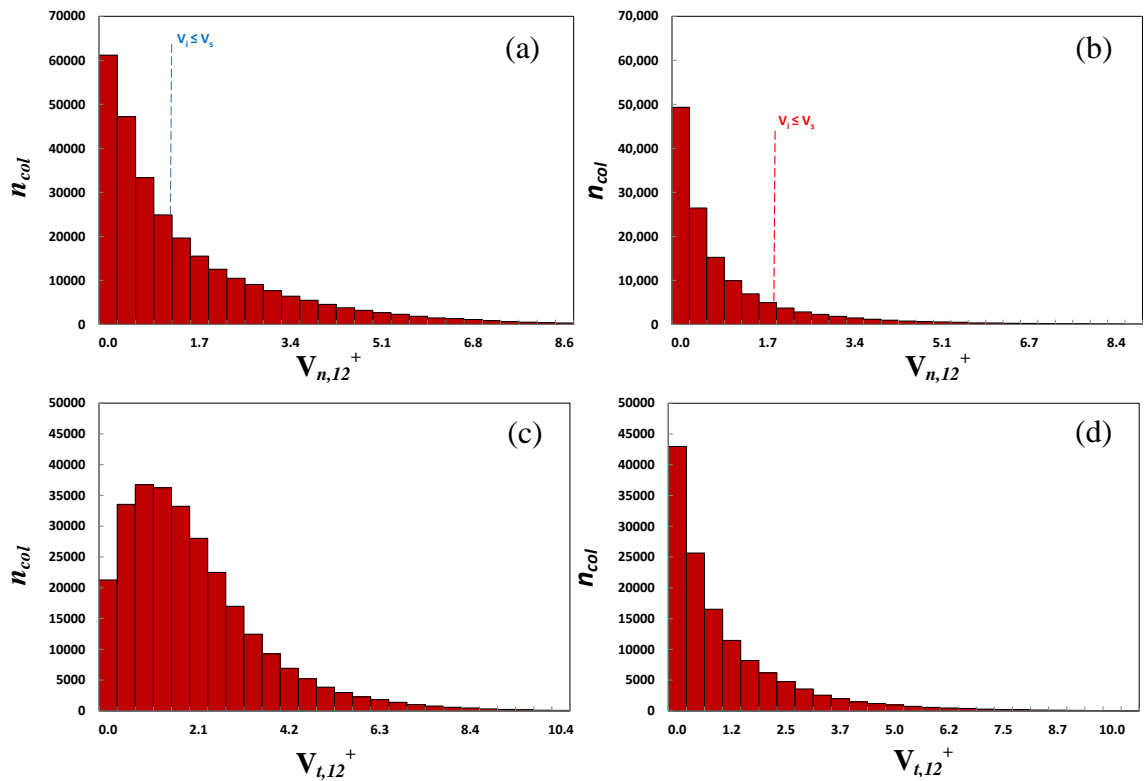


Figure 6.14 Total number of particle-particle collisions, n_p , and their relative velocity for (a) 0.01 J m^{-2} , (b) 0.05 J m^{-2} (normal), (c) 0.01 J m^{-2} ; (d) 0.05 J m^{-2} (tangential), at $t^+ = 0 - 7,948$. Vertical dashed blue and red lines indicate the maximum sticking velocity for 0.01 and 0.05 J m^{-2} particles, respectively.

Table 6-2 Sticking velocity of different surface energy particles

Surface Energy (J m^{-2})	0.01	0.05
Sticking Velocity ⁺	1.01	3.85

Figure 6.15 shows the cumulative normal, tangential and total loss of energy as a function of time for the 0.01 and 0.05 J m^{-2} particles. The normal and tangential energy loss is the energy lost during a collision due to the normal and tangential overlap (i.e. dissipation), respectively. The total energy loss is obtained by summing these two values. The results show that generally energy loss increases with relative velocity. From closer analysis it is seen that both the normal and tangential energy losses are higher for the 0.05 J m^{-2} particles, and this discrepancy increasing with time. Furthermore, the difference is more prevalent for the normal energy. This can be explained as follows, the collisions between particles gradually reduce particle velocity. Part of the initial kinetic energy is radiated into the particles as elastic waves. Here, the contact forces reach a maximum value (maximum de-acceleration) and the particle velocities drop to zero. This is followed by a recovery stage; stored elastic energy is released and converted into kinetic energy and the particle moves with a rebound velocity in the opposite direction. A higher surface energy contributes to larger agglomerates and consequently greater particle momentum which leads to greater energy loss.

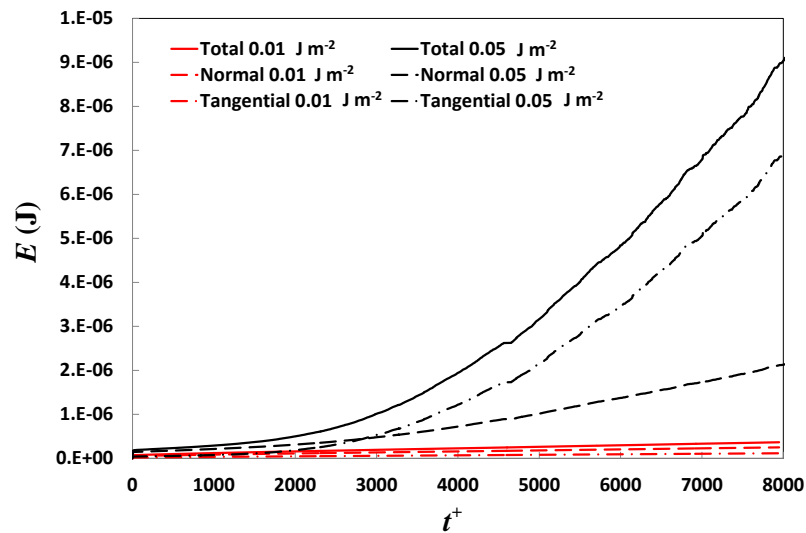


Figure 6.15 Cumulative average particle-particle collision energy loss as a function of time t^+

To quantitatively analyse the effect of fluid turbulence on particle and agglomeration, Figure 6.16 shows the streamwise and wall-normal components of the mean coupling force $F_{i,coupling}$ between the phases across the channel height at the final time step $t^+ = 7,948$. Low $F_{i,coupling}$ indicates that the particles and agglomerates track the fluid flow,

whereas a $F_{i,coupling}$ suggests that they react slowly to the fluid motion. In Figure 6.16a, generally, the magnitude of $F_{x,coupling}$ increases from the channel centre towards the walls where it reaches a maximum in the viscous sublayer before decreasing at the walls. The profile is negative in the region $0 < z^+ < 11$, which signifies that some of the particles are either being pushed backwards by the swirling fluid turbulence as they approach the walls. Such particles will have a very high individual value of $F_{x,coupling}$, causing the average value to be negative. This does not suggest that the majority of the particles are moving counter to the flow direction in this region. Further scrutiny of the results in Figure 6.16a shows that the coupling force does not reach zero at the walls for the 0.01 and 0.05 $J m^{-2}$ particles. Moreover, it is seen that $F_{x,coupling}$ is lower for the 0.01 $J m^{-2}$ particles between $0 < z^+ < 3$ compared to the 0.05 $J m^{-2}$ particles. The behaviour of inertial particles is determined by competing turbulence flow effects and gravity. Near wall phenomena decouples particle motion from the structure of the fluid turbulence, in so doing altering the wall-normal distribution and accumulation rate of individual particles at the wall (mainly the 0.01 $J m^{-2}$ particles). The turbulence structure effects the motion of these particles, causing them to be pushed towards the walls, although, due to their relatively low inertia the particles are vulnerable to near fluid turbulence. Fluid turbulence dominates the behaviour of all particles in the wall-normal and spanwise direction, this effect is greater for the particles and small agglomerates. Therefore, the larger agglomerates formed by 0.05 $J m^{-2}$ particles are less effected by the no slip wall conditions in the streamwise direction and have a more uniform velocity (smaller velocity gradient) across the channel height (due to their larger mass and therefore momentum, assuming the difference in velocity is not considerably high compared to the smaller agglomerates. On that basis, it is possible to deduce that the low surface energy particles are more effected by the shearing of fluid at the walls, causing particles in this region to slow down in the stream wise direction, however, this does not imply that the mean particle velocity in the channel centre is less for the 0.01 $J m^{-2}$ particles compared to the 0.05 $J m^{-2}$ particles, instead, it suggests a larger velocity gradient exists for the smaller particles. In the case of the wall-normal component $F_{z,coupling}$ in Figure 6.16 (b), again for $t^+ = 7,948$. In general, $F_{z,coupling}$ indicates that the relative velocity is directed upwards between $5 < z^+ < 83$ and downwards between $0 < z^+ < 5$. Comparing the 0.01 and 0.05 $J m^{-2}$ particles, the magnitude of the 0.01 $J m^{-2}$ is higher between $0 < z^+ < 5$ causing these particles to segregate out more. Whereas, the disproportional increase for the 0.05 $J m^{-2}$ particles between $5 < z^+ < 83$ means that the

agglomerates are more influenced by the wall normal fluctuations. These agglomerates have a higher inertia and are not seen to settle on the base of the channel, instead the fluid turbulence drives them upwards into the buffer layer and log-region.

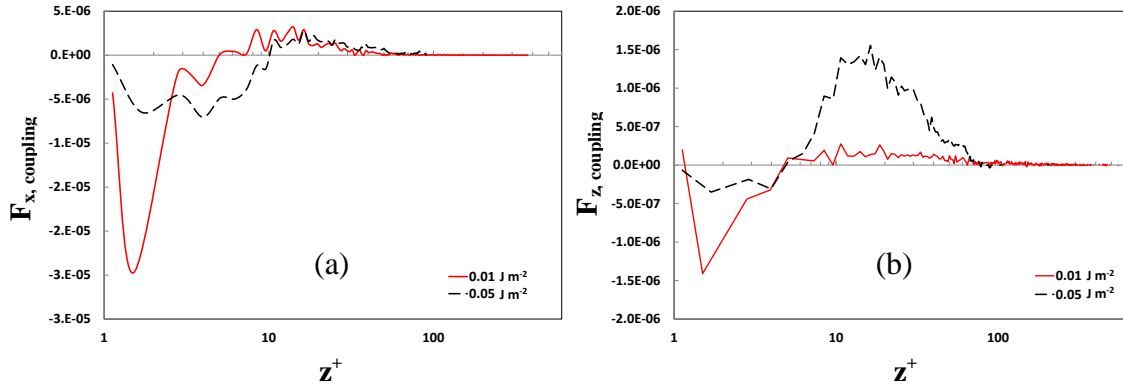


Figure 6.16 Total particle coupling force as a function of distance from the wall z^+ : (a) Streamwise; (b) Wall-normal ($t^+ = 0 - 7,948$)

Table 6-3 gives the mean streamwise ($F_{x,coupling}$) and wall-normal ($F_{z,coupling}$) coupling forces in the channel at $t^+ = 7,948$. For the 0.01 J m^{-2} particles, the value of $F_{z,coupling}$ is only slightly higher than $F_{x,coupling}$. This suggests that drag force and gravity have an almost equal influence on particle motion in both the wall-normal and streamwise directions, explaining why these particles are well dispersed throughout the channel cross-section. In the case of the 0.05 J m^{-2} particles however, $F_{z,coupling}$ is greater than $F_{x,coupling}$ by half an order of magnitude, suggesting that gravity dominates the motion of these particles. Moreover the coupling force of the 0.05 J m^{-2} particles, is five times greater for $F_{x,coupling}$ and almost one order of magnitude greater for $F_{z,coupling}$ compared to the 0.01 J m^{-2} particles. This occurrence can be contributed to particle surface energy. The fluid turbulence leads to the formation of particle agglomerates that have high inertia; therefore, they will maintain their velocity components as they approach the channel floor. In such a case the larger agglomerates deposited at the walls lose magnitude in the wall-normal and spanwise direction sooner than the smaller agglomerates and particles. Moreover, the increased local concentration close to the floor further promotes particle agglomeration. These results comprehend the behaviour shown by the concentration profiles and velocity distributions in the previous sections.

Table 6-3 Comparison of effect of main forces (Gravity, Lift, and Drag) on particles ($t^+ = 7,948$)

Surface Energy (J m^{-2})	Coupling Force (N)	
	$F_{x,coupling}$	$F_{z,coupling}$
0.01	2.77×10^{-10}	3.37×10^{-10}
0.05	7.45×10^{-10}	1.79×10^{-9}

Figure 6.17 and Figure 6.18 use coloured isocontours to illustrate the instantaneous distribution of particles and their velocities in the channel at the final time step $t^+ = 7,948$. The channel is shown at three different angles. The 0.01 J m^{-2} (Figure 6.17) particles deposited in the wall region have not attained a uniform distribution in the spanwise direction; the particle locations correlate with streamwise velocity streaks. This behaviour was not seen in the results of Chapter 4 in which gravity was neglected. The results suggest that gravity is preventing these particles from dispersing out of these streaks upon particle-particle collision. The quantifying of particle preferential distribution in the fluid velocity streaks is outside the scope of this thesis and will be left to further work. In contrast, the 0.05 J m^{-2} (Figure 6.18) particles have formed large agglomerates and are mainly situated above the channel floor. Figure 6.19 uses coloured bins to illustrate the areas of higher particle density close to the wall at the final time step $t^+ = 7,948$. Each bin is coloured based on the total particle volume in a cell ψ (m^3). The grid used to calculate ψ contains $30 \times 15 \times 1$ cells and the cell thickness selected is in dimensionless wall units 150 (0.01m). This general visualisation of particle flow structure complements the velocity statistics discussed earlier. The dynamic self-organisation of particles that occurs due to the competing effects between the structuring related to particle collisions and agglomeration and their destruction due to the fluid turbulence is a robust phenomenon. By comparing the 0.01 J m^{-2} (Figure 6.19a) with 0.05 J m^{-2} particles (Figure 6.19b), these results demonstrate qualitatively the effects of particle surface energy on the formation of structured particle fields. In general, the 0.05 J m^{-2} simulation is seen to contain higher number density regions for a transient particle-fluid flow. The increase in particle surface energy leads to the creation of higher density regions, and therefore it can be concluded from this analysis and those above that particle-particle contact strength contributes not only to the formation of agglomerates but also to an increase in segregation, i.e. coherent particle structures. Particle surface energy plays an important role in the structuring of particle fields in the channel; the particle-particle contact decreases the velocity difference between the two

particles after collision. Albeit the contact formation is not successful, the probability that the particles remain close to each other is more than prior to impact.

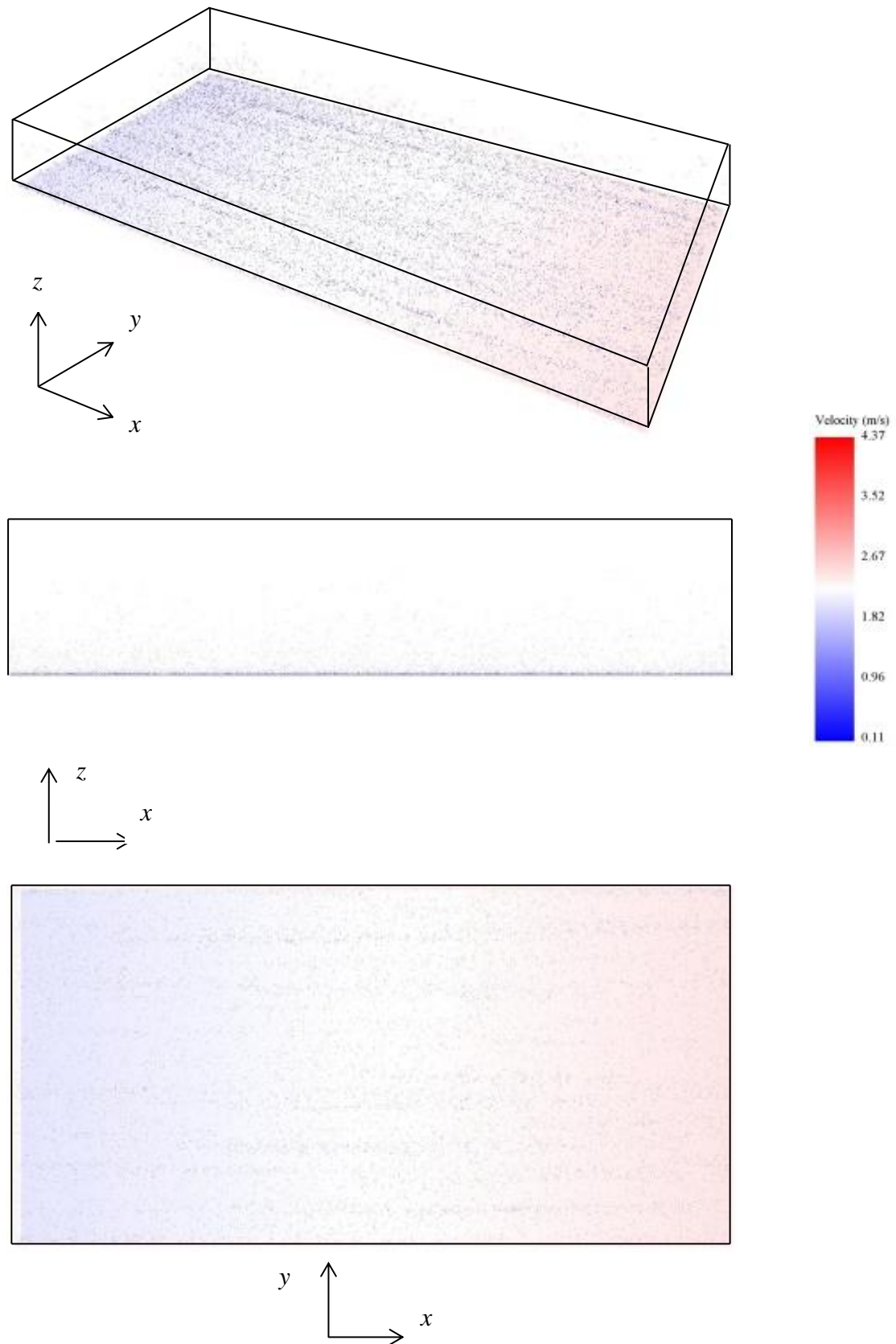


Figure 6.17 Iso-surface of particle velocity magnitude in the channel (m s^{-1}) for 0.01 J m^{-2} particles, at $t^+ = 7,948$.

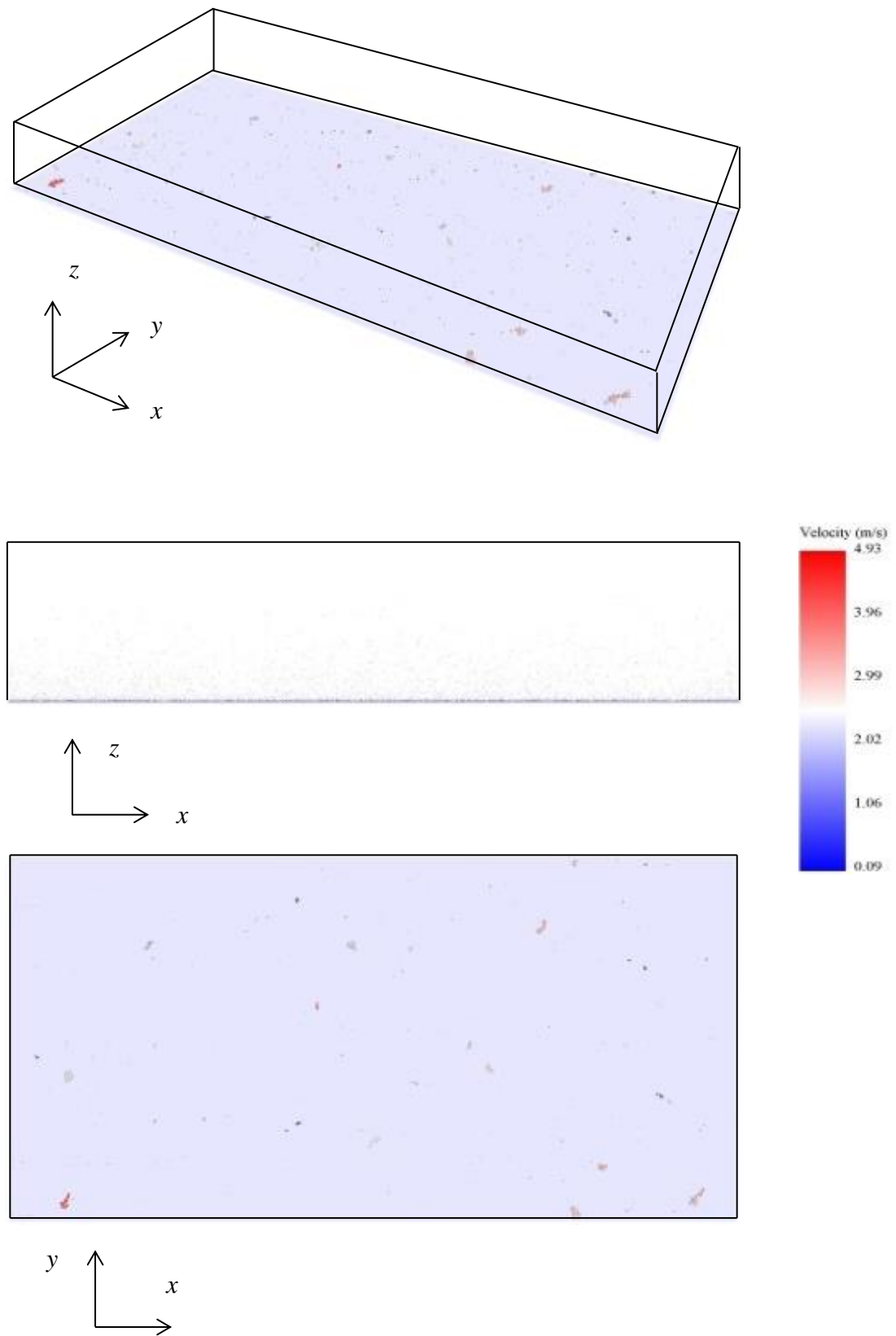


Figure 6.18 Iso-surface of particle velocity magnitude in the channel (m s^{-1}) for 0.05 J m^{-2} particles, at $t^+ = 7,948$.

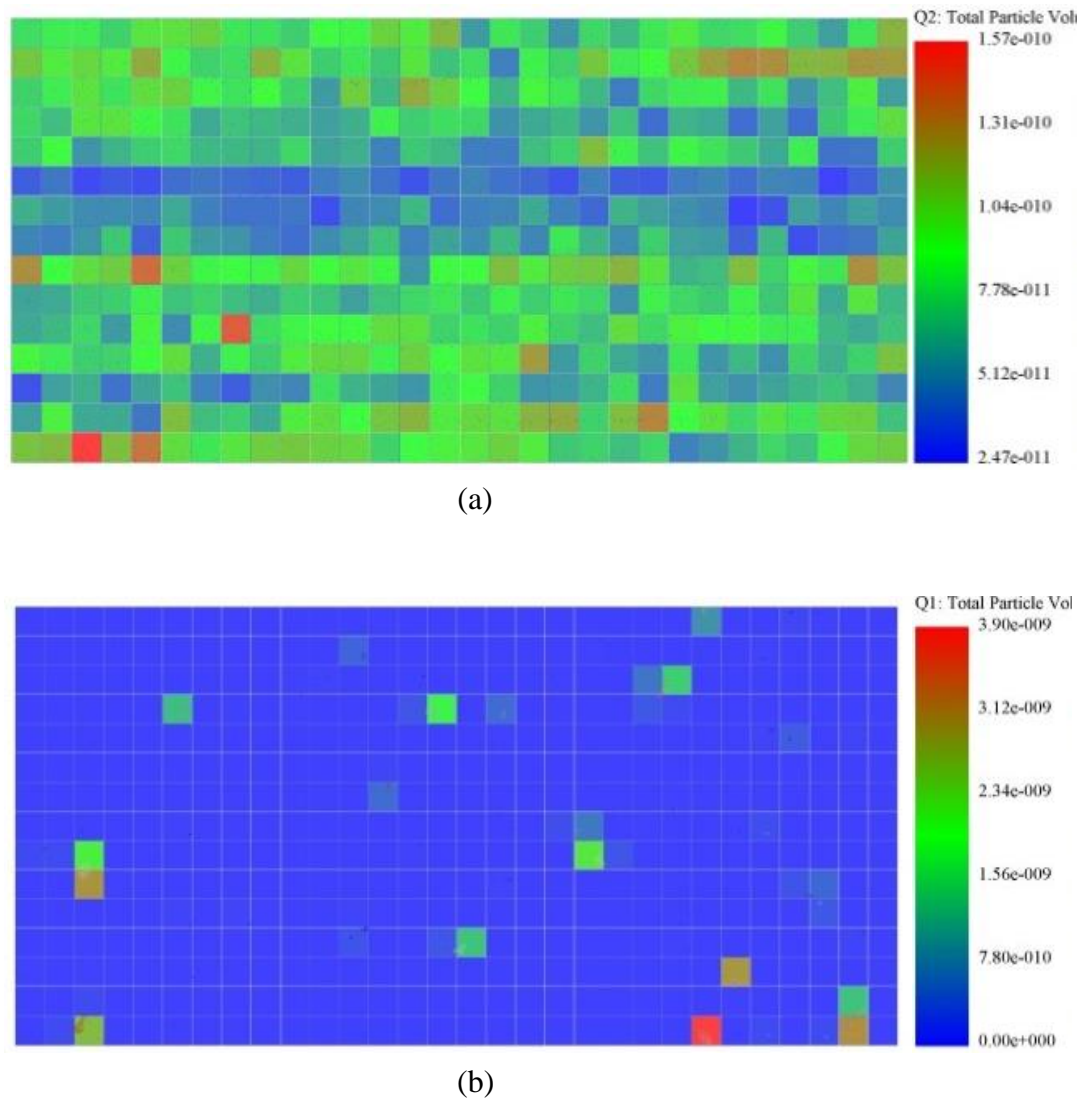


Figure 6.19 Iso-surface of total particle volume per cell (m^3) for (a) 0.01 J m^{-2} and (b) 0.05 J m^{-2} particles, at $t^+ = 7,948$ (particle at $z^+ = 0-5$).

6.3 Conclusions to Particle Dispersion, Deposition and Agglomeration

In the channel flow, the behaviour of inertial particles is determined by competing gravity and turbulence flow effects. Gravity decouples particle motion from the structure of the fluid turbulence, in so doing altering the wall-normal distribution and deposition rate of these particles. The turbulence structure largely influences the motion of individual particles and small agglomerates, causing them to be thoroughly distributed in the flow. Gravity dominates the behaviour of large particle agglomerates in the wall-normal direction. The incorporation of particle cohesion lead to large

amount of particle agglomeration, this increased with particle surface energy. Two particle surface energies were used 0.01 and 0.05 J m⁻². Scrutiny of the particle dispersion function for the channel showed that an increase in particle surface energy leads to a faster deposition rate. Moreover, the results showed even at very low volume fractions of approximately 10⁻⁵, particle-particle interactions are capable of affecting dispersion and deposition characteristics of the particles.

7. Conclusion and Further Work

In this final chapter, the conclusions for the findings of the three results chapters are given consecutively (Section 7.1) followed by the suggestions for future work (Section 7.2).

7.1 Conclusion

The work described in this thesis was undertaken to gain insight into fundamental aspects of turbulent gas-particle flows with relevance to processes employed in a wide range of applications, such as oil and gas flow assurance in pipes, powder dispersion from dry powder inhalers, and particle re-suspension in nuclear waste ponds, to name but a few. In particular, the influence of particle interaction and fluid phase behaviour in turbulent flow on particle dispersion in a horizontal channel is investigated. The mathematical modelling technique used is based on the large eddy simulation (LES) methodology embodied in the commercial CFD code FLUENT, with flow solutions provided by this approach coupled to a second commercial code, EDEM, based on the discrete element method (DEM) which is used for the prediction of particle motion and interaction.

The results generated by LES for the fluid phase have been validated against direct numerical simulations for three different channel flows with shear Reynolds numbers, $Re_\tau = 150, 300$ and 590 (Marchioli et al., 2008, Marchioli and Soldati, 2007, and Moser et al., 1999, respectively). Since LES is renowned for mispredicting low Reynolds number flow, prior to validation a sensitivity analysis was carried out on the $Re_\tau = 300$ flow. Direct comparison between the LES and DNS statistics allows clear cut observation of (i) how the LES performs when applied to the same problem with a well-defined simulation setting and (ii) how the accuracy of the LES results depends on the choices made in terms of sub-grid scale modelling, simulation parameter values, and grid spacing. LES was able to produce results that were in very good agreement for the mean streamwise-velocity profile. The RMS profiles were under/over predicted by the SGS, as with the common theme the discrepancy was greater for the spanwise and transverse components. Overall the SGS is capable of predicting the complex turbulent

regions close to the walls with a reasonable amount of accuracy; indicated by the magnitude and position of the maximum and minimum peaks of the RMS profiles. Such predictions cannot be made by RANS as the modelling approach averages out all of the fluid turbulence, including regions close to the walls. Overall, the LES shows good agreement with the latter results, with mean velocities and normal and shear stresses matching those of the DNS in both magnitude and position. Furthermore considered herein, the $Re_\tau = 300$ flow was also used to further investigate particle phase behaviour, with predictions again validated against one-way coupled DNS results.

In the rectangular channel flow, fluid turbulence effects govern the dispersion of inertial particles. Shearing at the walls magnify drag, in particular in the wall normal direction, thereby affecting the wall-normal distribution and segregation rate of particles. The fluid turbulence dominates the behaviour of $150 \mu\text{m}$ ($St = 216$) particles, causing them to be distributed throughout the flow. Because of their high inertia however, these particles do not fully track the flow and consequently concentrate at the walls. The results show full coupling, even at very low volume fractions of approximately 10^{-5} , are capable of having some effect on the characteristics of the fluid and particle phase. Comparing the fluid regime in the four-way coupling to the single phase flow, no major difference was seen in the mean fluid profile, although a decrease in the skin-friction was noticed. Moreover, the velocity fluctuations in all three directions were increased. For the streamwise component this increase was in the region $0 < z^+ < 20$, and for the spanwise and wall-normal it was between $0 < z^+ < 70$. The effects of four-way coupling were most prevalent in regions of high collision frequency, i.e. in the near wall region ($z^+ < 5$) and in the large velocity gradient region ($z^+ < 30$) where particle mixing occurs in the wall-normal direction, while in the channel centre region, the velocity gradient is small and so the trend differs. The incorporation of particle surface energy did not add to these effects. The conclusions vis-à-vis turbulence modulation in turbulent channel flow are generally in line with the experimental findings for similar inertia particles and volume fractions.

In terms of the effects of particle agglomeration on the particle velocity statistics, no clear effects were noticed. However, agglomeration does effect the dispersion and segregation near the walls. The concentration and corresponding number of collisions for cohesive particles are less in this region compared to non-cohesive particles.

Moreover, the components of $F_{i,coupling}$ are seen to increase with particle surface energy. From further scrutiny, the differences between the 0.0 and 0.05 J m⁻² particles are greater for the wall-normal ($F_{z,coupling}$) coupling force compared to the streamwise ($F_{x,coupling}$). The proportional increase for the wall-normal direction means that the agglomerates are more influenced by the wall normal velocities and their fluctuations which are responsible for particle drift towards and away from the walls. However, because the velocity magnitude is higher in the streamwise direction, $F_{x,coupling}$ contributes to a larger discrepancy in the velocity distribution as seen in Figure 4.21. What's more, the largest differences for particle coupling force between the two particles are in regions of high turbulence (buffer layer) and high velocity (outer region). Therefore, there is an effect of particle agglomeration on concentration and velocity distribution. It is important to mention that particle agglomeration results in higher inertia; this lowers the ability of agglomerates to track the flow which potentially leads to more collisions and further agglomeration.

The work reported has focused on the prediction of those conditions that favour particle agglomeration and dispersion within turbulent channel flows. This has been achieved by minimising the number of degrees of freedom by keeping the simulation setting as simple as possible thereby allowing particle interaction with the flow structures alone to influence the particle motion. For that reason the effect of gravity was neglected. The work is to elucidate the physics of how turbulence influence the locations of particle interaction and agglomeration. Simulations have been carried out to investigate the effects of particle density, size and concentration on particle agglomeration. Furthermore, particles with different surface properties have been simulated in three channel flows with different levels of flow turbulence, achieved by increasing the Reynolds number of the flow. The simulations mimic the conditions of two-phase, fluid-solid flows frequently encountered in domestic, commercial and industrial applications, for example, air conditioning and refrigeration units, heat exchangers, oil and gas suction and pressure lines. The particle densities, sizes, volume fractions and surface energies selected are 250, 1000, and 2159 kg m⁻³, 45.6, 102 and 150 μm, 7.84×10^{-6} , 2.8×10^{-5} , 1×10^{-4} and 50, 500, and 5000 mJ m⁻², respectively; such properties are associated with particles found in soil, as well as metals and oxides prevalent in turbulent bounded fluid-solid flows due to erosion and corrosion of inner pipe walls. The Reynolds numbers are representative of a wide range of flow velocities encountered

in practice, from pipes used in domestic applications to industrial hydraulic systems designed for working at high pressures.

It has been found that the turbulence structure of the flow dominates the motion of the particles, creating particle-particle interactions, with most of these interactions taking place at locations close to the channel walls and in regions of high turbulence where their agglomeration is aided both by the high levels of turbulence and the high concentration of particles. A positive relationship between particle surface energy, density, concentration and size, and agglomeration, was observed. Moreover, the results derived for the three Reynolds numbers considered show that the rate of agglomeration is strongly influenced for high surface energy particles by, and increases with, the intensity of the flow turbulence. In contrast, for lower surface energy particles, the rate of agglomeration diminishes with an increase in flow turbulence intensity.

When gravity is introduced into the channel flow, the behaviour of inertial particles is determined by competing gravity and turbulence flow effects. Gravity decouples particle motion from the structure of the fluid turbulence, in so doing altering the wall-normal distribution and deposition rate of these particles. The turbulence structure largely influences the motion of individual particles and small agglomerates, causing them to be thoroughly distributed in the flow. Gravity dominates the behaviour of large particle agglomerates in the wall-normal direction. The incorporation of particle cohesion lead to large amount of particle agglomeration, this increased with particle surface energy. Two particle surface energies were used 0.01 and 0.05 J m⁻². Scrutiny of the particle dispersion statistics for the channel showed that an increase in particle surface energy leads to a faster deposition rate. Moreover, the results showed even at very low volume fractions of approximately 10⁻⁵, particle-particle interactions are capable of affecting dispersion and deposition characteristics of the particles. The effects of particle surface energy are most prevalent in regions of high collision frequency, i.e. in the near wall region ($z^+ < 5$) and in the buffer region ($z^+ < 30$). Close to the floor, the particle number density increases with surface energy. Conversely, more low surface energy particles are deposited. From force analysis, it is revealed that the wall-normal particle coupling force shows a strong positive increase with surface energy. This increase in the distribution and magnitude of particle coupling force is

particularly high in the buffer layer causing large agglomerates to drift away from the channel floor.

The research makes an original contribution to the literature in applying advanced predictive techniques which have not been coupled and applied to the problem of particle-interaction effects in turbulent flows before. It yields fundamental understanding of how particles interact, and how those interactions result in the formation of agglomerates which affect the dispersion and deposition of particles within the flow. Such an understanding is required in the processing and transportation of fluid-solid flows, where particle agglomeration adds to their propensity to form solid beds. The formation of particle beds can result in blockages to pipes and equipment and lead to difficulties in obtaining dispersed particle flows from storage equipment for subsequent processing. An understanding of how these flows behave during transportation is of clear benefit to more cost-effective process design, continued operation, and accelerated waste clean-up. The overall results are also relevant, and underpinning, to the transportation of fluid-solid flow in a wide range of applications in the industrial and health sectors.

7.2 Recommendations for Further Work

A list of suggestions for future work based on the findings of this study is given below.

1. A quantitative comparison of LES with experimental and/or DNS data for higher Reynolds number flow in turbulent bounded flow. The results from other LES studies could also be used to assess the credentials of the SGS model and highlight possible improvements. For these comparisons to be accurate, detailed information of the flow conditions and properties are also required, e.g. friction and slip velocities.
2. Analysis in the influence of particles and cohesive inter-particle collisions on the particle and fluid phase characteristics for turbulent bounded flows laden at higher volume fractions ($> 10^{-3}$).
3. Application of LES-DEM to more complex geometries such as pipes and ducts, in particular to see additional effects of secondary flows. Also in different fluid

mediums such as water, where the density ratio is much low and the effects buoyancy noticeable.

4. Increase in the run times to see the longer effects of fluid turbulence and gravity. This would require more computational power and licenses. Currently the simulations are only short times, with low concentrations and relatively large particles.
5. Long range interaction forces that are not restricted to near contact detection radius. This would allow the simulating the agglomeration of particles that have surface charges.

Bibliography

- Abdilghanie, A. M., Collins, L. R. & Caughey, D. A. 2009. "Comparison of turbulence modeling strategies for indoor flows". *Journal of Fluids Engineering*, 131, 051402.
- Abe, H., Kawamura, H. & Choi, H. 2004a. "Very large-scale structures and their effects on the wall shear-stress fluctuations in a turbulent channel flow up to $Re_{\tau} = 640$ ". *Journal of Fluids Engineering*, 126, 835-843.
- Abe, H., Kawamura, H. & Matsuo, Y. 2001. "Direct numerical simulation of a fully developed turbulent channel flow with respect to the Reynolds number dependence". *Journal of fluids Engineering*, 123, 382-393.
- Abe, H., Kawamura, H. & Matsuo, Y. 2004b. "Surface heat-flux fluctuations in a turbulent channel flow". *International Journal of Heat and Fluid Flow*, 25, 404-419.
- Afkhami, M., Hassanpour, A., Fairweather, M. & Njobuenwu, D. O. (2015). "Fully-Coupled LES-DEM of Particle Interaction and Agglomeration in a Turbulent Channel Flow". *Computers & Chemical Engineering*.
- Ahmadi, G., Nasr, H. & McLaughlin, J. B. 2010. "Turbulent Two-Phase Flows and Particle Deposition in a Duct at High Concentrations". [ASME 2010 3rd Joint US-European Fluids Engineering Summer Meeting collocated with 8th International Conference on Nanochannels, Microchannels, and Minichannels, 2010]. *American Society of Mechanical Engineers*, 257-263.
- Alexander, L.G., Coldren C. L. 1951. "Droplet Transfer from Suspending Air to Duct Walls". *Industrial & Engineering Chemistry*, 43: 1325-1331.
- Alletto, M. & Breuer, M. 2012. "One-way, two-way and four-way coupled LES predictions of a particle-laden turbulent flow at high mass loading downstream of a confined bluff body". *International Journal of Multiphase Flow*, 45, 70-90.
- Alletto, M. & Breuer, M. 2013. "Prediction of turbulent particle-laden flow in horizontal smooth and rough pipes inducing secondary flow". *International Journal of Multiphase Flow*, 55, 80-98.
- Alvandifar, N., Abkar, M., Mansoori, Z., Avval, M. S. & Ahmadi, G. 2011. "Turbulence modulation for gas-particle flow in vertical tube and horizontal channel using four-way Eulerian-Lagrangian approach". *International Journal of Heat and Fluid Flow*, 32, 826-833.
- Antony, S.J., 2000. "Evolution of force distribution in three-dimensional granular media". *Physical Review*, E 63, 011302.
- Arastoopour, H., 2001. "Numerical simulation and experimental analysis of gas/solid flow systems". *Powder Technology*, 119, 59-67.
- Arcen, B., Tanire, A. & Oesterle, B. 2006. "On the influence of near-wall forces". *Particle-Laden Channel Flows*. 32. 1339.
- Armenio, V. and Fiorotto, V. 2001. "The importance of the forces acting on particles in turbulent flows." *Physics of Fluids* (1994-present) 13.8: 2437-2440.
- Armenio, V., Piomelli, U. & Fiorotoo, V. 1999. "Effect of the subgrid scales on particle motion". *Physics of Fluids* (1994-present), 11, 3030-3042.
- Azimian, M., Lichti, M. & Bart, H. 2014. "Investigation of Particulate Flow in a Channel by Application of CFD, DEM and LDA/PDA". *Open Chemical Engineering Journal*, 8, 1-11.
- Babler, M. U., Biferale, L., Brandt, L., Feudel, U., Guseva, K., Lanotte, A. S., Marchioli, C., Picano, F., Sardina, G. & Soldati, A. 2014. "Numerical

- simulations of aggregate breakup in bounded and unbounded turbulent flows". *arXiv preprint arXiv:1406.2842*.
- Banerjee. 2015. "Nonlinear finite elements/Lagrangian and Eulerian descriptions". [ONLINE] Available at:http://en.wikiversity.org/wiki/Nonlinear_finite_elements/Lagrangian_and_Eulerian_descriptions. [Accessed 27 April 15].
- Barsoum, M. 1997. *Fundamentals of Ceramics*, New York: McGrawHill Companies Inc.
- Bauchhage, K. 1988. "The Phase-Doppler-Difference-Method, a New Laser-Doppler Technique for Simultaneous Size and Velocity Measurements. Part 1: Description of the method". *Particle & Particle Systems Characterization*, 5, 16-22.
- Belytschko, T., Liu, W. K., Moran, B., & Elkhodary, K. 2013. *Nonlinear Finite Elements for Continua and Structures*. New York: John Wiley & Sons.
- Berrouk, A. S. & WU, C. 2010. "Large eddy simulation of dense two-phase flows: Comment on DEM-LES study of 3-D bubbling fluidized bed with immersed tubes". *Chemical Engineering Science*, 65, 1902-1903.
- Bewley, T. R., Moin, P. & Temam, R. 2001. "DNS-based predictive control of turbulence: an optimal benchmark for feedback algorithms". *Journal of Fluid Mechanics*, 447, 179-225.
- Biggs, S. & Spinks, G. 1998. "Atomic force microscopy investigation of the adhesion between a single polymer sphere and a flat surface". *Journal of adhesion science and technology*, 12, 461-478.
- Bird, R. B., Stewart, W. E., Lightfoot, E. 1960. *Transport Phenomena*, New York: John Wiley & Sons.
- Bitter, J. 1963. "A study of erosion phenomena: Part II". *Wear*, 6, 169-190.
- Boree J, Caraman N. 2005. "Dilute bidispersed tube flow: Role of interclass collisions at increased loadings". *Physics of Fluids*. 17: 055108.
- Bouillard, J.X., Lyczkowski, R.W., Gidaspow, D., 1989. "Porosity distributions in a fluidized bed with an immersed obstacle". *A.I.Ch.E. Journal* 35, 908-922.
- Breuer, M. & Alletto, M. 2012. "Efficient simulation of particle-laden turbulent flows with high mass loadings using LES". *International Journal of Heat and Fluid Flow*, 35, 2-12.
- Brosh, T., Kalman, H., Levy, A., Peyron, I. & Richard, F. 2014. "DEM-CFD simulation of particle comminution in jet-mill". *Powder Technology*, 257, 104-112.
- Calvert, G. Hassanpour, A. and Ghadiri, M. "Analysis of aerodynamic dispersion of cohesive clusters." *Chemical Engineering Science* 86 (2013): 146-150.
- Calvert, G., Hassanpour, A. and Ghadiri, M. 2011. "Mechanistic analysis and computer simulation of the aerodynamic dispersion of loose aggregates". *Chemical Engineering Research and Design*. 89.5: 519-525.
- Caraman N, Boree J, Simonin O. 2003. "Effect of collisions on the dispersed phase fluctuation in a dilute tube flow: Experimental and theoretical analysis". *Physics of Fluids*. 15: 3602-3612.
- Cargnelutti, M. & Portela, L. 2007. "Influence of the turbulence structure on the particle sedimentation in wall-bounded flows". *Particle-Laden Flow*. Springer.
- Chamberlain A. 1967. "Transport of Lycopodium spores and other small particles to rough surfaces". *Proceedings of the Royal Society of London. Series A. Mathematical and Physical Sciences* 296: 45.

- Chang, Y. I., Chen, S. C. & Lee, E. 2003. "Prediction of Brownian particle deposition in porous media using the constricted tube model". *Journal of Colloid and Interface Science*, 266, 48-59.
- Chang, Y., Collis, S. S. & Ramakrishnan, S. 2002. "Viscous effects in control of near-wall turbulence". *Physics of Fluids (1994-present)*, 14, 4069-4080.
- Chang, Y.-I., Huang, Y.-T., Luo, Z. L. & Zhang, G.Z. 2008. "A study on particle deposition morphology within a constricted tube in the presence and absence of the detachment mechanism". *Separation and Purification Technology*, 63, 566-576.
- Chaumeil, F. & Crapper, M. 2013. "Using the DEM-CFD method to predict Brownian particle deposition in a constricted tube". *Particuology*.
- Chen, X., LI, D., Luo, K. & Fan, J. 2011. "Direct numerical simulation of a three-dimensional particle laden plane mixing layer considering inter-particle collisions". *Chemical Engineering Science*, 66, 6232-6243.
- Cheng, S. 2012. "Numerical and experimental study of cyclone separators for aerosol drug delivery". *Clare Hall College, University of Cambridge*.
- Chibbaro, S. & Minier, J. P. 2008. "Langevin PDF simulation of particle deposition in a turbulent pipe flow". - 39, - 571.
- Chin, C., Monty, J. & Choi, A. 2014. "Reynolds number effects in DNS of pipe flow and comparison with channels and boundary layers". *International Journal of Heat and Fluid Flow*, 45, 33-40.
- Choi, H.G., Joseph, D.D., 2001. "Fluidization by lift of 300 circular particles in plane Poiseuille flow by direct numerical simulation". *Journal of Fluid Mechanics*. 438, 101–128.
- Cleary, P.W., Sawley, M.L., 2002. "DEM modelling of industrial granular flows: 3D case studies and the effect of particle shape on hopper discharge". *Applied Mathematical Modelling*. 26, 89–111.
- Comte-Bellot G. 1976. "Hot-Wire Anemometry". *Annual Review of Fluid Mechanics*. 8: 209-231.
- Crowe CT, Sharma M, Stock DE. 1977. "The particle-source-in cell (PSI-CELL) model for gas-droplet flows". *Journal of Fluids Engineering*. 99: 325.
- Crowe, C. T. 2000. "On models for turbulence modulation in fluid–particle flows". *International Journal of Multiphase Flow*, 26, 719-727.
- Crowe, C., Sommerfeld, M. & Tsuji, Y. 1998. *Multiphase flows with particles and droplets*. New York: CRC Press.
- Cundall, P.A. & Strack, O.D.L., 1979. "A discrete numerical model for granular assemblies". *Geotechnique*, 29, 47-65.
- Dandy, D. S., & Dwyer, H. A. 1990. "A sphere in shear flow at finite Reynolds number: effect of shear on particle lift, drag, and heat transfer". *Journal of Fluid Mechanics*, 216, 381-410.
- Dantec Dynamics. 2015. "Measurement Principles for LDA". [ONLINE] Available at: <http://www.dantecdynamics.com/measurement-principles-of-lda>. [Accessed 27 April 15].
- De Gennes, P.G., 1999. "Granular matter: a tentative view". *Reviews of Modern Physics*. 71, 374–382.
- De Souza, F. J., Silva, A. L. & Utzig, J. 2014. "Four-way coupled simulations of the gas–particle flow in a diffuser". *Powder Technology*, 253, 496-508.
- Deardorff, J. W. 1970. "A numerical study of three-dimensional turbulent channel flow at large Reynolds numbers". *Journal of Fluid Mechanics*, 41, 453-480.

- Deen, N. & Kuipers, J. 2014. "Direct Numerical Simulation (DNS) of mass, momentum and heat transfer in dense fluid-particle systems". *Current Opinion in Chemical Engineering*, 5, 84-89.
- DEM-Solutions (2014). *EDEM User Manual*. DEM-Solutions.
- Derevich IV. 2000a. "Statistical modeling of mass transfer in turbulent two-phase dispersed flows -- 2.Calculation results". *International Journal of Heat and Mass Transfer* 43: 3725-3734.
- Derevich IV. 2000b. "Statistical modeling of mass transfer in turbulent two-phase dispersed flows -- 1.Model development". *International Journal of Heat and Mass Transfer* 43: 3709-3723.
- Derjaguin, B.V., Muller, V.M., Toporov, Y.P., 1975. "Effect of contact deformation on the adhesion of particles". *Journal of Colloid Interface Science*. 53, 314–326.
- Di Felice, R., 1994. "The voidage function for fluid–particle interaction systems". *International Journal of Multiphase Flow*. 20, 153–159.
- Di Renzo, A., Cello, F., & Di Maio, F. P. 2011. "Simulation of the layer inversion phenomenon in binary liquid--fluidized beds by DEM–CFD with a drag law for polydisperse systems". *Chemical Engineering Science*, 66(13), 2945-2958.
- Di Renzo, A., Di Maio, F.P., 2004. "Comparison of contact-force models for the simulation of collisions in DEM-based granular flow codes". *Chemical Engineering Science*. 59, 525–541.
- Durst, F. & Kikpura, H. 1995. "Low Reynolds number effects on a fully developed turbulent channel flow". *10th Symposium on Turbulent Shear Flows*, Pennsylvania State University, University Park.
- Duursma, G., Crapper, M., Whitelaw, S. & Wong, W. S. 2009. "DEM-CFD Modelling of Voidage and Heat Transfer in Fluidized Beds". *8th World Congress on Chemical Engineering*. Montreal, Canada.
- Eaton, J. K. & Fessler, J. 1994. "Preferential concentration of particles by turbulence". *International Journal of Multiphase Flow*, 20, 169-209.
- Ebrahimi, M., Crapper, M. & Ooi, J. Y. 2014. "Experimental and Simulation Studies of Dilute Horizontal Pneumatic Conveying". *Particulate Science and Technology*, 32, 206-213.
- Echizen, H. & Unno, H. 2001. "Concentration of Fat Globules in Milk by an Oscillating Membrane Unit: Experiment Using Model Emulsified Solutions". *Food and Bioproducts Processing*, 79, 3-12.
- El Khoury, G. K., Scheatter, P., Brethouwear, G. & Johansson, A. V. 2014. "Turbulent pipe flow: Statistics, Re-dependence, structures and similarities with channel and boundary layer flows". *Journal of Physics: Conference Series*, IOP Publishing, 012010.
- Elghobashi SE, Abou-Arab TW. 1983. A two-equation turbulence model for two-phase flows. *Physics of Fluids* 26: 931-938.
- ENEA. 2015.DNS, LES and RANS. [ONLINE] Available at:<http://www.uttei.enea.it/combustione-sostenibile/img-combustione-sostenibile/DNSLESRANS.jpg/view>. [Accessed 27 April 15].
- Enwald H, Peirano E, Almstedt AE. 1996. "Eulerian two-phase flow theory applied to fluidization". *International Journal of Multiphase Flow* 22: 21-66.
- Ergun, S., 1952. "Fluid flow through packed columns". *Chemical Engineering and Processing* 48, 89–94.
- Fairweather, M. & Yao, J. 2009. "Mechanisms of particle dispersion in a turbulent, square duct flow". *AIChE Journal*, 55, 1667-1679.

- Fang, M., Luo, K., Yang, S., Zhang, K. & Fan, J. 2013. "LES-DEM investigation of gas–solid flow dynamics in an internally circulating fluidized bed". *Chemical Engineering Science*, 101, 213-227.
- Farmer R, Griffith P, Rohsenow WM. 1970. "Liquid Droplet Deposition in Two-Phase Flow". *Journal of Heat Transfer*. 92: 587-594.
- Feng, Y.Q., Pinson, D., Yu, A.B., Chew, S.J., Zulli, P., 2003. "Numerical study of gas–solid flow in the raceway of a blast furnace". *Steel Research International* 74, 523–530.
- Feng, Y.Q., Yu, A.B., 2004a. "Assessment of model formulations in the discrete particle simulation of gas–solid flow". *Industrial and Engineering Chemistry Research*. 43, 8378–8390.
- Feng, Y.Q., Yu, A.B., 2004b. "Comments on “Discrete particle-continuum fluid modelling of gas–solid fluidised beds”". by Kafui et al. [Chemical Engineering Science 57 (2002) 2395–2410]. *Chemical Engineering Science* 59, 719–722.
- Fraige, F. & Langston, P. 2006. "Horizontal pneumatic conveying: a 3d distinct element model". *Granular Matter*, 8, 67-80.
- Fried, J. 1995. *Polymer Science and Technology*. Englewood Cliffs, NJ: Prentice Hall PTR.
- Fureby, C. & Grinstein, F. F. 2002. "Large eddy simulation of high-Reynolds-number free and wall-bounded flows". *Journal of Computational Physics*, 181, 68-97.
- Gallas, J.A.C., Sokolowski, T., 1993. "Grain non-sphericity effects on the angle of repose of granular material". *International Journal of Modern Physics*. B 7, 2037–2046.
- Gao, C., 1997. "Theory of menisci and its applications". *Applied Physics Letters*. 71, 1801–1803.
- Germano, M. 1992. "Turbulence: the filtering approach". *Journal of Fluid Mechanics*, 238, 325-336.
- Geurts, B. J. & Frohlich, J. 2002. "A framework for predicting accuracy limitations in large-eddy simulation". *Physics of Fluids (1994-present)*, 14, L41-L44.
- Geurts, B. J. 2011. "Large-eddy simulation of multiscale particle dynamics at high volume concentration in turbulent channel flow". *Multiscale Methods in Computational Mechanics*. Springer.
- GHOSH, S. & COLLIER, A. 2007. "Inhaled insulins". *Postgraduate Medical Journal*, 83, 178-181.
- Glowinski, R., Pan, T.W., Hesla, T.I., Joseph, D.D., Periaux, J., 2000. "A distributed Lagrange multiplier/fictitious domain method for the simulation of flow around moving rigid bodies: application to particulate flow". *Computer Methods in Applied Mechanics and Engineering*. 184, 241–267.
- Goldensoph, G. M. 2006. *The influence of filtering on the motion of heavy particles in gas-phase turbulence*. Arizona State University.
- Gore RA, Crowe CT. 1991. "Modulation of turbulence by dispersed phase". *Journal of Fluids Engineering* 113: 304-307.
- Gore, R.A., Crowe, C.T., 1989. "Effect of particle size on modulating turbulent intensity". *International Journal of Multiphase Flow*. 15,279–285.
- Grehan, G., Gouesbet, G., Naqwi, A. & Durst, F. 1993. "Particle trajectory effects in phase Doppler systems: computations and experiments". *Particle & particle systems characterization*, 10, 332-338.
- Gui, N., Fan, J. R. & Luo, K. 2008. "DEM–LES study of 3-D bubbling fluidized bed with immersed tubes". *Chemical Engineering Science*, 63, 3654-3663.
- Guingo, M. & Minier, J. P. 2008. "A stochastic model of coherent structures for particle deposition in turbulent flows". - 20.

- Haig, C., Hursthouse, A., McIlwain, S. & Sykes, D. 2014. "The effect of particle agglomeration and attrition on the separation efficiency of a Stairmand cyclone". *Powder Technology*, 258, 110-124.
- Hamaker, H. C. (1937). "The London—van der Waals attraction between spherical particles." *Physica* 4(10): 1058-1072.
- Han, T., Levy, A., Kalman, H., 2003. "DEM simulation for attrition of salt during dilute-phase pneumatic conveying". *Powder Technology*. 129, 92–100.
- Helmfel, A.T., Mockros, L.F., 1966. "Motion of discrete particles in a turbulent fluid". *Applied Scientific Research*. 16, 149–161.
- Hildich, R. G. & Zhang, G. M. 1995. "Internal fouling of microporous cross-flow filtration membranes with dilute latex suspensions". *The Chemical Engineering Journal and the Biochemical Engineering Journal*, 60, 31-37.
- Hilton, J. & Clearly, P. 2011. "The influence of particle shape on flow modes in pneumatic conveying". *Chemical Engineering Science*, 66, 231-240.
- Hogberg, M., Bewley, T. & Henningson, D. S. 2003. "Relaminarization of $Re\tau=100$ turbulence using gain scheduling and linear state-feedback control". *Physics of Fluids (1994-present)*, 15, 3572-3575.
- Hollander, P. A., Blonde, L., Rowe, R., Mehta, A. E., Milburn, J. L., Hershon, K. S., Chiasson, J.-L. & Levin, S. R. 2004. "Efficacy and Safety of Inhaled Insulin (Exubera) Compared With Subcutaneous Insulin Therapy in Patients With Type 2 Diabetes Results of a 6-month, randomized, comparative trial". *Diabetes Care*, 27, 2356-2362.
- Hou, Q., Zhou, Z. & Yu, A. 2012. "Micromechanical modeling and analysis of different flow regimes in gas fluidization". *Chemical Engineering Science*, 84, 449-468.
- Hoyas, S. & Jimenez, J. 2006. "Scaling of the velocity fluctuations in turbulent channels up to $Re\tau=2003$ ". *Physics of Fluids (1994-present)*, 18, 011702.
- Hu, H. H., 1996. "Direct simulation of flows of solid–liquid mixtures". *International Journal of Multiphase Flow*. 22, 335–352.
- Hughes, D., Tirlapur, U. K., Field, R. & Cui, Z. 2006. "In situ 3D characterization of membrane fouling by yeast suspensions using two-photon femtosecond near infrared non-linear optical imaging". *Journal of Membrane Science*, 280, 124-133.
- Humphrey, C. D., Cook, E. & Bradley, D. W. 1990. "Identification of enterically transmitted hepatitis virus particles by solid phase immune electron microscopy". *Journal of Virological Methods*, 29, 177-188.
- Hyatt, N., Biggs, S., Livens, F., Young, J. & Evans, N. Diamond. 2009. "Academic Innovation in Support of UK Radioactive Waste Management". Workshop TRePro II, 2009. Cambridge Univ Press, no. 22.
- Ilori TA. 1971. *Turbulent deposition of aerosol particles inside pipes*. Minneapolis, Minnesota: University of Minnesota.
- Institute of Aerodynamics and flow Technology. 2015. "Principle PIV-Setup". [ONLINE] Available at:http://www.dlr.de/as/en/DesktopDefault.aspx/tabid-183/251_read-12796/gallery-1/gallery_read-Image.5.1574/. [Accessed 27 April 15].
- Iwamoto, K., Suzuki, Y. & Kasagi, N. 2002. "Reynolds number effect on wall turbulence: toward effective feedback control". *International journal of heat and fluid flow*, 23, 678-689.
- Iwashita, K., Oda, M., 1998. "Rolling resistance at contacts in simulation of shear band development by DEM". *Journal of Engineering Mechanics*. 124, 285–292.

- Iwashita, K., Oda, M., 2000. "Micro-deformation mechanism of shear banding process based on modified distinct element method". *Powder Technology*, 109, 192–205.
- Johnson, K. L., Li, X. & Yal, G. 2007. "Colloid Retention in Porous Media: Mechanistic Confirmation of Wedging and Retention in Zones of Flow Stagnation". *Environmental Science & Technology*, 41, 1279-1287.
- Johnson, K. L., Kendall, K. & Roberts, A. D. 1971. "Surface Energy and the Contact of Elastic Solids. *Proceedings of the Royal Society of London. A. Mathematical and Physical Sciences*, 324, 301-313.
- Johnson, W. P., Pazmino, E. & Ma, H. 2004. "Direct observations of colloid retention in granular media in the presence of energy barriers, and implications for inferred mechanisms from indirect observations". *Water Research*, 44, 1158-1169.
- Kader, B. 1981. "Temperature and concentration profiles in fully turbulent boundary layers. International". *Journal of Heat and Mass Transfer*, 24, 1541-1544.
- Kaftori, D., Hetsroni, G. & Banerjee, S. 1998. "The effect of particles on wall turbulence". *International Journal of Multiphase Flow*, 24, 359-386.
- Kafui, K.D., Thornton, C., Admas, M.J., 2004. "Reply to comments by Feng and Yu on 'Discrete particle-continuum fluid modelling of gas–solid fluidized beds'". *Chemical Engineering Science*, 59, 723–725.
- Kawaguchi, T., Tanaka, T., Tsuji, Y., 2000b. "Numerical analysis of density wave in dense gas–solid flows in a vertical pipe". *Progress of Theoretical Physics Supplement*, 696–701.
- Kawamura, H., Ohsaka, K., Abe, H. & Yamamoto, K. 1998. "DNS of turbulent heat transfer in channel flow with low to medium-high Prandtl number fluid". *International Journal of Heat and Fluid Flow*, 19, 482-491.
- Kim, J., Moin, P. & Moser, R. 1987. "Turbulence statistics in fully developed channel flow at low Reynolds number". *Journal of Fluid Mechanics*, 177, 133-166.
- Kraichnan, R. H. 1976. "Eddy viscosity in two and three dimensions". *Journal of the Atmospheric Sciences*, 33, 1521-1536.
- Kreplin, H. P. & Eckelmann, H. 1979. "Behavior of the three fluctuating velocity components in the wall region of a turbulent channel flow". *Physics of Fluids (1958-1988)*, 22, 1233-1239.
- Kuang, S., Chu, K., Yu, A., Zou, Z. & Feng, Y. 2008. "Computational investigation of horizontal slug flow in pneumatic conveying". *Industrial & Engineering Chemistry Research*, 47, 470-480.
- Kuang, S., Li, K., Zou, R., Pan, R. & Yu, A. 2013. "Application of periodic boundary conditions to CFD-DEM simulation of gas–solid flow in pneumatic conveying". *Chemical Engineering Science*, 93, 214-228.
- Kuerten, J. 2006. "Subgrid modeling in particle-laden channel flow". *Physics of Fluids (1994-present)*, 18, 025108.
- Kuipers, J.A.M., van Swaij, W.P.M., 1997. "Application of computational fluid dynamics to chemical reaction engineering". *Reviews in Chemical Engineering*, 13, 1118.
- Kuroda, A., Kasagi, N. & Hirata, M. 1989. "A direct numerical simulation of the fully developed turbulent channel flow at a very low Reynolds number". *ISCFD Nagoya 1989-3rd International Symposium on Computational Fluid Dynamics*, 1174-1179.
- Kuznar, Z. A. & Elimich, M. 2007. "Direct microscopic observation of particle deposition in porous media: Role of the secondary energy minimum". *Colloids and Surfaces A: Physicochemical and Engineering Aspects*, 294, 156-162.

- Lain, S. & Sommerfeld, M. 2012. "Numerical calculation of pneumatic conveying in horizontal channels and pipes: Detailed analysis of conveying behaviour". *International Journal of Multiphase Flow*, 39, 105-120.
- Lain, S. 2014. "Pneumatic Conveying of Solids along a Channel with Different Wall Roughness". *Chemical Engineering Communications*, 201, 437-455.
- Lain, S., Sommerfeld, M. & Kussin, J. 2002. "Experimental studies and modelling of four-way coupling in particle-laden horizontal channel flow". *International Journal of Heat and Fluid Flow*, 23, 647-656.
- Langston, P.A., Al-Awamleh, M.A., Fraige, F.Y., Asmar, B.N., 2004. "Distinct element modelling of non-spherical frictionless particle flow". *Chemical Engineering Science*. 59, 425–435.
- Langston, P.A., Tuzun, U., Heyes, D.M., 1994. "Continuous potential discrete particle simulations of stress and velocity-fields in hoppers—transition from fluid to granular flow". *Chemical Engineering Science*. 49, 1259–1275.
- Laube, B. L., Benedict, G. W. & Dobs, A. S. 1998. "Time to peak insulin level, relative bioavailability, and effect of site of deposition of nebulized insulin in patients with noninsulin-dependent diabetes mellitus". *Journal of Aerosol Medicine*, 11, 153-173.
- Leite, F., Riul, A. & Herrmann, P. 2003. "Mapping of adhesion forces on soil minerals in air and water by atomic force spectroscopy (AFS)". *Journal of Adhesion Science and Technology*, 17, 2141-2156.
- Lelouvetel, J., Bigillon, F., Doppler, D., Vinkovic, I. & Champagne, J. Y. 2009. "Experimental investigation of ejections and sweeps involved in particle suspension". *Water Resources Research*, 45.
- Lesieur, M. & Metais, O. 1996. "New trends in large-eddy simulations of turbulence". *Annual Review of Fluid Mechanics*, 28, 45-82.
- Li, J. H., 2000. "Compromise and resolution—exploring the multi-scale nature of gas–solid fluidization". *Powder Technology*. 111, 50–59.
- Li, J., Kuipers, J.A.M., 2003. "Gas–particle interactions in dense gas-fluidized beds". *Chemical Engineering Science*. 58, 711–718.
- Li, J., Wang, H., Liu, Z., Chen, S. & Zheng, C. 2012. "An experimental study on turbulence modification in the near-wall boundary layer of a dilute gas-particle channel flow", *Experiments in fluids*, 53, 1385-1403.
- Li, J., Webb, C., Pandilla, S., Campbell, G., Dyakowski, T., Cowell, A. & McGlinchey, D. 2005b. "Solids deposition in low-velocity slug flow pneumatic conveying". *Chemical Engineering and Processing: Process Intensification*, 44, 167-173.
- Li, S. Q. & Marshall, J. 2007. "Discrete element simulation of micro-particle deposition on a cylindrical fiber in an array". *Journal of Aerosol Science*, 38, 1031-1046.
- Li, Y., Zhang, J.P., Fan, L.S., 1999. "Numerical simulation of gas–liquid–solid fluidization systems using a combined CFD-VOF-DPM method, bubble wake behaviour". *Chemical Engineering Science*. 54, 5101–5107.
- Li, Z., Wang, Y. & Zhang, Y. 2014. "A numerical study of particle motion and two-phase interaction in aeolian sand transport using a coupled large eddy simulation–discrete element method". *Sedimentology*, 61, 319-332.
- Lilly, D. 1992. "A proposed modification of the Germanosubgrid-scale closure method". *Physics of Fluids and Fluid Dynamics*, 4, 633.
- Lilly, D. K. 1967. "The representation of small scale turbulence in numerical simulation experiments".

- Limtrakul, S., Rotjanavijit, W. & Vatanatham, T. 2007. "Lagrangian modeling and simulation of effect of vibration on cohesive particle movement in a fluidized bed". *Chemical Engineering Science*, 62, 232-245.
- Liu, Z., Adrian, R. & Hanratty, T. 2001. "Large-scale modes of turbulent channel flow: transport and structure". *Journal of Fluid Mechanics*, 448, 53-80.
- Loth, E. 2008. "Drag of non-spherical solid particles of regular and irregular shape". *Powder Technology*, 182, 342-353.
- Lourenco, L., Riethmuller, M.L., Essers, J.-A., 1983. "The kinetic model for gas particle flow and its numerical implementation". Presented at *International Conference on the Physical Modelling of Multi-Phase Flow*, Coventry, England, April 19–21.
- Luding, S., 2005. "Molecular Dynamics Simulations of Granular Materials", in *The Physics of Granular Media*. New York: John Wiley. p. 297-324.
- Lun, C. & Liu, H. 1997. "Numerical simulation of dilute turbulent gas-solid flows in horizontal channels". *International Journal of Multiphase Flow*, 23, 575-605.
- Luo, K., Fang, M., Yang, S., Zhang, K. & Fan, J. 2013. "LES-DEM investigation of an internally circulating fluidized bed: Effects of gas and solid properties". *Chemical Engineering Journal*.
- Ma, H., Pedel, J., Fife, P. & Johnson, W. P. 2009. "Hemispheres-in-Cell Geometry to Predict Colloid Deposition in Porous Media". *Environmental Science & Technology*, 43, 8573-8579.
- Mallouppas, G. & Van Wachem, B. 2013. "Large Eddy Simulations of turbulent particle-laden channel flow". *International Journal of Multiphase Flow*, 54, 65-75.
- Mansoupour, Z., Mostoufi, N. & Sotudeh-Gharebagh, R. 2014. "Investigating agglomeration phenomena in an air-polyethylene fluidized bed using DEM-CFD approach". *Chemical Engineering Research and Design*, 92, 102-118.
- Marchioli, C. & Soldati, A. 2007. "Reynolds number scaling of particle preferential concentration in turbulent channel flow". *Advances in Turbulence XI*. Springer.
- Marchioli, C., Giusti, A., Salvetti, M.V., Soldati, A. 2003. "Direct numerical simulation of particle wall transfer and deposition in upward turbulent pipe flow". *International Journal of Multiphase Flow*. 29, 1017–1038 (2003)
- Marchioli, C., Salvetti, M. V. & Soldati, A. 2008a. "Appraisal of energy recovering sub-grid scale models for large-eddy simulation of turbulent dispersed flows. 201, - 296.
- Marchioli, C., Salvetti, M. V. & Soldati, A. 2008b. "Some issues concerning large-eddy simulation of inertial particle dispersion in turbulent bounded flows". 20.
- Marchioli, C., Salvetti, M. V. & Soldati, A., Kuerten, J., Arcen, B., Taniere, A., Goldensoph, G., Squires, K., Cargnelutti, M. & Portela, L. 2008. "Statistics of particle dispersion in direct numerical simulations of wall-bounded turbulence: results of an international collaborative benchmark test". *International Journal of Multiphase Flow*, 34, 879-893.
- Marshall, J. 2007. "Particle aggregation and capture by walls in a particulate aerosol channel flow". *Journal of aerosol science*, 38, 333-351.
- Mason, P. J. 1994. "Large-eddy simulation: A critical review of the technique". *Quarterly Journal of the Royal Meteorological Society*, 120, 1-26.
- Matais, O. & Lesieur, M. 1992. "Spectral large-eddy simulation of isotropic and stably stratified turbulence". *Journal of Fluid Mechanics*, 239, 157-194.
- Matsouka, H. & Kato, T. 1995. "Adhesion forces between mica surfaces in air and liquids". *International Tribology Conference*, Yokohama.

- Matuttis, Hans-Georg, and Jian Chen. 2014. *Understanding the Discrete Element Method: Simulation of Non-Spherical Particles for Granular and Multi-body Systems*. New York: John Wiley & Sons.
- McLaughlin, J. B. (1991). "Inertial migration of a small sphere in linear shear flows". *Journal of Fluid Mechanics*, 224, 261-274.
- Mei, R. 1992. "An approximate expression for the shear lift force on a spherical particle at finite Reynolds number". *International Journal of Multiphase Flow*, 18, 145-147.
- Meneveau, C. & Katz, J. 2000. "Scale-invariance and turbulence models for large-eddy simulation". *Annual Review of Fluid Mechanics*, 32, 1-32.
- Meyers, J., Geurts, B. J. & Baelmans, M. 2003. "Database analysis of errors in large-eddy simulation". *Physics of Fluids (1994-present)*, 15, 2740-2755.
- Meyers, J., Geurts, B. J. & Baelmans, M. 2005. "Optimality of the dynamic procedure for large-eddy simulations". *Physics of Fluids (1994-present)*, 17, 045108.
- Mindlin, R. D. and H. Deresiewicz (1953). "Elastic spheres in contact under varying oblique forces". *Journal of Applied Mechanics*, 20: 327-344.
- Mohaupt, M., Minier, J. P. & Taniere, A. 2011. "A new approach for the detection of particle interactions for large-inertia and colloidal particles in a turbulent flow". *International Journal of Multiphase Flow*, 37, 746-755.
- Moin, P. & Mahesh, K. 1998. "Direct numerical simulation: a tool in turbulence research". *Annual Review of Fluid Mechanics*, 30, 539-578.
- Monty, J. & Chong, M. 2009. "Turbulent channel flow: comparison of streamwise velocity data from experiments and direct numerical simulation". *Journal of Fluid Mechanics*, 633, 461-474.
- Monty, J. P. 2005. *Developments in smooth wall turbulent duct flows*, University of Melbourne, Department of Mechanical and Manufacturing Engineering.
- Moreno, R., Ghadiri, M., Antony, S.J., 2003. "Effect of the impact angle on the breakage of agglomerates: a numerical study using DEM". *Powder Technology*, 130, 132-137.
- Moreno-Atansio, R. 2012. "Energy dissipation in agglomerates during normal impact". *Powder technology*, 223, 12-18.
- Moser, R. D., Kim, J. & Mansour, N. N. 1999. "Direct numerical simulation of turbulent channel flow up to $Re = 590$ ". *Physics Fluids*, 11, 943-945.
- Nalaskowski, J., Drelich, J., Hupka, J. & Miller, J. D. 2003. "Adhesion between hydrocarbon particles and silica surfaces with different degrees of hydration as determined by the AFM colloidal probe technique". *Langmuir*, 19, 5311-5317.
- Narayanan, C. & Lakehal, D. 2013. "Four-Way Coupling of Dense Particle Beds of Black Powder in Turbulent Pipe Flows". ASME 2010 3rd Joint US-European Fluids Engineering Summer Meeting collocated with 8th International Conference on Nanochannels, Microchannels, and Minichannels, 2010. *American Society of Mechanical Engineers*, 269-274.
- Ng, H., Monty, J., Hutchins, N., Chong, M. & Marusic, I. 2011. "Comparison of turbulent channel and pipe flows with varying Reynolds number". *Experiments in fluids*, 51, 1261-1281.
- Niederschulte, M., Adrian, R. & Hanratty, T. 1990. "Measurements of turbulent flow in a channel at low Reynolds numbers". *Experiments in Fluids*, 9, 222-230.
- Nikuradse J. 1926. "Untersuchung über die Geschwindigkeitsverteilung in turbulenten Strömungen Thesis, Gottingen, 1926. V.D.I. - Forsch. 281.
- Nishiura, D., Wakita, Y., Shimosaka, A., Shirakawa, Y. & Hidaka, J. 2010. "Estimation of power during dispersion in stirred media mill by DEM-LES simulation". *Journal of Chemical Engineering of Japan*, 43, 841-849.

- Njobuenwu, D. & Fairweather, M. 2014. "Effect of Shape on Inertial Particle Dynamics in a Channel Flow". *Flow, Turbulence and Combustion*, 92, 83-101.
- Obligado, M., Baudet, C., Gagne, Y. & Bourgon, M. 2011. "Constrained dynamics of an inertial particle in a turbulent flow". *Journal of Physics: Conference Series*, 2011. IOP Publishing, 052016.
- Oliemans, R. V. A., Pots, B. F. M. & Trompe, N. 1986. "Modelling of annular dispersed two-phase flow in vertical pipes". - 12.
- Ouriev, B. & Windhab, E. 2002. "Rheological study of concentrated suspensions in pressure-driven shear flow using a novel in-line ultrasound Doppler method". *Experiments in fluids*, 32, 204-211.
- Paiva, J., Salcedo, R. & Araujo, P. 2010. "Impact of particle agglomeration in cyclones". *Chemical Engineering Journal*, 162, 861-876.
- Pan, T.W., Joseph, D.D., Bai, R., Glowinski, R., Sarin, V., 2002. "Fluidization of 1204 spheres: simulation and experiment". *Journal of Fluid Mechanics*. 451, 169–191.
- Pan, X., Liu, X., Li, G. & Li, T. 2011a. "Numerical investigation on gas–particle flows in horizontal channel under the reduced gravity environments". *Acta Astronautica*, 68, 133-140.
- Pan, Z., Hou, C. & Yan, F. 2011b. "Numerical simulation study of turbulent flow field in 90 bend pipe". *Journal of Chemical Industry & Engineering*, 3, 004.
- Patel, V. & Head, M. R. 1968. "Reversion of turbulent to laminar flow". *Journal of Fluid Mechanics*, 34, 371-392.
- Pelessone, D., 2003. "Discrete element simulations using macro-particles". in Bathe, K.J. (Ed.), *Computational Fluid and Solid Mechanics*. pp. 2089–2092.
- Peng, Z., Doroodchi, E. & Evans, G. 2010. "DEM simulation of aggregation of suspended nanoparticles". *Powder Technology*, 204, 91-102.
- Picciotto, M., Marchioli, C. & Soldati, A. 2005. "Characterization of near-wall accumulation regions for inertial particles in turbulent boundary layers". 17, 4.
- Piomelli, U. & Balaras, E. 2002. "Wall-layer models for large-eddy simulations". *Annual review of fluid mechanics*, 34, 349-374.
- Pope III, C. A. 2000. "Review: epidemiological basis for particulate air pollution health standards". *Aerosol Science & Technology*, 32, 4-14.
- Postma A. K., Schwendiman LC. 1960. "Studies in micrometrics: I. Particle deposition in conduits as a source of error in aerosol sampling". *Report no. HW-65308*
- Potic, B., Kersten, S.R.A., Ye, M., van der Hoef, M.A., Kuipers, J.A.M., van Swaaij, W.P.M., 2005. "Fluidization with hot compressed water in microreactors". *Chemical Engineering Science*. 60, 5982–5990.
- Pozorski, J. & Apre, S. V. 2009. "Filtered particle tracking in isotropic turbulence and stochastic modeling of subgrid-scale dispersion". *International Journal of Multiphase Flow*, 35, 118-128.
- Pritchett, J.W., Blake, T.R., Garg, S.K., 1978. "A numerical model of gas fluidized beds". *A.I.Ch.E. Symposium Series* 176, 134–148.
- Quattrin, T., Belanger, A., Bohannon, N. J. & Schwartz, S. L. 2004. "Efficacy and Safety of Inhaled Insulin (Exubera) Compared With Subcutaneous Insulin Therapy in Patients With Type 1 Diabetes Results of a 6-month, randomized, comparative trial". *Diabetes Care*, 27, 2622-2627.
- Rave, K. M., Nosek, L., De La Pena, A., Seger, M., Ernest, C. S., Heinann, L., Batycky, R. P. & Muchmore, D. B. 2005. "Dose response of inhaled dry-powder insulin and dose equivalence to subcutaneous insulin lispro". *Diabetes Care*, 28, 2400-2405.
- Rhie, C. & Chow, W. 1983. "Numerical Study of the Turbulent Flow Pastan Isolated Airfoil with Trailing Edge Separation". *AIAA*, 21.

- Richardson, J.F., 1971. "Incipient fluidization and particulate systems". in Davidson, J.F., Harrison, D. (Eds.), *Fluidization*. New York: Academic Press.
- Robinson, S. K. 1991. "Coherent motions in the turbulent boundary layer". *Annual Review of Fluid Mechanics*, 23(1), 601-639.
- Rosenstock, J. 2002. "Mealtime rapid-acting inhaled insulin (Exubera (R)) improves glycemic control in patients with type 2 diabetes failing combination oral agents: A 3-month, randomized, comparative trial". *Diabetes*, Amer Diabetes Association, USA, A132-A133.
- Saffman, P. G. 1965. "The lift on a small sphere in a slow shear flow". *Journal of Fluid Mechanics*, 22(02), 385-400.
- Saffman, P. G. 1968. "Conservation of circulation theorem for superfluids. *Physics of Fluids* (1958-1988), 11(12), 2505-2507.
- Schmidt, T., Assadi, H., Gärtner, F., Richter, H., Stoltenhoff, T., Kreye, H., & Klassen, T. 2009. "From particle acceleration to impact and bonding in cold spraying" *Journal of Thermal Spray Technology*, 18(5-6), 794-808.
- Schultz, M. & Flack, K. 2013. "Reynolds-number scaling of turbulent channel flow". *Physics of Fluids (1994-present)*, 25, 025104.
- Schumann, U. 1975. "Subgrid scale model for finite difference simulations of turbulent flows in plane channels and annuli". *Journal of computational physics*, 18, 376-404.
- Sehmel GA. 1968. "Aerosol deposition from turbulent airstreams in vertical conduits". Report no. BNWL-578, Richland, Washington: Pacific Northwest Laboratory.
- Seville, J. P. K., C. D. Willett, et al. 2000. "Interparticle forces in fluidisation: a review." *Powder Technology*, 113(3): 261-268.
- Shaikh, I., Jadhav, K., Ganga, S., Kadam, V. & Pisal, S. 2005. "Advanced approaches in insulin delivery". *Current Pharmaceutical Biotechnology*, 6, 387-395.
- Shimosaka, A., Asahi, R., Nishiura, D., Shirakawa, Y. & Hidaka, J. 2012. "Design of Nanoparticle Dispersion Process in Stirred Media Mill Using DEM-LES Coupling Method". *Journal of Chemical Engineering of Japan*, 45, 801-810.
- Shotorban, B. & Mashayek, F. 2005. "Modeling subgrid-scale effects on particles by approximate deconvolution". No. 17.
- Shotorban, B., Zhang, K. K. Q. & Mashyeyk, F. 2007. "Improvement of particle concentration prediction in large-eddy simulation by defiltering". No. 50, - 3739.
- Singh, P., Joseph, D.D., Hesla, T.I., Glowinski, R., Pan, T.W., 2000. "A distributed Lagrange multiplier/fictitious domain method for viscoelastic particulate flows". *Journal of Non-Newtonian Fluid Mechanics*. 91, 165-188.
- Sippola M. R., Nazaroff ,WW. 2002. " Particle deposition from turbulent flow: Review of published research and its applicability to ventilation ducts in commercial buildings".
- Sippola M. R., Nazaroff ,WW. 2004. "Experiments Measuring Particle Deposition from Fully Developed Turbulent Flow in Ventilation Ducts". *Aerosol Science and Technology*, 38: 914 - 925.
- Smagorinsky, J. 1963. "General Circulation Experiments with the Primitive Equations I: the basic experiment, *Monthly weather review*, 91, 99-164.
- Soldati, A. & Andreussi, P. 1996. "The influence of coalescence on droplet transfer in vertical annular flow. 51, 363.
- Soldati, A. & Marchioli, C. 2009. "Physics and modelling of turbulent particle deposition and entrainment: Review of a systematic study". *International Journal of Multiphase Flow*, 35, 827-839.

- Soldati, A. 2005. "Particles turbulence interactions in boundary layers: Plenary lecture" presented at the *75th Annual GAMM Conference*, Dresden/Germany, 22-26 March 2004. - 85, - 699.
- Sommerfeld M, Zivkovic G. 1992. "Recent advances in the numerical simulation of pneumatic conveying through pipe systems". *Computational methods in applied sciences*, 201.
- Sommerfeld M. and Qiu. H. H. 1995. "Particle concentration measurements by phase-doppler anemometry in complex dispersed two-phase flows. *Exp. Fluids*, 18:187–198.
- Sommerfeld, M. & Kussin, J. 2004. "Wall roughness effects on pneumatic conveying of spherical particles in a narrow horizontal channel". *Powder Technology*, 142, 180-192.
- Sommerfeld, M., Huber, N., 1999. "Experimental analysis and modelling of particle-wall collisions". *International Journal Multiphase Flow*. 25, 1457–1489.
- Sommerfeld. M. 1998. "Modellierung und numerischeberechnung von partikelbeladenenturbulentenströmungenmithilfe des euler/lagrange-verfahrens". *International Journal Heat Fluid Flow*, 19:10–22.
- Sommerfeld. M. 2000. "Theoretical and experimental modelling of particulate flows". Technical Report Lecture Series 2000-06, *von Karman Institute for Fluid Dynamics*.
- Squires, K. D. & Eaton, J. K. 1990. "Particle response and turbulence modification in isotropic turbulence". *Physics of Fluids A: Fluid Dynamics*, 2, 1191.
- Stratton, R. & Wensrich, C. 2011. "Horizontal slug flow pneumatic conveying: Numerical simulation and analysis of a thin slice approximation". *Powder Technology*, 214, 477-490.
- Sturm. M, Wirtz. S, Viktor, S., (2009). "Coupled Discrete Element (DEM)–Continuous Fluid (CFD) Method for the Application of Pneumatic Conveyed Granular Media", *Paper no. PVP2009-77240* pp. 547-556 (10 pages)
- Subero, J., Ning, Z., Ghadiri, M., Thornton, C., 1999. "Effect of interface energy on the impact strength of agglomerates". *Powder Technology*. 105, 66–73.
- Takeda, Y. 1986. "Velocity profile measurement by ultrasound Doppler shift method". *International journal of heat and fluid flow*, 7, 313-318.
- Taniere, A., Oesterle, B. & Monnier, J. 1997. "On the behaviour of solid particles in a horizontal boundary layer with turbulence and saltation effects". *Experiments in Fluids*, 23, 463-471.
- Thornton, C. & Ning, Z. 1998. "A theoretical model for the stick/bounce behaviour of adhesive, elastic-plastic spheres". *Powder Technology*, 99, 154-162.
- Thornton, C. and K. K. Yin (1991). "Impact of Elastic of Elastic Spheres With and without Adhesion." *Powder Technology*. 65(1-3): 153-166.
- Tomac, I. & Gutierrez, M. 2014. "Fluid lubrication effects on particle flow and transport in a channel". *International Journal of Multiphase Flow*.
- Tong, Z., Yang, R., Chu, K., Yu, A., Adi, S. & Chan, H. 2010. "Numerical study of the effects of particle size and polydispersity on the agglomerate dispersion in a cyclonic flow". *Chemical Engineering Journal*, 164, 432-441.
- Tsuji, Y. 2000. "Activities in discrete particle simulation in Japan". *Powder Technology*, 113, 278-286.
- Tsuji, Y., 1993. "Discrete particle simulation of gas–solid flows (from dilute to dense flow). *KONA (Powder and Particles)* 11, 57–68.
- Tsuji, Y., Tanaka, T., Ishida, T., 1992. "Lagrangian numerical simulation of plug flow of cohesionless particles in a horizontal pipe". *Powder Technology*. 71, 239–250.

- Tsukahara, T. 2014. "DNS of turbulent channel flow at very low Reynolds numbers". *arXiv preprint arXiv:1406.0248*.
- Van der Hoef, M.A., et al., 2006. "Multiscale Modeling of Gas-Fluidized Beds", in *Advances in Chemical Engineering*. New York: Academic Press. p. 65-149
- Vande Wall, R. & Soo, S. 1997. "Measurement of transport properties of a gas-solid suspension using phase Doppler anemometry". *Powder technology*, 94, 141-151.
- Varaksin, A.Y., Polezhaev, Y.V., Polyakov, A.F., 1998. "Experimental investigation of the effect of solid particles on turbulent flow of air in a pipe". *High Temp.* 36, 744–752.
- Varaksin, A.Yu., Polezhaev, Y.V., Polyakov, A.F., 1999. "Effect of the particles concentration on fluctuating velocity of the disperse phase for turbulent pipe flow. in *Turbulence and Shear Flow Phenomena*, First International Symposium, September 12–15, Santa Barbara, CA.
- Vincent, S., Brandle De Motta, J. C., Sarthou, A., Estivalezes, J.-L., Simonin, O. & Climent, E. 2014. "A Lagrangian VOF tensorial penalty method for the DNS of resolved particle-laden flows". *Journal of Computational Physics*, 256, 582-614.
- Vinkovic, I., D'Oopler, D., Lelouvetel, J. & Buffat, M. 2011. "Direct numerical simulation of particle interaction with ejections in turbulent channel flows". *International Journal of Multiphase Flow*, 37, 187-197.
- Visser, J. (1989). "Van der Waals and other cohesive forces affecting powder fluidization." *Powder Technology* 58(1): 1-10.
- Vreman, B., Geurts, B. & Kuerten, H. 1997. "Large-eddy simulation of the turbulent mixing layer". *Journal of Fluid Mechanics*, 339, 357-390.
- Wadell, H. 1935. "Volume, shape, and roundness of quartz particles". *The Journal of Geology*, 250-280.
- Wait, R., 2001. "Discrete element models of particle flows". *Mathematical Modelling and Analysis* 6, 156–164.
- Walton, O.R., 1993. "Numerical simulation of inclined chute flows of monodisperse inelastic, frictional spheres". *Mechanics of Materials* 16, 239–247.
- Walton, O.R., Braun, R.L., 1986a. "Viscosity, granular-temperature, and stress calculations for shearing assemblies of inelastic, frictional disks". *Journal of Rheology* 30, 949–980.
- Wang, X. S. & Rhodes, M. 2004. "Mechanistic study of defluidization by numerical simulation". *Chemical engineering science*, 59, 215-222.
- Wang, X., You, C., Liu, R. & Yang, R. 2011. "Particle deposition on the wall driven by turbulence, thermophoresis and particle agglomeration in channel flow". *Proceedings of the Combustion Institute*, 33, 2821-2828.
- Watano, S. 2006. "Mechanism and control of electrification in pneumatic conveying of powders". *Chemical Engineering Science*, 61, 2271-2278.
- Wells AC, Chamberlain AC. 1967. "Transport of small particles to vertical surfaces". *British Journal of Applied Physics*, 18: 1793.
- Wen, Y.C., Yu, Y.H. "Mechanics of fluidization". *Chemical Engineering Programme Symposium Series* 62, 100–111 (1966)
- Werner, H. & Wengle, H. 1993. "Large-eddy simulation of turbulent flow over and around a cube in a plate channel". *Turbulent Shear Flows* 8. Springer.
- Westerweel, J. 1997. "Fundamentals of digital particle image velocimetry". *Measurement Science and Technology*, 8, 1379.
- Wu, Y., Wang, H., Liu, Z., Li, J., Zhang, L. & Zheng, C. 2006. "Experimental investigation on turbulence modification in a horizontal channel flow at relatively low mass loading". *Acta Mechanica Sinica*, 22, 99-108.

- Xiong, Y.Q., Zhang, M.Y., Yuan, Z.L., 2005. "Three-dimensional numerical simulation method for gas–solid injector". *Powder Technology*, 160, 180–189.
- Xu, B.H., Feng, Y.Q., Yu, A.B., Chew, S.J., Zulli, P., 2001. "A numerical and experimental study of gas–solid flow in a fluid-bed reactor". *Powder Handling and Processing*, 13, 71–76.
- Xu, B.H., Yu, A.B., Chew, S.J., Zulli, P., 2000. "Numerical simulation of the gas–solid flow in a bed with lateral gas blasting". *Powder Technology*, 109, 13–26.
- Yamamoto, Y., Potthoff, M., Tanaka, T., Kajishima, T. & Tsuji, Y. 2001. "Large-eddy simulation of turbulent gas–particle flow in a vertical channel: effect of considering inter-particle collisions". *Journal of Fluid Mechanics*, 442, 303–334.
- Yamanaka, G., Kikura, H., Takeda, Y. & Aritomi, M. 2002. "Flow measurement on an oscillating pipe flow near the entrance using the UVP method". *Experiments in fluids*, 32, 212–220.
- Yang, R., Yu, A., Choi, S., Coates, M. & Chan, H. 2008. "Agglomeration of fine particles subjected to centripetal compaction". *Powder Technology*, 184, 122–129.
- Yang, S., Luo, K., Fang, M., Zhang, K. & Fan, J. 2013. "Three-Dimensional Modeling of Gas–Solid Motion in a Slot-Rectangular Spouted Bed with the Parallel Framework of the Computational Fluid Dynamics–Discrete Element Method Coupling Approach". *Industrial & Engineering Chemistry Research*, 52, 13222–13231.
- Yang, S., Luo, K., Qiu, K., Fang, M. & Fan, J. 2014. "Coupled Computational Fluid Dynamics and Discrete Element Method Study of the Solid Dispersion Behavior in an Internally Circulating Fluidized Bed". *Industrial & Engineering Chemistry Research*, 53, 6759–6772.
- Yeh, Y. & Cummins, H. 1964. "Localized fluid flow measurements with an He–Ne laser spectrometer". *Applied Physics Letters*, 4, 176–178.
- Yoder J, Silverman L. 1967. "Influence of turbulence on aerosol agglomeration and deposition in a pipe". *Paper No. 67-33 60th Annual Air Pollution Control, Association Meeting*. Cleveland, Ohio.
- Yoshida, Y., Katsumoto, T., Taniguchi, S., Shimosaka, A., Shirakawa, Y. & Hidaka, J. 2013. "Prediction of Viscosity of Slurry Suspended Fine Particles Using Coupled DEM-DNS Simulation". *Chemical Engineering*, 32.
- Young, J. & Leeming, A. 1997. "A theory of particle deposition in turbulent pipe flow". *Journal of Fluid Mechanics*, 340, 129–159.
- Zanoun, E., Nagib, H. & Durst, F. 2009. "Refined cf relation for turbulent channels and consequences for high-Re experiments". *Fluid dynamics research*, 41, 021405.
- Zhang J, Li A. 2008. "CFD simulation of particle deposition in a horizontal turbulent duct flow". *Chemical Engineering Research and Design*, 86: 95–106.
- Zhang, B., Jin, J., Wang, H.P., 1999a. "The calculation of retarded van der Waals interaction for practical applications". *Journal of Dispersion Science and Technology* 20, 1485–1500.
- Zhang, H., Trias, F. X., Gorobets, A., Yang, D., Oliva, A., Tan, Y. & Sheng, Y. 2014a. "Effect of collisions on the particle behavior in a turbulent square duct flow". *Powder Technology*.
- Zhang, J., Chen, W., Cheng, R., Williams, K., Jones, M. & Zhou, B. A. 2014b. "Comparative Study on the Influence of Particle Size on the Turbulence Characteristics within Gas-Solids Pneumatic Flows Using an Electrostatic Sensor and CFD-DEM Coupled Simulation. *Particle Science and Engineering*:

- Proceedings of UK-China International Particle Technology Forum IV*, Royal Society of Chemistry, 142.
- Zhang, J., Tao, B. & Katz, J. 1997. "Turbulent flow measurement in a square duct with hybrid holographic PIV". *Experiments in Fluids*, 23, 373-381.
- Zhang, J.P., Fan, L.S., Zhu, C., Pfeffer, R., Qi, D.W., 1999b. @Dynamic behaviour of collision of elastic spheres in viscous fluids. *Powder Technology* 106, 98–109.
- Zhang, S.J., Yu, A.B., Zulli, P., Wright, B., Tuzun, U., 1998. "Modelling of the solids flow in a blast furnace". *ISIJ International* 38, 1311–1319.
- Zhao, F. & Van Wachem, B. 2013. "Direct numerical simulation of ellipsoidal particles in turbulent channel flow". *Acta Mechanica*, 224, 2331-2358.
- Zhao, Y., Cheng, Y., Wu, C., Ding, Y. & Jin, Y. 2010. "Eulerian–Lagrangian simulation of distinct clustering phenomena and RTDs in riser and downer". *Particuology*, 8, 44-50.
- Zhou, H., Flamant, G. & Gauthier, D. 2004. "DEM-LES of coal combustion in a bubbling fluidized bed. Part I: gas-particle turbulent flow structure". *Chemical Engineering Science*, 59, 4193-4203.
- Zhou, Z., Kuang, S., Chu, K. & Yu, A. 2010. "Discrete particle simulation of particle–fluid flow: model formulations and their applicability". *Journal of Fluid Mechanics*, 661, 482-510.
- Zhu, H. P., Z. Y. Zhou, et al. (2007). "Discrete particle simulation of particulate systems: Theoretical developments". *Chemical Engineering Science*. 62(13): 3378-3396.
- Zhu, H. P., Z. Y. Zhou, et al. (2008). "Discrete particle simulation of particulate systems: A review of major applications and findings". *Chemical Engineering Science*. 63(23): 5728-5770.
- Zhu, H.P., Yu, A.B., 2003. "The effects of wall and rolling resistance on the couple stress of granular materials in vertical flow". *Physica A* 325, 347–360.
- Zhu, H.P., Yu, A.B., 2006. "A theoretical analysis of the force models in discrete element method". *Powder Technology*. 161, 122–129.
- Zhu, H.P., Zhou, Z.Y., Yang, R.Y., Yu, A.B., 2006. "Discrete particle simulation of particulate systems: applications". *Manuscript to be submitted for publication*.

Appendix A: Sensitivity study on fluid phase

In this section, a sensitivity study is carried out on the most important parameters required in setting up the flow in ANSYS FLUENT. The results are presented and discussed to achieve an LES solution that is both computationally efficient and accurate compared to DNS. It is important to mention here that all fluid velocity statistics presented in this thesis refer to a fully developed flow. This point is achieved, when the first- and second-order moments (specifically, the mean streamwise velocity, rms values for all three directions and the Reynolds stresses) remain constant with time. To achieve smooth profiles the fluid statistics have been both spatial- and time-averaged over 100's of thousands of time steps. In most cases a coarse mesh has been used to give faster run times. The results generated by the LES for the fluid phase were compared using DNS predictions for shear Reynolds flows of $Re_\tau = 300$ (Marchioli and Soldati, 2007).

A. 1 Mesh Size

Three different mesh sizes were compared, $65 \times 64 \times 64$, $81 \times 80 \times 80$ and $100 \times 100 \times 100$ have been compared against DNS. A more refined mesh was not selected due to the increase in computational expense. The work uses a four-way coupled approach, therefore, it necessary that minimum cell size at the wall for the fluid phase is at least 5 % larger than the particle size. For that reason, the minimum cell size at the wall was fixed at $160 \mu\text{m}$ in all cases. The 100^3 mesh showed the best results and has been selected for the final set up.

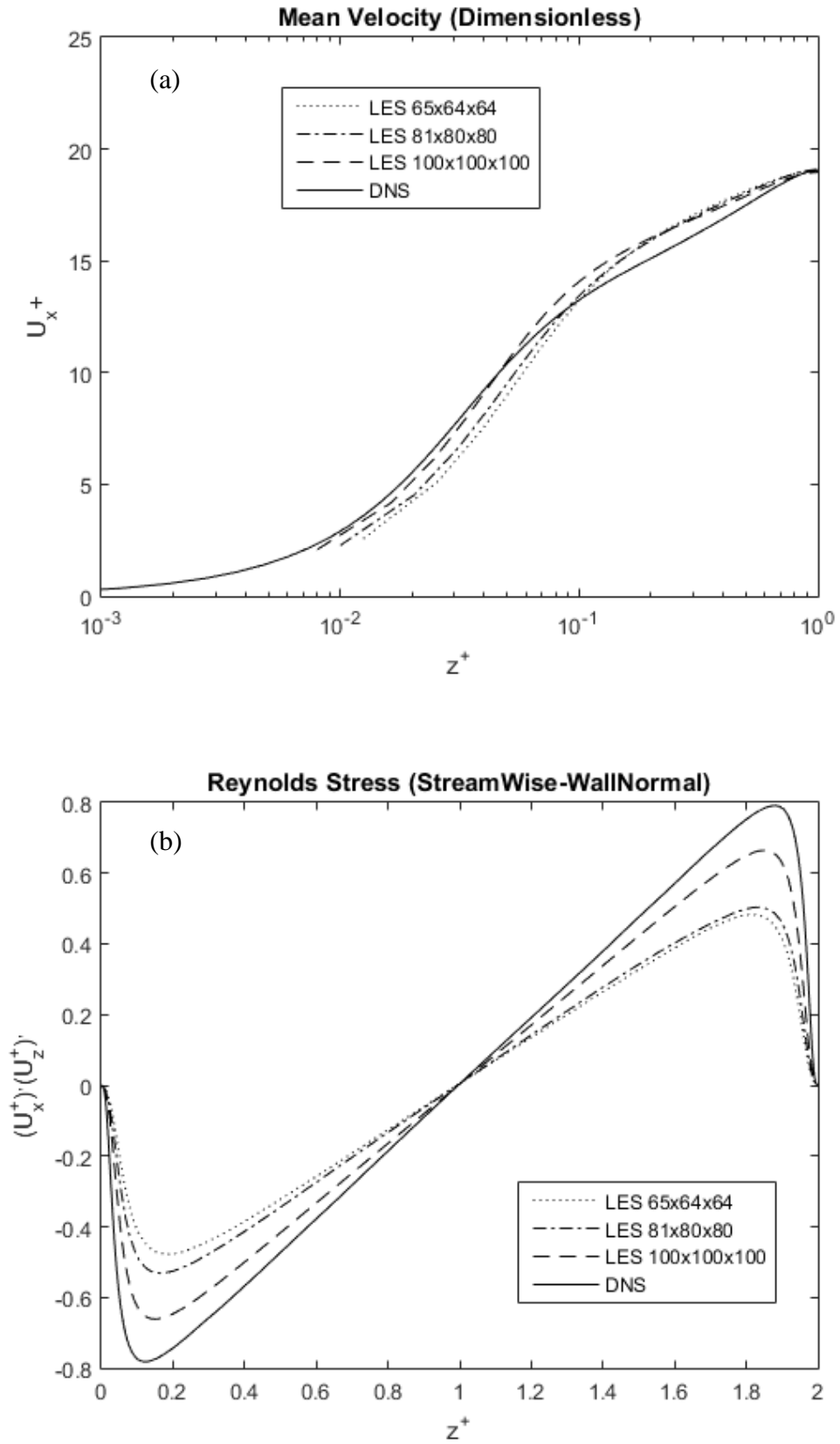


Figure A 1 (a) Mean streamwise fluid velocity; (b) Fluid Reynolds stress component. ($Re_\tau = 300$).

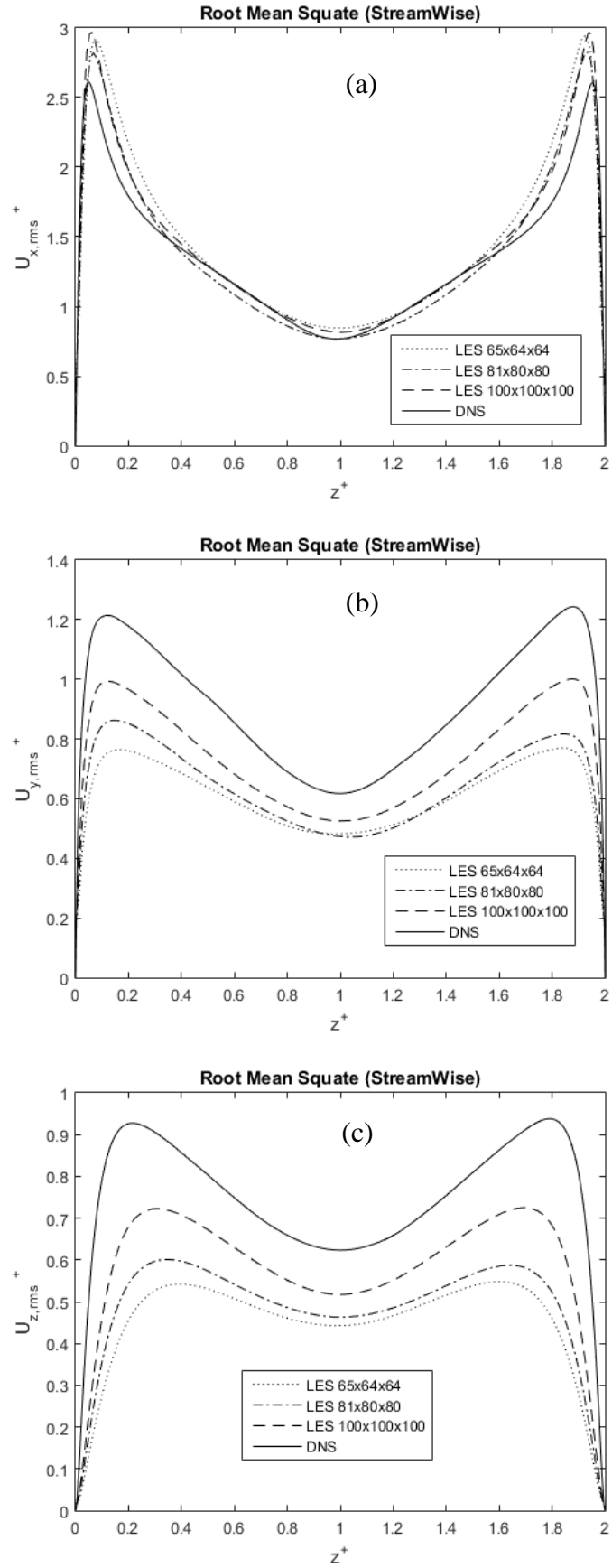


Figure A 2 Root mean square of fluid velocity fluctuation (a) streamwise rms component; (b) spanwise rms component; (c) wall-normal rms component. ($Re_\tau = 300$).

A. 2 Time Step

Three different time steps were compared, 3×10^{-5} , 1.5×10^{-5} and 1×10^{-5} s have been compared against DNS. The latter showed the best results and has been selected for the final set up.

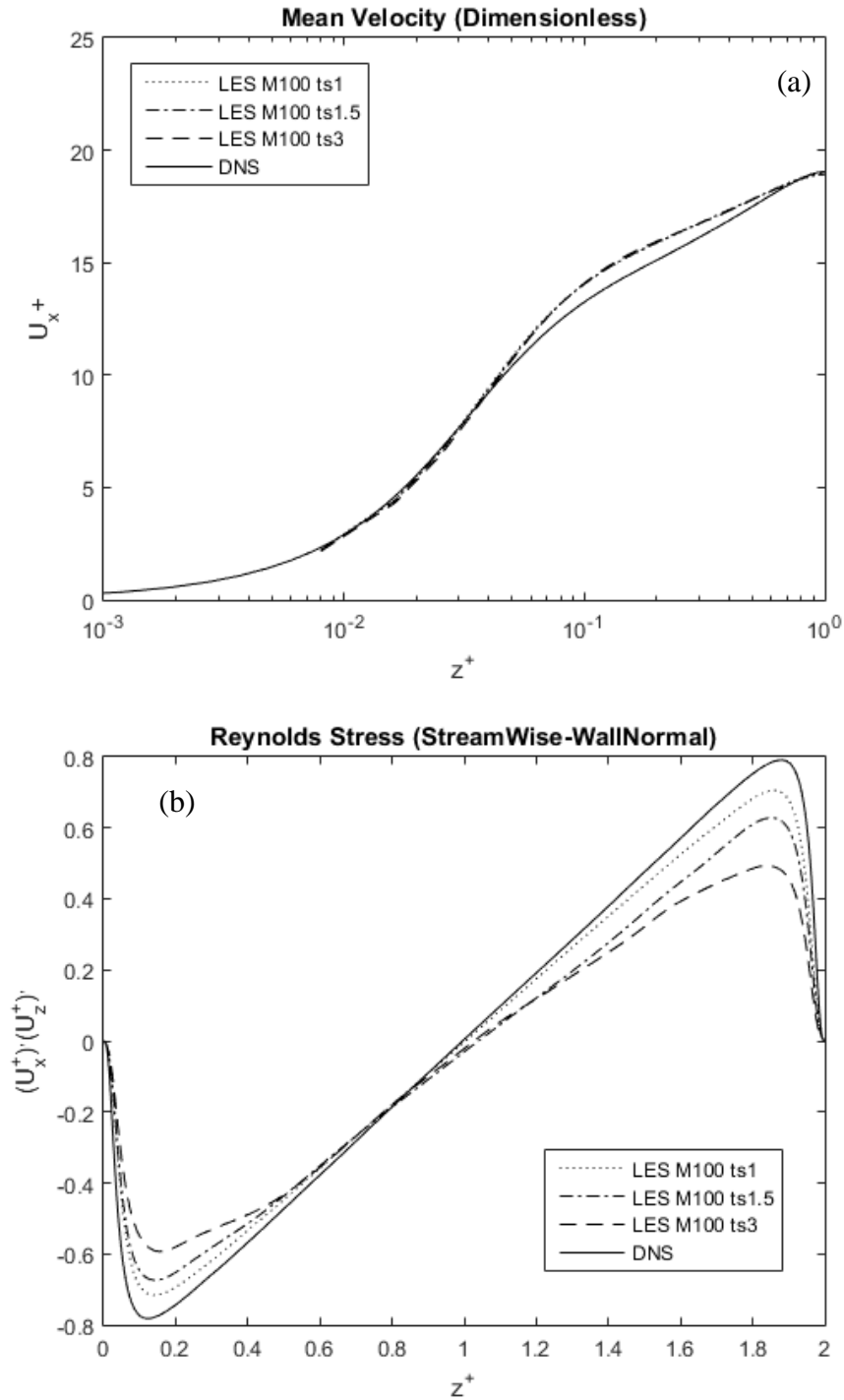


Figure A 3 (a) Mean streamwise fluid velocity; (b) Fluid Reynolds stress component. ($Re_\tau = 300$).

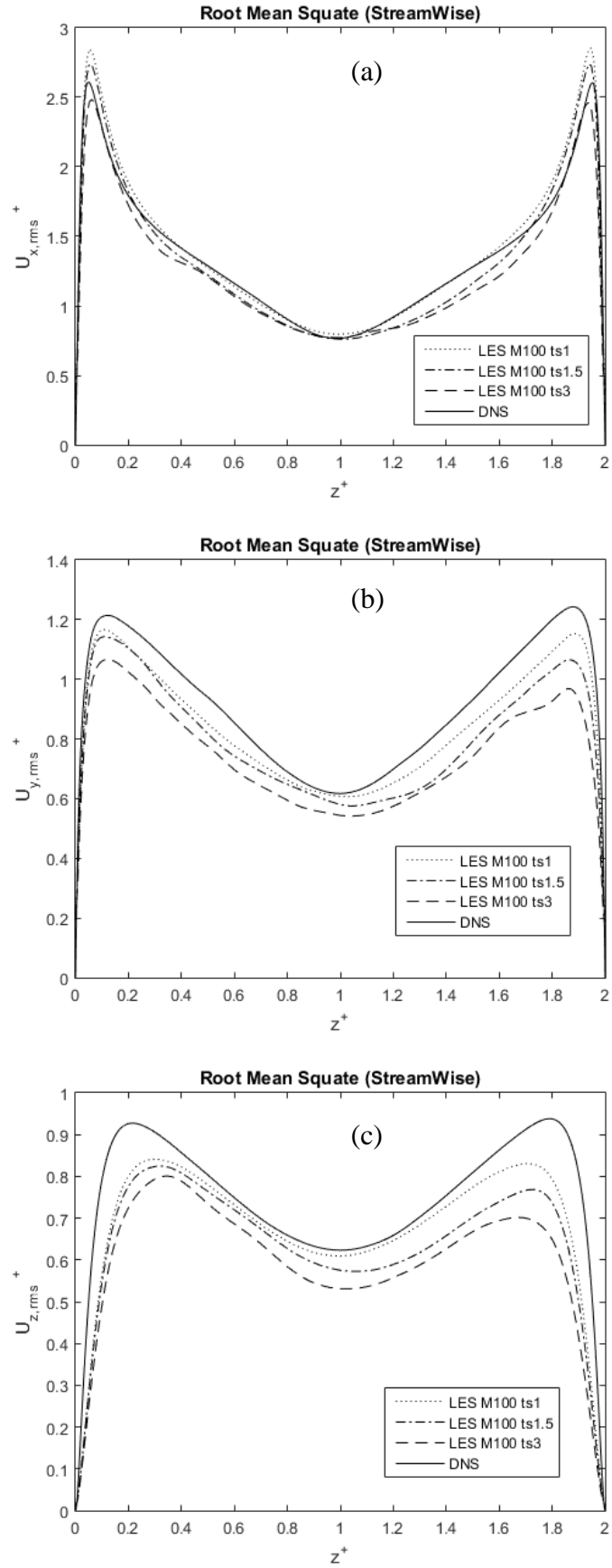


Figure A 4 Root mean square of fluid velocity fluctuation (a) streamwise rms component; (b) spanwise rms component; (c) wall-normal rms component. ($Re_\tau = 300$).

A. 3 Subgrid Scale Models

Three different subgrid scale models were compared; dynamic Smagorinsky, kinetic energy and wall-adapting local eddy-viscosity (WALE) have been compared against DNS. The dynamic smagorinsky SGS model showed the best results and has been selected for the final set up.

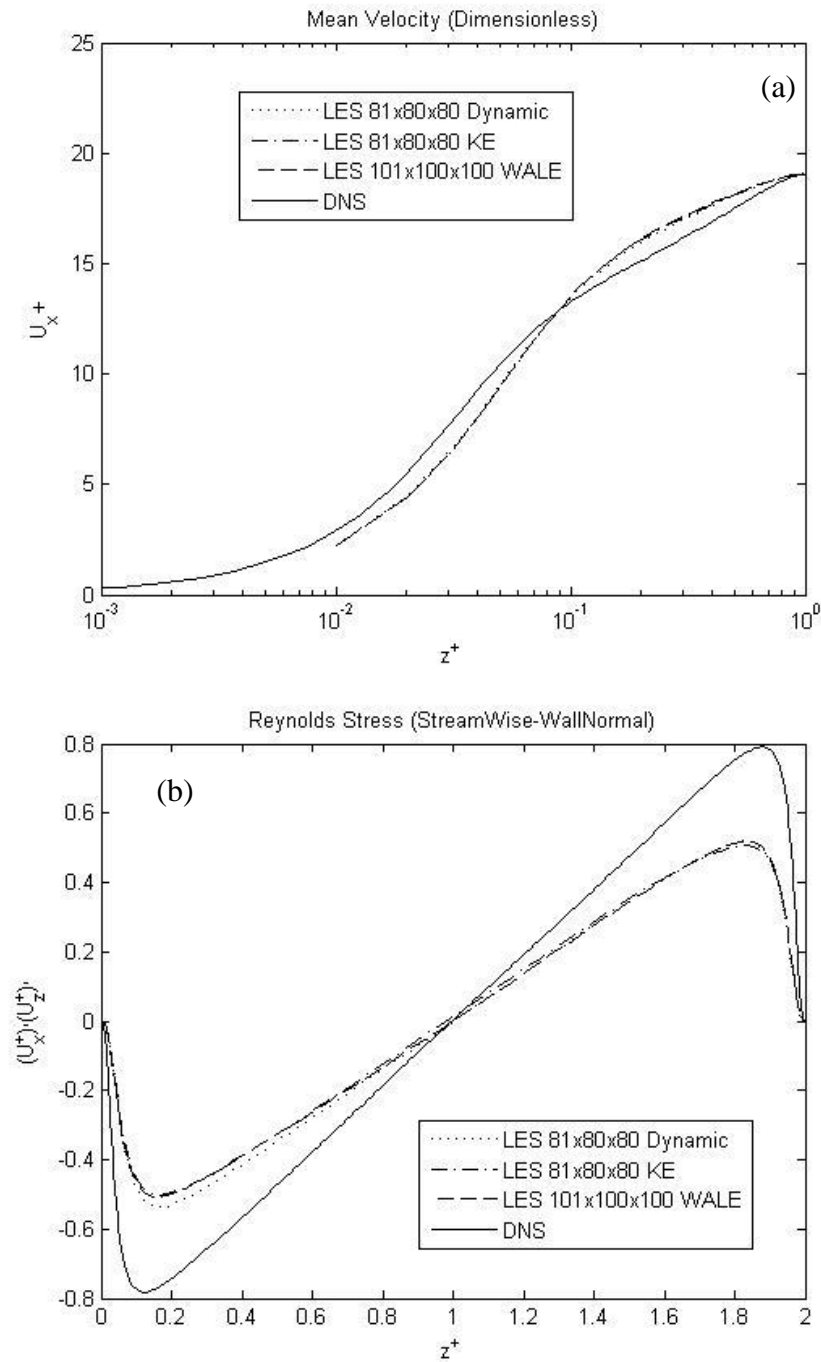


Figure A 5 (a) Mean streamwise fluid velocity; (b) Fluid Reynolds stress component. ($Re_\tau = 300$).

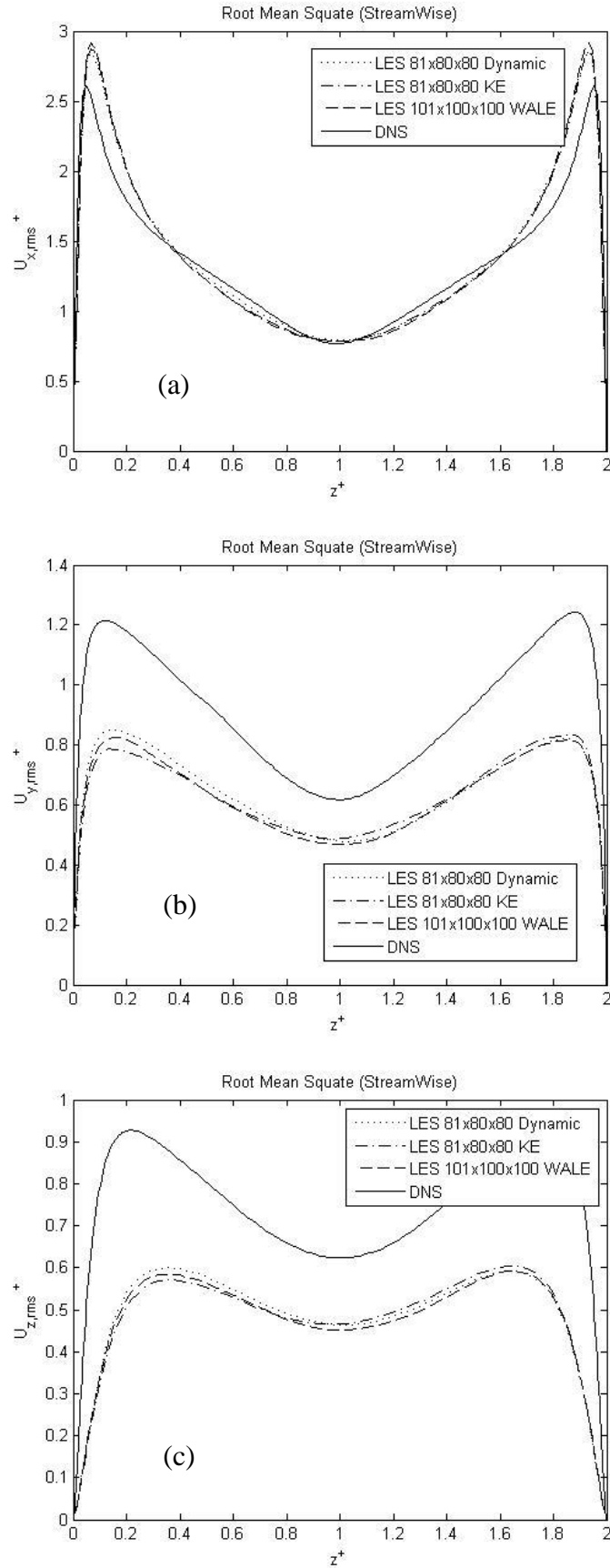


Figure A 6 Root mean square of fluid velocity fluctuation (a) streamwise rms component; (b) spanwise rms component; (c) wall-normal rms component. ($Re_\tau = 300$).

A. 4 Spatial Discretisation

Two different discretisation schemes were compared, bounded central differencing and central differencing against DNS. The latter showed the best results and has been selected for the final set up.

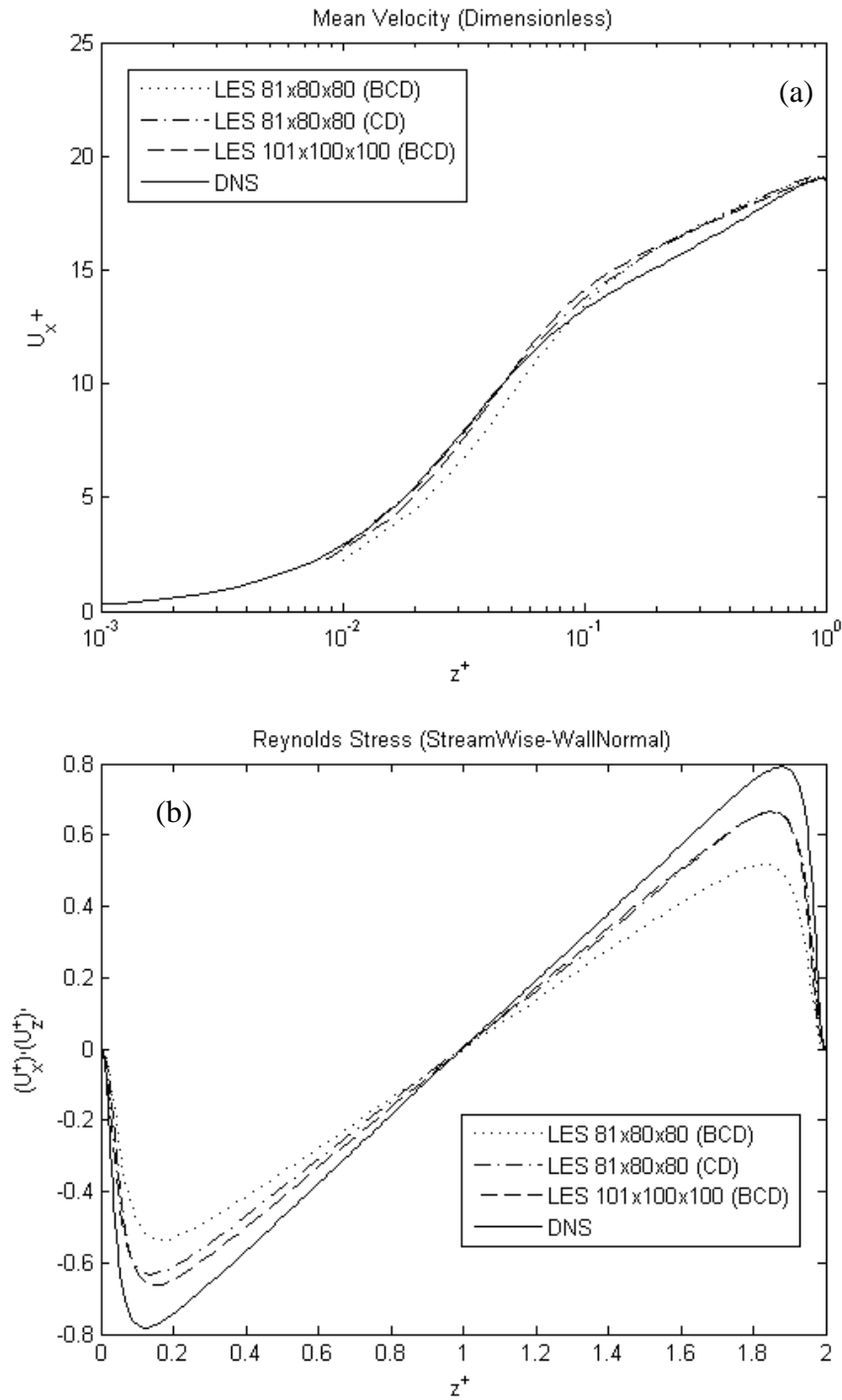


Figure A 7 (a) Mean streamwise fluid velocity; (b) Fluid Reynolds stress component. ($Re_\tau = 300$).

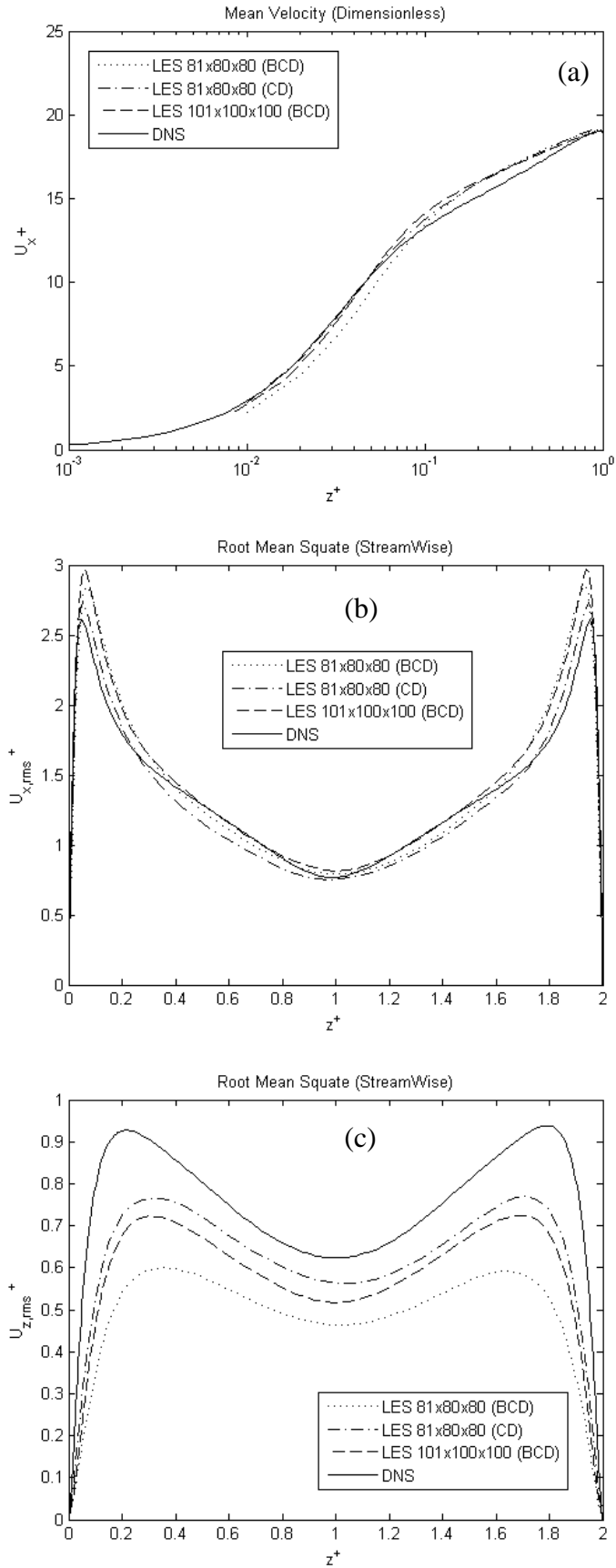


Figure A 8 Root mean square of fluid velocity fluctuation (a) streamwise rms component; (b) spanwise rms component; (c) wall-normal rms component. ($Re_\tau = 300$).

A. 5 Gradient and Derivatives

Two different gradients were compared, Green Gauss Node Based and Least Squares Cell Based against DNS. The latter showed the best results and has been selected for the final set up.

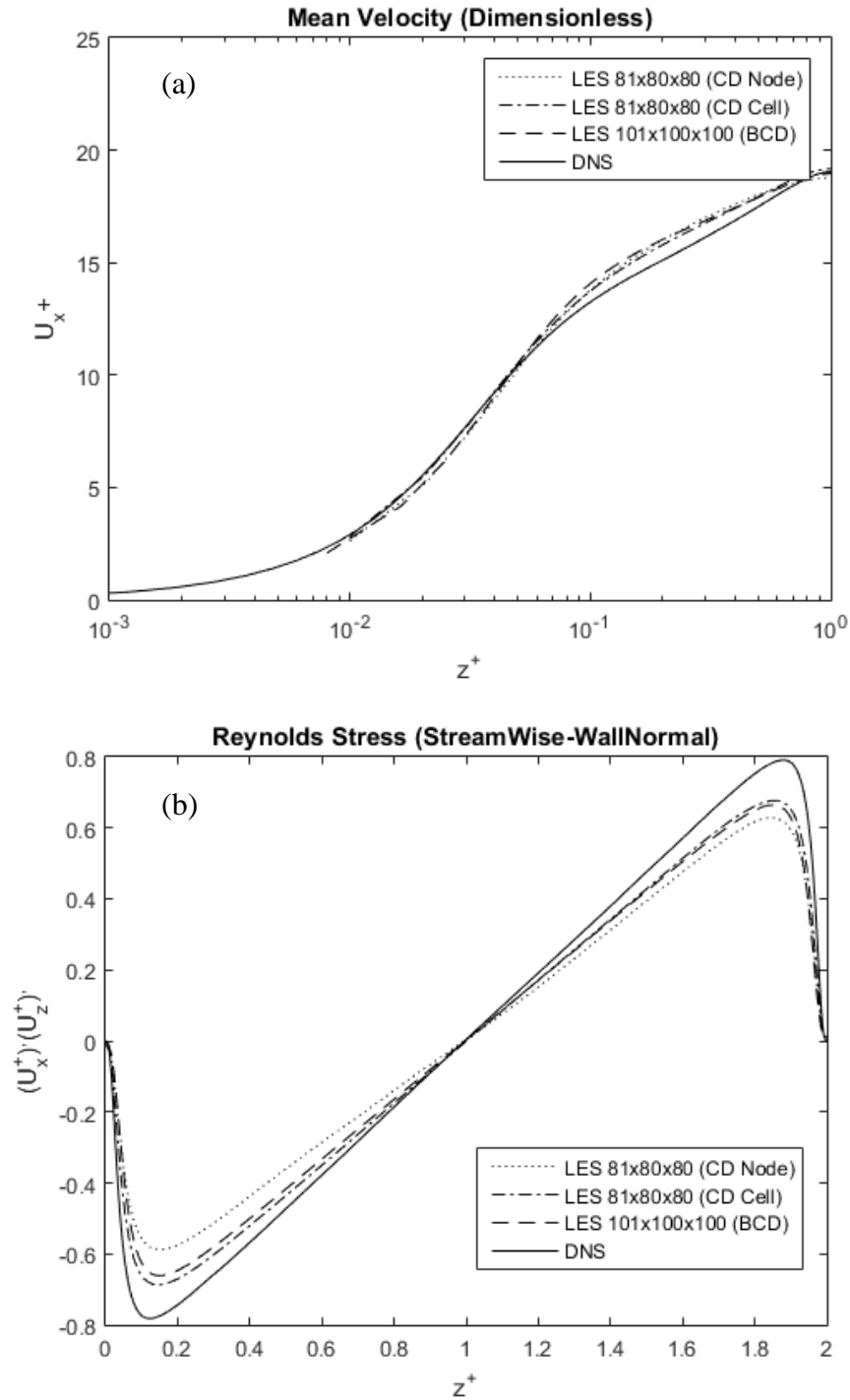


Figure A 9 (a) Mean streamwise fluid velocity; (b) Fluid Reynolds stress component. ($Re_\tau = 300$).

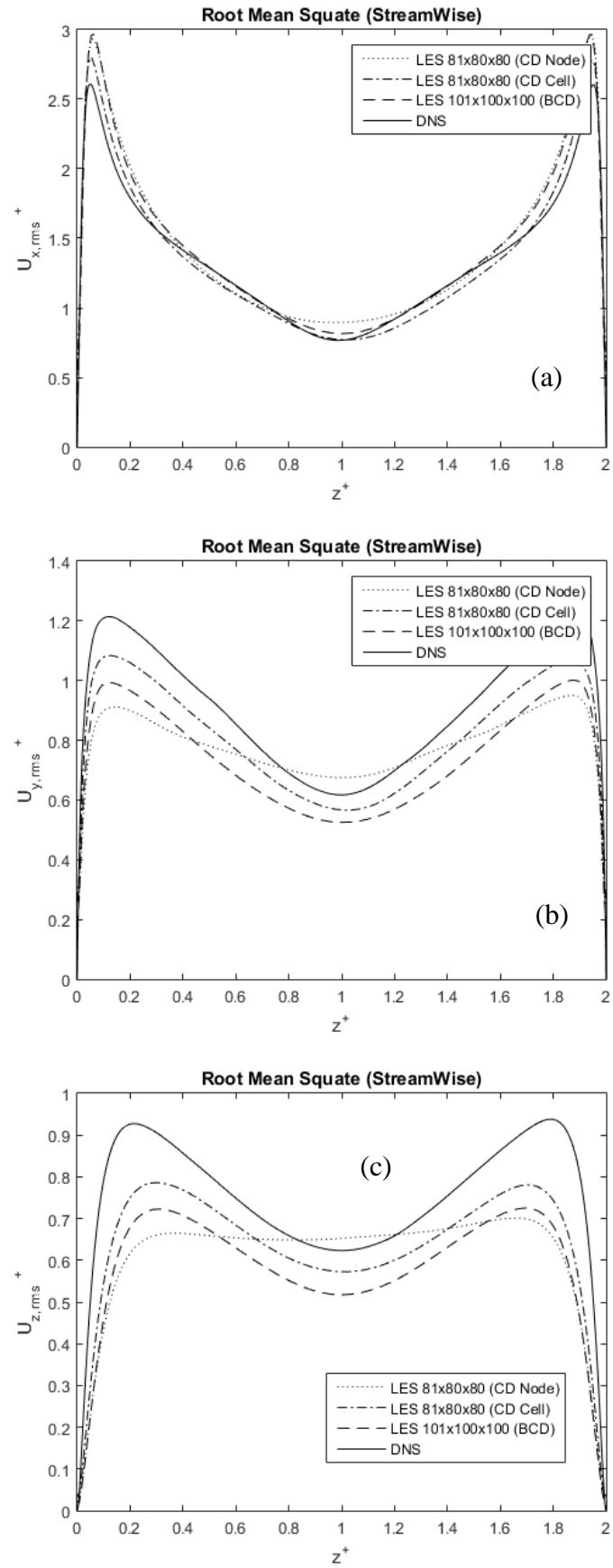


Figure A 10 Root mean square of fluid velocity fluctuation (a) streamwise rms component; (b) spanwise rms component; (c) wall-normal rms component. ($Re_\tau = 300$).

A. 6 Pressure-Velocity Coupling Method

Two different pressure-velocity coupling methods were compared, SIMPLEC and PISO against DNS. The latter showed the best results and has been selected for the final set up.

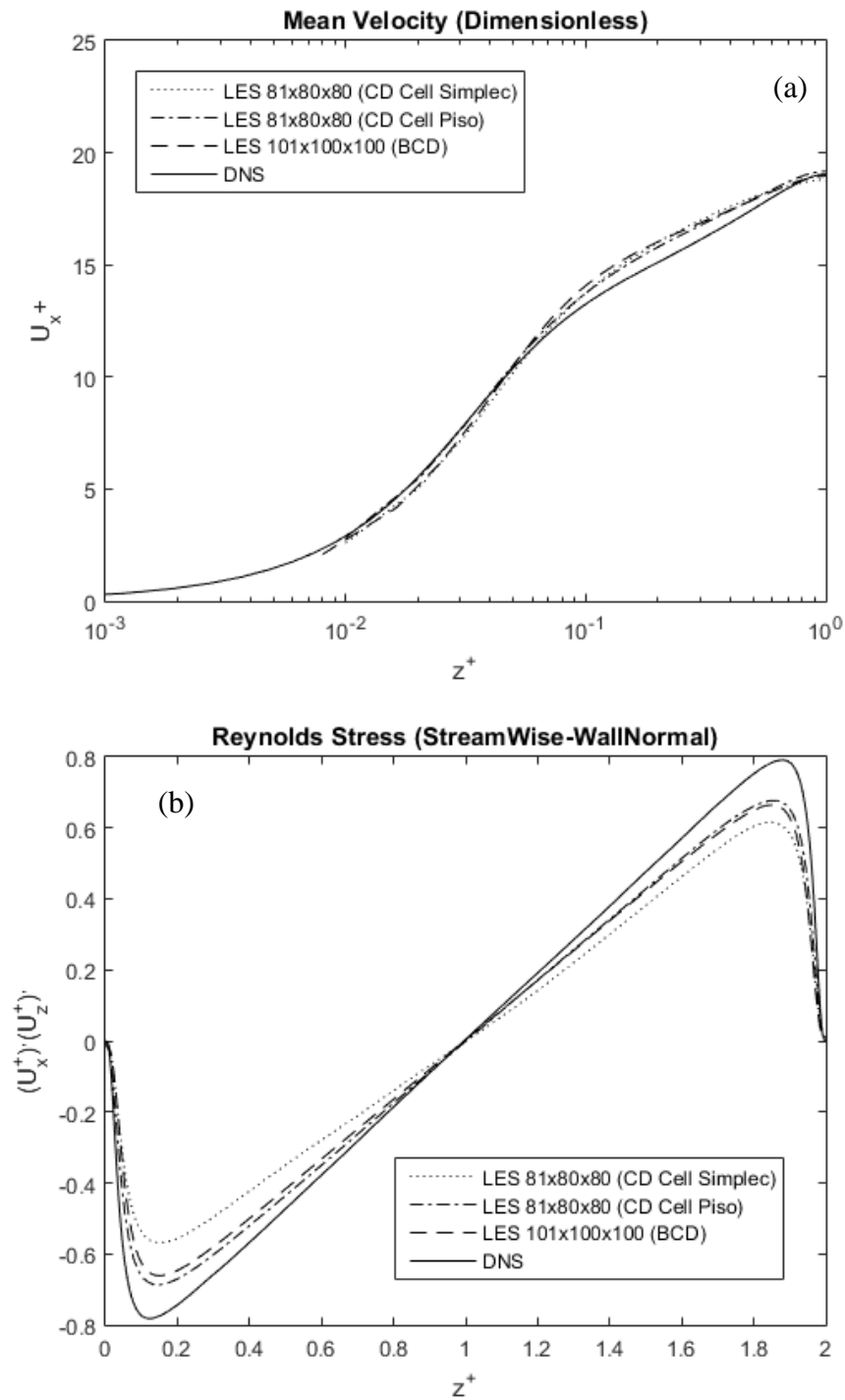


Figure A 11 (a) Mean streamwise fluid velocity; (b) Fluid Reynolds stress component. ($Re_\tau = 300$).

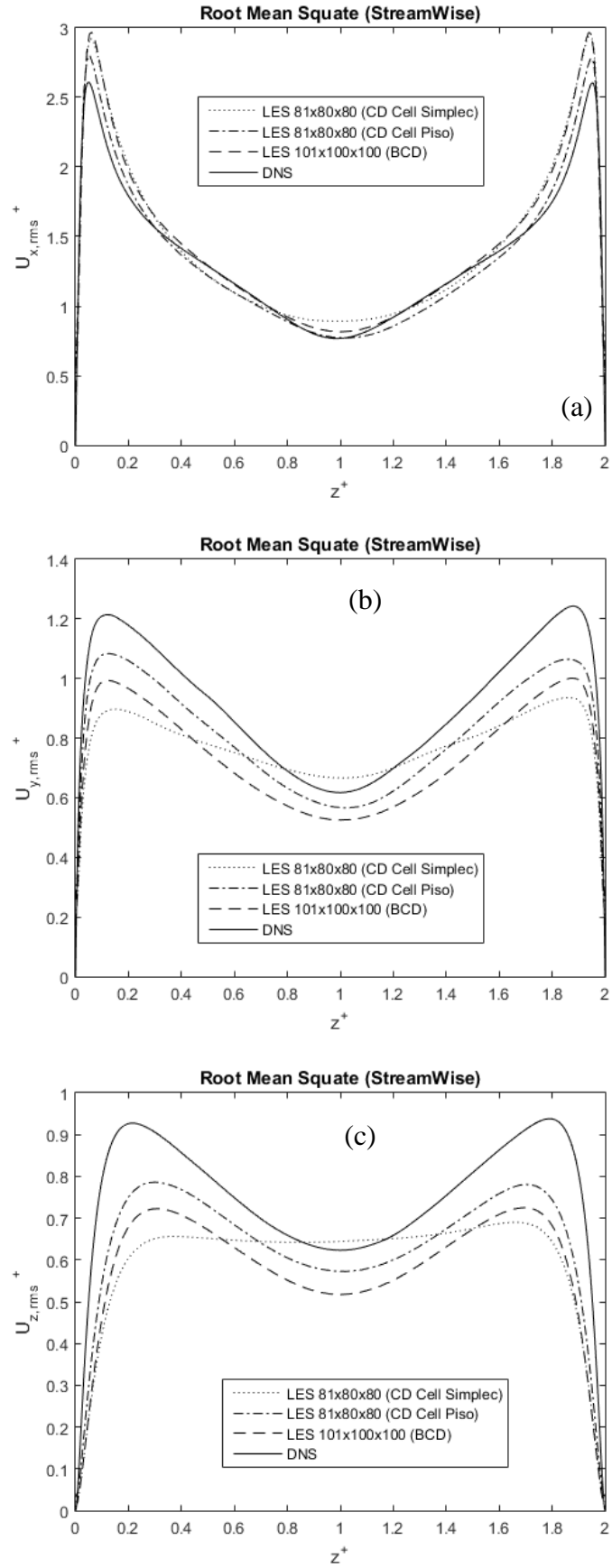


Figure A 12 Root mean square of fluid velocity fluctuation (a) streamwise rms component; (b) spanwise rms component; (c) wall-normal rms component. ($Re_\tau = 300$).

A. 7 Ending note to sensitivity study on fluid phase

Sensitivity studies have been conducted on the mesh size, time-step, SGS model, spatial discretisation, gradient and derivatives and pressure velocity coupling method, with the following selected 100^3 , 1×10^{-5} s, dynamic Smagorinsky, central differencing, cell and PISO, respectively.